

ISTANBUL TECHNICAL UNIVERSITY ★ GRADUATE SCHOOL

**DEVELOPMENT OF SINGLE-FRAME METHODS AIDED KALMAN-TYPE
FILTERING ALGORITHMS FOR ATTITUDE ESTIMATION OF
NANO-SATELLITES**

Ph.D. THESIS

Demet ÇILDEN GÜLER

Department of Aeronautics and Astronautics Engineering

Aeronautics and Astronautics Engineering Programme

AUGUST 2021

ISTANBUL TECHNICAL UNIVERSITY ★ GRADUATE SCHOOL

**DEVELOPMENT OF SINGLE-FRAME METHODS AIDED KALMAN-TYPE
FILTERING ALGORITHMS FOR ATTITUDE ESTIMATION OF
NANO-SATELLITES**

Ph.D. THESIS

**Demet ÇILDEN GÜLER
(511162104)**

Department of Aeronautics and Astronautics Engineering

Aeronautics and Astronautics Engineering Programme

**Thesis Advisor: Prof. Dr. Cengiz HACIZADE
Thesis Co-Advisor: Prof. Dr. Zerefşan KAYMAZ**

AUGUST 2021

İSTANBUL TEKNİK ÜNİVERSİTESİ ★ LİSANSÜSTÜ EĞİTİM ENSTİTÜSÜ

**NANO-UYDULARDA YÖNELİM KESTİRİMİ İÇİN
TEK-ÇERÇEVE YÖNTEMLERE DAYALI
KALMAN-TİPİ FİLTRELEME ALGORİTMALARININ GELİŞTİRİLMESİ**

DOKTORA TEZİ

**Demet ÇILDEN GÜLER
(511162104)**

Uçak ve Uzay Mühendisliği Anabilim Dalı

Uçak ve Uzay Mühendisliği Programı

**Tez Danışmanı: Prof. Dr. Cengiz HACIZADE
Eş Danışman: Prof. Dr. Zerefşan KAYMAZ**

AĞUSTOS 2021

Demet Çilden Güler, a Ph.D. student of ITU Graduate School student ID 511162104, successfully defended the dissertation entitled “DEVELOPMENT OF SINGLE-FRAME METHODS AIDED KALMAN-TYPE FILTERING ALGORITHMS FOR ATTITUDE ESTIMATION OF NANO-SATELLITES”, which she prepared after fulfilling the requirements specified in the associated legislations, before the jury whose signatures are below.

Thesis Advisor : **Prof. Dr. Cengiz HACIZADE**

Istanbul Technical University

Co-advisor : **Prof.Dr. Zereřsan KAYMAZ**

Istanbul Technical University

Jury Members : **Prof. Dr. Alim Rüstem ASLAN**

Istanbul Technical University

Assoc. Prof. Dr. Nazım Kemal ÜRE

Istanbul Technical University

Assoc. Prof. Dr. Janset DAŞDEMİR

Yildiz Technical University

Asst. Prof. Dr. Levent UCUN

Yildiz Technical University

Asst. Prof. Dr. Halil Ersin SÖKEN

Middle East Technical University

Date of Submission : 29 July 2021

Date of Defense : 20 August 2021

To Doğuş,

FOREWORD

I would like to express my deepest gratitude to my advisor Prof. Dr. Cengiz HACIZADE (Chingiz HAJIYEV) for his endless support, wise guidance, enthusing suggestions. Without his guidance and persistent help, this dissertation would not have been possible. I also would like to thank my co-advisor Prof. Dr. Zerefsan KAYMAZ for her valuable advice and support. They both believed in me, guided me, and helped me grow academically and personally.

Many thanks to the rest of the committee members of my dissertation, Assoc. Prof. Dr. Nazim Kemal URE, Assoc. Prof. Dr. Janset DASDEMIR, and Asst. Prof. Dr. Levent UCUN. I also thank a former committee member, Prof. Dr. Georgi DIMIROVSKI for his efforts.

I would like to thank Prof. Dr. Nikolai TSYGANENKO for sharing the most updated version of his models, and Asst. Prof. Dr. Halil Ersin SOKEN for the collaborative works that we carried out.

This research was supported through several scholarships: "Ph.D. Scholarship for Turkish Academicians" generously provided by ASELSAN (Military Electronic Industries), "2211-C - National Ph.D. Scholarship Programme in Priority Areas" by The Scientific and Technological Research Council of Turkey (TUBITAK). I was awarded the "Amelia Earhart Fellowship" in 2018 for my doctoral studies by Zonta International Foundation.

A research was carried out with the Positioning Algorithms research group at Tampere University of Technology (Tampere University), Finland, and was supported by EDUFI - Finnish Government Scholarship for 4 months. I thank my supervisor there, Prof. Dr. Robert PICHE for his guidance with regards to research and Dr. Matti RAITOHARJU for fruitful discussions and feedback.

Some part of the work was carried out in the Autonomous Vehicle Systems (AVS) Laboratory of the University of Colorado Boulder, USA for 12 months. I would like to thank Prof. Dr. Hanspeter SCHAUB who provided me supervision during this visit. I have learned a lot from him. Thank you to all my colleagues in the AVS lab for the insightful ideas. This research visit was supported under the "Visiting Student Researcher Programme" by Fulbright for the first 6 months and "2214-A - International Research Fellowship Programme for Ph.D. Students" by TUBITAK for the last 6 months.

A Ph.D. thesis project (No: 42097) was completed under the support of Istanbul Technical University, Scientific Research Projects (BAP) Department. A TUBITAK 1002 project (No: 120M859) was accepted for which I am the principal investigator. I also acknowledge these supports.

I would like to thank my close relatives Pakize UNALDI –my beloved aunt-, Ozgur UNALDI, Lena UNALDI, and Sevil GUNEL for supporting me without hesitation.

Last but not the least, I thank my parents, Sabire CILDEN and Sefik CILDEN, who always encouraged me and supported me, and my sister, Damla CILDEN, who learned about "albedo" more than she ever wanted. I thank my husband, Dogus GULER, for his loving and constant support. Everything is so much more bearable with you around.

August 2021

Demet ILDEN GÜLER
(Astronautical Engineer)

TABLE OF CONTENTS

	<u>Page</u>
FOREWORD	ix
TABLE OF CONTENTS	xi
ABBREVIATIONS	xv
SYMBOLS	xvii
LIST OF TABLES	xxi
LIST OF FIGURES	xxiii
SUMMARY	xxvii
ÖZET	xxxi
1. INTRODUCTION	1
1.1 Literature Review	2
1.1.1 Attitude estimation filters.....	2
1.1.2 External magnetic field	6
1.1.3 Planet’s albedo	10
1.2 Research Overview	12
2. SVD-AIDED EKF ATTITUDE ESTIMATION WITH UD FACTORIZED MEASUREMENT NOISE COVARIANCE	17
2.1 Abstract	17
2.2 Introduction	17
2.3 Mathematical Models	20
2.3.1 Satellite’s rotational motion	20
2.3.2 Measurement models	21
2.4 Singular Value Decomposition (SVD).....	22
2.5 SVD-Aided Extended Kalman Filter	23
2.5.1 UD decomposition of the measurement noise covariance matrix.....	24
2.5.2 EKF design for attitude and rate estimation.....	26
2.6 Analysis of Simulation Results	27
2.6.1 Simulation results for the satellite without gyros.....	28
2.6.2 Simulation results for the satellite having gyros.....	31
2.7 Conclusion.....	33
3. NANOSATELLITE ATTITUDE ESTIMATION FROM VECTOR MEASUREMENTS USING SVD-AIDED UKF ALGORITHM	35
3.1 Abstract	35
3.2 Introduction	35
3.3 Satellite Equations of Motion and Measurement Models	38
3.3.1 Satellite Equations of Motion	38
3.3.2 Sensor Models	40
3.4 SVD-Aided UKF Algorithm	41
3.4.1 Singular Value Decomposition Method.....	42
3.4.2 Unscented Kalman Filter	43
3.4.3 Attitude and Attitude Rate Estimation Using SaUKF	44
3.5 Simulations for a Nanosatellite	45
3.6 Conclusion.....	51

4. NANOSATELLITE ATTITUDE ESTIMATION USING KALMAN-TYPE FILTERS WITH NON-GAUSSIAN NOISE.....	53
4.1 Abstract.....	53
4.2 Introduction	53
4.3 Filtering Algorithms	56
4.3.1 Gaussian filter (GF) and unscented Kalman filter (UKF).....	57
4.3.2 R-adaptive Kalman filter (RUKF).....	59
4.3.3 Kullback-Leibler partitioned update Kalman filter (KLPUKF).....	60
4.3.4 Outlier-robust Kalman filter (ORKF)	61
4.3.5 Single-frame methods based Kalman filter (SFMKF)	62
4.4 Mathematical Models for Nanosatellite’s Rotational Motion	64
4.4.1 Equations of rotational motion	64
4.4.2 Measurement models.....	66
4.4.3 Magnetometer noise distribution analysis.....	68
4.5 Analysis and Results.....	69
4.5.1 Nominal operation mode	71
4.5.2 Operation with noise-increment magnetometer fault.....	73
4.6 Conclusions	76
5. EVALUATION OF GEOMAGNETIC FIELD MODELS USING MAGNETOMETER MEASUREMENTS FOR SATELLITE ATTITUDE DETERMINATION SYSTEM AT LOW EARTH ORBITS: CASE STUDIES	79
5.1 Abstract.....	79
5.2 Introduction	80
5.3 Data and Methodology	82
5.3.1 Geomagnetic models	83
5.3.2 Coordinate systems	85
5.3.3 Satellite observations	86
5.4 Analysis and Results.....	88
5.5 Discussion and Summary	104
6. GEOMAGNETIC DISTURBANCE EFFECTS ON SATELLITE ATTITUDE ESTIMATION.....	109
6.1 Abstract.....	109
6.2 Introduction	109
6.3 Satellite Equations of Motion.....	113
6.4 Components of Satellite Attitude Determination System	115
6.4.1 Geomagnetic field models.....	115
6.4.1.1 International geomagnetic reference field model.....	115
6.4.1.2 Tsyganenko’s model	116
6.4.2 Simulated magnetometer measurements	117
6.4.3 Simulated sun sensor measurements	118
6.4.4 Simulated rate gyro measurements	118
6.5 Attitude Estimation Algorithm	119
6.6 Dependence on Geomagnetic Activity	121
6.7 Influence of the Geomagnetic Activity on the Accuracy of Attitude.....	125
6.8 Conclusions	132
7. ATTITUDE ESTIMATION WITH ALBEDO INTERFERENCE ON SUN SENSOR MEASUREMENTS	135
7.1 Abstract.....	135
7.2 Introduction	135

7.3 Albedo and Coarse Sun Sensor Modeling.....	139
7.3.1 Mathematical model for a planet’s albedo.....	139
7.3.2 Albedo coefficients	142
7.3.3 Modeling of coarse sun sensor measurements in the presence of albedo.....	145
7.4 Gaussian Estimation Filters.....	146
7.4.1 Measurement models of the attitude sensors	149
7.5 Two-Stage Albedo Estimation Filter using Auto Regressive Model.....	150
7.6 Analysis and Results	152
7.6.1 Earth’s albedo data and sun sensor measurements	152
7.6.2 Spacecraft’s attitude estimation using earth’s albedo interfered sun sensors	160
7.7 Conclusion.....	170
8. CONCLUSIONS AND RECOMMENDATIONS.....	171
REFERENCES.....	177
CURRICULUM VITAE.....	189

ABBREVIATIONS

ADCS	: Attitude Determination and Control System
AE	: Auroral Electrojet Index
AIC	: Akaike's Information Criterion
AR	: Auto-Regressive
CERES	: Clouds and Earth Radiant Energy System
CME	: Coronal Mass Ejection
CSS	: Coarse Sun Sensor
C/NOFS	: Communication/Navigation Outage Forecast System
DSS	: Digital Sun Sensor
ECEF	: Earth-Centered, Earth-Fixed
ECI	: Earth-Centered Inertial
EKF	: Extended Kalman Filter
FOV	: Field of View
GEO	: Geographic Coordinates
GF	: Gaussian Filter
GRP	: Generalized Rodrigues Parameters
HSS	: High Speed Stream
IAGA	: International Association of Geomagnetism and Aeronomy
IGRF	: International Geomagnetic Reference Field
IS	: Interplanetary Shock
IMU	: Inertial Measurement Unit
IMP	: Interplanetary Magnetic Field
KF	: Kalman Filter
KLD	: Kullback-Leibler Divergence
KLPUKF	: Kullback-Leibler Partitioned Update Kalman Filter
Kp	: Planetary K-Index (Planetarische Kennziffer)
LEO	: Low Earth Orbit
MAG	: Geomagnetic Coordinates
MCUKF	: Maximum Correntropy Unscented Kalman Filter
MGS	: Mars Global Surveyor

MODIS	: Moderate Resolution Imaging Spectroradiometer
MRP	: Modified Rodrigues Parameter
NRMSE	: Normalized Root Mean Square Error
ORKF	: Outlier-Robust Kalman Filter
PDF	: Probability Density Function
QUEST	: Quaternion Estimator
RG	: Rate Gyro
RLS	: Recursive Least Squares
RMSE	: Root Mean Square Error
RNG	: Random Number Generator
RUKF	: R-Adaptive Kalman Filter
SFM	: Single-Frame Method
SFMKF	: Single-Frame Methods based Kalman Filter
SGP4	: Simplified General Perturbation Version 4
SVD	: Singular Value Decomposition
TAM	: Three-Axis Magnetometer
TES	: Thermal Emission Spectrometer
TOA	: Top of the Atmosphere
TOMS	: Total Ozone Mapping Spectrometer
TRMM	: Tropical Rainfall Measuring Mission
UAV	: Unmanned Aerial Vehicle
UKF	: Unscented Kalman Filter
WLS	: Weighted Least Square
WMM	: World Magnetic Model

SYMBOLS

\mathbf{a}_j	: Inverse Variance of Sensor j
A	: Area, m^2
\mathbf{A}	: Transformation Matrix
\mathbf{A}_{opt}	: Optimum Transformation Matrix
\mathbf{b}	: Sensor Observation Vector in Body Coordinates
\mathbf{B}	: Magnetic Field, nT
$[BN]$: Direction Cosine Matrix from Inertial Coordinates to Body Coordinates
$[BR]$: Direction Cosine Matrix from Reference Coordinates to Body Coordinates
$dA, \Delta A$: Incremental Area, m^2
$f(\cdot)$: System Function
F	: Solar Flux, W/m^2
$\mathbf{g} \times$: Skew-Symmetric Matrix
\mathbf{G}	: Gravitational Constant
$h(\cdot)$: Measurement Function
\mathbf{H}	: Measurement Matrix
I	: Output Current, A
J_x, J_y, J_z	: Components of the Principal Moments of Inertia, $\text{kg} \cdot \text{m}^2$
\mathbf{K}	: Kalman Gain Matrix
K_p	: Planetary K-Index (Planetarische Kennziffer)
M_E	: Earth's Mass
$\hat{\mathbf{n}}$: Unit Normal Vector
N_A	: Number of Differential Areas
N_x, N_y, N_z	: External Torque, $\text{N} \cdot \text{m}$
p	: Number of Previous Measurements
\mathbf{P}_{SVD}	: Rotation Angle Error Covariance Matrix of SVD

\mathbf{q}	: Euler Parameters, Quaternion Vector
\mathbf{Q}	: System Noise Covariance Matrix
\mathbf{r}	: Measurement Model Vector in Reference Coordinates
\mathbf{R}	: Measurement Noise Covariance Matrix
\mathbf{r}_{sc}	: Spacecraft Position Vector from an Incremental Area, m
$\hat{\mathbf{r}}_{sc}$: Spacecraft Direction Vector from an Incremental Area
$\hat{\mathbf{S}}$: Sun Heading Vector
\mathbf{U}	: Zero-Mean Gaussian Noise Vector with Covariance \mathbf{Q}
V	: Output Voltage, V
\mathbf{V}	: Zero-Mean Gaussian Noise Vector with Covariance \mathbf{R}
$\mathbf{v}_B, \mathbf{v}_S$: Measurement Noise Vector for Magnetometer and Sun Sensor respectively
\mathbf{W}	: Zero-Mean Gaussian Noise Vector with Covariance \mathbf{Q}
\mathbf{x}_0	: Initial State with Mean $\boldsymbol{\mu}_0$ and Covariance \mathbf{P}_0
$\mathbf{x}_k, \mathbf{X}_k$: State Vector at Time t_k
$\mathbf{y}, \mathbf{Z}, \mathbf{z}$: Measurement Vector
$\hat{\mathbf{y}}$: Prediction Vector
z_k	: Albedo Measurement at Time t_k
α	: Albedo Coefficient
δ	: Kronecker symbol
$\boldsymbol{\varepsilon}$: Zero-Mean Gaussian Noise Vector with Covariance \mathbf{R}
φ_i	: i^{th} Model Parameter
μ	: Standard Gravitational Parameter
$\boldsymbol{\omega}$: Angular Velocity, rad/s
$\boldsymbol{\sigma}_{B/R}$: Modified Rodrigues Parameters in Body Coordinates wrt Reference
Ξ	: Scaling Term
<i>Subscripts</i>	
A	: Central Point of dA on a Planet
ad	: Aerodynamic Disturbance
BI	: Body Frame with respect to Inertial Frame
BR	: Body Frame with respect to Reference Frame
d	: Caused by Sun

<i>gg</i>	: Gravity Gradient
I	: Instrument
<i>in</i>	: Incoming
<i>m</i>	: Measured
<i>max</i>	: Maximum
<i>md</i>	: Magnetic Dipole
<i>o</i>	: Orbit Frame
<i>out</i>	: Outgoing
P	: Planet
<i>s</i>	: Sunlit
<i>sc</i>	: Spacecraft
<i>sp</i>	: Solar Pressure
α	: Caused by Albedo

LIST OF TABLES

	<u>Page</u>
Table 2.1 : RMSE results of attitude angles (gyro-free).	30
Table 2.2 : RMSE results of attitude angles (with gyro).....	32
Table 3.1 : Computation times for each algorithm.	51
Table 4.1 : Akaike’s information criterion (AIC) analysis of distributions for magnetometer noise.	69
Table 4.2 : RMSE of estimations during $t \geq 1500$ s, averaged over 100 simulations.	73
Table 4.3 : Filter RMSE during faulty period, averaged over 100 simulations.	76
Table 5.1 : Orbital properties of the spacecraft used in this study.	87
Table 5.2 : Magnetically quiet and active days selected for the study.....	89
Table 5.3 : Classification of geomagnetic storm and substorms based on Dst, K _p , and AE magnetic indices. [133,134]	90
Table 5.4 : RMS errors for C/NOFS (Case-1) comparisons for the geomagnetically quiet day (left) and active day (right).....	96
Table 5.5 : RMS errors for C/NOFS (Case-2) comparisons for the geomagnetically quiet day (left) and active day (right).....	98
Table 5.6 : RMS errors for SWARM A (Case-3) comparisons for the geomagnetically quiet day (left) and active day (right).	101
Table 5.7 : Overall evaluation of average angles.	104
Table 6.1 : K_p index and model parameter IOPT range in T89 model.....	117
Table 6.2 : NRMSE between estimated and actual attitude angles.....	130
Table 7.1 : 11-year averaged albedo coefficients over regions and seasons indicated (Clear-sky).....	154
Table 7.2 : 11-year averaged albedo coefficients over regions and seasons indicated (All-sky).	156
Table 7.3 : Details of the models used for albedo estimation.	163
Table 7.4 : Performance comparison of the albedo models considered.....	167
Table 7.5 : Attitude angle estimation performance.	168
Table 7.6 : Performance comparison of the attitude estimation algorithms considered (Averaged over 100 simulations).	169

LIST OF FIGURES

	<u>Page</u>
Figure 1.1 : Illustration of external magnetic field and planet’s albedo affecting the spacecraft.....	13
Figure 2.1 : UD decomposition algorithm structure.	25
Figure 2.2 : Integrated SVD/EKF attitude and rate estimation block diagram with UD factorization.....	27
Figure 2.3 : Roll angle estimations, error, and variance of only SVD and SVD-aided EKF using UD factorization (gyro-free).	29
Figure 2.4 : Pitch angle estimations, error, and variance of only SVD and SVD-aided EKF using UD factorization (gyro-free).	29
Figure 2.5 : Yaw angle estimations, error, and variance of only SVD and SVD-aided EKF using UD factorization (gyro-free).	30
Figure 2.6 : Roll angle estimations, error, and variance of only SVD and SVD-aided EKF using UD factorization (with gyro).....	31
Figure 2.7 : Pitch angle estimations, error, and variance of only SVD and SVD-aided EKF using UD factorization (with gyro).....	32
Figure 2.8 : Yaw angle estimations, error, and variance of only SVD and SVD-aided EKF using UD factorization (with gyro).....	32
Figure 3.1 : Scheme for the attitude and attitude rate estimation using the SaUKF.	45
Figure 3.2 : Estimation error for quaternion q_1 ; comparison of the UKF and SVD only estimations with the SaUKF. Subfigure a zooms to the indicated part in the main figure.	46
Figure 3.3 : Quaternion estimation error for the SaUKF with different process noise covariance, Q , values.	47
Figure 3.4 : Norm of attitude estimation errors.	48
Figure 3.5 : Estimation of the angular rate around x axis.	48
Figure 3.6 : A block diagram of attitude and attitude rate estimation for the proposed algorithm.	49
Figure 3.7 : Estimation of the quaternions by SaUKF (outside of the eclipse) and UKF (in eclipse).	50
Figure 4.1 : Algorithm schemes of GF (a), KLPUKF (b), ORKF (c).....	58
Figure 4.2 : SFMKF algorithm scheme.	64
Figure 4.3 : Distribution fitting for magnetometer measurement noises on x, y, and z axes.....	69
Figure 4.4 : Work vs accuracy for 5 filters.	72
Figure 4.5 : Attitude (left) and angular velocity (right) estimation errors for normal operation mode, single simulation.	72
Figure 4.6 : Box plots of estimation errors during averaged over 100 simulations.	72
Figure 4.7 : RUKF scaling factor for long-term (a) and short-term (b) magnetometer fault.	74

Figure 4.8 : RUKF scaling factor for normal and t-distributions without any magnetometer faults.	75
Figure 4.9 : Attitude errors for long-term (a) and short-term (b) magnetometer faults, single simulation.....	75
Figure 5.1 : Flow chart for the comparisons.	85
Figure 5.2 : A sketch showing the coordinate systems along with a circular trajectory of a satellite.	86
Figure 5.3 : An example of orbit averaged data. C/NOFS magnetic field components on March 7, 2009. The black line is the original data while the blue line is the orbit averaged data.....	91
Figure 5.4 : Differences between the observations and the model result for magnetic field components from C/NOFS satellite on March 7, 2009, when there is no geomagnetic activity (left); and on March 17, 2013, when there is a geomagnetic storm (right).	92
Figure 5.5 : Angles, between the vector magnetic fields from the models and the observations, for the C/NOFS satellite on March 7, 2009, when there is no geomagnetic activity (left); and on March 17, 2013, when there is a geomagnetic storm (right).	95
Figure 5.6 : Differences between the observations and the model result for magnetic field components from C/NOFS satellite on January 5, 2013, when there is no geomagnetic activity (left); and on August 4, 2010, when there is a geomagnetic storm (right).	97
Figure 5.7 : Angles, between the vector magnetic fields from the models and the observations, for the C/NOFS satellite on January 5, 2013, when there is no geomagnetic activity (left); and on August 4, 2010, when there is a geomagnetic storm (right).	98
Figure 5.8 : Differences between the observations and the model result for magnetic field components from SWARM A satellite on January 18, 2014, when there is no geomagnetic activity (left); and on February 20, 2014, when there is a geomagnetic storm (right).....	99
Figure 5.9 : Angles, between the vector magnetic fields from the models and the observations, for SWARM A satellite on January 18, 2014, when there is no geomagnetic activity (left); and on February 20, 2014, when there is a geomagnetic storm (right).	101
Figure 5.10 : Angle distributions for all cases for quiet (orange) and active (blue) cases. The upper panel is for the differences between the IGRF model and observations while the bottom panels are for the differences between the T89 model and observations.....	102
Figure 5.11 : Comparison of the difference in angles from the models: Blue is for active day and orange for quiet days.	104
Figure 6.1 : Attitude estimation scheme using different magnetic field models and different sensors.	120
Figure 6.2 : Noise, constant bias, accumulated bias, and a sample of external magnetic field disturbance for different K_p levels.	122
Figure 6.3 : The angle between IGRF and T89 magnetic field vectors for different K_p levels in the T89 model.	123
Figure 6.4 : Variations in angle with geomagnetic activity for low- (a), mid- (b) and high- (c) latitudes.....	124

Figure 6.5 : Dependence of external field ($\mathbf{B}_{EXT}/\mathbf{B}_{model}$) on satellite's altitude obtained from T89 model for IOPT = 1 and IOPT = 7 in T89 model..	125
Figure 6.6 : Estimated and actual attitude angles using the T89 model in traditional EKF for the active geomagnetic conditions and for magnetometer configuration only (scenario 1).	126
Figure 6.7 : Estimated errors using IGRF model during a quiet time for each attitude component (a) and for each scenario (b).	128
Figure 6.8 : Estimated errors for IGRF model predictions of the attitude angles during the quiet (solid) and active (dashed) geomagnetic conditions...	129
Figure 6.9 : Differences between the errors associated with both models for quiet (a) and active (b) days.	129
Figure 7.1 : Illustration of considered radiation sources on a spacecraft.....	136
Figure 7.2 : Illustration of the unit normal, sun, and spacecraft heading vectors. ..	140
Figure 7.3 : Illustration of the observed illuminated area.	141
Figure 7.4 : Illustration of the albedo influence on an instrument from observed incremental areas of a planet.	143
Figure 7.5 : Illuminated field of view area with regular (a) and irregular (b) grid examples.....	143
Figure 7.6 : Albedo coefficients averaged over CERES 2018 monthly data under clear-sky (a) and all-sky (b) conditions.....	144
Figure 7.7 : The process for simulating the CSS albedo readings.	145
Figure 7.8 : Monthly albedo box plots for 11 years under clear-sky (bottom) and all- sky (top) conditions.....	153
Figure 7.9 : 11-year averaged global albedo coefficients over 4-seasons under clear- sky (left) and all-sky (right) conditions.....	155
Figure 7.10 : Illustration of CSS placement on each platform.....	156
Figure 7.11 : Illustration of sun, spacecraft, and Earth positions for Scenario 1...	157
Figure 7.12 : CSS field of views on Face 4 of the satellite at 800 km altitude.....	158
Figure 7.13 : CSS-1 field of view on Face 4 of the satellite at three different altitudes (left to right: 500 km, 5000 km, and 10000 km).	159
Figure 7.14 : Altitude dependent CSS current outputs on Face 4 of the satellite. ..	159
Figure 7.15 : Longitude dependent CSS-1 current outputs on Face 4 of the satellite at 800 km under clear-sky (left) and all-sky (right) conditions.....	160
Figure 7.16 : Albedo estimation procedure based on albedo data based models (a) and AR albedo model (b).	161
Figure 7.17 : Albedo model outputs of Reference Model 1 and 2 for three orbits.	163
Figure 7.18 : Albedo model outputs of several models comparing to Reference Model 1 (left) and Reference Model 2 (right).	164
Figure 7.19 : Attitude estimation framework based on albedo data based models (a) and AR albedo model (b).	166
Figure 7.20 : Attitude error norms of the SVD, SVD-aided EKF and EKF methods using TAM and CSS with albedo interference based on Model 4 (a) and AR Model (b).	167
Figure 7.21 : Attitude error norms of EKF using CSS with albedo interference based on Model 4 (a) and AR Model (b).	168

DEVELOPMENT OF SINGLE-FRAME METHODS AIDED KALMAN-TYPE FILTERING ALGORITHMS FOR ATTITUDE ESTIMATION OF NANO-SATELLITES

SUMMARY

There is a growing demand for the development of highly accurate attitude estimation algorithms even for small satellite e.g. nanosatellites with attitude sensors that are typically cheap, simple, and light because, in order to control the orientation of a satellite or its instrument, it is important to estimate the attitude accurately. Here, the estimation is especially important in nanosatellites, whose sensors are usually low-cost and have higher noise levels than high-end sensors. The algorithms should also be able to run on systems with very restricted computer power. One of the aims of the thesis is to develop attitude estimation filters that improve the estimation accuracy while not increasing the computational burden too much. For this purpose, Kalman filter extensions are examined for attitude estimation with a 3-axis magnetometer and sun sensor measurements.

In the first part of this research, the performance of the developed extensions for the state of art attitude estimation filters is evaluated by taking into consideration both accuracy and computational complexity. Here, single-frame method-aided attitude estimation algorithms are introduced. As the single-frame method, singular value decomposition (SVD) is used that aided extended Kalman filter (EKF) and unscented Kalman filter (UKF) for nanosatellite's attitude estimation. The development of the system model of the filter, and the measurement models of the sun sensors and the magnetometers, which are used to generate vector observations is presented. Vector observations are used in SVD for satellite attitude determination purposes. In the presented method, filtering stage inputs are coming from SVD as the linear measurements of attitude and their error covariance relations. In this step, UD is also introduced for EKF that factorizes the attitude angles error covariance with forming the measurements in order to obtain the appropriate inputs for the filtering stage. The necessity of the sub-step, called UD factorization on the measurement covariance is discussed. The accuracy of the estimation results of the SVD-aided EKF with and without UD factorization is compared for the estimation performance. Then, a case including an eclipse period is considered and possible switching rules are discussed especially for the eclipse period, when the sun sensor measurements are not available.

There are also other attitude estimation algorithms that have strengths in coping well with nonlinear problems or working well with heavy-tailed noise. Therefore, different types of filters are also tested to see what kind of filter provides the largest improvements in the estimation accuracy. Kalman-type filter extensions correspond to different ways of approximating the models. In that sense, a filter takes the non-Gaussianity into account and updates the measurement noise covariance whereas another one minimizes the nonlinearity. Various other algorithms can be used for adapting the Kalman filter by scaling or updating the covariance of the filter. The

filtering extensions are developed so that each of them is designed to mitigate different types of error sources for the Kalman filter that is used as the baseline.

The distribution of the magnetometer noises for a better model is also investigated using sensor flight data. The filters are tested for the measurement noise with the best fitting distribution. The responses of the filters are performed under different operation modes such as nominal mode, recovery from incorrect initial state, short and long-term sensor faults.

Another aspect of the thesis is to investigate two major environmental disturbances on the spacecraft close enough to a planet: the external magnetic field and the planet's albedo. As magnetometers and sun sensors are widely used attitude sensors, external magnetic field and albedo models have an important role in the accuracy of the attitude estimation. The magnetometers implemented on a spacecraft measure the internal geomagnetic field sources caused by the planet's dynamo and crust as well as the external sources such as solar wind and interplanetary magnetic field. However, the models that include only the internal field are frequently used, which might remain incapable when geomagnetic activities occur causing an error in the magnetic field model in comparison with the sensor measurements. Here, the external field variations caused by the solar wind, magnetic storms, and magnetospheric substorms are generally treated as bias on the measurements and removed from the measurements by estimating them in the augmented states. The measurement, in this case, diverges from the real case after the elimination. Another approach can be proposed to consider the external field in the model and not treat it as an error source. In this way, the model can represent the magnetic field closer to reality.

If a magnetic field model used for the spacecraft attitude control does not consider the external fields, it can misevaluate that there is more noise on the sensor, while the variations are caused by a physical phenomenon (e.g. a magnetospheric substorm event), and not the sensor itself. Different geomagnetic field models are compared to study the errors resulting from the representation of magnetic fields that affect the satellite attitude determination system. For this purpose, we used magnetometer data from low Earth-orbiting spacecraft and the geomagnetic models, IGRF and T89 to study the differences between the magnetic field components, strength, and the angle between the predicted and observed vector magnetic fields. The comparisons are made during geomagnetically active and quiet days to see the effects of the geomagnetic storms and sub-storms on the predicted and observed magnetic fields and angles. The angles, in turn, are used to estimate the spacecraft attitude, and hence, the differences between model and observations as well as between two models become important to determine and reduce the errors associated with the models under different space environment conditions. It is shown that the models differ from the observations even during the geomagnetically quiet times but the associated errors during the geomagnetically active times increase more. It is found that the T89 model gives closer predictions to the observations, especially during active times and the errors are smaller compared to the IGRF model. The magnitude of the error in the angle under both environmental conditions is found to be less than 1 degree. The effects of magnetic disturbances resulting from geospace storms on the satellite attitudes estimated by EKF are also examined. The increasing levels of geomagnetic activity affect geomagnetic field vectors predicted by IGRF and T89 models. Various sensor combinations including magnetometer, gyroscope, and sun sensor are evaluated for magnetically quiet and active times. Errors are calculated for estimated attitude angles

and differences are discussed. This portion of the study emphasizes the importance of environmental factors on the satellite attitude determination systems.

Since the sun sensors are frequently used in both planet-orbiting satellites and interplanetary spacecraft missions in the solar system, a spacecraft close enough to the sun and a planet is also considered. The spacecraft receives electromagnetic radiation of direct solar flux, reflected radiation namely albedo, and emitted radiation of that planet. The albedo is the fraction of sunlight incident and reflected light from the planet. Spacecraft can be exposed to albedo when it sees the sunlit part of the planet. The albedo values vary depending on the seasonal, geographical, diurnal changes as well as the cloud coverage. The sun sensor not only measures the light from the sun but also the albedo of the planet. So, a planet's albedo interference can cause anomalous sun sensor readings. This can be eliminated by filtering the sun sensors to be insensitive to albedo. However, in most of the nanosatellites, coarse sun sensors are used and they are sensitive to albedo. Besides, some critical components and spacecraft systems e.g. optical sensors, thermal and power subsystems have to take the light reflectance into account. This makes the albedo estimations a significant factor in their analysis as well. Therefore, in this research, the purpose is to estimate the planet's albedo using a simple model with less parameter dependency than any albedo models and to estimate the attitude by comprising the corrected sun sensor measurements.

A three-axis attitude estimation scheme is presented using a set of Earth's albedo interfered coarse sun sensors (CSSs), which are inexpensive, small in size, and light in power consumption. For modeling the interference, a two-stage albedo estimation algorithm based on an autoregressive (AR) model is proposed. The algorithm does not require any data such as albedo coefficients, spacecraft position, sky condition, or ground coverage, other than albedo measurements. The results are compared with different albedo models based on the reference conditions. The models are obtained using either a data-driven or estimated approach. The proposed estimated albedo is fed to the CSS measurements for correction. The corrected CSS measurements are processed under various estimation techniques with different sensor configurations. The relative performance of the attitude estimation schemes when using different albedo models is examined.

In summary, the effects of two main space environment disturbances on the satellite's attitude estimation are studied with a comprehensive analysis with different types of spacecraft trajectories under various environmental conditions. The performance analyses are expected to be of interest to the aerospace community as they can be reproducible for the applications of spacecraft systems or aerial vehicles.

NANO-UYDULARDA YÖNELİM KESTİRİMİ İÇİN TEK-ÇERÇEVE YÖNTEMLERE DAYALI KALMAN-TİPİ FİLTRELEME ALGORİTMALARININ GELİŞTİRİLMESİ

ÖZET

Yüksek doğruluklu yönelim kestirim algoritmalarının geliştirilmesi, uzay aracının veya aletin yöneliminin kontrolündeki öneminden dolayı küçük uydularda dahi talep edilmektedir. Bu çalışmanın konusu olan nano-uydulara genellikle ucuz, basit ve hafif olan yönelim algılayıcıları tercih edilmektedir. Burada, kestirim algoritmaları, yüksek kalitede üretilmiş algılayıcılara göre daha yüksek gürültü seviyelerine sahip düşük maliyetli nano-uydular için özellikle önem taşımaktadır. Geliştirilen algoritmalar, bilgisayar gücü çok kısıtlı olan sistemlerde de çalışabilmelidir. Bu tez kapsamında hesaplama yükünü çok fazla artırmadan kestirim doğruluğunu artıran yönelim kestirim filtrelerinin geliştirilmesi amaçlanmaktadır. Bu nedenle, Kalman filtre uzantıları, 3 eksenli manyetometre ve güneş sensörü ölçümleri kullanılarak yönelim kestirimi için incelenmiştir.

Araştırmanın ilk bölümünde, gelişmiş yönelim kestirim filtreleri için tasarlanan uzantıların performansı hem doğruluk hem de hesaplama yükü dikkate alınarak değerlendirilmiştir. Burada, öncelikle tek-çerçeve yöntemi destekli yönelim kestirim algoritmaları tanıtılmaktadır. Nano-uyduların yönelim kestirimi için genişletilmiş Kalman filtresi (GKF) veya sezgisiz Kalman filtresi (SKF)'ne destek veren tek çerçeve yöntemi olarak tekil değer ayrışımı (TDA) yöntemi kullanılmıştır. Filtrenin sistem modeli ve vektör gözlemlerini oluşturan güneş sensörleri ve manyetometrelerin ölçüm modelleri sunulmuştur. Vektör gözlemleri, uydu durum vektörünün belirlenmesi amacıyla TDA'da kullanılır. Sunulan yöntemde filtre aşamasına ait girdiler, yönelim açılarının doğrusal ölçümleri ve bunların hata kovaryans terimleri olarak TDA'dan gelmektedir. Bu adımda UD, filtreleme aşaması için uygun girdileri elde etmek üzere ölçümleri yeniden oluştururken, yönelim açıları hata kovaryansını da faktörize etmektedir. Ölçme kovaryansı üzerinde UD faktörizasyonu adı verilen alt basamağın gerekliliği tartışılmıştır. UD kullanılarak ve kullanılmadan oluşturulan TDA destekli GKF algoritmasının yönelim kestirim sonuçlarının doğruluğu karşılaştırılmıştır. Ardından, gezegenin güneş almayan tarafındaki eklips periyodu durumu göz önüne alınmış ve olası anahtarlama kuralları, güneş sensörü ölçümlerinin mevcut olmadığı bu periyot çerçevesinde yorumlanmıştır.

Doğrusal olmayan problemlerle başa çıkmada veya ağır kuyruklu dağılımlarla çalışmada avantajlı yanları olan yönelim kestirim algoritmaları da sıklıkla kullanılmaktadır. Bu nedenle, kestirim doğruluğunda ne tür bir filtrenin en büyük iyileştirmeyi sağladığını görmek için farklı filtre türleri de test edilmiştir. Farklı Kalman tipi filtre uzantıları, modelleri yakınsamada farklı yollar kullanmaya karşılık gelmektedir. Bu anlamda, çalışmada bir filtre Gauss olmayan gürültüyü hesaba katıp ölçüm gürültü kovaryansını güncellerken bir diğeri ise doğrusal olmayan model etkisini en aza indirmektedir. Bunun dışında, filtredeki ölçüm kovaryansını ölçeklendirerek veya güncelleyerek Kalman filtresine bir uyarılma kuralı tanımlayan

çeşitli algoritmalar da kullanılmıştır. Filtreleme uzantıları, her birinde temel olarak kullanılan Kalman filtresi için farklı hata kaynağı türlerini azaltmak üzere tasarlanacak şekilde geliştirilmiştir.

Daha iyi bir model için manyetometre gürültülerinin dağılımı, algılayıcıya ait uçuş verileri kullanılarak incelenmiştir. Filtreler, en uygun dağılıma sahip ölçüm gürültüsü modeli için test edilmiştir. Filtrelerin tepkileri, nominal mod, yanlış başlangıç durumundan kurtarma, kısa ve uzun süreli sensör hataları gibi farklı çalışma modları altında incelenmiştir.

Tezin bir başka amacı da bir gezegene yeterince yakın olan bir uzay aracı üzerindeki iki büyük çevresel bozuntunun araştırılmasıdır: dış manyetik alan ve gezegen albedosu. Manyetometreler ve güneş sensörleri yaygın olarak kullanılan yönelim sensörleri olduğundan, dış manyetik alan ve albedo modelleri, yönelim kestiriminin doğruluğunda önemli bir role sahiptir. Bir uzay aracında kullanılan manyetometreler, gezegenin dinamosu ve kabuğunun neden olduğu iç jeomanyetik alan kaynaklarını, ayrıca güneş rüzgârı ve gezegenler arası manyetik alan gibi dış kaynakları ölçmektedir. Bununla birlikte, yalnızca iç manyetik alanı içeren modeller sıklıkla kullanılmaktadır ve bu modeller, sensör ölçümlerine kıyasla manyetik alan modelinde hataya neden olan jeomanyetik aktiviteler meydana geldiğinde yetersiz kalabilmektedir. Burada, güneş rüzgârı ve manyetik fırtınaların neden olduğu dış alan değişiklikleri ve manyetosferik alt fırtınalar genellikle ölçümlerde kayma olarak ele alınmakta ve artırılmış durumlarda kestirilerek ölçümlerden çıkarılmaktadır. Bu durumda ölçüm, eleme yapıldıktan sonra gerçek durumdan uzaklaşmaktadır. Modeldeki dış alanı dikkate almak ve onu bir hata kaynağı olarak ele almamak için başka bir yaklaşım önerilmektedir. Bu şekilde model, manyetik alanı gerçeğe daha yakın temsil edebilmektedir.

Uzay aracı yönelim kontrolü için kullanılan manyetik alan modeli dış manyetik alanı dikkate almazsa, aslında fiziksel bir durumdan (örneğin, manyetosferik alt fırtına) kaynaklı değişimleri sensörün kendisinden kaynaklı daha fazla gürültüye sahip olarak yanlış değerlendirmektedir. Uydu yönelim belirleme sistemini etkileyen manyetik alanların temsilinden kaynaklanan hataları incelemek için farklı jeomanyetik alan modelleri karşılaştırılmıştır. Bu amaçla, kestirilen ve gözlemlenen vektör manyetik alanlar arasındaki açıları, manyetik alan bileşenleri ve büyüklükleri arasındaki farkları incelemek için düşük Dünya yörüngesinde seyreden bir uzay aracı gözlemleri ile IGRF ve T89 jeomanyetik modellerinden elde edilen manyetometre verileri kullanılmıştır. Jeomanyetik fırtınaların ve alt fırtınaların tahmin edilen ve gözlemlenen manyetik alanlar ve açılar üzerindeki etkilerini görmek için jeomanyetik olarak aktif ve sakin günlerde karşılaştırmalar yapılmıştır. Manyetik alan vektörleri, uzay aracının yönelimini kestirmek için kullanılmakta ve bu nedenle, model ve gözlemler arasındaki ve iki model arasındaki farklılıklar, farklı uzay ortamı koşullarında modellerle ilişkili hataları belirlemek ve azaltmak için önemli hale gelmektedir. Jeomanyetik olarak sakin zamanlarda bile modellerin gözlemlerden farklı olduğu ancak jeomanyetik olarak aktif zamanlarda ilgili hataların arttığı gözlemlenmiştir. T89 modelinin özellikle aktif zamanlarda gözlemlere daha yakın tahminler verdiği ve hataların IGRF modeline göre daha küçük olduğu gözlemlenmiştir. Her iki uzay ortamı koşulunda da açıda hatanın büyüklüğünün 1 dereceden az olduğu bulunmuştur. Jeomanyetik uzay fırtınalarından kaynaklanan manyetik bozulmaların GKF tarafından kestirilen uydu yönelimi üzerindeki etkileri de incelenmiştir. Artan jeomanyetik aktivite seviyeleri, IGRF ve T89 modelleri tarafından kestirilen jeomanyetik alan vektörlerinin doğruluğunu etkilemektedir. Manyetometre, jiroskop ve güneş sensörü gibi çeşitli

sensörler farklı kombinasyonlar altında manyetik olarak sakin ve aktif zamanlar için değerlendirilmiştir. Yönelim açıları için kestirim hataları hesaplanmış ve sonuçlar tartışılmıştır. Çalışmanın bu bölümü, uydu yönelim belirleme sistemleri üzerinde uzay ortamı faktörlerinden dış manyetik alanın önemini vurgulamaktadır.

Güneş sensörleri hem gezegen yörüngesindeki uydularda hem de güneş sistemindeki gezegenler arası uzay aracı görevlerinde sıklıkla kullanıldığından, güneşe ve bir gezegene yeterince yakın bir uzay aracı ele alınmıştır. Burada güneş akısının elektromanyetik radyasyonu, yansıyan ışın yani albedo ve o gezegenin yaydığı radyasyon, uzay aracına etki etmektedir. Albedo, gezegene ulaşan güneş ışınının ve gezegenden yansıyan ışının oranıdır. Uzay aracı, gezegenin güneşli olan kısmını gördüğünde albedoya maruz kalmaktadır. Albedo değerleri, mevsimsel, coğrafi, günlük değişimlerin yanı sıra bulutluluk durumuna bağlı olarak da değişmektedir. Güneş sensörü yalnızca güneşten gelen ışını değil, aynı zamanda gezegenin albedosunu da ölçmektedir. Bu nedenle, bir gezegenin albedo bozuntusu, güneş sensöründe hatalı okumalara neden olabilmektedir. Bu hatalı okumalar, güneş sensörlerini albedoya duyarsız olacak şekilde filtreleyerek ortadan kaldırılabilmektedir. Ancak nanouyduların çoğunda kaba güneş sensörleri kullanılmaktadır ve bu sensörler albedoya duyarlıdırlar. Ayrıca, optik sensörler, termal ve güç alt sistemleri gibi bazı hassas bileşenler ve uzay aracı sistemleri, analizlerinde ve operasyonlarında gezegenden yansıyan ışınları hesaba katmaktadırlar. Bu, albedo tahminlerini bu tip sistemler için de önemli bir faktör haline getirmektedir. Bu nedenle bu çalışmada amaç, gezegenin albedosunu kompleks albedo modellerinden daha az parametre bağımlılığı olan basit bir model kullanarak kestirmek ve düzeltilmiş güneş sensörü ölçümlerini içerecek bir yönelim kestirim algoritması tasarlamaktır. Böylece, üç eksenli bir yönelim kestirim prosedürü, üzerinde albedo bozuntusu olan ucuz, küçük boyutlu ve güç tüketiminde hafif olan kaba güneş sensörleri (KGS) kullanılarak sunulmuştur. Bozuntunun modellenmesi için, otoregresif modele dayalı iki aşamalı bir albedo kestirim algoritması önerilmiştir. Algoritma, albedo ölçümleri dışında albedo katsayıları, uzay aracı konumu, gökyüzü veya coğrafi durum gibi herhangi bir veriye ihtiyaç duymamaktadır. Sonuçlar, referans modellere dayalı olarak farklı albedo modelleriyle karşılaştırılmıştır. Modeller ya veriye dayalı ya da kestirime dayalıdır. Önerilen albedo kestirimi, düzeltme için KGS ölçümlerine beslenmektedir. Düzeltilmiş KGS ölçümleri, farklı sensör konfigürasyonları ile çeşitli kestirim teknikleri altında işlenmiştir. Yönelim kestirim şemalarının farklı albedo modellerini kullandığı durumlar için performansları incelenmiştir.

Özetle, uzay ortamındaki iki ana bozuntunun uydunun yönelim kestirimi üzerindeki etkileri, çeşitli uzay ortamı koşulları altında farklı uzay aracı yörüngeleri kullanılarak kapsamlı bir analizle incelenmiştir. Performans analizleri, uzay aracı sistemlerine veya hava araçlarına yönelik çalışmalarda tekrar uygulanabilir ve gerçekleştirilebilir şekilde sunulmuştur.

1. INTRODUCTION

Spacecraft and their instruments need to be oriented to achieve mission directives in space. The object is oriented using the attitude determination and control system (ADCS) of the spacecraft [1–3]. Depending on the mission, there may be strict performance requirements in terms of attitude estimation or necessity to a safe-mode operation or sanity checks. For these purposes, attitude sensors such as magnetometers and sun sensors can be utilized with less accuracy but less power need, lower cost, and smaller size [4,5]. However, the overall achievable attitude determination accuracy is limited with these sensors mainly as a result of their inherent limitations and unavailability of one of the sensor’s measurements e.g. malfunctions, eclipse period, etc. To mitigate the limitations of the inaccurate sensors, attitude estimation algorithms need to be improved, and because of limited computational resources, the algorithms should have low computational complexity.

Magnetometers are one of the attitude sensors that are commonly used on small satellites at low Earth orbit (LEO). On-board magnetometers and the model of the planet’s magnetic field are used in the attitude estimation stage. The conventional methodology while estimating the satellite’s attitude involves the angle between the magnetic field vectors from the magnetometer and the model of the geomagnetic field. Therefore, the accuracy of the geomagnetic fields from the model is critical for a precise attitude determination. As scientific payloads, the magnetometers return data in space within their built-in precision and are placed one or two meters away from the spacecraft body on a boom in order to avoid the magnetic effects created by the satellite itself and its nearby surrounding environment. For simulating the magnetometers, the magnetic field direction can be predicted using a geomagnetic field model, most widely, international geomagnetic reference field (IGRF) [6]. The magnetometers include several error sources that can affect the satellite’s attitude. Current state-of-the-art satellite magnetometers are highly improved both in accuracy, and precision and resolution as well as in physical size. Among several satellite magnetometers, two of the most often used ones are the flux-gate magnetometers and search coil

magnetometers that use tri-axial configuration. The magnetometers implemented on a LEO satellite measure the internal geomagnetic field sources caused by the Earth's dynamo and crust as well as the external sources such as those created by the interplanetary magnetic field and solar wind. In ADCSs, the IGRF model [6] is frequently used as the major magnetic field model. Yet, it might remain incapable when geomagnetic activities occur, which can produce an error in the magnetic field model in comparison with the sensor measurements.

Sun sensors are frequently used in both planet-orbiting satellites and interplanetary spacecraft missions in the solar system. They can be divided into two classes as fine or digital sun sensors (DSSs), and coarse sun sensors (CSSs), which are commonly used in a form of photodiodes [7]. CSSs function almost proportional to the cosine angle between the sensor's boresight and the sun direction vector from the spacecraft. They are often used on platforms including multiple CSSs. A spacecraft close enough to the sun and a planet receives electromagnetic radiation of direct solar flux, reflected radiation namely albedo, and emitted radiation of that planet. The solar flux is the largest source of radiation for the spacecraft while the albedo is the fraction of sunlight incident and reflected light from the planet. Spacecraft can be exposed to albedo when it sees the sunlit part of the planet. The albedo values vary depending on the seasonal, geographical, diurnal changes as well as the cloud coverage. The CSS not only measures the light from the sun but also the albedo of the planet [8]. So, a planet's albedo interference can cause anomalous sun sensor readings [9]. On the other hand, albedo might be an important factor in selecting the characteristics of optical-sensor systems such as cameras or star trackers, and in spacecraft thermal and power design.

1.1 Literature Review

Attitude estimation with magnetometer and sun sensor measurements is addressed in many research and various algorithms that intend to improve the estimation accuracy.

1.1.1 Attitude estimation filters

The conventional approach to attitude estimation of a satellite is to use an extended Kalman filter (EKF) [10] or its derivative-free version, the unscented Kalman filter (UKF) [11]. Kalman filtering algorithms can be used for integrating the measurements under the propagation model of the satellite dynamics and estimate the satellite attitude

possibly along with the sensor biases. For example, in [5] two filtering algorithms are proposed, both based on the multiplicative extended Kalman filter. The first algorithm is used for the estimation of attitude quaternions, gyro biases, and sun sensor calibration parameters and the second estimates only the quaternions and gyro biases excluding the sun sensor calibration parameters. The main drawback of both algorithms is the degradation in the estimation results when the satellite is in eclipse so the sun sensor data is not available. Similar phenomenon can be seen in [4] for the unscented Kalman filter estimations.

Another approach to attitude estimation, the single-frame method, is introduced in [4,12–14]. In this method, measurements at each time step are preprocessed to produce a set of linear measurements and associated covariances that are fed to the Kalman filter. The preprocessing involves the minimization of Wahba's loss function [15]. In [16], a comparison of minimization methods concludes that the singular value decomposition (SVD) and q methods are the most robust for single-frame attitude estimation methods. Deterministic methods such as the algebraic method (TRIAD - two-vector algorithm) or optimization methods such as the quaternion estimator (QUEST) can also be used [17]. As a drawback, these methods only rely on the measurements; they do not use any information about the satellite dynamics. Attitude estimation methods, which take the advantage of system's mathematical model, may increase the attitude estimation accuracy significantly. In [18], sun-eclipse phases are considered to use both traditional and non-traditional methods depending on the sun sensor being operational or not. In the sun sensor operational mode, the Gauss-Newton method obtains the quaternion estimates for the usage in EKF. In eclipse mode, only traditional EKF is used. Measurement covariance values in EKF are not provided by the deterministic method to the filter but selected manually.

The conventional approaches to design a Kalman filter (KF) for satellite attitude estimation use the nonlinear measurements of reference directions (e.g. sun direction) [4,11,19,20]. The measurement models in the filter are based on the nonlinear models of the reference directions so the measurements and states have nonlinear relations. In the linear measurement-based approach, on the other hand, the attitude angles are first determined by using the vector measurements under a suitable single-frame attitude determination method [17]. Then, these attitude estimates are used as measurements within the KF. The filter measurement model is linear in this case since the single-

frame attitude estimator provides directly the states linear to the measurements. Such algorithms may be named single-frame method aided attitude estimation filter.

An earlier study on single-frame method aided attitude filtering is carried out in [12]. In this study, the authors integrate TRIAD and EKF algorithms to estimate the attitude angles and angular velocities. Magnetometers, sun sensors, and horizon sensors are used as measurement devices and three different two-vector algorithms based on the Earth's magnetic field, sun, and nadir vectors are utilized. An EKF is designed to obtain the satellite's angular motion parameters with the desired accuracy. The measurement inputs for the EKF are the attitude estimates of the two-vector algorithms. Interest in single-frame method-aided attitude filtering is seen in literature [21–23]. The attitude determination concept of Kyushu University mini-satellite QSAT is based on a combination of the weighted-least-square (WLS) and KF [21,22]. The WLS method produces the optimal attitude-angle observations at a single frame by using the Sun sensor and magnetometer measurements. The KF combines the WLS angular observations with the attitude rate measured by the gyros to produce the optimal attitude solution. In [23], an interlaced filtering method is presented for nanosatellite attitude determination. In this integrated system, the optimal-REQUEST and UKF algorithms are combined to estimate the attitude quaternion and gyro drifts. The optimal-REQUEST, which cannot estimate gyroscope drifts, is run for the attitude estimation. Then the UKF is used for the gyro-drift estimation on the basis of linear measurements obtained as optimal-REQUEST estimates. There are also similar applications for unmanned aerial vehicle (UAV) attitude estimation. De Marina et al. introduce an attitude heading reference system based on the UKF using the TRIAD algorithm as the observation model in [24].

An EKF is proposed by [25] for real-time estimation of solid body orientation using developed MARG (Magnetic, Angular Velocity, and Gravity) sensors which include a three-axis magnetometer, three-axis angular velocity sensor, and three-axis accelerometer. The modeled system converts angular velocities to quaternion rates and obtains quaternion ratios and integrates them to obtain quaternions. The Gauss-Newton iteration algorithm is used to find the optimal quaternion. The quaternion is used as part of the measurements of the Kalman filter which is a non-traditional form of the Kalman filter. The authors tested the proposed algorithm for different cases including high noise levels as well as major initial faults.

In [26], the problem of attitude estimation is considered for UAV using inertial measurement unit (IMU) in Kalman filter. The kinematic model of aircraft behavior is not linear; therefore, a version of the Kalman filter is proposed, which can handle nonlinearities. A common solution to satellite attitude determination is to use the TRIAD algorithm, which is an observation model in the filter. Using the TRIAD algorithm, it is easy to select the most reliable sensors at different stages of a flight.

There are also studies where a single-frame attitude method is used together with an attitude filter but not for providing the linear measurements [13]. Another non-traditional approach is presented by [13] which integrates the q-method with an EKF to generate a qEKF filter. In the filter, the attitude vector measurements are first processed using the q method, which is a single-frame method solving Wahba's problem directly, without nonlinear assumptions. The remaining measures are processed for updating obscure situations using the conventional EKF algorithm. For linear measurements, it is equivalent to the first update the attitude using the single-frame estimator and subsequently to use this updated portion of the state to update the remainder of the state. However in [13,27], the measurement model is nonlinear. A nonlinear update for the attitude is obtained solving Wahba's problem and subsequently used to update the non-attitude states using the optimal gain for the linear measurement case. Therefore, in these studies, the attitude is updated using the single-frame estimator and all remaining non-attitude states used the standard nonlinear attitude filters.

Several algorithms are proposed to improve the ability of Kalman-type filters to cope with highly nonlinear situations. The filter introduced in [28] can automatically process multiple measurements in an optimized order so that the errors caused by nonlinearities are minimized. Normal distribution-based statistical estimation is vulnerable to outliers. In [29], the authors compare different geomagnetic orbit determination filters under different measurement noise distributions: normal, Student's t, and uniform in the simulations. They concluded that an unscented particle filter, which can make use of non-Gaussian noise models, is more accurate than EKF and UKF, which use Gaussian models. However, the computational complexity for particle filters is typically much greater than for Kalman-type filters.

In [30], a generalization and extension of a linear Student's t filter are proposed. In the paper, simulation results show that the proposed methods provide better accuracy than

the existing methods in an application with the heavy-tailed process and measurement noises. In [31], an outlier-robust Kalman-type filter for nonlinear dynamical models is proposed based on Student's t-distribution in the measurement model. In the paper, the filter is compared to alternative filters in a computer simulation and is found to provide a good trade-off between accuracy and computational efficiency.

A nonlinear Kalman-type filter called maximum correntropy unscented Kalman filter (MCUKF) is proposed in [32] for spacecraft relative state estimation. Heavy-tailed non-Gaussian measurement noises are considered in the paper. The proposed MCUKF uses a non-linear regression model combined with maximum correntropy to update the measurement information. A practical test of the relative motion of two spacecraft is performed and it is found that the proposed filter gives better performance than the other filters such as EKF and UKF.

A noise-covariance adapting EKF algorithm is proposed in [33] to cope with sensor faults in the attitude estimation of a small satellite equipped with only a three-axis magnetometer. Similarly, a covariance adapting UKF with multiple measurement noise scaling factor is presented in [34] for nanosatellite attitude estimation and is found to be more accurate than EKF, UKF, and the covariance-adapting UKF with the single scaling factor. In [35], it is shown that the covariance-adapting filters are much more accurate than UKF and EKF in the faulty period and have faster recovery after the end of a fault. Furthermore, according to that study, the covariance-adapting UKF outperforms all other considered filters.

1.1.2 External magnetic field

The orientation of the geomagnetic field is one of the most critical data in the determination and control of the satellite's attitude especially at LEO [36–39]. More accurate measurements of the geomagnetic field lead to more accurate predictions of the satellite's attitude. The simulated magnetometers are constructed on the ground before the satellite launch to reproduce the satellite's magnetometer measurements of real space. In other words, a simulated magnetometer is an object simulated by software for obtaining the geomagnetic field used to estimate the satellite's attitude. In order to design a simulated magnetometer, a geomagnetic field model, the statistical characteristics of the magnetic field measurements in space and characteristics of on-board satellite magnetometers are needed. The most commonly used geomagnetic

field model to predict the Earth's magnetic field at the satellite location is the IGRF model [6,40]. However, the angle between the magnetic field vector from the IGRF model and the magnetic field vector from the simulated magnetometer affects the accuracy of the attitude angles, namely roll, pitch, and yaw. When transformed vectors in the same coordinates, the smaller this angle is the more precisely the attitude angles are determined. Therefore, the choice of geomagnetic field model used in the simulated magnetometer is very important in achieving high accuracy in attitude angles.

The main source of the geomagnetic field is the Earth's dynamo in its core that produces dipolar magnetic fields in the near-Earth space environment [41–43]. However, solar activities such as solar wind, coronal mass ejections (CMEs), high-speed streams (HSSs), interplanetary shocks (ISs), and their magnetospheric consequences geomagnetic storms and magnetospheric substorms produce disturbances superimposed on the dipole field of the Earth at different strengths [44]. Charged particles from the geomagnetic tail flow into the upper atmosphere and drive electrical currents at the LEO altitudes which in turn modify the geomagnetic field at those altitudes [45–47]. We will refer to the variations caused by these or external sources as magnetic disturbances or magnetic anomalies. While on-board spacecraft magnetometer measurements inherently include these deviations from the dipole field, they need to be represented in the simulated magnetometer or within the geomagnetic field models for accurate predictions of the near-Earth magnetic fields.

In reality, neither the geomagnetic field models of the Earth nor the magnetometers are accurate. They both have various error sources resulting from several factors. The simulated magnetometers include bias and noise errors. Many of the bias and random errors from the magnetometers may be reduced or prevented before the launch during the ground tests or on-orbit after the launch with having an additional sensor for calibration on the satellite. There are several methods proposed in the literature for sensor calibration for possible anomalies or faulty measurements. One of the most commonly known methods is the TWOSTEP algorithm for the magnetometer calibration without attitude information. After the centering approximation, it uses a second step employing the centered estimation as an initial value to be used by in an iterative Gauss-Newton method that avoids divergence problems while other algorithms cannot [48,49]. In parallel to the advancing technologies in the space industry, providing that the errors that may be resulted from real magnetometer sensors

on board are negligible to affect the attitude, the source of most of the errors then would be associated with the environmental conditions in case of the real magnetometers and from the bias, noise and scaling factors in case of the simulated magnetometers and how they are handled during onboard processing in space.

The errors in magnetometer measurements are determined in the literature using different approaches. An approach that is suggested by [50] is to compare the magnetometer measurements with the magnetic fields predicted by the IGRF geomagnetic model and aims to remove the bias and scaling errors. In this case, IGRF predictions are used to calibrate and optimize the simulated magnetometer magnetic fields [50,51]. The other approach involves the conversion of the IGRF model magnetic field to the satellite body coordinates. In these studies, the IGRF model is assumed to represent the geomagnetic field correctly. These studies imply that a good representation of the geomagnetic field is an essential part of the attitude determination process and the closer the geomagnetic model results to the real geomagnetic fields in space at the satellite's altitude, the more accurate the satellite attitude is estimated.

While in many studies, magnetic disturbances in the space environment are treated as bias, in several others, they are accepted as noise [50,51]. However, in these studies, it should be reminded that the magnitude of the geomagnetic field deviations due to the magnetospheric storms can be obscured by the sensor-related noise used in the simulated magnetometers [52]. In order to estimate the magnetic moment of the satellite accurately, magnetometer bias resulting from other electrical devices on the satellite should be estimated and removed precisely. Therefore, online and offline magnetometer calibration methods for time-variable errors arising from both magnetometer bias and the magnetic anomaly are introduced in [53] for two nanosatellites that need geomagnetic field data as accurate as possible for their mission requirements. In [53] and its extended version [54], the authors treated the magnetic anomaly as bias in the simulated magnetometer to improve the attitude estimation. In addition to the bias associated with the magnetic anomaly, they also added magnetometer bias to build their simulated magnetometer. Both the magnetic anomaly bias and the magnetometer bias are used as the state vector elements within the simulated magnetometer. But, here we should also note that the magnetic anomalies in the space environment are not the errors resulting from the magnetometer itself, but they are the magnetic deviations overlapped on the geomagnetic field resulting from

the magnetic storms and magnetospheric substorms. In other words, they have a physical cause and their properties vary depending on the properties of the source and they cannot be predicted using linear models. With this, it is meant that simply adding them as bias or noise error does not correctly take into account their true nature and their contribution to the measurements of the simulated magnetometer. The studies in [53,54] treated the magnetic anomalies as a Gauss-Markov statistical process. Gauss-Markov model is a model frequently used to represent the sensor biases or disturbances [55–57]. However, it only depends on time and thus, it may be an inadequate representation of magnetic anomaly events which are linked to the geomagnetic storm and magnetospheric substorms, since these storms and substorms are not only time-dependent but also their effects vary depending on the location, namely magnetic latitude, the height in the atmosphere, and also the strength of the magnetospheric activity, i.e. magnetotail dynamics, but ultimately on the solar activity [58–61]. While auroral substorms occur more frequently and affect high latitudes, variations in the ring current strength, or the motion of the magnetopause boundary affect the magnetic structure of the Earth at the equatorial latitudes [26 and references therein]. In addition, the magnetic anomalies associated with the magnetic storms increase during the high solar activity periods and decrease as the solar activity ceases. These indicate that it would be incorrect to consider them as noise. In [63], the authors stated that the magnetic anomalies should be modeled separately to avoid tuning problems but they stated that the external disturbances hard to model because of their complex ambient nature.

Early models of the Earth's magnetic field represent only the dipole geomagnetic fields resulting from the Earth's internal dynamo. The effects of magnetic disturbances are not included in these early models. As the satellite observations of the geospace environment increase, these models, consequently modeling the LEO environment, are improved such that the physics of the magnetic environment are incorporated in the models. The IGRF model is one of these early models of the geomagnetic field used for attitude determination at LEO altitudes. The accuracy of the IGRF models is investigated in several studies and is usually found satisfactory in predicting the satellite attitude [50,51,64].

First studies that take into account the effects of magnetic anomalies from the spacecraft attitude perspective are presented in [65–67]. These studies used IGRF and

T89 models to evaluate the geomagnetic field at LEO altitudes during geomagnetically active days. T89 model developed by Tsyganenko in 1989 is an empirical geomagnetic field model [68,69] that is derived using a large amount of magnetic field data from 11 Earth-orbiting spacecraft measurements at various distances from LEO to 30 Earth Radii behind the Earth and thus covering vast magnetospheric regions including plasmasphere, the plasma sheet, radiation belts, neutral sheet, near-Earth magnetospheric tail, and the magnetospheric boundary [70]. In contrast to the IGRF model, the T89 model includes contributions from external magnetospheric sources such as ring current, magnetotail current system, magnetopause currents, and large-scale system of field-aligned currents. The model employs several physical conditions such as dipole tilt angle effects, neutral sheet curvature, and more or less realistic magnetopause boundary as well as the effects from the magnetospheric activity. In [65–67], the predicted and observed magnetic fields, and angles between magnetic field vectors from IGRF and T89 are analyzed for three selected geomagnetic storm events and compared the variations with those obtained during the quiet day. They showed that the T89 model gives closer magnetic field predictions to the observations, and the errors are smaller compared to those from the IGRF model.

1.1.3 Planet's albedo

A spacecraft close enough to the sun and a planet receives electromagnetic radiation of direct solar flux, reflected radiation namely albedo, and emitted radiation of that planet. The solar flux is the largest source of radiation for the spacecraft while the albedo is the fraction of sunlight incident and reflected light from the planet. Spacecraft can be exposed to albedo when it sees the sunlit part of the planet. The albedo values vary depending on the seasonal, geographical, diurnal changes as well as the cloud coverage. The most reflectance is caused by thickest, highest clouds while the least by snowing clouds [71]. The CSS not only measures the light from the sun but also the albedo of the planet [8]. So, a planet's albedo interference can cause anomalous sun sensor readings. According to Reference [9], albedo might worsen the sun pointing accuracy by more than 20 degrees. On the other hand, albedo might be an important factor in selecting the characteristics of optical-sensor systems such as cameras or star trackers, and in spacecraft thermal and power design. For example, Reference [72] underlines that the thermal control system on the spacecraft must consider the light reflectance and emittance of the planets as it causes a highly dynamic variation in

thermal load. Another study on a spacecraft thermal analysis is carried out in order to evaluate the thermal conditions for temperature stability of sensitive instruments and radiators by using the albedo data from NASA's clouds and Earth radiant energy system (CERES) instruments [73].

The mathematical model of the sun sensors can include diffusive and specular reflections from the planet which represents the perturbed sun sensor measurements. In Reference [74], perturbed sun sensor measurements are validated by the telemetry data of the Ørsted satellite. The currents of the modeled CSSs are improved about three times more than the case not including any albedo model on the measurements in Reference [74], and four times in Reference [75]. A sun heading estimation algorithm is also applied by Reference [76] using EKF. The sun direction is estimated with accuracy under 4-degrees based on albedo interfered CSS and rate gyro (RG) measurements, and 10 degrees without RGs despite the fact that an underdetermined sun sensor coverage is considered in the study [76].

References [77] and [78] present extended consider Kalman filter based on modified Rodrigues parameters (MRPs) for CSS calibration. The presented filters require inertial attitude measurements but it gives scale factor accuracy less than 1% and misalignment accuracy about 1-degree even under poor attitude knowledge. Another calibration filter is proposed for photodiodes through the estimation of attitude and calibration parameters simultaneously [79]. An arbitrary number of photodiodes along with an albedo model, are calibrated using both an EKF and an unscented filter. The filter estimates improve the sun vector measurements by 10-degrees and attitude by 1-degree, by combining a three-axis magnetometer (TAM) and RG in the study. In order to make the albedo model less burden in computations, two constant albedo coefficients are applied rather than various spatial data in Reference [80]. From the analyses, the errors are reduced by taking the average albedo coefficient as 0.105 instead of 0.30. Even though the presented model provides a significantly better CSS accuracy for most of the times than uncorrected outputs, its predictions based on the 0.30 value may occasionally overcorrect the CSS. This overcorrection causes an increase in the sensor error. It is stated that the detailed mathematical model including the albedo coefficient changes depending on the active surface elements can be used for the most accurate case but it is computationally expensive for online usage. Reference [80] concludes that because of the albedo model complexity, it is more

reasonable to use a filter on the sun sensor that restricts the sensor not sensitive to the albedo. This suggestion might be more suitable for DSSs. In Reference [81], a less complex albedo model is generated via polynomial functions with 13 parameters for each albedo component including functions based on latitude and longitude. The polynomial is fitted to the reflectivity dataset from Earth Probe's total ozone mapping spectrometer (TOMS) instead of using excessive data in look-up tables. The work also estimates the spacecraft attitude states with 1-degree accuracy in nominal mode and 2-degrees in worst mode by EKF with 0.5% noisy measurements from TAM and corrected CSS.

1.2 Research Overview

The motivation in this dissertation lies on the fact that the increasing dependence of the human life on the satellite technologies requires even better estimations of satellite attitude. This fact led us to consider and improve the available algorithms of attitude estimation and the factors that affect the attitude. In this context, several adaptive attitude estimation algorithms are proposed to improve the ability of Kalman type filters to cope with faults [34], nonlinearity [28], non-Gaussianity [32], etc. by adapting their measurement noise covariance. This research investigates attitude estimation filters with inherent adaptation against measurement faults. The single-frame method aided attitude estimation algorithm eliminates the possibility of poorly chosen initial attitude as it initializes the attitude using a single-frame method. The performance of the developed extensions for the state-of-the-art filters for attitude estimation is evaluated by taking into consideration both accuracy and computational complexity.

Another aspect of the research is to investigate two major environmental disturbances on the spacecraft close enough to a planet: the external magnetic field and the planet's albedo (see Figure 1.1). As magnetometers and sun sensors are widely used attitude sensors, external magnetic field and albedo models have an important role in the accuracy of the attitude estimation. The magnetometers implemented on a spacecraft measure the internal geomagnetic field sources caused by the planet's dynamo and crust as well as the external sources such as solar wind and interplanetary magnetic field. However, the models that include only the internal field are frequently used, which might remain incapable when geomagnetic activities occur causing an error in the magnetic field model in comparison with the sensor measurements. Sun sensors

are frequently used in both planet-orbiting satellites and interplanetary spacecraft missions in the solar system. The sun sensor not only measures the light from the sun but also the albedo of the planet [8]. So, a planet's albedo interference can cause anomalous sun sensor readings. This can be eliminated by calibrating the sun sensors [79]. However, in this research, the purpose is to estimate the planet's albedo using a simple model with less parameter dependency than any albedo models and to estimate the attitude by comprising the corrected sun sensor measurements. The effects of the space environment on the satellite's attitude estimation are studied using statistical analysis with different types of spacecraft trajectories at different altitudes, within different near-planet space environment conditions.

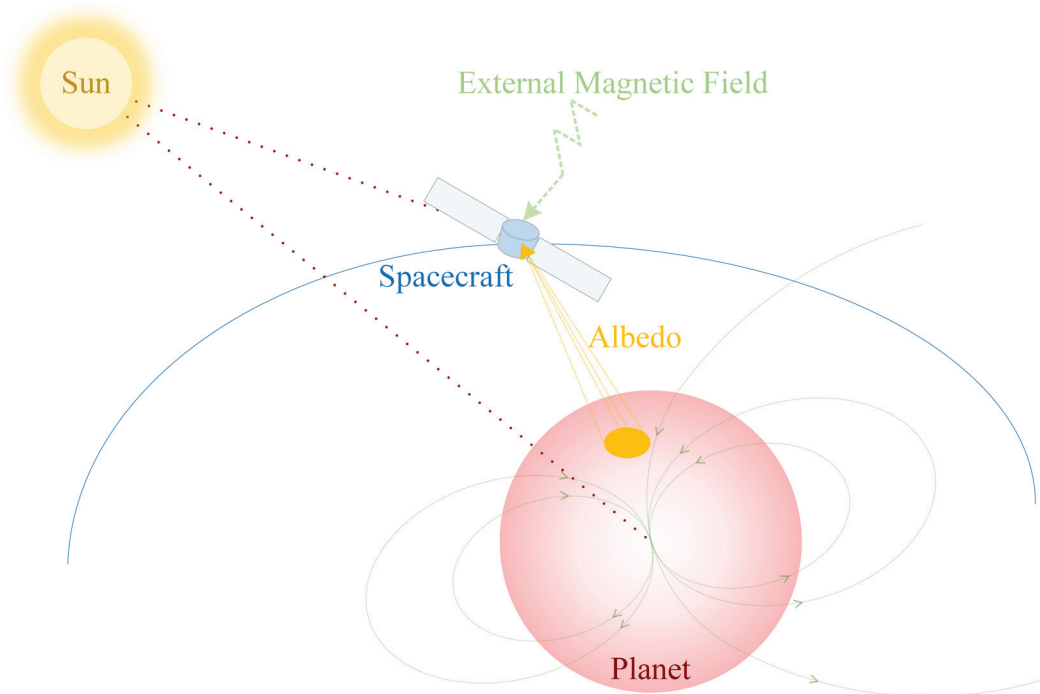


Figure 1.1 : Illustration of external magnetic field and planet's albedo affecting the spacecraft.

The tests are carried out for a broad performance evaluation to determine how dominant the external influence is, how much the filter reduces the disturbance effects on the satellite's attitude, and how much accuracy of attitude estimation can be improved. The analyses are also expected to be a basis for applications to other systems such as aircraft and unmanned aerial vehicles.

This study addresses the following research questions:

- How much accuracy can a spacecraft ADCS achieve in attitude estimation within the computational budget?
- Which filters are computationally lighter or more accurate under which measurement conditions?
- How do the attitude estimation filters cope with measurement faults?
- What is the best distribution model in fitting the magnetometer measurement noise?
- How well does the magnetic field vector predicted by the geomagnetic field model accurately represent the real geomagnetic field at LEO altitudes?
- How much does the Earth's geomagnetic field vary during the magnetic storms and substorms at LEO altitudes?
- What is the error that the angle between the measured magnetic field and the field from the geomagnetic model would create in spacecraft attitude?
- How can the planet's albedo be modeled using a simple schema with less parameter dependency than any albedo models?
- How much does the planet's albedo affect the attitude estimation results?

This dissertation is prepared using the author versions of the published scientific articles indexed by Science Citation Index (SCI) or SCI-Expanded of which the Ph.D. candidate is the first author. Every chapter is composed of a scientific paper that is indicated in the footnote. Each chapter maintains its content integrity within itself, and it is coherent to the general flow of the thesis. The thesis is organized as follows.

Chapter 2: SVD-aided EKF attitude estimation with UD factorized measurement noise covariance [82]

In this chapter, an SVD-aided EKF algorithm using UD factorization is presented. The measurement error covariance matrix of the filter is factorized without using the assumption of neglecting the non-diagonal elements and the new measurement vector with the uncorrelated error components is redefined. The algorithm is divided into two phases as the first step, SVD, and the second step, EKF forms the attitude estimation algorithm. In this approach of the Kalman filter, inputs from SVD are the attitude angles as the linear measurements and their error covariance values in a matrix form

computed every step. However, in order to achieve the required inputs for the EKF algorithm, decomposition of the attitude angles error covariance matrix from SVD into diagonalized covariance matrix should be performed. In order to achieve the diagonalization, the UD decomposition method is presented and applied to the first step before the filtering stage. The measurement vector introducing the attitude angles having uncorrelated error components is redefined for the filter input.

Chapter 3: Nanosatellite attitude estimation from vector measurements using SVD-aided UKF algorithm [83]

This chapter integrated SVD and UKF methods to estimate the attitude and attitude rates of a nanosatellite. Quaternion attitude representation is used for this purpose. A possible switching rule is also discussed specifically for eclipse where the sun sensor measurements are not available. The SVD method fails in the eclipse period because of no sun observations. On the other hand, the SVD-aided UKF estimates the attitude in eclipse although it is a coarse estimate. The proposed ideal algorithm is composed of both SVD-aided UKF and conventional UKF.

Chapter 4: Nanosatellite attitude estimation using Kalman-type filters with non-Gaussian noise [84]

In this chapter, the performance of state-of-the-art filters for attitude estimation is presented by taking into consideration both accuracy and computational complexity. The magnetometer errors are modeled with t-distribution and four attitude estimation operational modes are considered: (1) attitude recovery after de-tumbling phase: this mode is simulated by initializing the filter with an incorrect initial state, (2) steady-state, after the attitude recovery phase error has settled, (3) short-term noise increment in one magnetometer channel, which simulates a sensor fault due to transient disturbance, (4) long-term noise increment, simulating the onset of a persistent disturbance.

Chapter 5: Evaluation of geomagnetic field models using magnetometer measurements for satellite attitude determination system at low earth orbits: case studies [65]

In this chapter, the effects of the LEO orbit geomagnetic environmental conditions, which are superimposed on the Earth's geomagnetic field as a result of magnetospheric substorms, on the satellite attitude system are investigated. As these effects are not

taken into account in commonly used reference models, the magnetic field at the satellite altitude during activity times might be underestimated by the simulated magnetometers or the model.

Chapter 6: Geomagnetic disturbance effects on satellite attitude estimation [85]

This chapter investigates how the angle between the magnetic field vectors predicted by the models varies with the increasing levels of geomagnetic activity. It is shown that how these geomagnetic activity effects are propagated onto the satellite attitude angles. This chapter also investigates the effects of the presence of one or more attitude sensors onboard the satellite in addition to the magnetometer. The sun sensors and gyroscopes are considered for this purpose. The mathematical models of these sensors can be implemented into the attitude estimation methods using e.g. Kalman-type filters.

Chapter 7: Attitude estimation with albedo interference on sun sensor measurements [86]

The main purpose of this chapter is to estimate another major space environment disturbance, the planet's albedo by using a simple model with less parameter dependency than any albedo models and to estimate the attitude by comprising the corrected CSS measurements. As a simple model, the AR albedo model is proposed. Here, the purpose is to estimate the albedo without using any data related to albedo coefficients that depend on position, time, ground, and cloud coverage parameters. However, spacecraft's attitude information is necessary to estimate the albedo based on the AR model. So, an attitude estimation procedure is also presented using the estimated albedo. The attitude estimation procedure is composed by estimating the albedo first and correcting the CSS after. In this way, no albedo model is considered in the last output equations in the attitude estimation filter.

Chapter 8: Conclusions and recommendations

This chapter is a summary of the thesis with concluding remarks and recommendations for future work.

2. SVD-AIDED EKF ATTITUDE ESTIMATION WITH UD FACTORIZED MEASUREMENT NOISE COVARIANCE*

2.1 Abstract

This study describes singular value decomposition (SVD) aided extended Kalman filter (EKF) for nanosatellite's attitude estimation. The development of the filter kinematic/dynamic model, and the measurement models of the sun sensors, and the magnetometers which are used to generate vector measurements is presented. Vector measurements are used in SVD for satellite attitude determination purposes. In the proposed method, EKF inputs are coming from SVD as the linear measurements of attitude angles and their error covariance. In this step, UD is factorizing the attitude angles error covariance with forming the measurements in order to obtain the appropriate inputs for the filtering stage. Results are presented and analyzed in addition that the necessity of the sub-step which is the UD factorization on the measurement covariance is discussed. The accuracy of the estimation results of the SVD-aided EKF with and without UD factorization is compared for the estimation performance.

2.2 Introduction

Satellites need to be oriented in space and depending on the mission requirements they can have specific restrictions for attitude accuracy. Especially the nanosatellites are required to keep the attitude as desired with micro-sized attitude sensors because they are cheap, simple, light, etc. as needed. Mostly, the nanosatellites are having magnetometers and sun sensors onboard which are very common with limited achievable attitude accuracy due to the unavailability of the data. For attitude determination, reference directions should be described and those vectors as sensor output and the models related to them can be placed in a single-frame algorithm to process the results in order to improve under the EKF after the coarse attitude

* This chapter is based on the paper “Cilden-Guler, D., Hajiyev, C. (2019). SVD-aided EKF attitude estimation with UD factorized measurement noise covariance, *Asian Journal of Control*, **21** (4), 1423-1432, doi: 10.1002/asjc.1979”.

determination phase. Single-frame methods' aim is to minimize the Wahba's loss function defined in 1965 [1,15]. By minimizing the loss between the measurements and the models for the sun and magnetic field directions, attitude and their covariance can be determined. In this study, SVD is used as the single-frame method in the first step because of its robustness performance. In [87,88], studies make a critical comparison of those estimators in the sense of robustness in which the SVD and the q method are found to be the most robust in principle.

Basically, attitude estimation of the satellite can be performed using the EKF by assigning initial values, integrating the measurements under the propagation model of the satellite dynamics, and estimate the attitude of the satellite. The traditional approaches to the design of the Kalman filter for satellite attitude and rate estimation use the nonlinear measurements of reference directions [10,11,19,89]. However, in this study, the non-traditional Kalman estimation technique is executed. In [90], a review is carried out on gyroless attitude determination methods for small satellites. In that paper, both traditional and non-traditional Kalman filters and their comparisons are presented. The non-traditional approach based on linear measurements is used in several studies [12,14,91]. In this case, determined coarse attitude angles, and covariance from one of the single-frame methods are used directly in the filter which shapes the second part of the non-traditional algorithm.

At Kyushu University, the weighted least square method is integrated to linearized Kalman filter for developed microsatellite having the same attitude sensors and it is stated that the estimator decreases the random noise effect and determines the attitude in accordance with the mission requirements in [22].

An extended Kalman filter is proposed by [25] for real-time estimation of solid body orientation in 2001 using developed MARG (Magnetic, Angular Velocity, and Gravity) sensors which include a three-axis magnetometer, three-axis angular velocity sensor, and three-axis accelerometer. The modeled system in the paper, converts angular velocities to quaternion rates and obtains quaternion ratios, and integrates them to obtain quaternions. The Gauss-Newton iteration algorithm is used to find the optimal quaternion. The quaternion is used as part of the measurements of the Kalman filter which is a non-traditional form of the Kalman filter. The authors tested the proposed algorithm for different cases include high noise levels as well as major initial faults and resulted that the filter achieves very good estimations.

In the research presented by [26], the problem of attitude estimation is considered for unmanned aerial vehicles (UAV) using inertial measurement units (IMU) in the Kalman filter. The kinematic model of aircraft behavior is not very linear; therefore, a version of the Kalman filter is proposed, which can handle nonlinearities. A common solution to satellite attitude estimation is the TRIAD algorithm, which is an observation model in the filter. Using the TRIAD algorithm, it is easy to select the most reliable sensors at different stages of a flight.

Another non-traditional approach is presented by [13] which integrates the q-method with an EKF to generate the qEKF filter. In the filter, the attitude vector measurements are first processed using the q method, which is a single-frame method that solves Wahba's problem directly, without nonlinear assumptions. The remaining measures are processed for updating obscure situations using the conventional EKF algorithm. The authors are stated to confirm the validity of the proposed approach by numerical simulations and the comparison to the conventional EKF.

In [14], the authors use a gyro-free attitude estimation system having magnetometer and sun sensor in the non-traditional Kalman filter and show the superiority of the non-traditional approach to the traditional ones for the attitude accuracy of the satellite. The authors considered the non-diagonal elements of the covariance matrix of the SVD to be small compared to the diagonal elements. Therefore, the non-diagonal elements are neglected, and the error covariance matrix is considered diagonally [14,83]. In this study, an SVD-aided EKF method using UD factorization is considered as an extended version of [92]. As the simulations are performed for nanosatellites, EKF is selected because they are light and easy to implement compared to UKF [93,94]. In the case of using UD in the algorithm, the error covariance matrix is factorized without using the assumption of neglecting the non-diagonal elements, and the new measurement vector with the uncorrelated error components is redefined. The algorithm is shaped in two phases as the first step, SVD, and the second step, EKF forms the nanosatellite's non-traditional attitude estimation algorithm. For the non-traditional approach of the Kalman filter, inputs from SVD are the attitude angles as the linear measurements and their error covariance values in a matrix form computed every step. However, in order to achieve the required inputs for the EKF algorithm, decomposition of the attitude angles error covariance matrix from SVD into diagonalized covariance matrix should be performed. In order to achieve the diagonalization, the UD decomposition method

[95] is presented and applied to the first step before the filtering stage. Moreover, the measurement vector introducing the attitude angles which will be having uncorrelated error components is redefined for the filter input.

The structure of this chapter is as follows. Section 2.3 gives mathematical models of the satellite's rotational motion and sensor measurements. The details of the magnetic field direction vector, sun direction vector measurement model are presented in this section. In Section 2.4, Wahba's optimization problem and its solution by the SVD method are given. In Section 2.5, SVD aided EKF for satellite attitude estimation based on linear measurements is presented with the introduction of UD decomposition of the measurement noise covariance matrix and details of EKF design. The simulation results of the non-traditional approach including the UD factorized measurements are presented in Section 2.6. The last section gives a brief summary of the obtained results and conclusions.

2.3 Mathematical Models

2.3.1 Satellite's rotational motion

If the kinematics of the small satellite is derived in the base of Euler angles, then the mathematical model can be expressed with a 6-dimensional system vector which is made of attitude Euler angles (φ is the roll angle about x axis; θ is the pitch angle about y axis; ψ is the yaw angle about z axis) vector and the body angular rate vector with respect to the inertial axis frame,

$$\mathbf{x} = [\varphi \quad \theta \quad \psi \quad \omega_x \quad \omega_y \quad \omega_z]^T. \quad (2.1)$$

Also for consistency with the further explanations, the body angular rate vector with respect to the inertial axis frame should be stated separately as;

$$\boldsymbol{\omega}_{BI} = [\omega_x \quad \omega_y \quad \omega_z]^T, \quad (2.2)$$

where $\boldsymbol{\omega}_{BI}$ is the angular velocity vector of the body frame with respect to the inertial frame. Besides, dynamic equations of the satellite can be derived by the use of the angular momentum conservation law;

$$J_x \frac{d\omega_x}{dt} = N_x + (J_y - J_z) \omega_y \omega_z, \quad (2.3.a)$$

$$J_y \frac{d\omega_y}{dt} = N_y + (J_z - J_x) \omega_z \omega_x, \quad (2.3.b)$$

$$J_z \frac{d\omega_z}{dt} = N_z + (J_x - J_y) \omega_x \omega_y, \quad (2.3.c)$$

where J_x , J_y and J_z are the principal moments of inertia and N_x , N_y and N_z are the terms of the external moment affecting the satellite.

Kinematic equations of motion of the nanosatellite with the Euler angles can be given as,

$$\begin{bmatrix} \dot{\varphi} \\ \dot{\theta} \\ \dot{\psi} \end{bmatrix} = \begin{bmatrix} 1 & s(\varphi)t(\theta) & c(\varphi)t(\theta) \\ 0 & c(\varphi) & -s(\varphi) \\ 0 & s(\varphi)/c(\theta) & c(\varphi)/c(\theta) \end{bmatrix} \begin{bmatrix} p \\ q \\ r \end{bmatrix}. \quad (2.4)$$

Here $t(\cdot)$ stands for tangent function and p , q and r are the components of $\boldsymbol{\omega}_{BR}$ the vector which indicates the angular velocity of the body frame with respect to the reference frame. $\boldsymbol{\omega}_{BI}$ and $\boldsymbol{\omega}_{BR}$ can be related via,

$$\boldsymbol{\omega}_{BR} = \boldsymbol{\omega}_{BI} - \mathbf{A} \begin{bmatrix} 0 \\ -\omega_o \\ 0 \end{bmatrix} \quad (2.5)$$

where \mathbf{A} is the transformation matrix, ω_o denotes the angular velocity of the orbit with respect to the inertial frame, found as $\omega_o = (\mu / r_0^3)^{1/2}$.

2.3.2 Measurement models

Two attitude sensors are considered in this study to estimate the attitude using SVD-aided EKF. Magnetometer and sun sensor measurements should be modeled in order to obtain the first-step measurements by SVD.

IGRF model defines the magnetic field direction vector [6] in the orbit frame. Here, the magnetometer measurements are needed to be modeled too. Three onboard magnetometers of the satellite measure the components of the magnetic field vector in the body frame. Therefore, for the measurement model, which characterizes the measurements in the body frame, gained magnetic field terms must be transformed by

the use of the direction cosine matrix, \mathbf{A} . Overall measurement model may be given as;

$$\mathbf{B}_m(k) = \mathbf{A}(k)\mathbf{B}_o(k) + \mathbf{v}_B(k), \quad (2.6)$$

where $\mathbf{B}_m(k)$ is the measured Earth magnetic field vector as the direction cosines in the body frame, $\mathbf{v}_B(k)$ is the magnetometer measurement noise. The sun direction vector measurements can be expressed in the following form:

$$\mathbf{S}_m(k) = \mathbf{A}(k)\mathbf{S}_o(k) + \mathbf{v}_S(k), \quad (2.7)$$

where $\mathbf{S}_m(k)$ is the measured sun direction vector as the direction cosines in the body frame, $\mathbf{S}_o(k)$ represent the sun direction vector in the orbit frame as a function of time and orbit parameters, \mathbf{v}_S is the sun sensor measurement noise.

2.4 Singular Value Decomposition (SVD)

In this section, the SVD method, the prefix of the non-traditional approach, is briefly described. After defining Wahba's optimization problem, two or more vectors can be used in statistical methods to reduce losses the most [15]. In Equation (8), the loss can be seen as the difference between the measurements and the models found in the unit vectors.

$$L(\mathbf{A}) = \frac{1}{2} \sum_i a_i |\mathbf{b}_i - \mathbf{A}\mathbf{r}_i|^2 \quad (2.8)$$

$$\mathbf{B}_{svd} = \sum a_i \mathbf{b}_i \mathbf{r}_i^T \quad (2.9)$$

$$L(\mathbf{A}) = \lambda_0 - tr(\mathbf{A}\mathbf{B}_{svd}^T) \quad (2.10)$$

where \mathbf{b}_i (set of unit vectors in body frame) and \mathbf{r}_i (set of unit vectors in reference frame) with their a_i (non-negative weight) are the loss function variables obtained for instant time intervals and λ_0 is the sum of non-negative weights. Further, the matrix \mathbf{B}_{svd} is defined to reduce the loss function into equation (2.10). Here, maximizing the trace ($tr(\mathbf{A}\mathbf{B}_{svd}^T)$) means minimizing the loss function (L). In this study, the SVD method is chosen to reduce the loss function to the minimum [88,96].

$$\mathbf{B}_{svd} = \mathbf{U}\mathbf{S}\mathbf{V}^T = \mathbf{U}diag[S_{11} S_{22} S_{33}]\mathbf{V}^T \quad (2.11)$$

$$\mathbf{A}_{opt} = \mathbf{U}diag[1 \ 1 \ \det(\mathbf{U})\det(\mathbf{V})]\mathbf{V}^T \quad (2.12)$$

The \mathbf{U}, \mathbf{V} matrices are orthogonal left and right matrices respectively and the primary singular values (S_{11}, S_{22}, S_{33}) can be calculated in the algorithm. To find the angle of rotation of the satellite, the transformation matrix must first be found in equation (2.12) with an equation. The "diag" operator returns a square diagonal matrix with the elements of the vector in the main diagonal. Rotation angle error covariance matrix (\mathbf{P}_{SVD})

$$\mathbf{P}_{SVD} = \mathbf{U}diag[(s_2+s_3)^{-1} \ (s_3+s_1)^{-1} \ (s_1+s_2)^{-1}]\mathbf{U}^T \quad (2.13)$$

is required to determine the instantaneous times that give higher error results than desired. Here $s_1 = S_{11}, s_2 = S_{22}, s_3 = \det(\mathbf{U})\det(\mathbf{V}) S_{33}$.

2.5 SVD-Aided Extended Kalman Filter

For the non-traditional approach of the Kalman filter, inputs from the single-frame methods are the attitude angles as the linear measurements

$$\begin{aligned} z_\varphi(k) &= \varphi(k) + v_\varphi(k), \\ z_\theta(k) &= \theta(k) + v_\theta(k), \\ z_\psi(k) &= \psi(k) + v_\psi(k) \end{aligned} \quad (2.14)$$

and their error covariance values in a matrix form computed every step. In Eq. (14), $\varphi(k)$, $\theta(k)$ and $\psi(k)$ are the attitude angles determined by the SVD method, $v_{(\cdot)}(k)$ is the measurement noise of the attitude angles.

In order to achieve the required inputs for the EKF algorithm, decomposition of the \mathbf{P}_{SVD} into diagonalized covariance matrix should be performed. For this purpose, the UD decomposition method is presented and applied in the first step before the filtering stage. After UD factorization of the \mathbf{P}_{SVD} matrix, the diagonal measurement noise covariance matrix $\tilde{\mathbf{R}}$ is obtained and used in the filter as the input from the SVD. Furthermore, the measurement vector with the uncorrelated error components should

be redefined. Consequently, in this study SVD gives the uncorrelated observation inputs to the EKF framework.

2.5.1 UD decomposition of the measurement noise covariance matrix

With the decomposition of the attitude angles measurement error covariance matrix P_{SVD} , the measurement vector which will be having uncorrelated error components should be redefined. Also, because of the new uncorrelated measurement vector definition measurement error covariance will be updated as diagonal matrix format [95,97].

If the measurement vector \mathbf{Z} coming from the firstly introduced single-frame method is defined as,

$$\mathbf{z} = \mathbf{H}\mathbf{x} + \mathbf{v} \quad (2.15)$$

with measurement matrix \mathbf{H} and measurement noise \mathbf{V} .

Corresponding covariance matrix which is not diagonal matrix can be represented as,

$$E[\mathbf{v}\mathbf{v}^T] = \mathbf{P}_{SVD} = \mathbf{R} \quad (2.16)$$

UD can also be called modified Cholesky decomposition seen in elemental matrix form as,

$$\mathbf{P}_{SVD} = \mathbf{U} \times \mathbf{D} \times \mathbf{U}^T \quad (2.17)$$

$$\begin{bmatrix} r_{11} & r_{12} & r_{13} \\ r_{21} & r_{22} & r_{23} \\ r_{31} & r_{32} & r_{33} \end{bmatrix} = \begin{bmatrix} 1 & u_{12} & u_{13} \\ 0 & 1 & u_{23} \\ 0 & 0 & 1 \end{bmatrix} \begin{bmatrix} d_{11} & 0 & 0 \\ 0 & d_{22} & 0 \\ 0 & 0 & d_{33} \end{bmatrix} \begin{bmatrix} 1 & 0 & 0 \\ u_{21} & 1 & 0 \\ u_{31} & u_{32} & 1 \end{bmatrix}$$

The loop can be composed using i and j variables with the row/column size of n for the \mathbf{R} matrix.

$$\begin{aligned} n &= \text{length}(\mathbf{R}) \\ \text{Init: } \mathbf{U} &= \mathbf{D} = \text{zeros}(n) \\ D_{nn} &= R_{nn} \\ U_{in} &= \begin{cases} i & i = n \\ R_{in} / D_{nn} & i = n-1, n-2, \dots, 1 \end{cases} \end{aligned} \quad (2.18)$$

$$j \in \{n-1, n-2, \dots, 1\}$$

$$D_{jj} = R_{jj} - \sum_{k=j+1}^n D_{kk} U_{jk}^2 \quad (2.19)$$

$$U_{ij} = \begin{cases} 0 & i > j \\ 1 & i = j \\ \left(R_{ij} - \sum_{k=j+1}^n D_{kk} U_{ik} U_{jk} \right) & i = j-1, \dots, 1 \end{cases}$$

Covariance matrix (\mathbf{R}) can be factored in order to find diagonalized and uncorrelated matrix (\mathbf{D}) consisting of the pivots in addition to the unit upper triangular part (\mathbf{U}) whose diagonal entries are equal to 1 and forms the measurement vector again.

$$\mathbf{R} = \mathbf{U}\mathbf{D}\mathbf{U}^T \quad (2.20)$$

$$\tilde{\mathbf{z}} = \mathbf{U}^{-1}\mathbf{z} = \mathbf{U}^{-1}(\mathbf{H}\mathbf{x} + \mathbf{v}) = (\mathbf{U}^{-1}\mathbf{H})\mathbf{x} + (\mathbf{U}^{-1}\mathbf{v}) = \tilde{\mathbf{H}}\mathbf{x} + \tilde{\mathbf{v}} \quad (2.21)$$

As it is clear from (2.21), the “new” measurement $\tilde{\mathbf{z}}$ has a measurement matrix $\tilde{\mathbf{H}} = \mathbf{U}^{-1}\mathbf{H}$ and measurement noise $\tilde{\mathbf{v}} = \mathbf{U}^{-1}\mathbf{v}$. The covariance matrix $\tilde{\mathbf{R}}$ of the measurement noise $\tilde{\mathbf{v}}$ is determined as [95],

$$\tilde{\mathbf{R}} = E[\tilde{\mathbf{v}}\tilde{\mathbf{v}}^T] = \mathbf{D} \quad (2.22)$$

Newly composed $\tilde{\mathbf{R}}$ and $\tilde{\mathbf{z}}$ can be used in the Kalman filter in order to be updated automatically by the single-frame output.

The algorithm structure for the UD decomposition and the newly composed measurement vector can be seen in Figure 2.1.

INPUT AND INITIAL VALUES	FIRST ASSIGNMENT	LOOP	$\begin{pmatrix} R = \mathbf{U}\mathbf{D}\mathbf{U}^T \\ D = \text{diag}(\bar{D}) \end{pmatrix}$
$R_{n \times n}$ $U_{n \times n} = \text{zeros}(n)$ $\bar{D}_n = \text{zeros}(1, n)$	$\bar{D}(n) = R(n, n)$ $U(:, n) = R(:, n) ./ \bar{D}(n)$	$FOR j = n-1:-1:1$ $\bar{D}(j) = R(j, j) - \sum (\bar{D}(j+1:n) \cdot U(j, j+1:n)^2)$ $U(j, j) = 1$ $FOR i = j-1:-1:1$ $U(i, j) = R(i, j) - \sum (\bar{D}(j+1:n) \cdot U(i, j+1:n) \cdot U(j, j+1:n))$ END END	$D = \text{diag}(\bar{D})$ $\tilde{R} = D$ $\tilde{z} = \mathbf{U}^{-1}\mathbf{z}$

Figure 2.1 : UD decomposition algorithm structure.

2.5.2 EKF design for attitude and rate estimation

If the state vector is arranged as (2.1) and the mathematical model of the LEO satellite's rotational motion about its center of mass, is linearized using the quasilinearization method. We will consider a real-time linear Taylor approximation of the system function at the previous state estimate. The filtering algorithm, in this case, is given below.

Innovation sequence and the equation of the estimation value,

$$\Delta(k+1) = \{\tilde{\mathbf{z}}(k+1) - \mathbf{H}\hat{\mathbf{x}}(k+1/k)\} \quad (2.23a)$$

$$\hat{\mathbf{x}}(k+1) = \hat{\mathbf{x}}(k+1/k) + \mathbf{K}(k+1) \times \Delta(k+1) \quad (2.23b)$$

Here $\tilde{\mathbf{z}}(k+1)$ is the measurement vector, \mathbf{H} is the measurement matrix, $\Delta(k+1)$ is the innovation sequence. In the investigated case the measurement matrix is composed of a unit matrix. For the gyroless satellites, $\tilde{\mathbf{z}}(k+1) = [\tilde{z}_\varphi(k+1) \quad \tilde{z}_\theta(k+1) \quad \tilde{z}_\psi(k+1)]$ measurement vector with $\mathbf{H} = \text{diag}([1 \quad 1 \quad 1 \quad 0 \quad 0 \quad 0])$ measurement matrix, for the satellites having gyros,

$$\tilde{\mathbf{z}}(k+1) = [\tilde{z}_\varphi(k+1) \quad \tilde{z}_\theta(k+1) \quad \tilde{z}_\psi(k+1) \quad \tilde{z}_{\omega_x}(k+1) \quad \tilde{z}_{\omega_y}(k+1) \quad \tilde{z}_{\omega_z}(k+1)]$$

measurement vector with $\mathbf{H} = \text{diag}([1 \quad 1 \quad 1 \quad 1 \quad 1 \quad 1]) = \mathbf{I}_{6 \times 6}$ measurement matrix are used. Normalized innovations are obtained as

$$\left\{ \hat{\Delta}(k+1) = \Delta(k+1) \times [\mathbf{H}\mathbf{P}(k+1/k)\mathbf{H}^T + \tilde{\mathbf{R}}(k)]^{-0.5} \right\}.$$

Equation of the extrapolation value,

$$\hat{\mathbf{x}}(k+1/k) = f[\hat{\mathbf{x}}(k), k] \quad (2.24)$$

Filter-gain of EKF,

$$\mathbf{K}(k+1) = \mathbf{P}(k+1/k)\mathbf{H}^T \times [\mathbf{H}\mathbf{P}(k+1/k)\mathbf{H}^T + \tilde{\mathbf{R}}(k)]^{-1} \quad (2.25)$$

The covariance matrix of the extrapolation error is,

$$\mathbf{P}(k+1/k) = \frac{\partial f[\hat{\mathbf{x}}(k), k]}{\partial \hat{\mathbf{x}}(k)} \mathbf{P}(k/k) \frac{\partial f^T[\hat{\mathbf{x}}(k), k]}{\partial \hat{\mathbf{x}}(k)} + \mathbf{Q}(k) \quad (2.26)$$

The covariance matrix of the filtering error is,

$$\mathbf{P}(k+1/k+1) = [\mathbf{I} - \mathbf{K}(k+1)\mathbf{H}]\mathbf{P}(k+1/k) \quad (2.27)$$

$\tilde{\mathbf{R}}$ is the diagonalized covariance matrix of measurement noise and \mathbf{Q} is the covariance matrix of the system noises.

Equations given as (2.23) - (2.27) represent the EKF, which fulfills recursive estimation of the satellite's rotational motion parameters about its mass center on the linear attitude measurements. The whole algorithm scheme for SVD-aided EKF attitude and rate estimation can be seen in Figure 2.2 including the sub-step of UD decomposition.

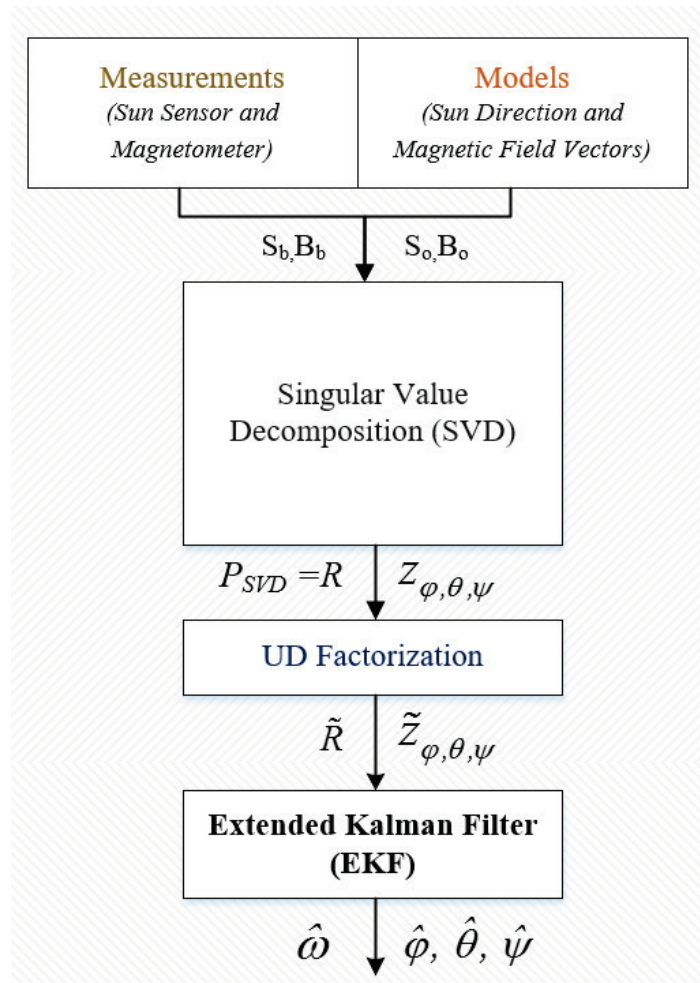


Figure 2.2 : Integrated SVD/EKF attitude and rate estimation block diagram with UD factorization.

2.6 Analysis of Simulation Results

Low Earth orbiting nanosatellite's orbit and structural parameters are used in order to perform the simulations. The principal moment of inertia

$\mathbf{J} = \text{diag}(2.1 \times 10^{-3} \quad 2.0 \times 10^{-3} \quad 1.9 \times 10^{-3})$ is used which belongs to a nanosatellite.

The satellite has attitude sensors as magnetometers and sun sensors. For the magnetometer measurements, the sensor noise is characterized by zero-mean Gaussian white noise with a standard deviation of $\sigma_m = 300 \text{ nT}$. The standard deviation for the sun sensor noise is taken as $\sigma_s = 0.002$ (for unit vector measurements).

Small satellites especially the nano and pico-satellites have a poor capability on the computations. One of the computationally heavy stages in the algorithms is taking the inverse of the measurement error covariance at each step which also might lead the filter to be unstable at some point. Since the computational sources are not sufficient at small satellites, it is better to use the measurement covariance matrix as a diagonal to reduce the computational burden. There are two ways in order to use this matrix diagonal. The first is to neglect the non-diagonal terms and the second is to use the UD factorization. For analyzing the simulation results, both methods are considered and compared.

After the UD factorized $\tilde{\mathbf{R}}$ matrix and newly formed measurement vector step, the SVD-aided EKF algorithm works recursively. It can be seen in Figure 2.2 that the attitude angles can be estimated by using this sub-step more realistically.

2.6.1 Simulation results for the satellite without gyros

In Figures 2.3 - 2.5, actual values and the estimations of the attitude angles by only SVD, integrated SVD&EKF can be seen in the first panels of the figures. The error changes in time also are plotted as the 2nd panels showing that acceptable attitude estimations can be obtained using the algorithm including the UD decomposed measurement error covariance matrix and newly formed measurement vector updated at each step.

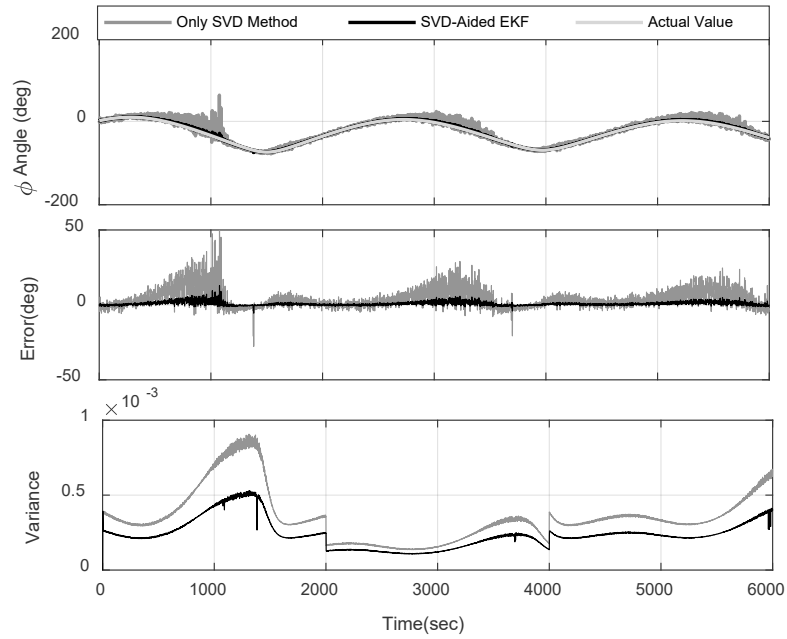


Figure 2.3 : Roll angle estimations, error, and variance of only SVD and SVD-aided EKF using UD factorization (gyro-free).

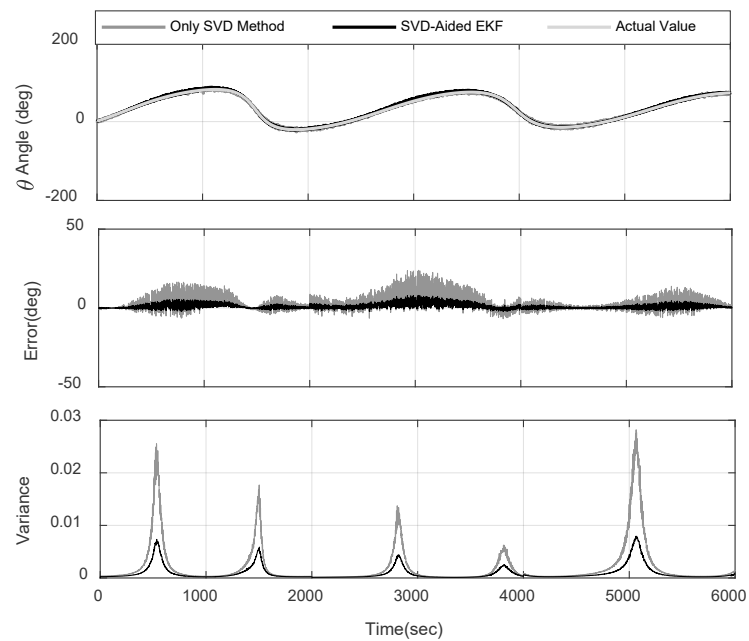


Figure 2.4 : Pitch angle estimations, error, and variance of only SVD and SVD-aided EKF using UD factorization (gyro-free).

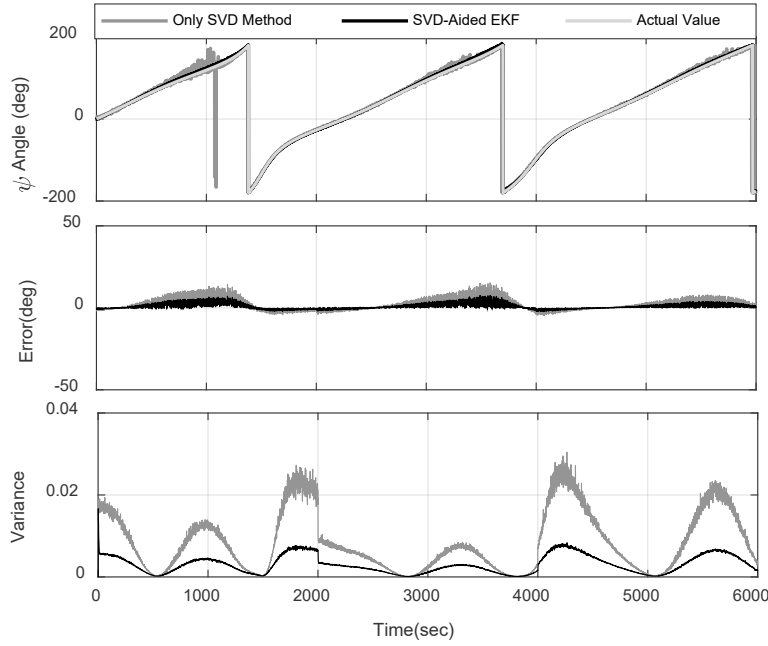


Figure 2.5 : Yaw angle estimations, error, and variance of only SVD and SVD-aided EKF using UD factorization (gyro-free).

The corresponding variance values to roll, pitch, and yaw attitude angles are presented in the third panels of Figures 2.3 – 2.5. As can be seen from the figures, the filter gains an adaptive form with the help of SVD using its variance values and develops it accordingly. Furthermore, in Table 2.1, the root mean square error (RMSE) of attitude angles is presented. The simulation results of the filter that uses UD factorization for the measurement noise covariance diagonalization and measurement update is called “With UD”. On the other hand, the simulation results of the filter that assumes the measurements are uncorrelated and eliminate the non-diagonal elements of the measurement noise covariance directly are called “With Assumption”.

Table 2.1 : RMSE results of attitude angles (gyro-free).

RMSE (deg)	Roll	Pitch	Yaw
With UD	0.2940	0.0881	0.0635
With Assumption	0.2354	0.0603	0.0426

As seen from Table 2.1, the SVD-aided EKF with assumption gives an unrealistic accuracy of the attitude angles due to neglecting of non-diagonal elements of SVD's angle error covariance matrix in which the measurements are not uncorrelated in

reality. In other words, the accuracy is exaggerated or overrated under the assumption of neglecting the non-diagonal elements as it assumes that the errors are not correlated at all but it is not the case in real applications. Therefore, it is expected to have less accurate results in the simulations for “With UD” but to have more realistic outputs instead.

2.6.2 Simulation results for the satellite having gyros

In order to simulate the three-axis rate gyros, the following equation is used,

$$\boldsymbol{\omega}_{Bl_m}(k) = \boldsymbol{\omega}_{Bl}(k) + \mathbf{v}_g(k) \quad (2.28)$$

For the calibration of the gyroscopes, the biases on gyros’ each axis can be estimated in the filter first as it is done in the studies of [98,99]. In this study, the gyros are assumed to be calibrated in-orbit before the simulations. The estimations of the roll, pitch, and yaw angles can be seen in Figures 2.6 – 2.8 in the first panels, errors in the second, and the related variance in the third. As can be seen from the figures that the SVD-aided EKF improves the attitude estimations as expected.

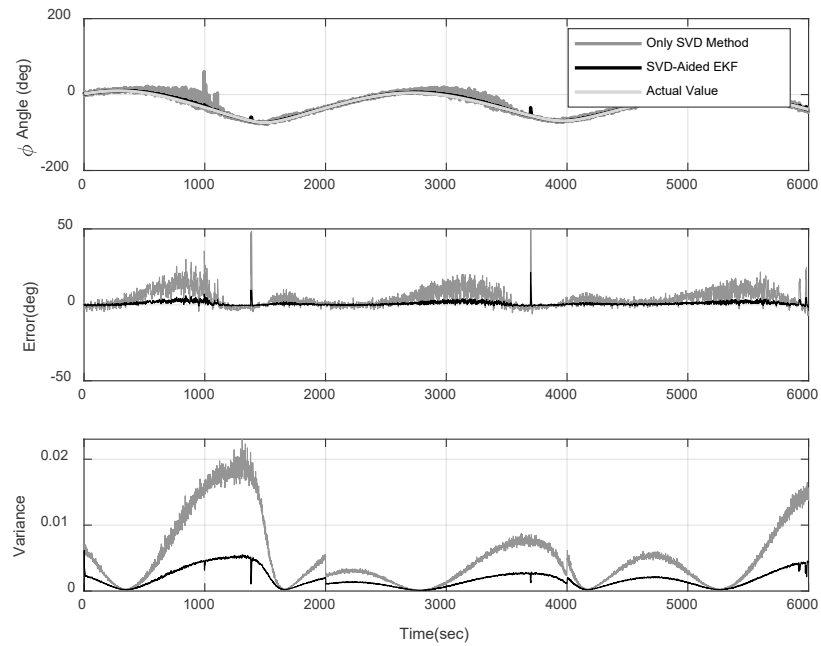


Figure 2.6 : Roll angle estimations, error, and variance of only SVD and SVD-aided EKF using UD factorization (with gyro).

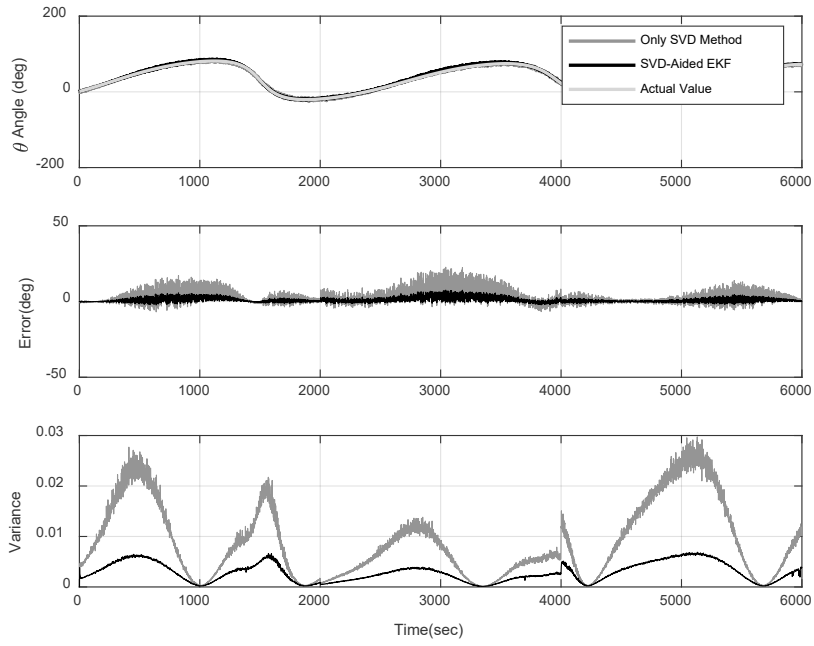


Figure 2.7 : Pitch angle estimations, error, and variance of only SVD and SVD-aided EKF using UD factorization (with gyro).

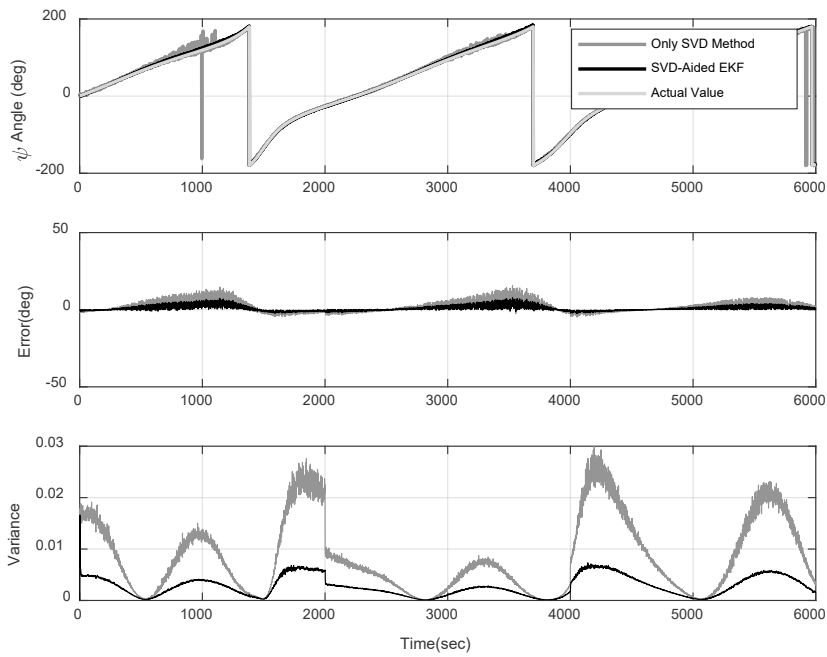


Figure 2.8 : Yaw angle estimations, error, and variance of only SVD and SVD-aided EKF using UD factorization (with gyro).

Table 2.2 : RMSE results of attitude angles (with gyro).

RMSE (deg)	Roll	Pitch	Yaw
With UD	0.0495	0.0782	0.0669
With Assumption	0.0350	0.0538	0.0614

Table 2.2 gives the RMSE of each attitude angle estimation with UD and with assumption. The simulations having UD factorization for the measurement noise covariance diagonalization and measurement update is called “With UD” while the simulations assuming the measurements are uncorrelated and eliminating the non-diagonal elements of the measurement noise covariance, is called “With Assumption”. SVD-aided EKF with assumption gives an accuracy of the attitude angles which are unrealistic. It can be stated that the gyroscopes improve the attitude estimations for both cases (with UD and with assumption cases) if it is compared with Table 2.1.

UD decomposition which is more realistic than neglecting the non-diagonal elements is also considered. It should be noted that for satellites that require high accuracy performance and error characteristics for their mission objectives, the UD factorization step is a significant stage. However, the difference between the RMSE results of algorithms using and not using the UD step is very small. From this, it can be concluded that the non-diagonal elements of the SVD's angle error covariance matrix can be removed and only the diagonal elements can be considered in the input of the EKF for most of the nanosatellite missions.

2.7 Conclusion

In this study singular value decomposition aided extended Kalman filter for nanosatellite's attitude estimation is presented. The sun sensors and the magnetometers are used as the attitude sensors in SVD. In the proposed method EKF inputs are coming from SVD as the linear measurements of attitude angles and their error covariance. UD is factorizing the attitude angles error covariance with forming the measurements in order to obtain the appropriate inputs for the EKF. Moreover, gyro and gyro-free cases are considered in the demonstrations. For the integrated SVD/EKF using the newly formed measurements and measurement noise covariance with UD factorization, the whole algorithm is run. Simulation results show that the SVD-aided EKF with the assumption which acts that the measurements are uncorrelated and removes the non-diagonal elements of the measurement noise covariance gives an overrated accuracy of the attitude angles. However, the proposed attitude estimation method with UD factorization provides the exact value of attitude accuracy.

The demonstrations show that the difference in the estimation results of the SVD-aided EKF with and without UD factorization is small. Therefore, it can be said that the non-

diagonal elements of SVD's angle error covariance matrix can be omitted from the input of the EKF if high accuracy of error characteristics are not required and, in this case, it is seen that the error caused by this assumption is small at a negligible level. Besides, if the computational load is a problem, then non-diagonal elements of the SVD error covariance matrix can be neglected without UD factorization. If high accuracy performance and error characteristics are required for the satellite mission, UD decomposition is recommended to be used which is an important step. The absence of this step for those missions might cause major problems eventually in attitude control of the satellite.

3. NANOSATELLITE ATTITUDE ESTIMATION FROM VECTOR MEASUREMENTS USING SVD-AIDED UKF ALGORITHM*

3.1 Abstract

Integrated singular value decomposition (SVD) and unscented Kalman filter (UKF) method can estimate the attitude and attitude rates of a nanosatellite recursively. At first, Wahba's loss function is minimized using the SVD and the optimal attitude angles are determined on the basis of the magnetometer and sun sensor measurements thereafter UKF makes use the SVD's attitude estimates as measurements and provides more accurate attitude information as well as the attitude rate estimates. "Rotation angle error covariance matrix" calculated for the SVD estimations are used in the UKF as the measurement noise covariance. The algorithm is compared with SVD and UKF only methods for estimating the attitude from vector measurements. Possible algorithm switching ideas are discussed specifically for eclipse where sun sensor measurements are not available.

3.2 Introduction

Sun sensors and magnetometers are common attitude sensors for nanosatellite missions; they are cheap, simple, light and available as commercial off-the-shelf equipment [4,5]. However, the overall achievable attitude determination accuracy is limited with these sensors mainly as a result of their inherent limitations and unavailability of the sun sensor measurements when the satellite is in eclipse.

Attitude estimation with magnetometer and sun sensor measurements has been addressed in many researches and various algorithms that intend improving the estimation accuracy have been proposed. A basic solution is to use a Kalman filtering algorithm for integrating the measurements under the propagation model of the

* This chapter is based on the paper "Cilden, D., Soken, H.E., and Hajiyev, C. (2017). Nanosatellite Attitude Estimation from Vector Measurements using SVD-aided UKF Algorithm, *Metrology and Measurement Systems*, **24**, 113-128, doi: 10.1515/mms-2017-0011".

satellite dynamics and estimate the satellite attitude possibly along with the sensor biases. For example in [5] two filtering algorithms are proposed, both based on the Multiplicative Extended Kalman Filter (EKF). The first algorithm is used for estimation of attitude quaternions, gyro biases and sun sensor calibration parameters and the second estimates only the quaternions and gyro biases excluding the sun sensor calibration parameters. The main drawback of both algorithms is the degradation in the estimation results when the satellite is in eclipse so the sun sensor data is not available. Similar phenomenon can be seen in [4] for the unscented Kalman filter (UKF) estimations. Another approach for nanosatellite attitude estimation is to solve for attitude using a single-frame attitude estimator. This method is based on computing sun and magnetic field vectors in the reference frame and measuring the same vectors in the body coordinate system. Then a deterministic method such as the TRIAD (two-vector algorithm) or an optimization method such as the QUEST can be used for the attitude estimation [17]. As a drawback these methods only rely on the measurements; they do not use any knowledge about the satellite dynamics. Attitude estimation methods, which take the advantage of system's mathematical model, may increase the attitude estimation accuracy significantly. In [18], sun-eclipse phases are considered to use both traditional and non-traditional methods depending on the sun sensor operational or not. In the sun sensor operational mode, Gauss-Newton method obtains the quaternion estimates for the usage in EKF. In eclipse mode, only traditional EKF is used. Measurement covariance values in EKF are not provided by the deterministic method to the filter and they are selected. This leads some jumps in the filter even outside of the eclipse. If the variance values of the first method are used as measurement noise covariance in EKF, filter would have compensated these errors.

The traditional approaches to design a Kalman filter (KF) for satellite attitude estimation use the nonlinear measurements of reference directions (e.g. sun direction) [4,11,19,20]. The measurement models in the filter are based on the nonlinear models of the reference directions so the measurements and states are related via nonlinear equations. In the linear measurements based approach the attitude angles are first found by using the vector measurements and a suitable single-frame attitude estimation method [17]. Then these attitude estimates are used as measurements within the KF. The filter measurement model is linear in this case, since the single-frame attitude

estimator provides directly the states themselves as measurements. We may name such algorithms as “single-frame estimator aided attitude filtering”.

An earlier study on single-frame estimator aided attitude filtering was carried out in [12]. In this study the authors integrate the algebraic method (TRIAD) and the EKF algorithms to estimate the attitude angles and angular velocities. The magnetometers, sun sensors, and horizon scanners/sensors are used as measurement devices and three different two-vector algorithms based on the Earth’s magnetic field, sun, and nadir vectors are proposed. An EKF is designed to obtain the satellite’s angular motion parameters with the desired accuracy. The measurement inputs for the EKF are the attitude estimates of the two-vector algorithms. Interest in “single-frame estimator aided attitude filtering” is higher in the more recent literature [21–23]. The attitude determination concept of the Kyushu University mini-satellite QSAT is based on a combination of the Weighted-Least-Square (WLS) and KF [21,22]. The WLS method produces the optimal attitude-angle observations at a single-frame by using the sun sensor and magnetometer measurements. The KF combines the WLS angular observations with the attitude rate measured by the gyros to produce the optimal attitude solution. In [23] an interlaced filtering method is presented for nanosatellite attitude determination. In this integrated system, the optimal-REQUEST and UKF algorithms are combined to estimate the attitude quaternion and gyro drifts. The optimal-REQUEST, which cannot estimate gyroscope drifts, is run for the attitude estimation. Then the UKF is used for the gyro-drift estimation on the basis of linear measurements obtained as optimal-REQUEST estimates. There are also similar applications for the UAV attitude estimation. De Marina et al. introduce an attitude heading reference system based on the UKF using the TRIAD algorithm as the observation model in [24].

Here, we may also refer to the studies where a single-frame attitude estimator used together with an attitude filter but not for providing the linear measurements [13,27]. For linear measurements, it is equivalent to first update the attitude using the single-frame estimator and subsequently use this updated portion of the state to update the remainder of the state as it is to update the entire state at once. However in [13,27], the measurement model is nonlinear. A nonlinear update for the attitude is obtained solving the Wahba’s problem and subsequently used to update the non-attitude states using the optimal gain for the linear measurement case. Therefore, in these studies, the

attitude is updated using the single-frame estimator and all remaining non-attitude states using the standard nonlinear attitude filters.

In this study we investigate a SVD-aided UKF (SaUKF) algorithm for nanosatellite attitude estimation. The nanosatellite has magnetometers and sun sensors as the attitude sensors on-board. In the first phase, Wahba's problem is solved by the Singular Value Decomposition (SVD) method and quaternion estimations are obtained for the satellite's attitude. These quaternion estimations are then used as measurements for an UKF, which forms the second phase of the algorithm. The SaUKF provides improved attitude knowledge and attitude rate estimates. The whole algorithm runs recursively. Main aim is to propose an easy to apply and accurate nanosatellite attitude estimation algorithm, which is also robust against estimation deteriorations when the satellite is in eclipse. Initial results are presented in [100]. In this study we compare the results with an UKF that uses nonlinear measurements. Besides we propose an algorithm that switches between the UKF with nonlinear measurements and the SaUKF to ensure both the accuracy and robustness.

3.3 Satellite Equations of Motion and Measurement Models

In this section we briefly review the satellite equations of motion and the measurement models for magnetometers and sun sensors.

3.3.1 Satellite Equations of Motion

The satellite's kinematics equation of motion derived using the quaternion attitude representation can be demonstrated as [1],

$$\dot{\mathbf{q}}(t) = \frac{1}{2} \Omega(\boldsymbol{\omega}_{BR}(t)) \mathbf{q}(t) \quad (3.1)$$

In equation (3.1), the quaternion, \mathbf{q} is formed of four attitude parameters, $\mathbf{q} = [q_1 \ q_2 \ q_3 \ q_4]^T$. Three terms of the quaternion, \mathbf{q} show a vector and the last term is the scalar one, then quaternion can be take a form of $\mathbf{q} = [\mathbf{g}^T \ q_4]^T$ and $\mathbf{g} = [q_1 \ q_2 \ q_3]^T$. Moreover in (1), $\Omega(\boldsymbol{\omega}_{BR})$ is the skew symmetric matrix as;

$$\Omega(\boldsymbol{\omega}_{BR}) = \begin{bmatrix} 0 & \omega_3 & -\omega_2 & \omega_1 \\ -\omega_3 & 0 & \omega_1 & \omega_2 \\ \omega_2 & -\omega_1 & 0 & \omega_3 \\ -\omega_1 & -\omega_2 & -\omega_3 & 0 \end{bmatrix}, \quad (3.2)$$

$\boldsymbol{\omega}_{BR}$ vector is composed of ω_1 , ω_2 and ω_3 which indicates the angular velocity of the body frame with respect to the orbit frame. Angular rate vector should be identified because of the sensor usage. Hence, the rate vector in the body frame with respect to the inertial coordinate system can be shown as; $\boldsymbol{\omega}_{BI} = [\omega_x \quad \omega_y \quad \omega_z]^T$. $\boldsymbol{\omega}_{BI}$ and $\boldsymbol{\omega}_{BR}$ can be related in the following formulation,

$$\boldsymbol{\omega}_{BR} = \boldsymbol{\omega}_{BI} - A[0 \quad -\omega_o \quad 0]^T. \quad (3.3)$$

Angular velocity of the satellite in orbit specifies ω_o with respect to inertial reference, found as $\omega_o = (\mu / r^3)^{1/2}$ for a circular orbit using μ , is the product of the two constants (GM_E). Here, G : gravitational constant, M_E is the mass of the Earth and r , the distance between satellite and Earth center of masses. In equation (3.3) A is the transformation matrix which can be related to the quaternions via;

$$A = (q_4^2 - \mathbf{g}^2)I_{3 \times 3} + 2\mathbf{g}\mathbf{g}^T - 2q_4[\mathbf{g} \times], \quad (3.4)$$

Unit matrix $I_{3 \times 3}$ has the dimension of 3×3 and $[\mathbf{g} \times]$ is the skew-symmetric matrix as the following,

$$[\mathbf{g} \times] = \begin{bmatrix} 0 & -g_3 & g_2 \\ g_3 & 0 & -g_1 \\ -g_2 & g_1 & 0 \end{bmatrix}. \quad (3.5)$$

Satellite's dynamic equations are necessary in order to estimate full state attitude including both the attitude and attitude rates. Based on the Euler's equations dynamic knowledge can be maintained found by;

$$J \frac{d\boldsymbol{\omega}_{BI}}{dt} = \mathbf{N}_d - \boldsymbol{\omega}_{BI} \times (J\boldsymbol{\omega}_{BI}), \quad (3.6)$$

Here, J is inertia matrix composed of $J = \text{diag}(J_x, J_y, J_z)$ which are the principal moments of inertia and the external torques affecting the satellite can be added in order to find resulting disturbance torque, N_d

$$N_d = N_{gg} + N_{ad} + N_{sp} + N_{md}. \quad (3.7)$$

N_{gg} is the gravity gradient torque, N_{ad} is the aerodynamic disturbance torque, N_{sp} is the solar pressure disturbance torque and N_{md} is the residual magnetic torque caused by the interaction of the satellite's residual dipole and the Earth's magnetic field [1].

3.3.2 Sensor Models

Magnetometer sensor for attitude determination is a very common sensor for small satellite missions. Earth's magnetic field measurements model can be given in equation (3.8) (magnetometers are assumed to be calibrated) [101,102],

$$\begin{bmatrix} B_x(\mathbf{q}, t) \\ B_y(\mathbf{q}, t) \\ B_z(\mathbf{q}, t) \end{bmatrix} = \mathbf{A} \begin{bmatrix} B_1(t) \\ B_2(t) \\ B_3(t) \end{bmatrix} + \boldsymbol{\eta}_1. \quad (3.8)$$

Components of the Earth's magnetic field, $B_1(t)$, $B_2(t)$ and $B_3(t)$ in orbital coordinate frame can be calculated by the common and accurate magnetic field model, International Geomagnetic Reference Field (IGRF) [102]. $B_x(\mathbf{q}, t)$, $B_y(\mathbf{q}, t)$ and $B_z(\mathbf{q}, t)$ are the vector components of measured magnetic field by the magnetometers therefore they are in the body reference system. Moreover, $\boldsymbol{\eta}_1$ is the zero mean Gaussian white noise

$$E[\boldsymbol{\eta}_{1k} \boldsymbol{\eta}_{1j}^T] = I_{3 \times 3} \sigma_m^2 \delta_{kj}, \quad (3.9)$$

σ_m is standard deviation and δ_{kj} is Kronecker symbol.

Sun direction with respect to the inertial coordinates with centered Earth only depends on the time in terms of the Julian Day (T_{TDB}). T_{TDB} can be derived using the satellite's reference epoch and the exact time. The variables are the mean anomaly (M_{Sun}) and

the mean longitude of ($\lambda_{M_{Sun}}$) of sun. Using equation (3.10), the ecliptic longitude of sun ($\lambda_{ecliptic}$) and its linear model (ε) can be found [103].

$$M_{Sun} = 357.5277233^0 + 35999.05034T_{TDB} \quad (3.10a)$$

$$\lambda_{ecliptic} = \lambda_{M_{Sun}} + 1.914666471^0 \sin(M_{Sun}) + 0.019994643 \sin(2M_{Sun}) \quad (3.10b)$$

$$\lambda_{M_{Sun}} = 280.4606184^0 + 36000.77005361T_{TDB} \quad (3.10c)$$

$$\varepsilon = 23.439291^0 - 0.0130042T_{TDB} \quad (3.10d)$$

From those relations in equation (3.10), sun direction vector (\mathbf{S}_{ECI}) in inertial coordinates can be found.

$$\mathbf{S}_{ECI} = \begin{bmatrix} \cos \lambda_{ecliptic} \\ \sin \lambda_{ecliptic} \cos \varepsilon \\ \sin \lambda_{ecliptic} \sin \varepsilon \end{bmatrix} \quad (3.11)$$

However, satellite rotating through its trajectory therefore the transformation of the unit sun direction vector into the orbital frame is necessary with using orbit propagation algorithm. Finally, the equation (3.12) showing the relation between the sun sensor measurement vector and the IGRF model vector results.

$$\mathbf{S}_b = \mathbf{A}\mathbf{S}_o + \boldsymbol{\eta}_2 \quad (3.12)$$

\mathbf{S}_o is the sun direction vector in orbit reference system and \mathbf{S}_b is the sun sensor measurements in body reference system having, $\boldsymbol{\eta}_2$ the zero mean Gaussian white noise with the characteristic of

$$E[\boldsymbol{\eta}_{2k}\boldsymbol{\eta}_{2j}^T] = I_{3 \times 3} \sigma_s^2 \delta_{kj}. \quad (3.13)$$

σ_s is the standard deviation of sun sensor error.

The satellite's orbital elements and position on the orbit must be known to model the Earth's magnetic field and sun vectors in the orbit frame.

3.4 SVD-Aided UKF Algorithm

The content of this part includes the estimation of the satellite's attitude and the angular velocities during the operational mode of the mission. The estimation process is

divided into two sections as SVD and UKF. Firstly, a single frame method, SVD minimizes the Wahba's loss function with using two vectors and finds the coarse attitude angles and variance values for each axis. Then, UKF use the SVD results as input values at each time step and provide filtered attitude and attitude rates with higher accuracy.

3.4.1 Singular Value Decomposition Method

As a single-frame method, SVD aims to solve Grace Wahba's proposed problem [15]. In every single time frames, SVD can estimate the coarse attitude only using the measurements and the model vectors. In the loss function (see equation (3.14)), \mathbf{b}_i and \mathbf{r}_i are set of unit vectors obtained in two different coordinates and obtained at every single time interval. From the optimal solution for the orthogonal A matrix, attitude angles can be found [88].

$$L(\mathbf{A}) = \frac{1}{2} \sum_i a_i |\mathbf{b}_i - \mathbf{A}\mathbf{r}_i|^2, \quad (3.14)$$

The unit vectors in the loss function represent sun direction and Earth's magnetic field vectors for orbit frame (\mathbf{r}_i), body frame (\mathbf{b}_i) and a_i is the non-negative weight. Loss can be reduced into equation (3.15) as,

$$L(\mathbf{A}) = \lambda_0 - \text{tr}(\mathbf{A}\mathbf{B}^T), \quad (3.15)$$

where,

$$\lambda_0 = \sum a_i, \quad (3.16a)$$

$$\mathbf{B} = \sum a_i \mathbf{b}_i \mathbf{r}_i^T. \quad (3.16b)$$

SVD method can be used here to maximize the trace function expressed in equation (3.15) with the most robust algorithm among the other single-frame methods [88]. \mathbf{B} matrix has the singular value decomposition:

$$\mathbf{B} = \mathbf{U} \Sigma^T \mathbf{V}^T = \mathbf{U} \text{diag}[\Sigma_{11} \quad \Sigma_{22} \quad \Sigma_{33}] \mathbf{V}^T, \quad (3.17)$$

matrices \mathbf{U} and \mathbf{V} are orthogonal and the singular values obey $\Sigma_{11} \geq \Sigma_{22} \geq \Sigma_{33} \geq 0$.

Then, optimal attitude matrix can be found.

$$\mathbf{U}^T \mathbf{A}_{opt} \mathbf{V} = \text{diag}[1 \quad 1 \quad \det(\mathbf{U})\det(\mathbf{V})], \quad (3.18)$$

$$\mathbf{A}_{opt} = \mathbf{U} \text{diag}[1 \quad 1 \quad \det(\mathbf{U}) \det(\mathbf{V})] \mathbf{V}^T. \quad (3.19)$$

Covariance analysis is an important process in the integrated filtering technique and the matrix, \mathbf{P}_{svd} can be obtained with defining secondary singular values $s_1 = \Sigma_{11}$, $s_2 = \Sigma_{22}$, $s_3 = \det(\mathbf{U}) \det(\mathbf{V}) \Sigma_{33}$ as follows,

$$\mathbf{P}_{svd} = \mathbf{U} \text{diag}[(s_2 + s_3)^{-1} \quad (s_3 + s_1)^{-1} \quad (s_1 + s_2)^{-1}] \mathbf{U}^T. \quad (3.20)$$

The method is expecting measurements at every single time to provide attitude angles accurately hence, method fails when the satellite is during the eclipse or two vectors are parallel.

3.4.2 Unscented Kalman Filter

The UKF uses an accurate approximation called the Unscented Transform for solving the multidimensional integrals instead of the linear approximation to the nonlinear equations as Extended Kalman Filter (EKF) does [104]. The essence is the fact that; the approximation of a nonlinear distribution is easier than the approximation of a nonlinear function or transformation. The conventional algorithm for the UKF is not presented here for brevity and the reader may refer to [105], specifically for attitude estimation using the UKF.

In case of using quaternion for the kinematic modeling of the satellite's motion, the UKF in standard format cannot be implemented straightforwardly. The reason of such drawback is the constraint of quaternion unity given by $\mathbf{q}^T \mathbf{q} = 1$. If the kinematics equation (3.1) is used in the filter directly, than there is no guarantee that the predicted quaternion mean of the UKF will satisfy this constraint.

In [105], the authors overcome this problem by using an unconstrained three component vector to represent an attitude-error quaternion instead of using all four components of the quaternion vector. They represent the local error-quaternion with the vector of Generalized Rodrigues Parameters (GRP). In this paper we use the same method.

Recall that we represent a quaternion with its vector and scalar parts as $\mathbf{q} = [\mathbf{g}^T \quad q_4]^T$.

After that when the local error-quaternion is denoted by $\delta \mathbf{q} = [\delta \mathbf{g}^T \quad \delta q_4]^T$, the vector of GRP may be given as,

$$\delta \mathbf{p} = f [\delta \mathbf{g} / (a + \delta q_4)]. \quad (3.21)$$

Here a is a parameter from 0 to 1 and f is the scale factor. When $a = 0$ and $f = 1$ then equation (3.21) gives the Gibbs vector and when $a = 1$ and $f = 1$ then Eq. (21) gives the standard vector of modified Rodrigues parameters. In the paper [105] - as well as in this paper - f is chosen as $f = 2(a + 1)$. The inverse transformation from $\delta \mathbf{p}$ to $\delta \mathbf{q}$ is given by

$$\delta q_4 = \frac{-a \|\delta \mathbf{p}\|^2 + f \sqrt{f^2 + (1 - a^2) \|\delta \mathbf{p}\|^2}}{f^2 + \|\delta \mathbf{p}\|^2}, \quad (3.22a)$$

$$\delta \mathbf{g} = f^{-1} (a + \delta q_4) \delta \mathbf{p}. \quad (3.22b)$$

3.4.3 Attitude and Attitude Rate Estimation Using SaUKF

Two methods are integrated and SaUKF algorithm is proposed for nanosatellite attitude estimation. Main purposes are:

As a standalone technique the SVD works well as long as minimum 2 vector measurements are available and not parallel. However, if there is only one vector measurement as satellite is in eclipse, the SVD fails to provide any attitude estimate.

The SVD method gives attitude estimates as frequent as the sampling rate of the sensor with lower measurement frequency (if there is no propagation). The SaUKF can provide attitude estimate with a higher frequency since it makes use of the attitude dynamics.

The SVD method does not estimate the attitude rates. For most of the cases satellite attitude rates must be estimated especially for control purposes. There are deterministic methods to estimate satellite's attitude rate from vector measurements [106], but usually a filtering based method gives more accurate estimates.

When the SVD method cannot give any estimation results, the covariance for the SVD estimations and so the elements of the R matrix increase. Therefore, the UKF is robust against the failures in the SVD estimations, as we see during the eclipse.

As attitude representation, quaternions are used in SVD algorithm. However, for SaUKF, attitude errors in terms of GRP is acquired seen in Eq. (3.23),

$$\delta \mathbf{q}_{obs} = \mathbf{q}_{mes} \otimes [\hat{\mathbf{q}}_0(k+1|k)]^{-1}, \quad (3.23)$$

Here, \mathbf{q}_{mes} , coming from the SVD method are quaternion-multiplied with the predicted mean quaternion. Then regarding $\delta \mathbf{q}_{obs} = [\delta \mathbf{g}_{obs}^T \quad \delta q_{4,obs}]^T$, measurement of the attitude error is calculated as,

$$\delta \mathbf{p}_{obs} = f[\delta \mathbf{g}_{obs} / (a + \delta q_{4,obs})] \quad (3.24)$$

The schema for the attitude and rate estimation algorithm of the integrated method is given in Figure 3.1.

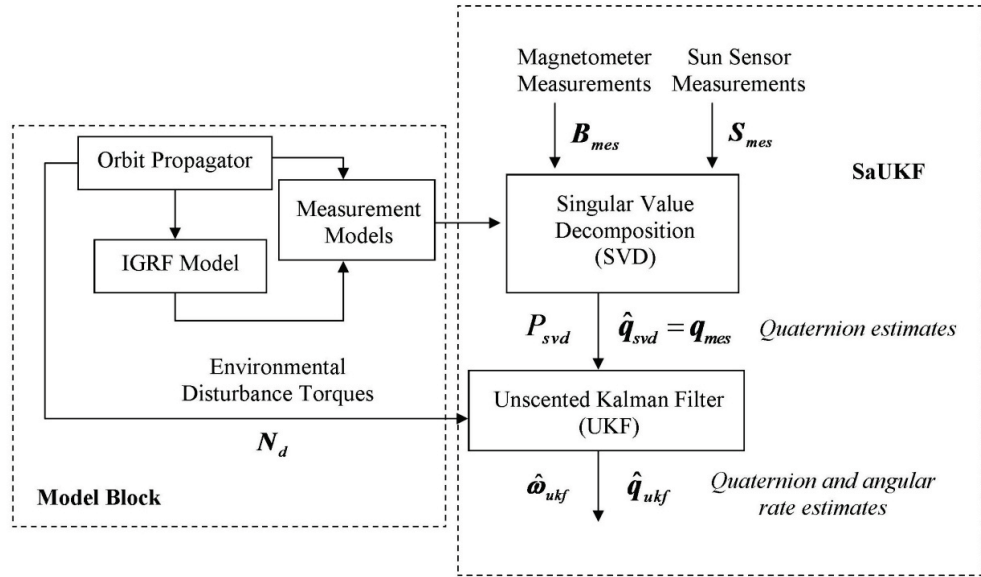


Figure 3.1 : Scheme for the attitude and attitude rate estimation using the SaUKF.

3.5 Simulations for a Nanosatellite

Several simulations were performed for evaluation of the attitude estimation algorithm. Three unit cube sized satellite is considered for the estimation scheme as about 3 kg mass and $J = diag(0.055 \quad 0.055 \quad 0.017)kg.m^2$ inertia matrix. Satellite has an almost circular orbit with an eccentricity of $e = 6.4 \times 10^{-5}$ and $i = 74^\circ$ inclination at 612 km altitude.

All sensors are assumed to be calibrated against biases, scale factors and so on. Therefore, only the sensor noise (zero mean Gaussian white noise) is considered in the algorithm with $\sigma_m = 300nT$ standard deviation for magnetometer and $\sigma_s = 0.002$ unit

for sun sensor. Total orbital time is close to 6000 sec. and the time step is taken as 1 second.

Both SaUKF and UKF use the process noise covariance for attitude and rates as 1×10^{-4} and 1×10^{-9} and have an eclipse period between 2000 – 4000 sec. In Figure 3.2, SaUKF, SVD and UKF only estimation error results can be seen and compared. As clearly seen the SaUKF estimates the attitude more accurately than both the SVD and UKF only methods except the eclipse period. In the eclipse duration, the SVD method fails by reason of no sun sensor data. The quaternion measurements for the SaUKF deteriorate and the terms for the R , which is coming from the covariance matrix of the SVD angle estimation errors (P_{svd}), increase. If the SaUKF gain gets very low values since R values are very high, the correction term of the UKF will become insignificant and the contribution of the propagation model to estimation becomes dominant. That enables attitude estimation during eclipse even though there is no measurement input to the filter.

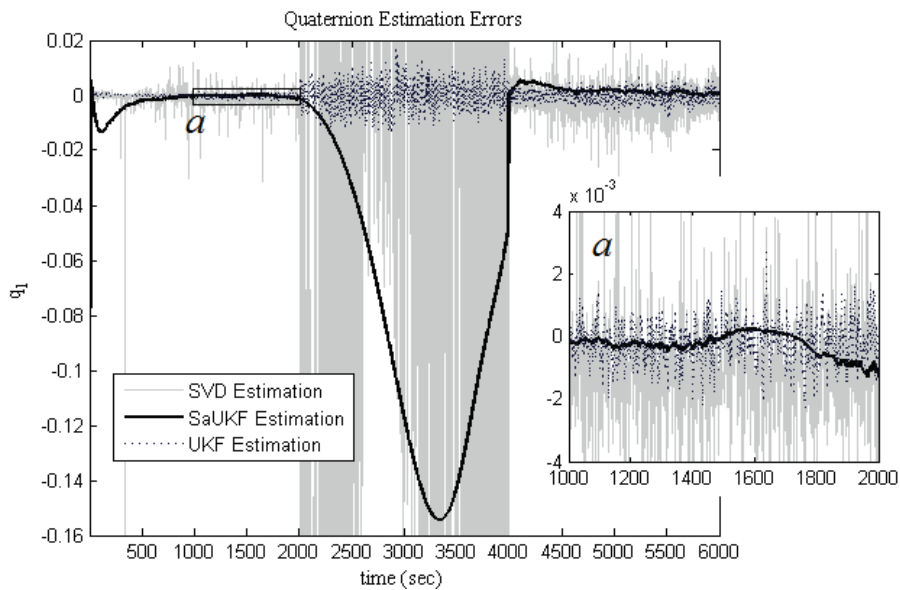


Figure 3.2 : Estimation error for quaternion q_1 ; comparison of the UKF and SVD only estimations with the SaUKF. Subfigure a zooms to the indicated part in the main figure.

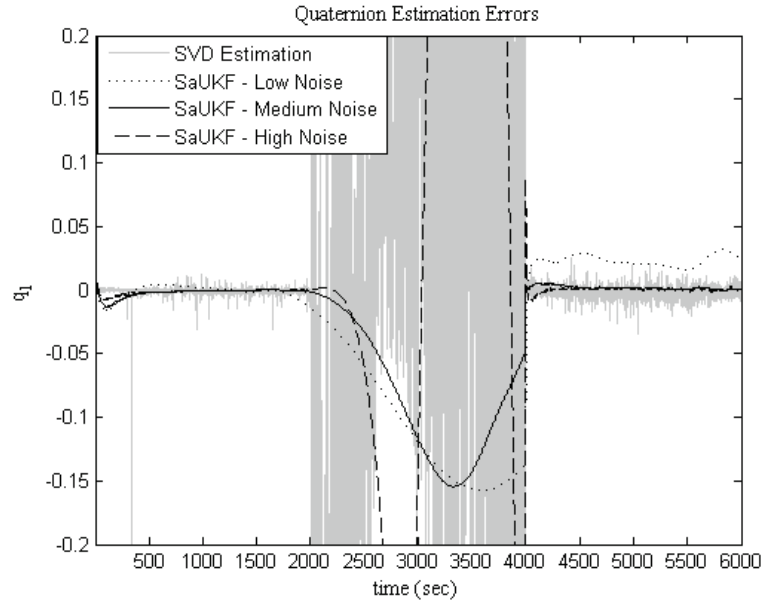


Figure 3.3 : Quaternion estimation error for the SaUKF with different process noise covariance, Q , values.

Process noise covariance, Q is a parameter that can enable filter to rely mostly on the measurements or the dynamics in the filter. In the filter, 1×10^{-4} and 1×10^{-9} pair is used as medium noise. Here, at the end of the eclipse period, before the sun sensor data are coming attitude angle has 10 degrees error. If the Q pair is 1×10^{-3} and 1×10^{-7} which is higher than the selected, results are close to the measurements and attitude angles are diverging more during the eclipse. On the other hand, with lower pair values such as 1×10^{-9} and 1×10^{-13} SaUKF becomes non-agile meaning that it has smaller convergence rate at the end of the eclipse or beginning of the orbit (Figure 3.3).

In eclipse, the UKF only method gives the most accurate attitude estimations. During that period it works only with the magnetometer measurements. Since the magnetometers are coarser sensors compared to the sun sensors, there is a clear increase in the UKF estimation error in the eclipse but still the estimations are accurate enough for a nanosatellite mission with this sensor configuration (less than 0.1 degrees – see Figure 3.4 for attitude estimation error norms).

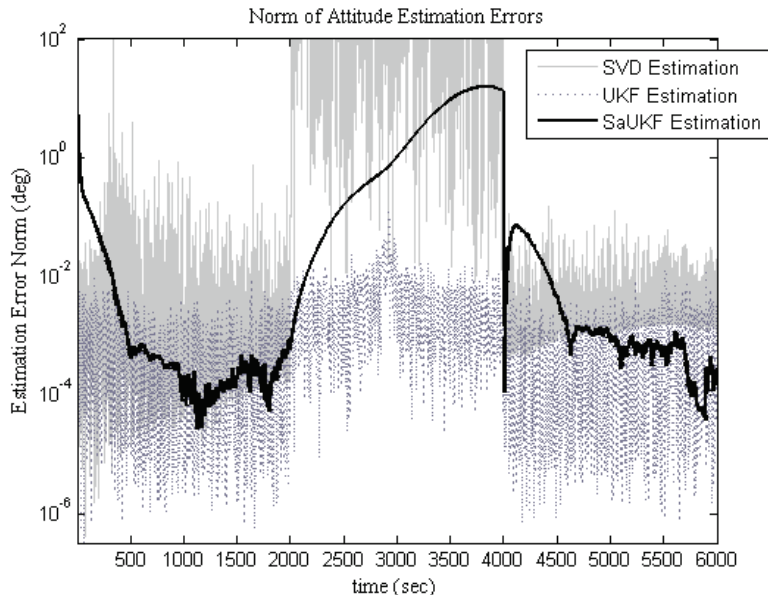


Figure 3.4 : Norm of attitude estimation errors.

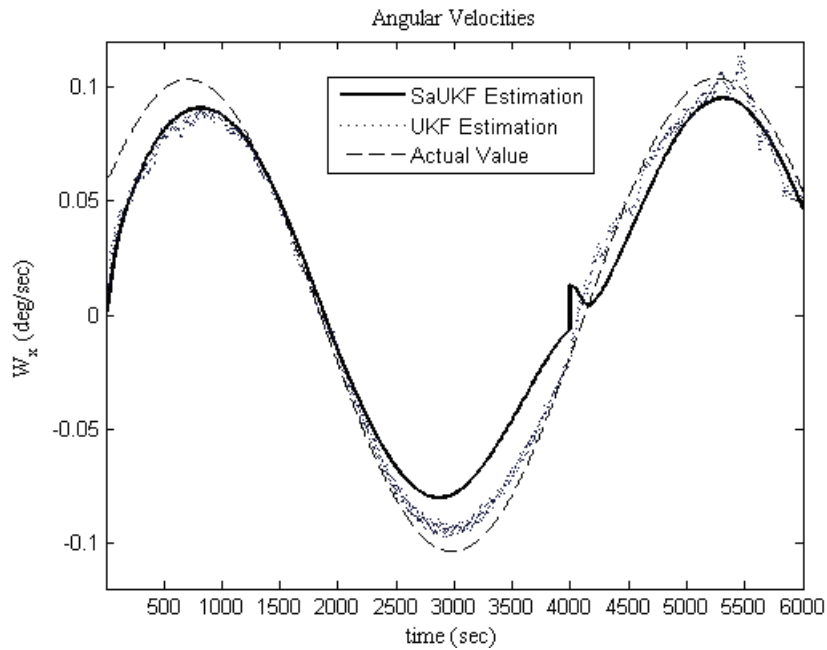


Figure 3.5 : Estimation of the angular rate around x axis.

Angular velocities of the satellite for each axis can be estimated by using SaUKF accurately (see Figure 3.5). During the eclipse the attitude rate estimations are not deteriorated as much as the attitude estimates as a result of accurate dynamic knowledge and low process noise for dynamics propagation. Rate estimates by the UKF are similar.

The main disadvantage of the proposed SaUKF method is requiring accurate measurements free of any bias, sensor misalignment and other sorts of errors. The sensors must be calibrated before using their measurements as input to the SaUKF. As

discussed in several papers [4,5,102] specifically for the magnetometers, such calibration should be performed on-orbit for the nanosatellite missions. In addition, as the simulation results clearly demonstrate, the estimation performance of the SaUKF degrades in eclipse and the UKF based on nonlinear measurements provides more accurate estimations. Regarding these facts, our suggestion is to use an algorithm which switches between several different filters in accordance with the flight mode. An example is given in Figure 3.6.

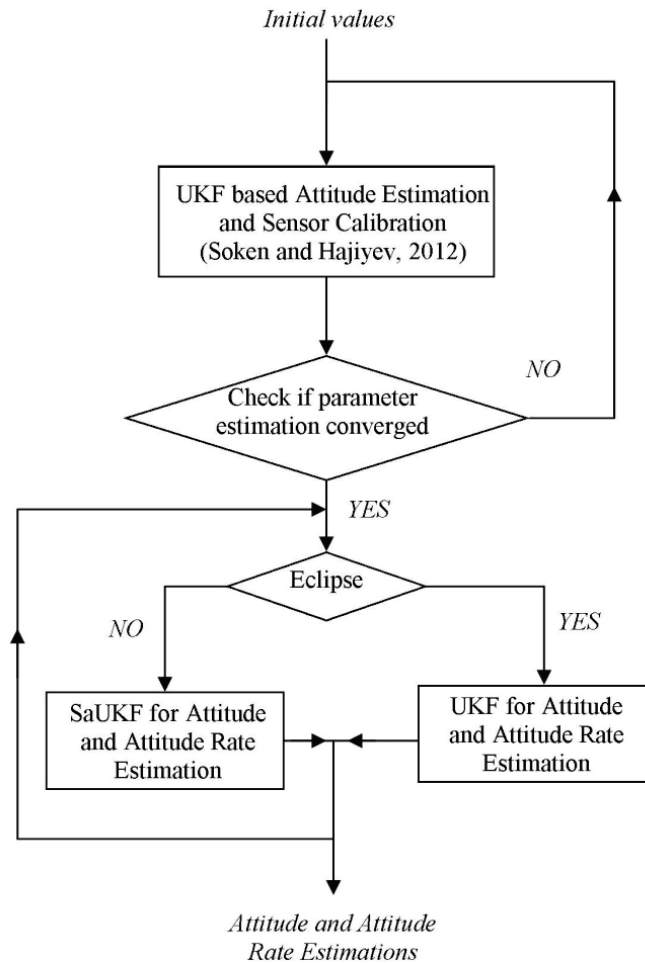


Figure 3.6 : A block diagram of attitude and attitude rate estimation for the proposed algorithm.

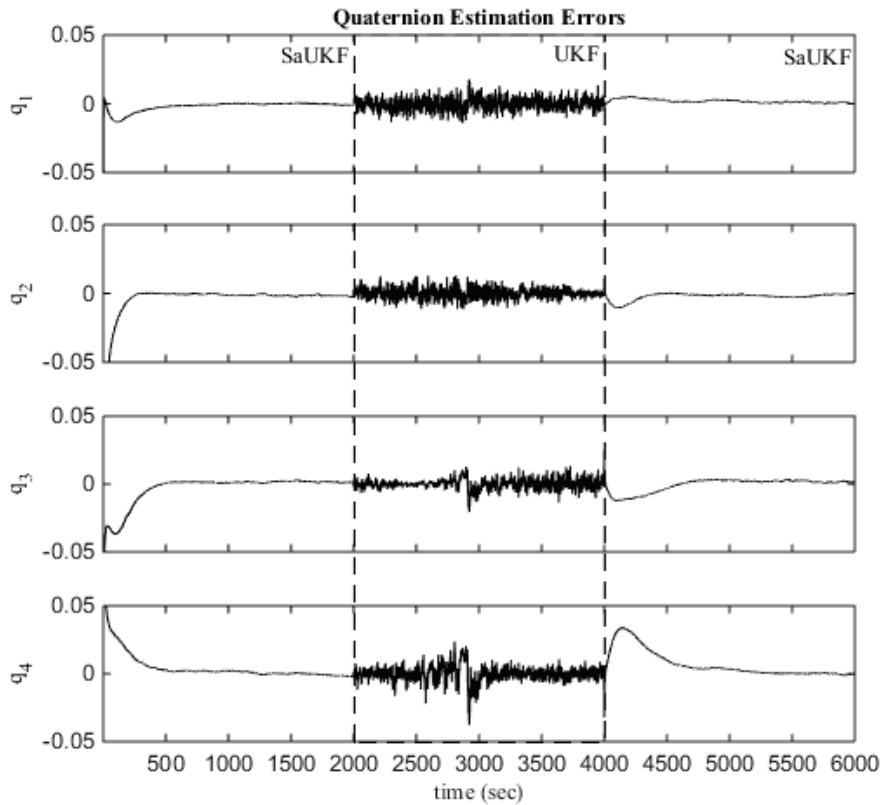


Figure 3.7 : Estimation of the quaternions by SaUKF (outside of the eclipse) and UKF (in eclipse).

In Figure 3.7, two methods are switched in/out of the eclipse for more accurate attitude estimation. As mentioned earlier, the SaUKF estimates the attitude more accurately than both the SVD and UKF only methods except the eclipse period that's why the SaUKF algorithm is used only outside of the eclipse. When the satellite is in the dark side of the Earth, the SVD method fails since there are no sun sensor measurements. The results of the UKF only method can be seen (see Figure 3.7).

Certainly for nanosatellite application we also need to investigate the computational load of each algorithm. Table 3.1 gives the running times for the algorithms for 6000 sec. simulation, details of which are discussed above. Simulations are performed on a computer with Intel® Core™ i7 @2.93 GHz CPU and 3.49 GB RAM. It shall be noted that all the presented data includes the computation time required for simulating the real attitude and measurements. We see that for the SaUKF algorithm, the SVD is the computationally heavier part and the SaUKF requires higher load compared to the UKF based on nonlinear measurements. Yet, the load is not heavy as much as to prevent nanosatellite application, especially if we consider the recent improvement in microprocessors capacity.

Table 3.1 : Computation times for each algorithm.

Computation time (sec)	SVD	SaUKF	UKF
<i>for 10 Monte Carlo runs</i>	14.30	17.96	10.49

3.6 Conclusion

In this paper, singular value decomposition (SVD) method and unscented Kalman filter (UKF) are integrated to determine attitude and attitude rate for 3 unit cubesat sized satellite. Quaternion representation is used to avoid any singularities based on the trigonometric equations. The SVD method fails in eclipse period because of no sun observations. On the other hand, the SVD-aided UKF (SaUKF) can estimate attitude in eclipse although it is a coarse estimate. Simulation results show that also the UKF with nonlinear vector measurements satisfies reasonable attitude estimation accuracy and in eclipse accuracy of the UKF is higher than the SaUKF's; for the rest of the estimation procedure the SaUKF is the most accurate estimation method. Ideal algorithm that we suggest for the examined case is composed of the SaUKF and UKF. The SaUKF is used whenever the sun sensor measurements are available and the algorithm switches to the UKF in eclipse.

4. NANOSATELLITE ATTITUDE ESTIMATION USING KALMAN-TYPE FILTERS WITH NON-GAUSSIAN NOISE*

4.1 Abstract

In order to control the orientation of a satellite, it is important to estimate the attitude accurately. Time-series estimation is especially important in micro and nanosatellites, whose sensors are usually low-cost and have higher noise levels than high-end sensors. Also, the algorithms should be able to run on systems with very restricted computer power. In this work, we evaluate five Kalman-type filtering algorithms for attitude estimation with 3-axis magnetometer and sun sensor measurements. The Kalman-type filters are selected so that each of them is designed to mitigate one error source for the unscented Kalman filter that is used as the baseline. We investigate the distribution of the magnetometer noises and show that the Student's t-distribution is a better model for them than the Gaussian distribution. We consider filter responses in four operation modes: steady-state, recovery from the incorrect initial state, short-term sensor noise increment, and long-term increment. We find that a Kalman-type filter designed for Student's t sensor noises has the best combination of accuracy and computational speed for these problems, which leads to a conclusion that one can achieve more improvements in estimation accuracy by using a filter that can work with heavy-tailed noise than by using a nonlinearity minimizing filter that assumes Gaussian noise.

4.2 Introduction

Satellites need to be oriented in space and there may be very strict requirements for the attitude estimation accuracy depending on the mission. Nanosatellites are required to maintain the attitude with attitude sensors that are typically cheap, simple, and light, and having poor accuracy. To mitigate the limitations of cheap and inaccurate sensors,

* This chapter is based on the paper “Cilden-Guler, D., Raitoharju, M., Piche, R., and Hajiyev, C. (2019). Nanosatellite attitude estimation using Kalman-type filters with non-Gaussian noise, *Aerospace Science and Technology*, **92**, 66-76, doi: 10.1016/j.ast.2019.05.055”.

better attitude estimation algorithms need to be used, and because of limited computational resources, the algorithms should have low computational complexity.

The conventional approach to attitude estimation of a satellite is to use the extended Kalman filter (EKF) [10] or its derivative-free version, the unscented Kalman filter (UKF) [11]. These algorithms are approximate solutions of the Bayesian filtering problem based on the nonlinear models of satellite motion and measurements, with Gaussian noises.

Another approach to attitude estimation, the single-frame method, is introduced in [4,12–14]. In this method, measurements at each time step are preprocessed to produce a set of linear measurements and associated covariances that are fed to the Kalman filter. The preprocessing involves the minimization of Wahba's loss function [15]. In [16], a comparison of minimization methods concludes that the singular value decomposition (SVD) and q methods are the most robust for single-frame attitude estimation methods.

Several algorithms are proposed to improve the ability of Kalman-type filters to cope with highly nonlinear situations. The filter introduced in [28] can automatically process multiple measurements in an optimized order so that the errors caused by nonlinearities are minimized.

Normal distribution-based statistical estimation is vulnerable to outliers. In [29], the authors compare different geomagnetic orbit determination filters under different measurement noise distributions: normal, Student's t, and uniform in the simulations. They concluded that an unscented particle filter, which can make use of non-Gaussian noise models, is more accurate than EKF and UKF, which use Gaussian models. However, the computational complexity for particle filters is typically much greater than for Kalman-type filters.

In [30], a generalization and extension of a linear Student's t filter are proposed. In the paper, simulation results show that the proposed methods provide better accuracy than the existing methods in an application with the heavy-tailed process and measurement noises. In [31], an outlier-robust Kalman-type filter for nonlinear dynamical models is proposed based on Student's t-distribution in the measurement model. In the paper, the filter is compared to alternative filters in a computer simulation and is found to provide a good trade-off between accuracy and computational efficiency.

A nonlinear Kalman-type filter called maximum correntropy unscented Kalman filter (MCUKF) is proposed in [32] for spacecraft relative state estimation. Heavy-tailed non-Gaussian measurement noises are considered in the paper. The proposed MCUKF uses a non-linear regression model combined with maximum correntropy to update the measurement information. A practical test of the relative motion of two spacecraft is performed and it is found that the proposed filter gives better performance than the other filters such as EKF and UKF.

A noise-covariance adapting EKF algorithm is proposed in [33] to cope with sensor faults in the attitude estimation of a small satellite equipped with only a three-axis magnetometer. Similarly, a covariance adapting UKF with multiple measurement noise scaling factor is presented in [34] for nanosatellite attitude estimation and is found to be more accurate than EKF, UKF, and the covariance-adapting UKF with the single scaling factor. In [35], it is shown that the covariance-adapting filters are much more accurate than UKF and EKF in the faulty period and have faster recovery after the end of a fault. Furthermore, according to that study, the covariance-adapting UKF outperforms all other considered filters.

In this work, we present a computer simulation study of the performance of state-of-the-art filters for attitude estimation, taking into consideration both accuracy and computational complexity. We show in section 4.4 that the magnetometer errors can be modeled with Student's t-distribution better than with a normal distribution. We consider four attitude estimation operational modes:

- attitude recovery after de-tumbling phase: this mode is simulated by initializing the filter with an incorrect initial state
- steady-state, after the attitude recovery phase error, has settled
- short-term noise increment in one magnetometer channel, which simulates a sensor fault due to transient disturbance
- long-term noise increment, simulating the onset of a persistent disturbance

The main purpose of this study is to give attention to the fact that the measurement noise of the magnetometers is not normal distributed as it is assumed in most of the studies and the filtering methods should be designed considering this fact. To the best of our knowledge, only a few studies are taking the magnetometer distributions as non-

Gaussian for attitude estimation purposes and they did not use onboard magnetometer measurements to examine the data but only simulated the distributions.

The rest of the chapter is organized as follows. In section 4.3, the filters used in this study are presented. The mathematical models of the satellite's rotational motion and of the measurements are given in section 4.4. In section 4.5, the results of the simulations performed are presented and discussed. Finally, in section 4.6, we summarize our conclusions and discuss possible further work.

4.3 Filtering Algorithms

In this section, five filtering algorithms considered for nanosatellite attitude estimation are presented. For all filters, the attitude estimation problem is formulated using the standard discrete-time nonlinear state-space model

$$\mathbf{x}_k = f(\mathbf{x}_{k-1}) + \mathbf{w}_k, \quad (4.1a)$$

$$\mathbf{y}_k = h_k(\mathbf{x}_k) + \boldsymbol{\varepsilon}_k, \quad (4.1b)$$

where $f(\cdot)$ and $h(\cdot)$ are nonlinear dynamic and measurement functions respectively, which will be explained in detail in section 4.4, \mathbf{x}_k is a n -vector of states at the time t_k , \mathbf{w}_k is a zero-mean noise with covariance \mathbf{Q} , \mathbf{y}_k is a d -vector of measurements, and $\boldsymbol{\varepsilon}_k$ is a zero-mean noise with covariance \mathbf{R}_k . The initial state \mathbf{x}_0 is assumed to be multivariate normal with mean $\boldsymbol{\mu}_0$ and covariance \mathbf{P}_0 ; its probability density function (PDF) is denoted $p(\mathbf{x}_0) = N(\mathbf{x}_0 | \boldsymbol{\mu}_0, \mathbf{P}_0)$. The random vectors $\mathbf{x}_0, \mathbf{w}_k, \boldsymbol{\varepsilon}_k$ ($k = 1, 2, \dots$) are assumed to be independent. The estimation problem is to determine, at each time t_k , the conditional distribution of the state \mathbf{x}_k given the values of the measurements obtained so far, y_1, y_2, \dots, y_k . Because this problem does not have a closed-form solution, approximations are used.

We choose 5 different Kalman type filtering algorithms to be tested in the nanosatellite attitude estimation problem:

- UKF is the baseline solution.
- Outlier-Robust Kalman Filter (ORKF) takes the non-Gaussianity into account and updates the measurement noise covariance.

- Kullback-Leibler Partitioned Update Kalman Filter (KLPUKF) minimizes the nonlinearity.
- Single-Frame Methods-based Kalman Filter (SFMKF) updates measurement noise covariance using the SFM.
- R-Adaptive Kalman Filter (RUKF) updates measurement noise covariance using the innovation sequence.

There are also other algorithms that have the same strengths e.g. Posterior Linearization Filter [107,108] also copes well with the nonlinear problems and MCKF [32] works well with the heavy-tailed noise. We choose different types of filters for our tests to see what kind of filter provides the largest improvements in the estimation accuracy.

4.3.1 Gaussian filter (GF) and unscented Kalman filter (UKF)

Many Kalman type approximations can be represented using the Gaussian filter (GF) formulation [109]. In this formulation, the filtering distribution is approximated by $p(\mathbf{x}_k | \mathbf{y}_{1:k}) = N(\mathbf{x}_k | \boldsymbol{\mu}_k, \mathbf{P}_k)$, where the parameters $\boldsymbol{\mu}_k, \mathbf{P}_k$ are computed recursively in two stages (see Figure 4.1a):

Prediction Stage:

Predicted mean:

$$\boldsymbol{\mu}_k^- = \int f(\mathbf{x}_{k-1}) N(\mathbf{x}_{k-1} | \boldsymbol{\mu}_{k-1}, \mathbf{P}_{k-1}) d\mathbf{x}_{k-1} \quad (4.2)$$

Predicted covariance:

$$\mathbf{P}_k^- = \int (f(\mathbf{x}_{k-1}) - \boldsymbol{\mu}_{k-1})(f(\mathbf{x}_{k-1}) - \boldsymbol{\mu}_{k-1})^T N(\mathbf{x}_{k-1} | \boldsymbol{\mu}_{k-1}, \mathbf{P}_{k-1}) d\mathbf{x}_{k-1} + \mathbf{Q} \quad (4.3)$$

Update Stage:

$$\hat{\mathbf{y}}_k = \int h_k(\mathbf{x}_k) N(\mathbf{x}_k | \boldsymbol{\mu}_k^-, \mathbf{P}_k^-) d\mathbf{x}_k \quad (4.4)$$

$$\boldsymbol{\Psi}_k = \int (\mathbf{x}_k - \boldsymbol{\mu}_k^-)(h_k(\mathbf{x}_k) - \hat{\mathbf{y}}_k)^T N(\mathbf{x}_k | \boldsymbol{\mu}_k^-, \mathbf{P}_k^-) d\mathbf{x}_k \quad (4.5)$$

$$\boldsymbol{\Phi}_k = \int (h_k(\mathbf{x}_k) - \hat{\mathbf{y}}_k)(h_k(\mathbf{x}_k) - \hat{\mathbf{y}}_k)^T N(\mathbf{x}_k | \boldsymbol{\mu}_k^-, \mathbf{P}_k^-) d\mathbf{x}_k \quad (4.6)$$

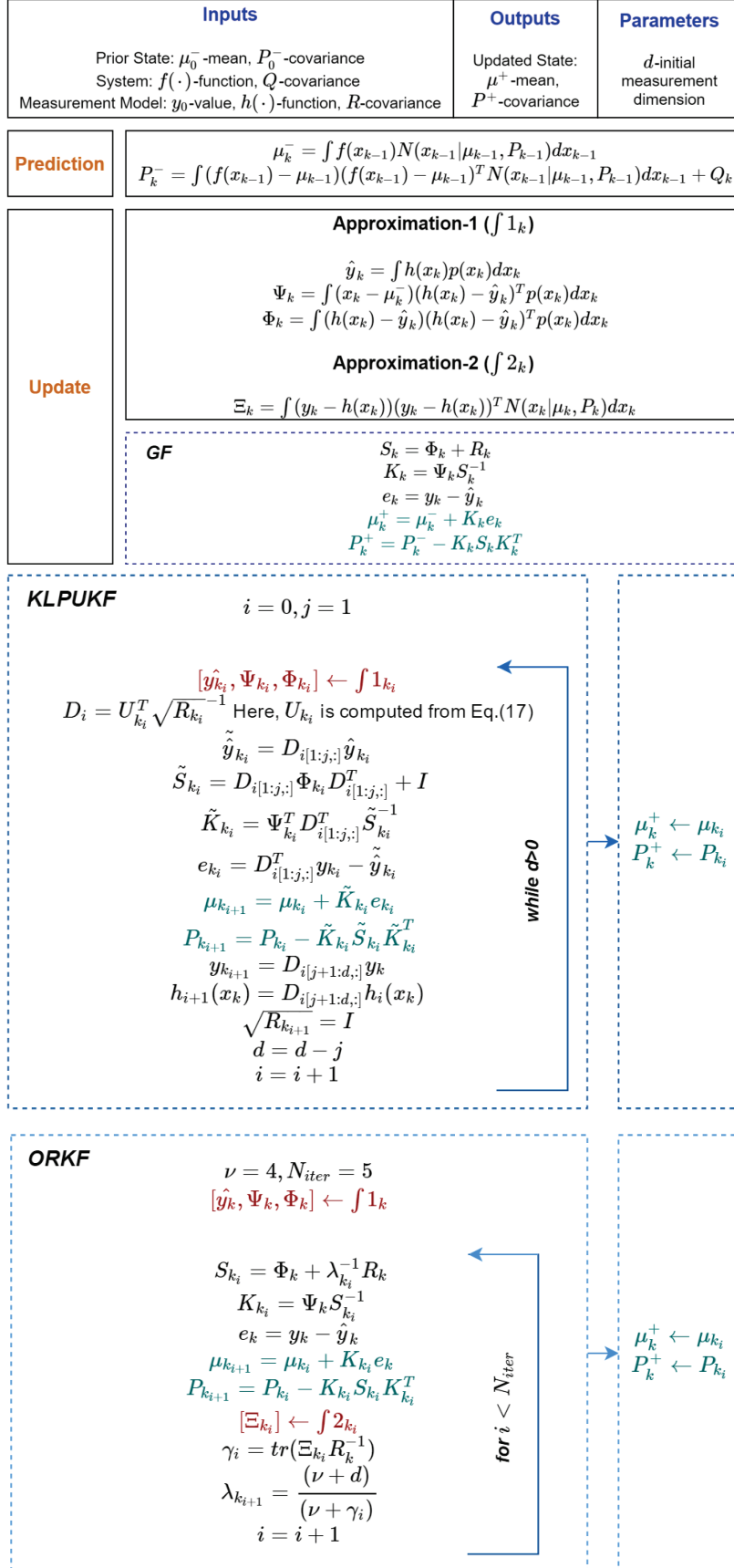


Figure 4.1 : Algorithm schemes of GF (a), KLPUKF (b), ORKF (c).

$$\text{Innovation:} \quad \mathbf{e}_k = \mathbf{y}_k - \hat{\mathbf{y}}_k \quad (4.7)$$

$$\text{Innovation covariance:} \quad \mathbf{S}_k = \mathbf{\Phi}_k + \mathbf{R}_k \quad (4.8)$$

$$\text{Kalman gain:} \quad \mathbf{K}_k = \mathbf{\Psi}_k \mathbf{S}_k^{-1} \quad (4.9)$$

$$\text{Posterior mean:} \quad \boldsymbol{\mu}_k = \boldsymbol{\mu}_k^- + \mathbf{K}_k \mathbf{e}_k \quad (4.10)$$

$$\text{Posterior covariance:} \quad \mathbf{P}_k = \mathbf{P}_k^- - \mathbf{K}_k \mathbf{S}_k \mathbf{K}_k^T \quad (4.11)$$

Different Kalman-type filters correspond to different ways of approximating the integrals in equations (4.2-4.6). EKF uses derivatives of the system and measurement functions, $f(\cdot)$ and $h(\cdot)$. UKF uses values of $f(\cdot)$ and $h(\cdot)$ evaluated on a set of points in state space ([110,111]). In this work, we use UKF.

4.3.2 R-adaptive Kalman filter (RUKF)

Various algorithms are proposed for adapting the Kalman filter starting with the earlier publications by Mehra [112]. One of these ideas is to scale the covariance of the filter. The parameters that are used for scaling can be calculated using different means [113,114]. This idea is also applicable to the UKF adaptation. In [115], the state estimation performance of the UKF is improved by proper tuning of both the unscented transform parameters and the process and measurement noise covariance matrices of the dynamic system model. The R-adaptive Kalman filter is introduced with the goal of making the estimate insensitive to measurement faults [35]. The filter makes use of the empirical covariance of the windowed innovation sequence

$$\tilde{\mathbf{S}}_k = \frac{1}{M} \sum_{j=k-M+1}^k \mathbf{e}_j \mathbf{e}_j^T, \quad (4.12)$$

where M is the width of the moving window. RUKF uses the UKF recursion of equations (4.2-4.11) except that the measurement covariance matrix \mathbf{R}_k in (8) is replaced by a scaling matrix $\mathbf{V}_k^* \mathbf{R}_k$ where the scaling matrix is $\mathbf{V}_k^* = \text{diag}(v_1^*, v_2^*, \dots, v_d^*)$, $v_i^* = \max\{1, V(i, i)\}$ $i=1, \dots, d$, and $\mathbf{V} = (\tilde{\mathbf{S}}_k - \mathbf{\Phi}_k) \mathbf{R}_k^{-1}$.

When a fault occurs in the i^{th} measurement the corresponding term of $\tilde{\mathbf{S}}_k(i, i)$ will

become larger and the faulty measurement influence will decrease because of having a lower gain.

4.3.3 Kullback-Leibler partitioned update Kalman filter (KLPUKF)

In general, the partitioned update Kalman filter performs the update stage of a multivariate measurement in several steps [28]:

1. Evaluate the nonlinearity of the measurements.
2. Minimize the nonlinearity of part of the measurement by applying a linear transformation.
3. Update the state using part of the measurement whose nonlinearity is small.
4. If the whole measurement has not yet been applied, use the partially updated state as the prior and the unused part of the measurements as a new measurement, and return to step 1.

In KLPUKF, the Kullback-Leibler divergence (KLD) of the error of approximation is used as the measure of nonlinearity. Denoting the approximated joint density of the state \mathbf{x}_k and the measurement \mathbf{y}_k in GF as $q(\mathbf{x}_k, \mathbf{y}_k)$ and the exact joint density as $p(\mathbf{x}_k, \mathbf{y}_k)$, the KLD of the error of the approximation is [116]

$$\boldsymbol{\eta}_k = \text{KLD}(p(\mathbf{x}_k, \mathbf{y}_k) \| q(\mathbf{x}_k, \mathbf{y}_k)) = \iint p(\mathbf{x}_k, \mathbf{y}_k) \log \left(\frac{p(\mathbf{x}_k, \mathbf{y}_k)}{q(\mathbf{x}_k, \mathbf{y}_k)} \right) d\mathbf{x}_k d\mathbf{y}_k, \quad (4.13)$$

which can be shown [117] to be

$$\boldsymbol{\eta}_k = \frac{1}{2} \log |\mathbf{I} + \mathbf{R}_k^{-1} \Upsilon_k|, \quad (4.14)$$

where

$$\Upsilon_k = \boldsymbol{\Phi}_k - \boldsymbol{\Psi}_k^T (\mathbf{P}_k^-)^{-1} \boldsymbol{\Psi}_k. \quad (4.15)$$

Here, it should be noted that some of the KF extensions such as EKF make linearization such that Υ_k always becomes zero; therefore, KLD cannot be found by using those extensions.

In [28] it is shown that the linear transformation in step 2 is the matrix

$$\mathbf{D}_k = \mathbf{U}_k^T \sqrt{\mathbf{R}_k}^{-1}, \quad (4.16)$$

where $\sqrt{\mathbf{R}_k}$ is the lower-triangular Cholesky factor of \mathbf{R}_k , ($\sqrt{\mathbf{R}_k} \sqrt{\mathbf{R}_k}^T = \mathbf{R}_k$), and \mathbf{U}_k is the orthogonal matrix in the eigenvalue decomposition

$$\mathbf{U}_k \mathbf{\Lambda}_k \mathbf{U}_k^T = \sqrt{\mathbf{R}_k}^{-1} \mathbf{\Upsilon}_k \sqrt{\mathbf{R}_k}^{-T}, \quad (4.17)$$

where the diagonal matrix $\mathbf{\Lambda}_k$ has the eigenvalues in the diagonal in ascending order. The transformed measurement noise covariance is

$$\tilde{\mathbf{R}}_k = \mathbf{U}_k^T \sqrt{\mathbf{R}_k}^{-1} \mathbf{R}_k \sqrt{\mathbf{R}_k}^{-T} \mathbf{U}_k = \mathbf{I}. \quad (4.18)$$

Here, the nonlinearity of the first measurement element is minimized by this transformation. In our implementation, we update one measurement at a time, i.e. steps 1-4 are carried out d times at each update. The algorithm scheme for KLPUKF can be seen in Figure 4.1b.

4.3.4 Outlier-robust Kalman filter (ORKF)

The variational Bayes based Student's t Kalman filter, ORKF [31] assumes that the measurement noises are distributed according to Student's t-distribution, which has "longer tails" than a Gaussian distribution. The Student's t distribution can be expressed using the auxiliary random variable λ_k as

$$p(\mathbf{y}_k | \mathbf{x}_k) = \int p(\mathbf{y}_k | \mathbf{x}_k, \lambda_k) p(\lambda_k) d\lambda_k, \quad (4.19)$$

where $\mathbf{y}_k | \mathbf{x}_k, \lambda_k \sim \mathcal{N}\left(h(\mathbf{x}_k), \frac{1}{\lambda_k} \mathbf{R}_k\right)$ and $\lambda_k \sim \text{Gamma}\left(\frac{\nu}{2}, \frac{\nu}{2}\right)$. Here, $\nu \geq 1$ is the degrees of freedom parameter which determines the distribution's kurtosis. If $\nu \rightarrow \infty$ the distribution converges to the normal distribution $\mathcal{N}(h(\mathbf{x}_k), \mathbf{R}_k)$.

In the prediction step, $p(\mathbf{x}_k | \mathbf{y}_{1:k-1})$ is approximated as having a Gaussian density $\mathcal{N}(\mathbf{x}_k | \bar{\boldsymbol{\mu}}_k, \bar{\mathbf{P}}_k)$ as in equations (4.2-4.3). The update step with non-Gaussian noise is computationally intractable so the ORKF uses a Variational-Bayes approximation as follows. The KLD between the true posterior and the product approximation $p(\mathbf{x}_k, \lambda_k | \mathbf{y}_{1:k}) \approx q(\mathbf{x}_k) q(\lambda_k)$ is

$$\text{KLD}\left(q(\mathbf{x}_k)q(\boldsymbol{\lambda}_k)\parallel p(\mathbf{x}_k,\boldsymbol{\lambda}_k|\mathbf{y}_{1:k-1})\right)=\int q(\mathbf{x}_k)q(\boldsymbol{\lambda}_k)\log\left(\frac{q(\mathbf{x}_k)q(\boldsymbol{\lambda}_k)}{p(\mathbf{x}_k,\boldsymbol{\lambda}_k|\mathbf{y}_{1:k})}\right)d\mathbf{x}_kd\boldsymbol{\lambda}_k. \quad (4.20)$$

The KLD is minimized with respect to $q(\boldsymbol{\lambda}_k)$ while keeping $q(\mathbf{x}_k)$ fixed by setting

$$\begin{aligned} \log q(\boldsymbol{\lambda}_k) &= \mathbb{E}_x(\log p(\mathbf{x}_k,\boldsymbol{\lambda}_k,\mathbf{y}_{1:k})) + \text{constant} \\ &= -\frac{1}{2}\boldsymbol{\lambda}_k\bar{\boldsymbol{\gamma}}_k + \left(\frac{\nu+d}{2}-1\right)\log\boldsymbol{\lambda}_k - \frac{\nu\boldsymbol{\lambda}_k}{2} + \text{constant}, \end{aligned} \quad (4.21)$$

where

$$\begin{aligned} \bar{\boldsymbol{\gamma}}_k &= \mathbb{E}_x\left(\left(\mathbf{y}_k - h(\mathbf{x}_k)\right)^T \mathbf{R}_k^{-1} \left(\mathbf{y}_k - h(\mathbf{x}_k)\right)\right) \\ &= \text{tr}\left\{\mathbb{E}_x\left(\left(\mathbf{y}_k - h(\mathbf{x}_k)\right)\left(\mathbf{y}_k - h(\mathbf{x}_k)\right)^T\right)\mathbf{R}_k^{-1}\right\}, \end{aligned} \quad (4.22)$$

where $\mathbb{E}(\cdot)$ is the expectation operator. Similarly, the KLD is minimized with respect to $q(\mathbf{x}_k)$ while keeping $q(\boldsymbol{\lambda}_k)$ fixed by setting

$$\begin{aligned} \log q(\mathbf{x}_k) &= \mathbb{E}_\lambda(\log p(\mathbf{x}_k,\boldsymbol{\lambda}_k,\mathbf{y}_{1:k})) + \text{constant} \\ &= -\frac{1}{2}\bar{\boldsymbol{\lambda}}_k\left(\mathbf{y}_k - h(\mathbf{x}_k)\right)^T \mathbf{R}_k^{-1} \left(\mathbf{y}_k - h(\mathbf{x}_k)\right) - \left(\mathbf{x}_k - \boldsymbol{\mu}_k^-\right)^T \left(\mathbf{P}_k^-\right)^{-1} \left(\mathbf{x}_k - \boldsymbol{\mu}_k^-\right) + \text{constant}, \end{aligned} \quad (4.23)$$

where

$$\bar{\boldsymbol{\lambda}}_k = \mathbb{E}_\lambda(\boldsymbol{\lambda}_k) = \int \boldsymbol{\lambda}_k q(\boldsymbol{\lambda}_k) d\boldsymbol{\lambda}_k = \frac{\nu+d}{\nu+\bar{\boldsymbol{\gamma}}_k}. \quad (4.24)$$

Then, equation (4.22) and equation (4.24) should be iterated to convergence or a fixed number of times. The update step of the GF in equations (4.4-4.11) is carried out with $\frac{1}{\bar{\boldsymbol{\lambda}}_k}\mathbf{R}_k$ measurement noise covariance which is updated in every iteration and every time step (see Figure 4.1c).

4.3.5 Single-frame methods based Kalman filter (SFMKF)

As a pre-processing step before the update stage, the linear attitude measurements are obtained from the single-frame method (SFM) by minimizing Wahba's loss function [15],

$$L(\mathbf{A}_k) = \frac{1}{2} \sum_j a_{j_k} \left| \mathbf{b}_{j_k} - \mathbf{A}_k \mathbf{r}_{j_k} \right|^2, \quad (4.25)$$

where \mathbf{A} is the orthogonal transformation matrix from reference coordinates to body coordinates fixed on the sensor body (Section 4.4.1), a_j is the inverse variance of the sensor j , \mathbf{b}_j is the unit vector of the 3-axis sensor measurements in the body coordinates, and \mathbf{r}_j is the unit vector of the measurement model in the reference coordinates (Section 4.4.2). Those linear attitude angle measurements can be used in the Gaussian filter instead of the nonlinear measurements. The loss function can be minimized using the SVD method, which has the best robustness compared to other minimization methods such as QUEST, q, FOAM [4,96,118,119]. Therefore, the SVD method is used as an SFM in this study.

The attitude measurement vector from SFM is,

$$\tilde{\mathbf{y}}_k = \mathbf{H} \mathbf{x}_k + \boldsymbol{\varepsilon}_k, \quad (4.26)$$

where the measurement matrix is taken as $\mathbf{H} = \begin{bmatrix} I_{3 \times 3} & \mathbf{0}_{3 \times 3} \end{bmatrix}$ in this study. However, it should be noted that if another SFM is used with attitude representation other than Euler angles, the determined attitude should be represented as Euler angles after necessary transformations. The GF with an update based on this linear measurement model is called SFMKF (see Figure 4.2 for the algorithm scheme). In the update stage, measurements $\tilde{\mathbf{y}}_k$ are coming from SFM with measurement covariance \mathbf{R}_k , which is updated in each step based on the single-frame method. In the GF, the innovation (4.9) is replaced by

$$\mathbf{e}_k = \tilde{\mathbf{y}}_k - \hat{\mathbf{y}}_k \quad (4.27)$$

and equation (4.7) can be replaced by

$$\mathbf{S}_k = \mathbf{H} \mathbf{P}_k^- \mathbf{H}^T + \mathbf{R}_k. \quad (4.28)$$

It should also be noted that the attitude measurements from SFM can be used as the initial attitude in the SFMKF. Therefore, this method might overcome the problem of having grossly incorrect initial values which affect the transient behavior of the filter.

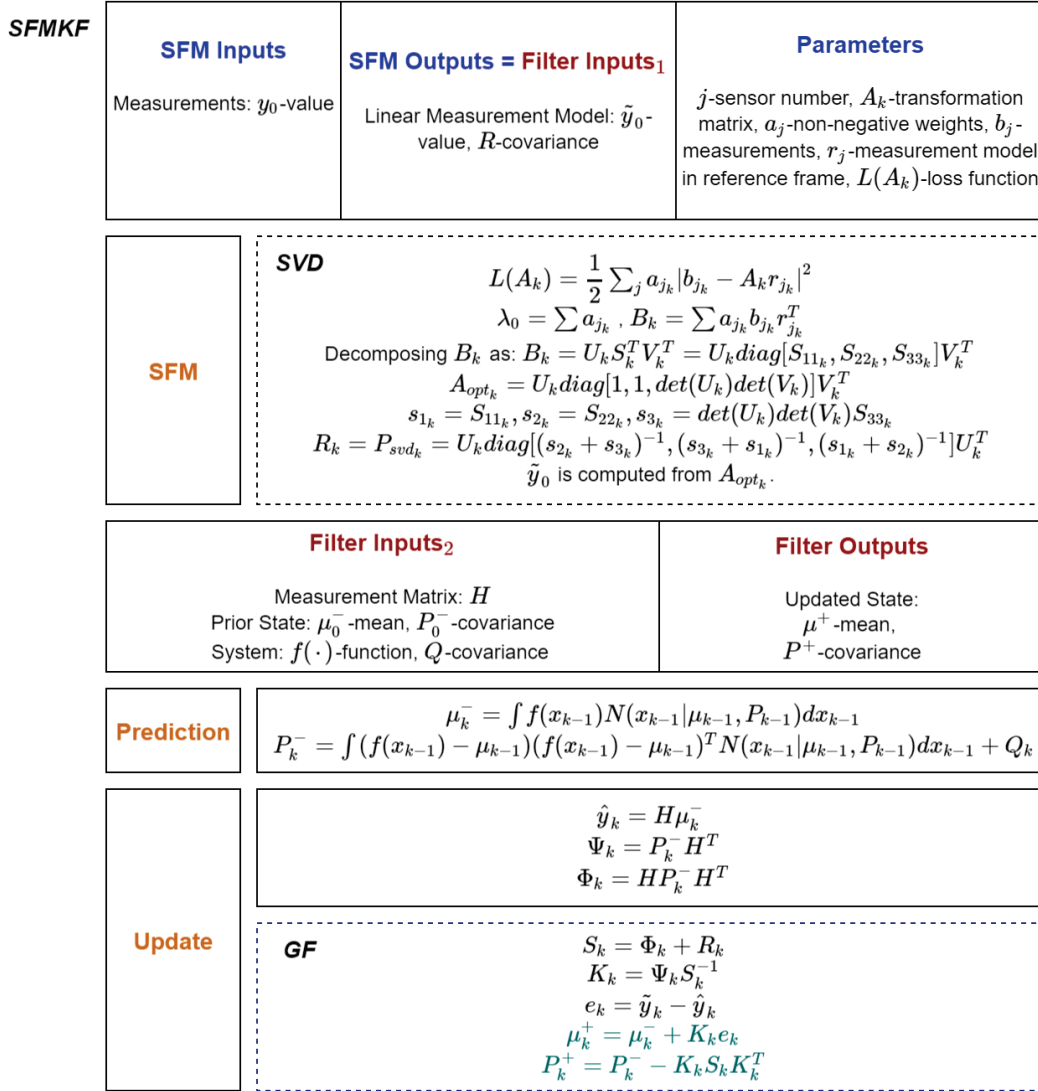


Figure 4.2 : SFMKF algorithm scheme.

4.4 Mathematical Models for Nanosatellite's Rotational Motion

4.4.1 Equations of rotational motion

The state vector for the continuous-time dynamic model is composed of attitude angles and angular velocities as

$$\mathbf{x} = [\varphi \quad \theta \quad \psi \quad \omega_x \quad \omega_y \quad \omega_z]^T, \quad (4.29)$$

where φ is roll (angle of rotation about x axis), θ is pitch (y axis), ψ is yaw (z axis) with respect to the orbital frame, $\omega_x, \omega_y, \omega_z$ are the angular velocities in the body axis set with respect to the inertial coordinate system. The transformation matrix from reference (orbital) coordinates to body coordinates is [1]

$$\mathbf{A}(\mathbf{x}) = \mathbf{A} = \begin{bmatrix} c(\theta)c(\varphi) & c(\theta)s(\varphi) & -s(\theta) \\ -c(\psi)s(\varphi) + s(\psi)s(\theta)c(\varphi) & c(\psi)c(\varphi) + s(\psi)s(\theta)s(\varphi) & s(\psi)c(\theta) \\ s(\psi)s(\varphi) + c(\psi)s(\theta)c(\varphi) & -s(\psi)c(\varphi) + c(\psi)s(\theta)s(\varphi) & c(\psi)c(\theta) \end{bmatrix}, \quad (4.30)$$

where $c(\cdot)$ and $s(\cdot)$ are cosine and sine functions. The dynamic equations, obtained by the principle of conservation of angular momentum, are [1]

$$J_x \frac{d\omega_x}{dt} = N_x + (J_y - J_z)\omega_y\omega_z, \quad (4.31.a)$$

$$J_y \frac{d\omega_y}{dt} = N_y + (J_z - J_x)\omega_z\omega_x, \quad (4.31.b)$$

$$J_z \frac{d\omega_z}{dt} = N_z + (J_x - J_y)\omega_x\omega_y, \quad (4.31.c)$$

where (J_x, J_y, J_z) are the principal moments of inertia, and (N_x, N_y, N_z) are the external disturbances. If only the ideal spherical body gravity of Earth is taken into consideration, the external disturbances are [120]

$$\begin{bmatrix} N_x \\ N_y \\ N_z \end{bmatrix} = -3 \frac{\mu^*}{r_0^3} \begin{bmatrix} (J_y - J_z)A_{23}A_{33} \\ (J_z - J_x)A_{13}A_{33} \\ (J_x - J_y)A_{13}A_{23} \end{bmatrix}, \quad (4.32)$$

where μ^* is the product of the universal gravitational constant and the mass of Earth, and r_0 is the distance between the satellite and Earth's center of mass. The angular velocity vector in the body axes, with respect to the reference (orbital) coordinate axes, is

$$\begin{bmatrix} p \\ q \\ r \end{bmatrix} = \begin{bmatrix} \omega_x \\ \omega_y \\ \omega_z \end{bmatrix} - \mathbf{A} \begin{bmatrix} 0 \\ -\omega_o \\ 0 \end{bmatrix}, \quad (4.33)$$

where ω_o is the orbital angular velocity with respect to the inertial reference,

$\omega_o = \left(\frac{\mu^*}{r_0^3} \right)^{1/2}$ for a circular orbit. The satellite's kinematics equation of motion derived

using the Euler angle attitude representation is [1],

$$\begin{bmatrix} \dot{\phi} \\ \dot{\theta} \\ \dot{\psi} \end{bmatrix} = \begin{bmatrix} 0 & s(\psi)/c(\theta) & c(\psi)/c(\theta) \\ 0 & c(\psi) & -s(\psi) \\ 1 & s(\psi)s(\theta)/c(\theta) & c(\psi)s(\theta)/c(\theta) \end{bmatrix} \begin{bmatrix} p \\ q \\ r \end{bmatrix}. \quad (4.34)$$

The system dynamics function f in (4.1a) is obtained by time-discretization of the differential equations (4.34) and (4.31) using Euler's method with constant time step, Δt :

$$\phi_{k+1} = \phi_k + \Delta t \left(\frac{s(\psi_k)}{c(\theta_k)} q_k + \frac{c(\psi_k)}{c(\theta_k)} r_k \right), \quad (4.35a)$$

$$\theta_{k+1} = \theta_k + \Delta t (c(\psi_k) q_k - s(\psi_k) r_k), \quad (4.35b)$$

$$\psi_{k+1} = \psi_k + \Delta t \left(p_k + s(\psi_k) \frac{s(\theta_k)}{c(\theta_k)} q_k + c(\psi_k) \frac{s(\theta_k)}{c(\theta_k)} r_k \right), \quad (4.35c)$$

$$\omega_{x_{k+1}} = \omega_{x_k} + \Delta t (N_{x_k} + \omega_{y_k} \omega_{z_k}) (J_y - J_z) / J_x, \quad (4.35d)$$

$$\omega_{y_{k+1}} = \omega_{y_k} + \Delta t (N_{y_k} + \omega_{z_k} \omega_{x_k}) (J_z - J_x) / J_y, \quad (4.35e)$$

$$\omega_{z_{k+1}} = \omega_{z_k} + \Delta t (N_{z_k} + \omega_{x_k} \omega_{y_k}) (J_x - J_y) / J_z. \quad (4.35f)$$

4.4.2 Measurement models

In this study, a nanosatellite system is considered to have as measurement sensors a sun sensor and a magnetometer. These sensors are commonly used for satellite missions in low Earth orbit.

International Geomagnetic Reference Field (IGRF) is used as the geomagnetic field model; its inputs are the date and position of the satellite [1,6]:

$$\mathbf{B}_o(t, \bar{r}, \text{colat}, \text{lon}) = -\nabla \left\{ a \sum_{n=1}^N \sum_{m=0}^n \left(\frac{a}{\bar{r}} \right)^{n+1} \times \left[g_n^m(t) c(m \text{ lon}(t)) + h_n^m(t) s(m \text{ lon}(t)) P_n^m(c(\text{colat}(t))) \right] \right\}, \quad (4.36)$$

where \mathbf{B}_o is the predicted magnetic field in nanoTesla (nT), \bar{r} is the distance between the mass centers of the satellite and Earth, $\text{colat}(t)$ is the co-latitude, $\text{lon}(t)$ is the longitude, $P_n^m(c(\text{colat}(t)))$ are the Schmidt quasi-normalized associated Legendre polynomials of degree n and order m , $a = 6371.2$ km is the geomagnetic conventional Earth's mean reference spherical radius, g_n^m and h_n^m are the Gaussian

coefficients given in units of nT [6]. The noiseless magnetometer measurements are obtained by transforming the geomagnetic field to the body frame:

$$\mathbf{B}_m(t, x) = \mathbf{A}(x) \mathbf{B}_o(t, \bar{r}(t), \text{colat}(t), \text{lon}(t)). \quad (4.37)$$

As the distance between the satellite and Earth's centers is negligible considering the distance between the sun and Earth's centers, sun direction with respect to the Earth-centered inertial (ECI) coordinates only depends on the Julian Day (T_{TDB}) and not on the satellite's position. The Julian Day can be derived from the satellite's reference epoch and the onboard clock time, t . The ecliptic longitude of sun ($\lambda_{\text{ecliptic}}$) and its linear model (ε) can be computed as [103].

$$M_{\text{Sun}} = 357.5277233^\circ + 35999.05034T_{TDB}, \quad (4.38.a)$$

$$\lambda_{\text{ecliptic}} = \lambda_{M_{\text{Sun}}} + 1.914666471^\circ \text{sind}(M_{\text{Sun}}) + 0.019994643 \text{sind}(2M_{\text{Sun}}), \quad (4.38.b)$$

$$\lambda_{M_{\text{Sun}}} = 280.4606184^\circ + 36000.77005361T_{TDB}, \quad (4.38.c)$$

$$\varepsilon = 23.439291^\circ - 0.0130042T_{TDB}, \quad (4.38.d)$$

where the mean anomaly and the mean longitude of sun are given by equations (4.38a), (4.38c), and sind is a degree-argument sine function. From these relations, sun direction vector (\mathbf{S}_{ECI}) in ECI coordinates can be found from

$$\mathbf{S}_{ECI}(t) = \begin{bmatrix} \text{cosd}(\lambda_{\text{ecliptic}}) \\ \text{sind}(\lambda_{\text{ecliptic}}) \text{cosd}(\varepsilon) \\ \text{sind}(\lambda_{\text{ecliptic}}) \text{sind}(\varepsilon) \end{bmatrix}. \quad (4.39)$$

The noiseless sun sensor measurements \mathbf{S}_m are obtained by transforming the sun direction to the body frame:

$$\mathbf{S}_m(t, x) = \mathbf{A}(x) \mathbf{L}(t) \mathbf{S}_{ECI}(t), \quad (4.40)$$

where \mathbf{L} is the transformation matrix from ECI to orbit coordinates. We compute the satellite's orbital elements (\mathbf{L}) and position on the orbit (\bar{r} , colat, lon) using the SGP4 orbital propagation model [121]*. For consistency, sun direction and magnetic field

* The code is available at <http://www.centerforspace.com/downloads/>.

measurements are used as unit vectors, and the state-space model's equation (4.1) measurement function is then

$$h_k(x) = \begin{bmatrix} B_m(t_k, x) \\ \|B_m(t_k, x)\| \\ S_m(t_k, x) \end{bmatrix}. \quad (4.41)$$

4.4.3 Magnetometer noise distribution analysis

It is investigated which distribution is the best fitting for the magnetometer noises. As representative magnetometer measurements, we use 11 nonconsecutive days' SWARM-A data from the ESA website (<ftp://swarm-diss.eo.esa.int/>) and we use the magnetic field model IGRF as a reference. The differences between the unit vectors of real magnetometer measurements of SWARM-A and the reference magnetic field model IGRF in 13th order having the date and position inputs from the satellite are used in order to construct the noise density. Three symmetric distributions are fitted to these errors using standard maximum likelihood methods: normal, t, and extreme value distribution. The PDF of the t-distribution shows the best agreement with the density histogram (Figure 4.3). This is also the distribution that gives the smallest Akaike information criterion (Table 4.1), which is defined as [122]

$$AIC_i = \ln(\text{MSE}_i) + \frac{2\bar{k}_i}{N_{mag}}, \quad (4.42)$$

where MSE_i is the mean square error of the i^{th} candidate distribution, \bar{k}_i is the number of fitting parameters, N_{mag} is the number of the observations. Therefore, t-distributed noise on magnetometer measurements is used for the simulations (Section 4.5). In the analysis, the non-normalized magnetic field noises are in the order of 100-200 nT.

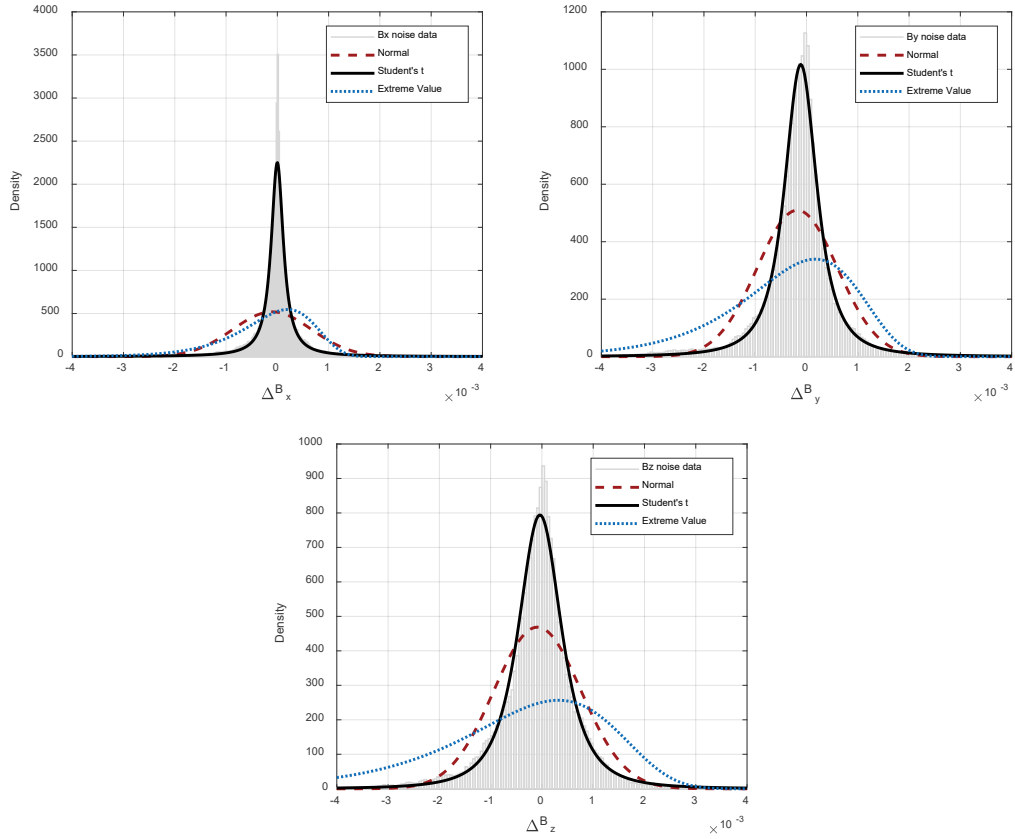


Figure 4.3 : Distribution fitting for magnetometer measurement noises on x, y, and z axes.

Table 4.1 : Akaike’s information criterion (AIC) analysis of distributions for magnetometer noise.

Model	AIC		
	x	y	z
Normal	3.999	2.694	6.693
t	3.998	2.690	6.531
Extreme value	4.001	2.700	6.721

4.5 Analysis and Results

In this section, we describe the numerical simulation tests and the results obtained. We begin by presenting the parameters common to all tests. We consider a nanosatellite with principal moments of inertia $\mathbf{J} = \text{diag}[2.1 \times 10^{-3} \quad 2.0 \times 10^{-3} \quad 1.9 \times 10^{-3}] \text{ kg m}^2$.

The orbit is almost circular with inclination $i = 87.4^\circ$, eccentricity $e = 0.0009$, and average altitude 500 km. Sun sensors and magnetometers have 3-axis measurements and both sensors have 1-Hz frequency; estimation time step is also 1 sec. The sensor noises are characterized using standard deviations $\sigma_b = 0.008$ for each measurement of the magnetometers and $\sigma_s = 0.002$ for sun sensors which is based on the angular deviation of the sun vector with respect to the actual direction of sun. The noises for magnetometer measurements are sampled from Student's t distribution and sun sensors are sampled from normal. The dynamic system's noise covariance is selected

as $\mathbf{Q} = \begin{bmatrix} 10^{-4} (\text{rad})^2 I_{3 \times 3} & 0 \\ 0 & 10^{-6} (\text{rad/s})^2 I_{3 \times 3} \end{bmatrix}$. The non-zero \mathbf{Q} matrix is introduced to

avoid numerical issues with the approximate nonlinear covariance propagation. We consider attitude estimation over a single orbit (6000 s) starting at position $\text{colat}_0 = 24^\circ$, $\text{lon}_0 = 173^\circ$, $\bar{r}_0 = 6878$ km and time 00:00:00 UT at January 1, 2014. The true initial state is $\mathbf{x}_0^{\text{true}} = [0.015 \quad 0.01 \quad 0.005 \quad 0.0005 \quad 0.00075 \quad 0.0005]^T$ with the units of the first three elements in radians and the last in radians per seconds, and the initial state of filters is

$$\mathbf{x}_0 = 2\mathbf{x}_0^{\text{true}} \quad (4.43)$$

(except SFMKF, which uses SFM). If process noise is applied to the true states in the simulation environment, the outputs will be different in different simulations. We wanted to concentrate only on the effect of the measurement noise and, thus, the true track is generated using (4.35) without added noise.

Filter algorithm parameters:

UKF: unscented transformation parameters from [110], $\alpha = 10^{-3}$, $\beta = 2$, $\kappa = 0$,

RUKF: sliding window width, $M = 20$,

ORKF: number of iterations, N_{iter} , and degrees of freedom parameter, $\nu = 4$.

4.5.1 Nominal operation mode

Error formulation used for the evaluation of the filters' attitude angle estimation accuracies in Figure 4.4 is the normalized root mean square of the norm of estimation errors $\sqrt{\sum_{k=1}^n \|\mathbf{e}_k\|^2} / \sqrt{\sum_{k=1}^n \|\mathbf{X}_k^{true}\|^2}$ where $\mathbf{e}_k = \mathbf{X}_k^{true} - \mathbf{X}_k^{est}$ is the absolute error vector between the true and the estimated data during the whole simulation time. Simulations are performed on a computer with Intel® Core™ i7 @2.93 GHz CPU and 8 GB RAM. Figure 4.4 shows the work-accuracy diagram for the 5 filter algorithms with one of them having 3 variants. The x-axis shows the average NRMSE from 100 simulations with different random number generator (RNG) seeds for the sensor noises. There is not much change in the results when the parameters are changed in the filters other than ORKF. Therefore, only ORKF is applied using $N_{iter} = \{2, 5, 10\}$ and the iteration number is shown at the filter label's subscript. KLPUKF, ORKF₅ and ORKF₁₀ are the most accurate algorithms, with KLPUKF and ORKF variations computationally the heaviest. The other three have smaller, roughly equal, computational load, but SFMKF and RUKF's accuracy, which is roughly equal, is much better than UKF's. For ORKF, ORKF₅ is selected and named without the subscript for the rest of the paper in order to have accurate but computationally light estimations. It should be noted that the non-Gaussianity seems to be the dominating factor compared to non-linearity that causes error to the UKF.

A time series of estimation errors from a single simulation (Figure 4.5) shows that all 5 filters behave similarly. Most of the error arises in the initial transient during which the filters recover from the incorrect initial state. Even SFMKF, which uses an initial state from SFM instead of (4.42), has a significant transient error. In order to evaluate the steady-state where errors arise mainly from sensor errors, we consider also the errors after 1500 s. Box plots (Figure 4.6) and RMSE (Table 4.2) indicate that all filters perform reasonably well in the steady-state regime, with ORKF having the smallest attitude RMSE.

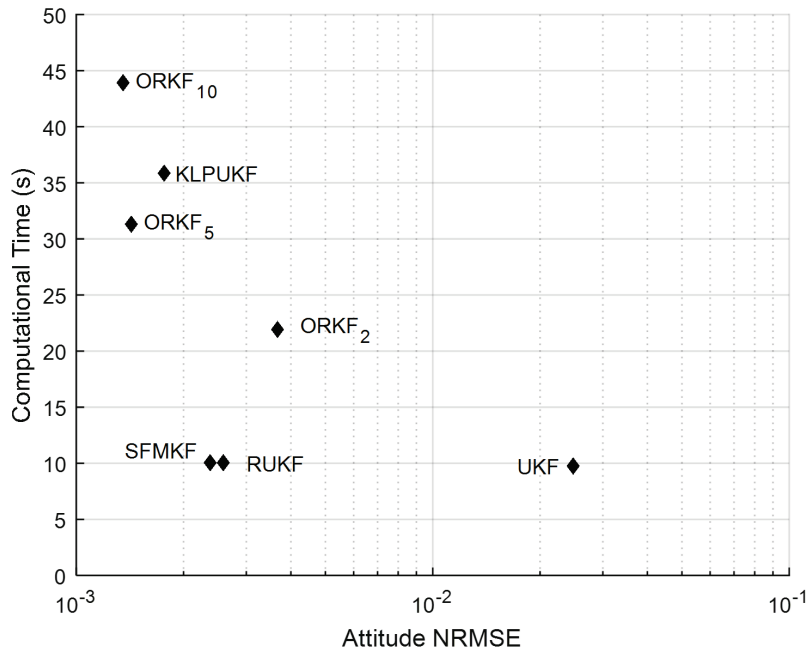


Figure 4.4 : Work vs accuracy for 5 filters.

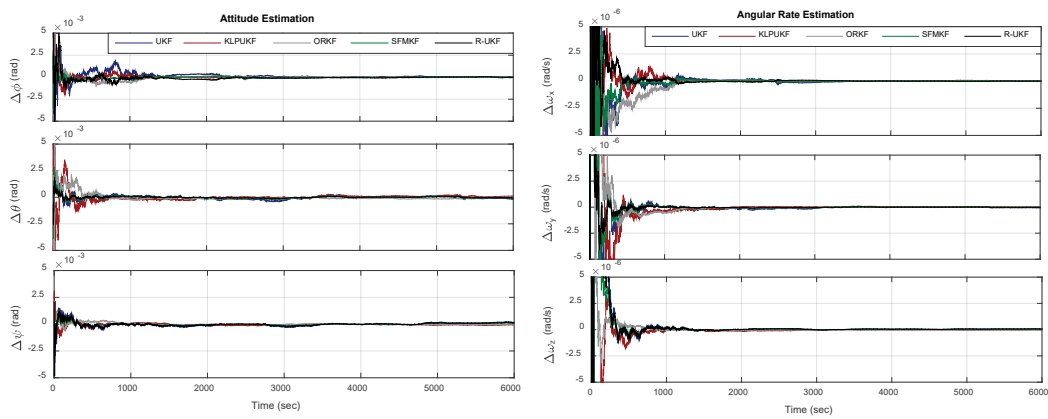


Figure 4.5 : Attitude (left) and angular velocity (right) estimation errors for normal operation mode, single simulation.

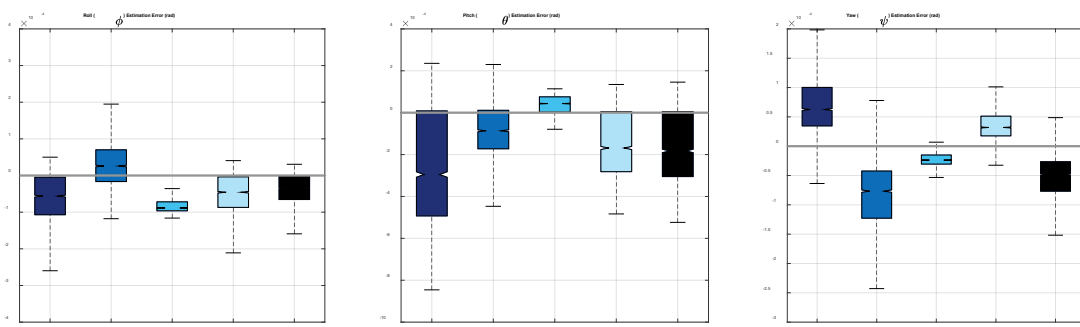


Figure 4.6 : Box plots of estimation errors during averaged over 100 simulations.

Table 4.2 : RMSE of estimations during $t \geq 1500$ s, averaged over 100 simulations.

RMSE	Roll	Pitch	Yaw	ω_x	ω_y	ω_z
	$(\times 10^{-3} \text{ rad})$			$(\times 10^{-6} \text{ rad/s})$		
UKF	0.659	0.664	0.065	0.2201	0.3562	0.9871
KLPUKF	0.171	0.183	0.078	0.0863	0.0591	0.0879
ORKF	0.075	0.133	0.041	0.0523	0.0163	0.0141
SFMKF	0.054	0.190	0.064	0.0883	0.2100	0.0419
RUKF	0.052	0.187	0.042	0.0801	0.2107	0.0378

4.5.2 Operation with noise-increment magnetometer fault

Magnetometers on satellite can easily be disturbed by other subsystems which are very close because of the small size of the nanosatellite. There can also be external disturbances. Those effects result in faults in the measurements. Generally, two types of error models are widely adopted to describe frequently encountered faults: the continuous bias model and the noise increment error model. For disturbances having continuous bias on the measurements, sensors should be calibrated first. Here, the noise increment type of magnetometer measurement fault is considered. Here, it is considered that a sensor-related fault occurred on the magnetometer's y channel, making the measurements noisy on that channel. The y magnetometer component $\varepsilon_{B_k}^y$ of the measurement noise term ε_k in (1b) is replaced by $\delta_k \varepsilon_{B_k}^y$, where δ_k is a scaling sequence. Two fault cases are considered: long-term fault

$$\delta_k = \begin{cases} 10 & \text{if } t > 4000 \\ 1 & \text{otherwise} \end{cases}, \quad (4.44)$$

and transient (short-term) fault

$$\delta_k = \begin{cases} 10 & \text{if } 3000 < t < 3400 \\ 1 & \text{otherwise} \end{cases}. \quad (4.45)$$

Figure 4.7 shows the time series of the y-magnetometer component of the RUKF scaling matrix derived from the windowed innovation sequence in equation (4.12). These show that the RUKF scale factor is adapting correctly: it changes from ~ 1 to ~ 100 during the fault.

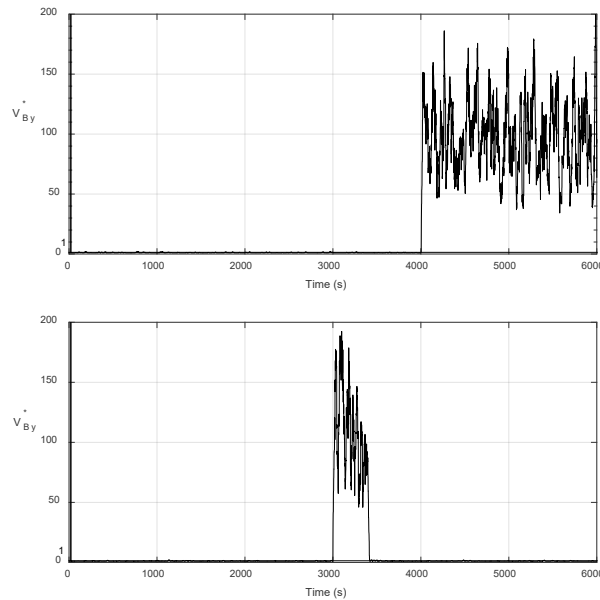


Figure 4.7 : RUKF scaling factor for long-term (a) and short-term (b) magnetometer fault.

The scale factors for normal and Student's t distribution cases without considering any faults are presented in Figure 4.8 in order to see how RUKF copes with the heavy tails. We see that RUKF compensates the heavy tails by increasing the scale factor. It should be noted that the x and z axes are similar to the y axis outputs. Figure 4.9 and Table 4.3 summarize the estimation errors for different filters. From these we see

- UKF and KLPUKF are generally the least accurate methods, especially for long-term fault. That's because these filters assume Gaussian noise and are not adaptive. Also, UKF is generally very slow in recovering after the end of the short-term fault.
- The remaining filters cope fairly well with both kinds of faults. ORKF is the most accurate, RUKF is almost as accurate, and SFMKF is the least accurate of the three. These three filters are adaptive in measurement noise covariance. So, the filter copes with faulty measurement by adapting the scaling factors and having a lower gain.

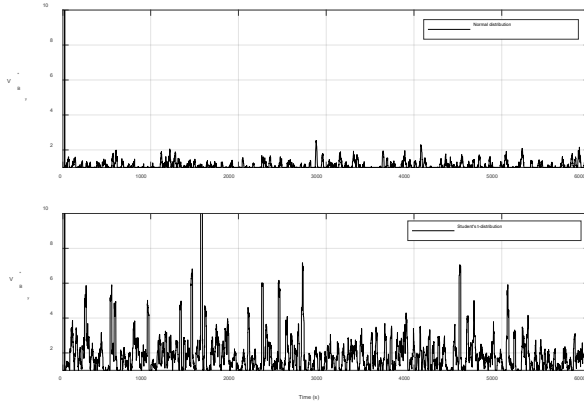


Figure 4.8 : RUKF scaling factor for normal and t-distributions without any magnetometer faults.

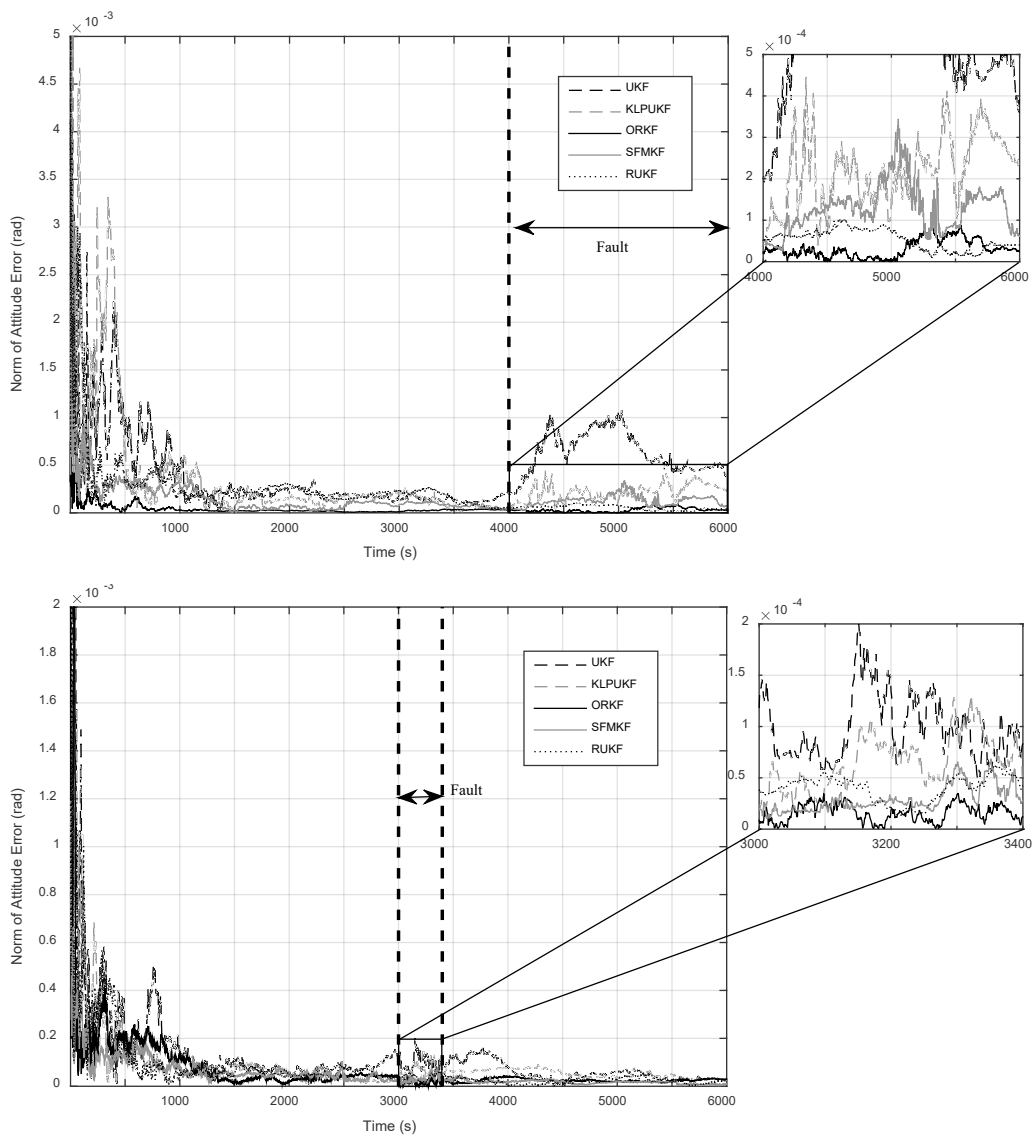


Figure 4.9 : Attitude errors for long-term (a) and short-term (b) magnetometer faults, single simulation.

Table 4.3 : Filter RMSE during faulty period, averaged over 100 simulations.

RMSE	<u>Long-term</u>			<u>Short-term</u>		
	Roll	Pitch	Yaw	Roll	Pitch	Yaw
	($\times 10^{-3}$ rad)	($\times 10^{-3}$ rad)	($\times 10^{-3}$ rad)	($\times 10^{-3}$ rad)	($\times 10^{-3}$ rad)	($\times 10^{-3}$ rad)
UKF	0.991	1.843	2.001	0.705	0.771	0.816
KLPU KF	0.213	1.102	0.201	0.198	0.683	0.155
ORKF	0.146	0.264	0.091	0.076	0.120	0.047
SFMK F	0.170	0.375	0.102	0.091	0.168	0.071
RUKF	0.159	0.275	0.114	0.084	0.141	0.059

4.6 Conclusions

From this study, we find:

1. Real magnetometer noises are better modeled by Student's t distribution than the normal distribution.
2. SFMKF, UKF, RUKF are the computationally lightest filters, KLPUKF and ORKF are 2-4 times slower.
3. In nominal operation mode, ORKF and KLPUKF are the most accurate; SFMKF and RUKF errors are about twice as large. UKF has much larger errors because it does not cope well with t-distributed noises.
4. ORKF and RUKF cope best with transient and long-term noise-increment faults in magnetometer. SFMKF copes reasonably well.

In summary, ORKF is the most accurate filter both for the nominal operation mode and for the operation with noise-increment magnetometer fault. We identified that the outliers caused the difference in the estimation accuracy. We suggest that it is important to check the noise distribution of the magnetometers. If they are non-

Gaussian as with the tested magnetometers the non-Gaussianity is a more significant source for estimation errors than nonlinearity and it is more important to use the limited computational resources in nanosatellites to compensate for non-Gaussianity than using more complex nonlinear filters.

For further work, algorithms can be tested for sensor faults of continuous bias type. This would require a calibration in which the state vector has more elements to be estimated. Other disturbances such as extraterrestrial magnetic field can be included in the models and results using different reduced-order IGRF models can be compared. In addition to these, different Student's *t* filters and the filter proposed in [123], which is a Kalman-type filter for measurements having non-Gaussian noises, could be implemented and compared with other considered filters for further comparative studies. Another interesting possibility would be to investigate whether the KLPUKF and ORKF algorithms could be fused into an algorithm that minimizes the nonlinearity and can cope with the heavy-tailed noises.

5. EVALUATION OF GEOMAGNETIC FIELD MODELS USING MAGNETOMETER MEASUREMENTS FOR SATELLITE ATTITUDE DETERMINATION SYSTEM AT LOW EARTH ORBITS: CASE STUDIES*

5.1 Abstract

In this study, different geomagnetic field models are compared in order to study the errors resulting from the representation of magnetic fields that affect the satellite attitude system. For this purpose, we used magnetometer data from two Low Earth Orbit (LEO) spacecraft and the geomagnetic models International Geomagnetic Reference Field (IGRF) [6] and Tsyganenko's magnetospheric model 89 (T89) [68] models to study the differences between the magnetic field components, strength and the angle between the predicted and observed vector magnetic fields. The comparisons are made during geomagnetically active and quiet days to see the effects of the geomagnetic storms and sub-storms on the predicted and observed magnetic fields and angles. The angles, in turn, are used to estimate the spacecraft attitude, and hence, the differences between model and observations as well as between two models become important to determine and reduce the errors associated with the models under different space environment conditions. We show that the models differ from the observations even during the geomagnetically quiet times but the associated errors during the geomagnetically active times increase. We find that the T89 model gives closer predictions to the observations, especially during active times and the errors are smaller compared to the IGRF-12 model. The magnitude of the error in the angle under both environmental conditions is found to be less than 1°. For the first time, the geomagnetic models are used to address the effects of the near-Earth space environment on the satellite attitude.

* This chapter is based on the paper “Cilden-Guler, D., Kaymaz, Z., and Hajiyev, C. (2018). Evaluation of geomagnetic field models using magnetometer measurements for satellite attitude determination system at low earth orbits: Case studies, *Advances in Space Research*, 61(1), 513-529, doi: 10.1016/j.asr.2017.10.041”.

5.2 Introduction

Magnetometers are one of the attitude determination sensors for small satellites at LEO. On-board magnetometers and a model of the Earth's magnetic field are needed for the prediction of the geomagnetic field at the satellite's altitude. The conventional methodology while estimating the satellite's attitude involves the angle between the magnetic field vectors from the simulated magnetometer and the model of the Earth's geomagnetic field. Therefore, the accuracy of the geomagnetic fields from the model is critical for a precise attitude determination. As scientific payloads, the magnetometers on-board the satellites return data in space within their built-in precision and are placed one or two meters away from the spacecraft body on a boom in order to avoid the magnetic effects created by the satellite itself and its nearby surrounding environment. Simulated magnetometers, on the other hand, use the magnetic field direction from a geomagnetic field model, most widely IGRF [6], to determine the parameters of the satellite attitude. Both magnetometers include several errors and bias sources that will affect the satellite's attitude. Current state-of-the-art satellite magnetometers are highly improved both in accuracy, and precision and resolution as well as in physical size. Among several satellite magnetometers, two of the most often used ones are the flux gate magnetometers and search coil magnetometers that use tri-axial configuration. Many of the bias and random errors may be reduced or prevented prior to the launch during the ground tests or on-orbit after the launch with having an additional sensor for calibration on the satellite. There are several methods proposed in the literature for magnetometer calibration without attitude information. The most commonly known method is the TWOSTEP algorithm that, after the centering approximation, uses a second step employing the centered estimation, found by an approximation, as an initial value to an iterative Gauss-Newton method that avoids divergence problems as other algorithms cannot [48,49]. In parallel to the advancing technologies in the space industry, providing that the errors that may be resulted from real magnetometer sensors on board are negligible to affect the attitude, the source of most of the errors then would be associated with the environmental conditions in case of the real magnetometers and from the bias, noise and scaling factors in case of the simulated magnetometers and how they are handled during onboard processing in space.

The errors in attitude determination are determined in the literature using different approaches. An approach that is suggested by [50] is to compare the magnetometer measurements with the magnetic fields predicted by the IGRF geomagnetic model and aims to remove the bias and scaling errors. In this case, IGRF predictions are used to calibrate and optimize the simulated magnetometer magnetic fields [50,51]. The other approach involves the conversion of the IGRF model magnetic field to the satellite body coordinates. In these studies, the IGRF model is assumed to represent the geomagnetic field correctly. These studies imply that a good representation of the geomagnetic field is an essential part of the attitude determination process and the closer the geomagnetic model results to the real geomagnetic fields in space at the satellite's altitude, the more accurate the satellite attitude.

For the determination of the satellite's attitude angles, extended Kalman filter (EKF), unscented Kalman filter (UKF), and similar filters or single-frame methods such as q, QUEST, SVD, etc. are widely used [4,12,13,90]. The source of the error in the determination of the attitude angles may come from the model magnetometer calibrated using IGRF predictions at the satellite altitude. Some of the inaccuracies related to the geomagnetic model, IGRF, used by the model magnetometer result from the model assumptions, the insufficient experimental data, or both. For epoch 2000, the coefficients are provided to degree and order 13 and 0.1 nT precision for the IGRF-12 model [6]. In this study, we investigate the effects of the LEO orbit environmental conditions on the satellite attitude system, which are superimposed on the Earth's geomagnetic field as a result of magnetospheric substorms. As these effects are not taken into account in IGRF, the magnetic field at the satellite altitude during these times is underestimated by the simulated magnetometer. Some of the specific questions that we address are:

1. How well does the magnetic field (magnitude and direction) estimated by the geomagnetic field model accurately represent the real geomagnetic field at LEO altitudes,
2. How much the Earth's geomagnetic field varies during the magnetic storms and substorms at LEO altitudes? Consequently, how much these variations affect the predictions of geomagnetic models, e.g. IGRF?

3. What is the error that these will create on the spacecraft attitude as referred from the angle between the measured magnetic field and the field from the geomagnetic model?
4. Which geomagnetic field model gives closer estimates to the measured magnetic field at the satellite altitude at LEO? i.e. determine and compare the performance of different models.

In the following sections, we first describe the data sets and the methodology used in this study and then present the results and discussion. In the last section, we give a summary and conclusions.

5.3 Data and Methodology

The first and the second questions given above are investigated by looking at the differences between the magnetic field vector measurements obtained from a real magnetometer placed on a LEO orbiting satellite and a chosen geomagnetic model during the geomagnetically active and quiet times. As for LEO orbiting satellites, we selected C/NOFS, and SWARM satellite magnetic field measurements. The data from these spacecraft are obtained from [124], and [125]. Both satellites use a fluxgate magnetometer placed on a boom away from the satellite. Regarding the geomagnetic field model of the Earth, in recent years, there have been several new geomagnetic models developed to represent the geomagnetic field under different external conditions such as Tsyganenko models [68,69,126–128], CHAOS [129,130], POMMES-6 [131], etc. in addition to the IGRF model. In this study, we used the 1989 version of T89 and the last version of the IGRF model to study the geomagnetic field of the Earth at LEO altitudes. The satellite attitude has been studied based on the angle between the magnetic field vectors measured on the satellite and from the model on orbit. The difference in the components of the magnetic field vectors is mostly used as a unit vector. Therefore, the angle between the magnetic field of the modeled and measured field affects the degree of accuracy in the satellite's attitude. In this study, it is our interest to evaluate these models by comparing their predictions with the magnetometer measurements from the selected satellites given above. For the attitude determination system, the IGRF model is the most commonly used model. However, the difference between the magnetic fields of the sensor and model increases when the geomagnetic activity occurs. Hence, several models that take into account the external

variations resulting from the solar wind and interplanetary magnetic field superimposed on the Earth's geomagnetic field are of great importance in the determination of the satellite's attitude correctly.

5.3.1 Geomagnetic models

The simplest model of Earth's geomagnetic field is the dipole field approximation. However, the dipole approximation fails to represent the geomagnetic field at distances far away from the Earth owing to the modifications of the geomagnetic field lines by the solar wind. As a result, the magnetometers are not reliable to be used as attitude sensors at farther distances from the Earth. In IGRF models, Earth's main magnetic field is described by the series of spherical harmonic coefficients that describe the secular variation of the Earth's magnetic field. Earth's magnetic field in the IGRF-12 model with the order of 13th is expressed as the gradient of a scalar potential function. In most of the nanosatellite missions, truncated versions as 7th to 10th order of IGRF are preferred and this might cause a reduced accuracy on the model outputs [132]. IGRF-12 is a model using several candidate models which are based on different groups of datasets and time intervals from the Swarm, CHAMP, Ørsted, SAC-C missions [6]. The accuracy of the IGRF-10 and IGRF-11 models is found to be accurate within 1° for 92% times in the upper atmosphere [64]. Based on long-term satellite observations, these models represent the average geomagnetic conditions and neglect the variations resulting from the geomagnetic disturbances superimposed on the main geomagnetic field at the satellites' altitudes. During the geomagnetic storms and sub-storms, Earth's main magnetic field undergoes several variations. These variations are treated as noise or error and cannot be fully represented in the attitude determination most of the time. The magnetic field strength and the direction change in time scale from seconds to hours and from a few nanoTeslas (nT) to orders of 1000s of nT depending on the altitude of the satellite. For example, in the geostationary orbit, the magnitude of the perturbations can be as large as on the orders of 200nT. Additionally, these phenomena occur several times in a week during the high solar activity periods while one or two occur during the low solar activity period. Therefore, the geomagnetic storms and substorms can have an appreciable effect on the satellite's attitude estimated by the IGRF model and subsequently the simulated magnetometer.

T89 model is an empirical model of the magnetosphere based on large satellite data from the low altitudes of the Earth to large distances in the magnetotail and in the solar

wind. Therefore, it covers a large spectrum of magnetospheric and solar wind conditions in addition to upper atmospheric conditions at LEO altitudes. The model uses IGRF as a base model of the geomagnetic field close to Earth but includes the external effects inherited in the data from several magnetospheric and solar wind satellites such as IMP, HEOS, ISEE spacecraft, etc. [68,128]. So that in addition to the main field (internal) given by IGRF (\mathbf{B}_{INT}), it includes extraterrestrial effects (\mathbf{B}_{EXT}). The magnetic field in space can be represented by adding these components [68]:

$$\mathbf{B}_{TOT} = \mathbf{B}_{INT} + \mathbf{B}_{EXT} \quad (5.1)$$

where,

$$\mathbf{B}_{EXT} = \mathbf{B}_{RC} + \mathbf{B}_{MP} + \mathbf{B}_{Region1-2} + \mathbf{B}_T \quad (5.2)$$

As seen in equation (5.2), more explicitly, \mathbf{B}_{EXT} includes effects from Ring current (\mathbf{B}_{RC}), tail current (\mathbf{B}_T), magnetopause currents (\mathbf{B}_{MP}), and Region 1 and 2 currents ($\mathbf{B}_{Region1-2}$). Data sets are categorized with respect to the geomagnetic activity index K_p which represents the geomagnetically active or quiet times for external sources. Hence, the inputs for the T89 model are K_p , the position of the satellite, and time of the year to generate external magnetic field effects at the satellite's altitude. Improved versions are available that include several other external sources that affect the total magnetic field. For example, the T05 source code is described for the dynamical empirical model of the inner storm-time magnetosphere, while T89 is a magnetic field model with the warped tail current sheet. We use the T89 version to determine the extraterrestrial effects on the magnetic field which can affect the attitude accuracy of small satellites. Since the T89 model uses the IGRF model for internal sources near the Earth, at LEO orbits altitudes, both models are expected to give similar results if there are no extraterrestrial effects. Earth's dipole field should dominate as we close to the Earth over the extraterrestrial sources. However, during the geomagnetically active times, differences from the dipole model arise due to the currents flowing from the magnetosphere into the Earth's atmosphere. The following sections present our preliminary results from the model-to-observation comparisons as well as the model-to-model comparisons and discuss their implications from the satellite attitude perspective. The sketch in Figure 5.1 outlines the procedures we apply for the model-model and model-observation comparisons.

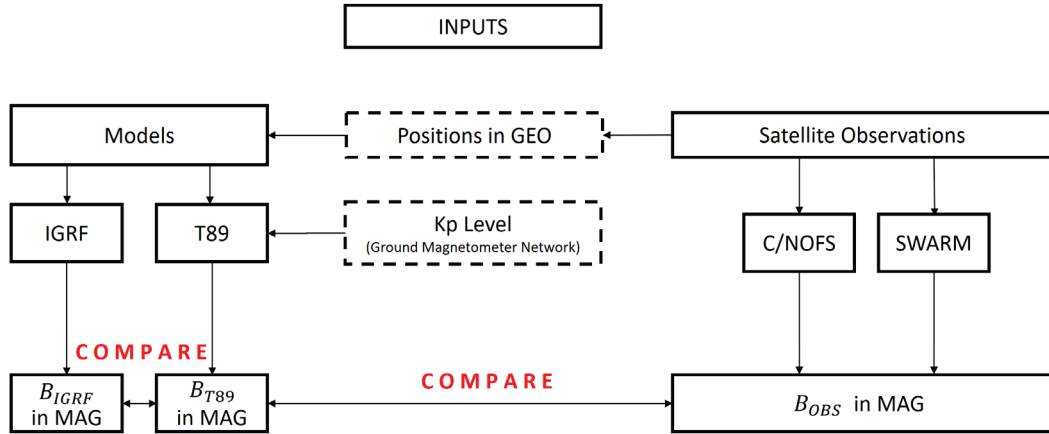


Figure 5.1 : Flow chart for the comparisons.

5.3.2 Coordinate systems

When dealing with the Earth’s geomagnetic field, it is unavoidable to work with different coordinate systems depending on the type of the problem. Figure 5.2 illustrates the coordinate systems involved in this study at the location of the satellite in space. The satellite magnetometer data are available mostly in Earth-Centered, Earth-Fixed (ECEF). In the ECEF system, the z-axis is along the spin axis of the Earth and pointing to the north pole. The x-axis points towards the intersection of the 0° latitude (i.e. the equator) and 0° longitude and the y-axis completes the right-handed coordinate system, passing through 0° latitude (i.e. the equator) and 90° longitude. Cartesian coordinates that the ECEF is represented as in the Geographic Coordinates (GEO) frame are also shown in Figure 5.2. In the figure, ENU indicates the East, North, and Up respectively.

As indicated in the sketch in Figure 5.1, throughout this study, we used Geomagnetic coordinates (MAG) for comparisons between the magnetic field vectors from the satellite magnetometer and the geomagnetic models. Both the model magnetic field and the satellite magnetic field data are obtained in this coordinate system. In the MAG system, the z-axis aligns with the dipole axis and the y-axis is perpendicular to the plane containing the dipole axis and the rotation axis of the Earth. The x-axis completes the right-handed system [133]. For near-Earth space regions, such as LEO, where the Earth’s magnetic field dominates, the magnetic fields are best represented in the MAG system [133,134].

Body and orbit reference frames are the main coordinate systems for the attitude determination system. The body frame of reference describes the vectors in a

coordinate system centered at the center of mass of the satellite. Orbital coordinate system, on the other hand, refers to the coordinate system when the satellite is in its orbit. Attitude angles are found using a transformation matrix from the orbital reference system to the body coordinate system. Satellite motion in each direction on orbit is described by the Euler angles (roll, pitch, yaw about x, y, z axes respectively) which can be determined in the filter by using the geomagnetic field direction at the location of the satellite.

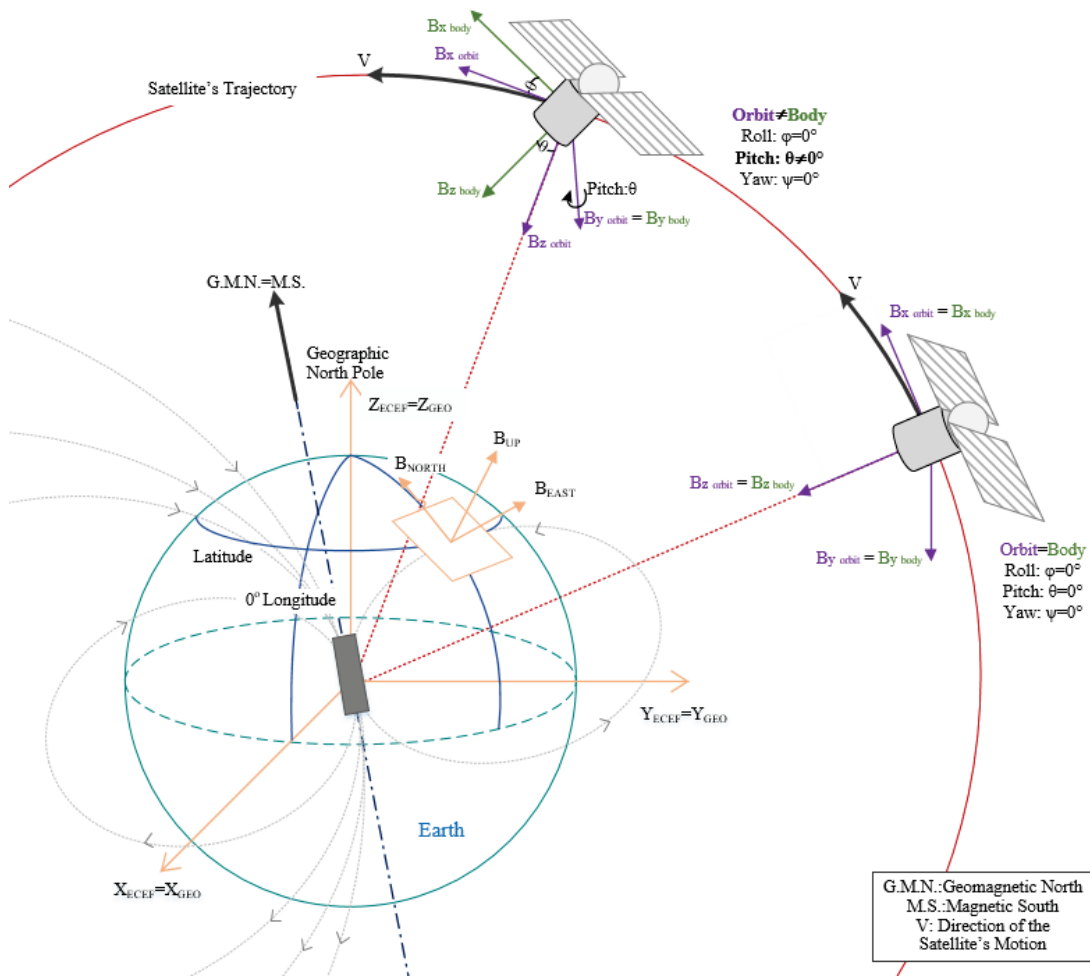


Figure 5.2 : A sketch showing the coordinate systems along with a circular trajectory of a satellite.

5.3.3 Satellite observations

Verification of the magnetic field models can be achieved by using observations from a reliable magnetometer such as fluxgate. In this study, C/NOFS, and SWARM satellites, which carry on-board fluxgate magnetometers, at LEO orbits are used for comparisons with the results from the geomagnetic field models and for the

determination of the attitude angles. The orbital and instrumental characteristics of these satellites are presented in Table 5.1 [135,136].

Table 5.1 : Orbital properties of the spacecraft used in this study.

Satellite	C/NOFS	SWARM A
Operation Time	April 16, 2008 Nov 28, 2015	Nov 22, 2013- Present
Orbit	Elliptical	Near-polar, circular
Eccentricity	0.032	0.0003099
Inclination (deg)	13	87.4
Apogee	853	466
Perigee	405	485
Altitude Range (km)	390-736	466-485
Period (min)	97.3	91
Magnetometer Type	Fluxgate	Fluxgate

C/NOFS (Communication/Navigation Outage Forecast System) is a US mini-satellite launched on April 16, 2008, and ended on November 22, 2015 [137]. It is designed to forecast the ionospheric irregularities in Earth's equatorial region. The spacecraft has an elliptical orbit with low inclination at altitudes varying from 405 to 853 km and an attitude better than 0.1° using the star sensors [138]. The accuracy of the magnetic field instrument on C/NOFS has an accuracy of 0.1 nT [139]. Additionally, the spacecraft is listed as having one of the most precise GPS receivers flown in space with between 1-45 cm accuracy [140]. SWARM (Geomagnetic LEO Constellation) is a mini-satellite constellation mission with 3 satellites, SWARM A (Alpha), SWARM B (Bravo), and SWARM C (Charlie), built by ESA. The constellation was launched on Nov. 22, 2013, and is still in operation. SWARM A and C satellites both have an altitude around 400 km (<450 km) with an inclination of 87.4° . SWARM B (Bravo)

has a higher altitude around 500 km (<530 km) with 88° inclination. The scientific mission of the SWARM constellation pair is to measure and study the magnetic variations of the Earth's geomagnetic field resulting from the Earth's core, mantle, crust, and oceans, as well as from the ionosphere and magnetosphere; to study sun's influence on Earth system; to understand the impact of solar wind on dynamics of the upper atmosphere. In this study, the magnetic field data from SWARM A satellite are used in our comparisons. The spacecraft carries a magnetic field instrument with accuracy under 0.5 nT, and has a precise orbit determination under 10 cm (RMS) in addition to 3-dimensional position measurements better than 20 m (3σ) and absolute accuracy under 1 arcsec for attitude knowledge [136]. In addition, both the magnetic field and position data from both spacecraft are obtained from the institutes' public web sites, which in the case of C/NOFS, it is NASA's CDAWeb and in the case of SWARM, it is ESA's website. Both data sets from both spacecraft are provided in 1-sec resolution. As C/NOFS's apogee is larger than that of SWARM A, it is expected that the extraterrestrial effects will be more dominant especially when the satellite is moving towards its apogee at higher altitudes. Higher altitudes are more susceptible to the effects originated from the Earth's magnetosphere and outside. Therefore, the altitude of the satellite is important in determining the degree of the geomagnetic storm effects.

5.4 Analysis and Results

As our purpose of the study is threefold, namely, one is to compare the geomagnetic field models with satellite observations at LEO orbits; two is to determine which model approximates the observations better, and three is to determine the effects of differences between the models and observations on the attitude angles by evaluating the angle between magnetic field orientations of the model and observations. These comparisons are made during the magnetically disturbed days to reveal the effects of the magnetic storms and magnetospheric sub-storms on the geomagnetic field at LEO and on the attitude angles. For the comparisons between the models and the observations, first, we looked for the time intervals when there are geomagnetic storms that occurred in the magnetosphere and both the magnetic field and the position data from the satellites exist during that time interval. Taking the operation times of these satellites given in Table 5.1 into account, we select 3 different magnetically quiet days

when there are no geomagnetic storms or magnetospheric substorms in the magnetosphere and 3 different magnetically disturbed days, i.e. when there are magnetic storms and substorms in the magnetosphere at various levels from weak to strong. Table 5.2 presents these cases to be studied in detail in the following sections.

Table 5.2 : Magnetically quiet and active days selected for the study.

Case No	Satellite	Quiet days	Active Days
Case 1	C/NOFS	7 March 2009	17 March 2013
Case 2	C/NOFS	5 January 2013	04 August 2010
Case 3	SWARM A	18 January 2014	20 February 2014

Quiet or disturbed days are chosen by looking at the geomagnetic indices, K_p , D_{st} , and AE [141]. These are the magnetic indices that show the level of extraterrestrial disturbances resulting from the interaction between the solar wind and Earth's magnetosphere. They are calculated based on the geomagnetic field measured on the ground magnetic observatories. D_{st} index refers to the Disturbance Storm Time index and conveniently shows the presence of the geomagnetic storms initiated when the solar wind first hits the Earth's magnetosphere on the dayside at the subsolar point. This compression depending on the strength of the solar wind dynamic pressure is detected in the D_{st} index as a positive discursion from the quiet time level of D_{st} which is known as the sudden commencement. During a typical geomagnetic storm, the sudden commencement starts at 20 nT. This is followed by a large drop in the geomagnetic field, which defines the geomagnetic storm main phase. D_{st} index is obtained from geomagnetic observatories located at the low latitudes around 20° of the equator. It is a good indicator of the ring current in the geomagnetic tail that increases as a result of increased tail currents during the geomagnetic storms following the initial compression on the dayside. Geomagnetic activity that causes D_{st} to drop below -40 nT is considered as a geomagnetic storm [142]. The more negative the D_{st} index, the stronger the geomagnetic activity is. Auroral Electrojet index (AE) index, on the other hand, gives the geomagnetic disturbances measured at the high latitudes resulting from the particles coming from the geomagnetic tail as a consequence of the magnetospheric substorms that create the auroral lights over the northern and southern high latitudes.

These particles give rise to strong electrical currents at high altitudes in the atmosphere which are known as Auroral Electrojet currents and measured by *AE* index. The magnetospheric substorms that result in *AE* index to be larger than 100 nT are considered as magnetospheric substorm. *K_p* (planetarische Kennziffer) index is the planetary index that shows the global geomagnetic activity level and measured using the magnetic field data from the mid latitude geomagnetic stations. A geomagnetic disturbance with *K_p* larger than 4 is considered as a storm. Table 5.3 indicates the level of the geomagnetic storm or substorm depending on the scale of these indices.

Table 5.3 : Classification of geomagnetic storm and substorms based on Dst, *K_p*, and AE magnetic indices. [143,144]

Magnetic Index	No-to-Weak Storm/Substorm	Moderate Storm/Substorm	Strong Storm/Substorm
<i>K_p</i>	<4	4-6	>6
Dst	>(-40)	(-40)-(-100)	<(-100)
AE	<100	100-1000	>1000

Figure 5.3 presents an example of the magnetic field data measured on-board C/NOFS satellite during the magnetically quiet day, March 7, 2009. It presents the magnetic field components in MAG coordinates, i.e. *B_x* in the north-south direction, *B_y* in the east-west direction, and *B_z* as the component in the z-direction which is parallel to Earth’s dipole moment, for a stretch of one day from 00:00 UT to 24:00 UT. The periodic variations seen in this figure are due to the orbital motion of the satellite. In order to make comparisons, the differences resulting from the orbital motion are removed by taking the period-averaged magnetic field data. The C/NOFS has an orbital period of 97.3 min (see Table 5.1). Therefore, a running mean procedure with a window length of 97.3 min (~1.5 hr) is applied to the magnetic field data in this case. This process eliminates the temporal variations of less than 1.5 hr as well as the latitudinal variations resulting from the orbit. For the purposes of our study, we think that this procedure is appropriate. In this figure, the black and blue lines give the magnetic field data and the period-averaged magnetic field data. As seen clearly, the running mean process removes the orbital periodicity. Still, a slight periodicity that the

running mean did not completely remove appears, however, this will not affect our comparisons.

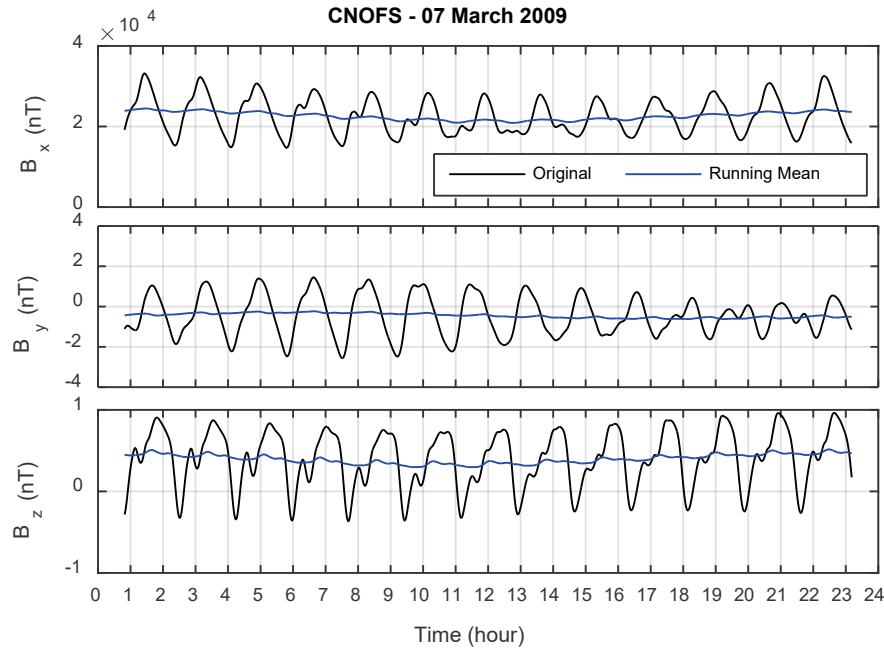


Figure 5.3 : An example of orbit averaged data. C/NOFS magnetic field components on March 7, 2009. The black line is the original data while the blue line is the orbit averaged data.

Figure 5.4 represents the first case from the C/NOFS satellite. The panels on the left in Figure 5.4 give the model-data comparisons for a quiet day recorded on March 7, 2009. The panels from top to bottom are K_p index (a), the differences between the magnetic field components measured by on-board magnetometer on C/NOFS satellite and the magnetic field predictions of the models, IGRF (b) and T89 (c), and the differences between two models (d). The blue, red, and black colors indicate differences in B_x , B_y , and B_z components. K_p index in panel (a) indicates that the level of geomagnetic activity is low. In fact, to this day, there isn't any geomagnetic activity, thus $K_p=0$. The line at $K_p=4$ indicates the threshold after which the day is considered as disturbed. For direct comparisons with the observed magnetic field, the same orbit-averaged running mean procedure is applied to the model magnetic field components as well.

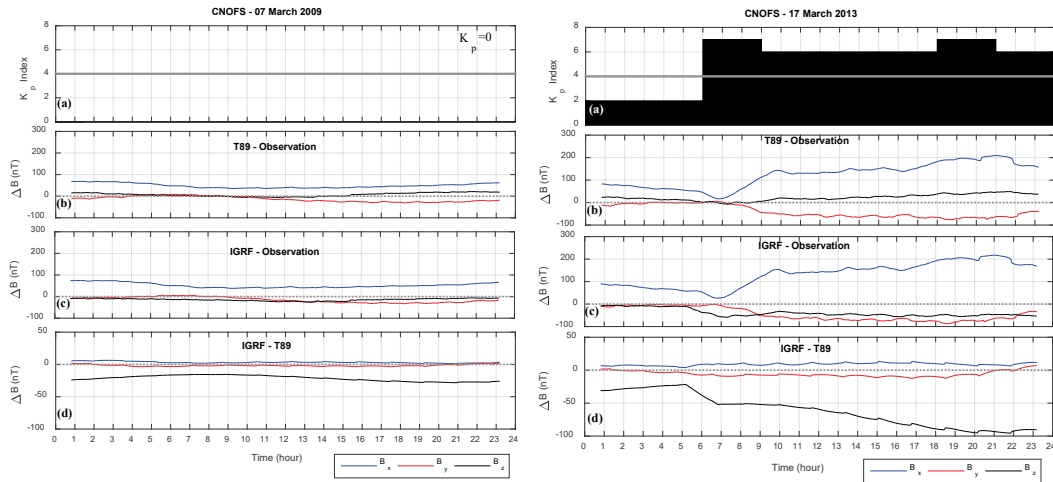


Figure 5.4 : Differences between the observations and the model result for magnetic field components from C/NOFS satellite on March 7, 2009, when there is no geomagnetic activity (left); and on March 17, 2013, when there is a geomagnetic storm (right).

The figure is constructed by simply subtracting the magnetic field components of the magnetic field measured on the satellite from those predicted by the models. Therefore, the panels compare the differences between the observed and geomagnetic model predicted magnetic field components. As a result, positive differences in these panels indicate that the model magnetic field is larger than the observed magnetic field while negative differences imply that the observed fields are larger than those of models. Even during this magnetically quiet day, namely in the absence of geomagnetic storms, the model magnetic fields are seen to be quite different than those observed. The largest differences in panels b and c are seen in the B_x component, the north-south component of the magnetic field, and the least difference is found in the B_z component. Both models overestimate the observed B_x component while on average they underestimate the B_y component. Both models, on average, give a slightly larger B_z component than the observed one. Although the differences are small for the B_z component, the T89 model gives positive differences meaning that the model slightly overestimates the B_z component while IGRF shows negative differences indicating the underestimation of the observed B_z . The differences are calculated as the maximum deviations of the models from the observations and any distribution is not assumed for the data. The differences between the models and the observations vary up to +60 nT for the B_x component and between 0 and -30 nT for B_y . The difference for the B_z component ranges from 0 to 20 nT in T89 and 0 to -20 nT in IGRF. Panel (d) displays the differences between IGRF and T89 models. In this case, T89 model results are

subtracted from those of the IGRF model. Both B_x and B_y are very close to each other within less than 5 nT but the two models differ the most in the B_z component and the difference is seen to be about -20 nT on average. This implies larger estimates from T89 compared to IGRF for the B_z component. While the model-to-observed magnetic field comparison shows that the models differ the most in the B_x component, model-to-model comparisons indicate the models differ from each other the most in estimating the B_z component. As for the total magnetic field, there are no differences between the model predictions so that the difference is close to zero but both models show a difference from the observations on the order of 50 nT (not shown, Table 5.4).

The panels on the right in Figure 5.4 give a similar comparison during a magnetically active day on March 17, 2013. The panels from top to bottom are the same as in panels on the left in Figure 5.4. In the first panel, we see that the K_p index is larger than 4 from 06:00 UT until the end of the day, with a maximum of 7+ from 06:00 UT to 10:00 UT and from 18:00 UT to 21:00 UT. The average K_p for the day is about 5+. Both panels b and c show that the models give the largest differences from the observations when the geomagnetic activity started at 06:00 UT. The geomagnetic activity stays high from 06:00 UT to 21:00 UT and we see that both IGRF and T89 models differ the most from the observations during this time interval. We can see that the differences in the B_x component before the geomagnetic activity is around 80 nT and increases slowly up to 130 nT after the geomagnetic storm starts and continues to increase to 205 nT till the end of the time scale given in this figure. Differences in both B_y and B_z are very close to zero before the geomagnetic storm, but increases after. Differences with the observations in B_y component in both models vary around -80 nT. However, the B_z component shows differences in the order of 30 to 40 nT in the T89 model, while it is around -40 nT in the IGRF12 model. Both panels show that the B_x component is overestimated and by component is underestimated in both models. B_z component, on the other hand, is overestimated in T89 while it is underestimated in IGRF. These comparisons are qualitatively the same as obtained in the quiet time case. However, quantitatively, compared to the same panels of the quiet day given in Figure 5.4, the differences between both models and the observations are larger during the geomagnetically active day by about a factor of 3. Panel d, similar to the quiet day case, indicates that the models differ mostly in B_z component up to 100 nT during the geomagnetic storm interval while the differences between predicted B_x and B_y

components are small, being on the order of 10 nT before the geomagnetic storm. We see that the T89 model gives a larger prediction of the B_z component than the IGRF. Although not given in these plots, both models exhibit differences with the observations around 200 nT for the total magnetic field during the geomagnetic storm interval while smaller, around 50 nT on average before the storm. Despite this difference with the observations, there are no discernable differences between the predictions of the total magnetic field from both models during the quiet and active day.

Figure 5.5 compares the angle (α) between the observed and model (T89 and IGRF) magnetic field vectors measured during the quiet (left) and active (right) day using C/NOFS data. The angle is calculated by taking the scalar product of two unit vectors. While the first two panels give the level of geomagnetic activity as seen in the D_{st} index for geomagnetic storm and the AE index for the auroral substorm, the third panel presents the angle calculated. Although D_{st} index variation is small during the active day, the AE index is larger than 100 nT indicating the presence of a magnetospheric substorm in the geomagnetic tail that results in aurora in the ionospheric altitudes. The differences between the quiet and active day angles as well as between the model predictions are clearly demonstrated in these panels. During the quiet day, both models indicate that the angle between predicted and observed vary around 0.15° in panel d on the left. In panel d on the right, T89 predicts smaller angles compared to the IGRF model. T89 prediction of the angles stays around 0.12° during the storm day while the angles predicted by IGRF increase after the storm starting at 06:00 UT. This indicates that the magnetic field vector predictions from the T89 model are closer to the observations. It is clear that larger differences with the observations during the active days are caused by the geomagnetic storms.

For small satellites, both magnetometer data and a magnetic field model are necessary for the attitude estimations. For most of the cases, the model predicted and measured magnetic field components are used as unit vectors. Therefore, the angle between the model and the observed magnetic field is a key parameter in determining the attitude angles, namely yaw, pitch, and roll. The closer the model predictions to the observed fields, the more accurate the attitude estimates will be. In Figure 5.5, we see that the angles calculated for both magnetically quiet and active days are small to cause a serious effect on the satellite's attitude. For most small satellite applications, accuracy

up to 1° for all attitude angles in x, y, and z directions is accepted to be sufficient to provide reliable attitudes [145]. The angles determined here appear to be very small to give rise to attitude angles greater than 1° . Even though the difference in angles is small, for more accurate and reliable attitude predictions, the model that gives smaller angles with the observations should be preferred, under especially geomagnetically active conditions when the deviations from observations are expected to be larger.

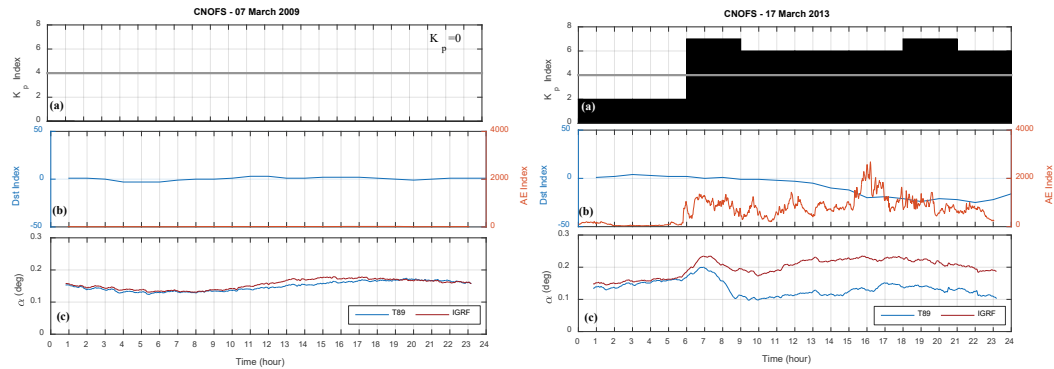


Figure 5.5 : Angles, between the vector magnetic fields from the models and the observations, for the C/NOFS satellite on March 7, 2009, when there is no geomagnetic activity (left); and on March 17, 2013, when there is a geomagnetic storm (right).

Table 5.4 compares the root mean square (RMS) error between the models and the observations during the quiet day (left) and active day (right). The second and third columns in both tables are the RMS errors for the differences between the magnetic field components of the models and the observations. Namely, the differences between the IGRF and the observations and (second column) and the differences between T89 and the observations (third column). Table 5.4 for the active conditions on the right is performed by using the differences for the data corresponding to the part of the differences corresponding to $K_p > 4$, defined as the active times. Comparison of right and left panels shows that the RMS errors in predicting the observed magnetic field components are smaller during the magnetically quiet day as opposed to the magnetically active day. Here we see that the RMS error for the total magnetic field is the largest compared to the RMS error in the components. For the components, RMS errors are smallest for B_z and largest for B_y . T89 model gives a much smaller RMS error than those of the IGRF model in both quiet and active conditions, implying its predictions are closer to the observations. The errors during the active times increase in both models. Overall, the T89 model, compared to IGRF, shows better performance in predicting both the magnetic field components and also the magnetic

field strength and agrees better with the observations based on RMS errors. One point that needs emphasis from the point of satellite attitude purposes is that even during the quiet days, noticeable differences with the observations occur in predictions of both IGRF and T89 models. Differences become larger during the active days, especially in the IGRF model.

Table 5.4 : RMS errors for C/NOFS (Case-1) comparisons for the geomagnetically quiet day (left) and active day (right).

C/NOFS	07 March 2009		17 March 2013	
	(Quiet Day)		(Active Day)	
RMS Error	IGRF	T89	IGRF	T89
Bx (nT)	64.9	69.5	74.43	69.70
By (nT)	36.9	34.6	104.42	105.92
Bz (nT)	20.8	2.1	25.12	4.80
Btot (nT)	79.3	79.4	120.78	117.82
Angle (deg)	0.1559	0.1499	0.1972	0.1335

The last row in Table 5.4 displays and quantifies differences in the angles averaged over the time intervals studied, i.e. 24 hours. We can see that the average angles from both models differ mostly during the geomagnetically active days. IGRF’s angles are found to be larger than that of T89 by about 32% during the geomagnetically active times while they differ by about 4% for quiet times.

Figure 5.6 presents the second case and from the C/NOFS angle. The quiet and active day panels are shown on the left and right respectively. Similar to the previous case, K_p is 0 throughout the day in this event as well. In this case, too, models give the largest difference for the B_x component and the smallest for the B_y component. The magnitude of the differences varies from 80 nT for B_x to -30 nT for B_z from both models. For B_y component, differences are around 10-20 nT in the case of T89 and close to 0 nT for IGRF. The right panels for an active day in Figure 5.6 display that K_p levels are around 4 and exceed 4 during the day, indicating that the geomagnetic activity increased. In

these panels, we can see the differences become large as the geomagnetic activity becomes stronger. IGRF shows slightly larger differences when compared to T89. Differences with the observations during the active day vary around 100 nT for the B_x component in both models while differences for B_y are seen to be around 30-40 nT. Differences in the B_z component are negative in the case of IGRF and positive in T89 models indicating IGRF predictions for B_z are smaller up to 40 nT and T89 models are larger up to 20 nT. Differences between the models indicate that both models B_x and B_y predictions are closer being IGRF slightly larger for B_x and slightly smaller for B_y . For B_z , however, IGRF is considerably smaller than T89 varying from 20 nT up to a maximum of 80 nT.

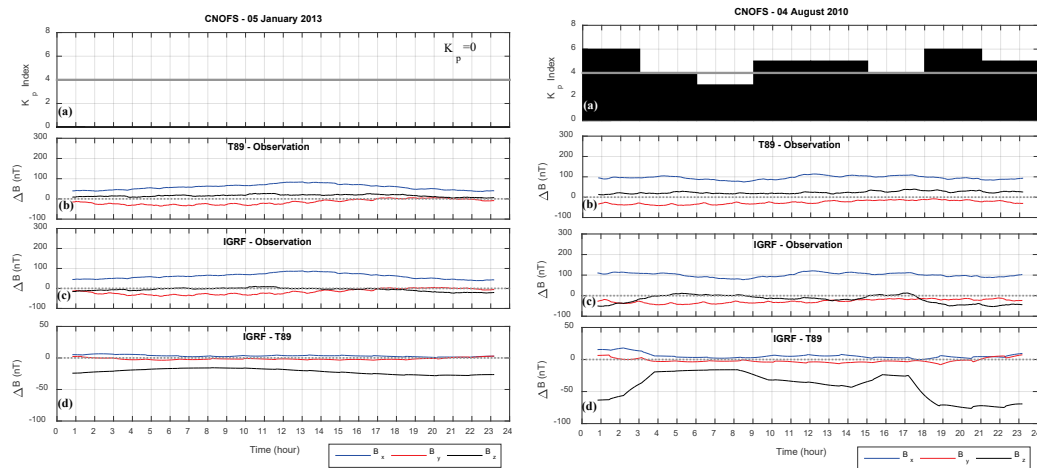


Figure 5.6 : Differences between the observations and the model result for magnetic field components from C/NOFS satellite on January 5, 2013, when there is no geomagnetic activity (left); and on August 4, 2010, when there is a geomagnetic storm (right).

Figure 5.7 illustrates the average angles for Case 2, January 5, 2013, and August 4, 2010. Both models give an angle on the order of 0.15° during the quiet day and differ during the active day between 0.1° and 0.2° . Differences are larger during the high geomagnetic activity periods seen from 0 to 06:00 UT, and 08:00 UT to 24:00 UT. When K_p reaches 6, the differences are seen to reach a maximum of 0.2° . During this event, AE is high at the beginning but becomes lower after 12:00 UT. However, D_{st} is seen to vary from -30 nT to -80 nT indicating geomagnetic storm presence, even when AE is low. The variations in average angle are due to the geomagnetic storm as associated with a coronal mass ejection (CME) in the solar wind (not given).

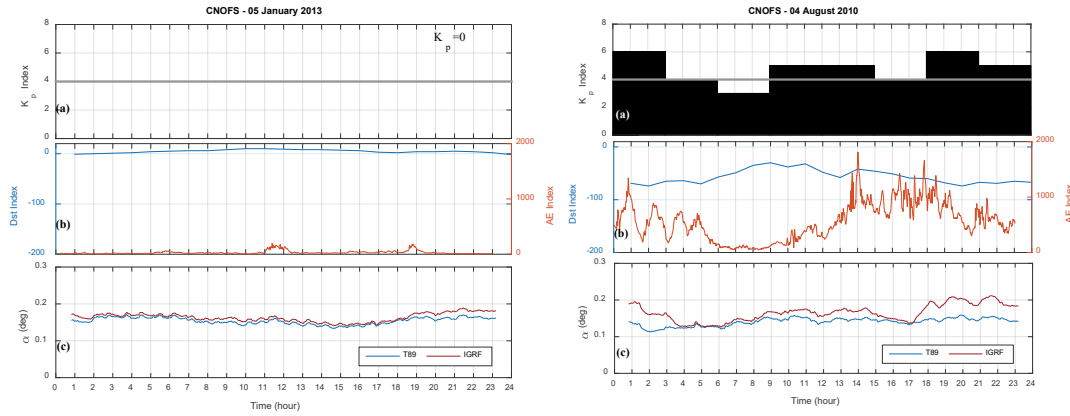


Figure 5.7 : Angles, between the vector magnetic fields from the models and the observations, for the C/NOFS satellite on January 5, 2013, when there is no geomagnetic activity (left); and on August 4, 2010, when there is a geomagnetic storm (right).

Table 5.5 gives the RMS errors for this case. As in the previous case, the largest RMS error is seen in B_{tot} , followed by B_y , B_x , and B_z respectively during both quiet and active days. The errors are larger, almost twice, during the active days and in IGRF predictions during both quiet and active times. The difference in average angles is slightly larger or equal during quiet days than active and in the IGRF model than in the T89 model. The range of angles is smaller than 1° in this example too.

Table 5.5 : RMS errors for C/NOFS (Case-2) comparisons for the geomagnetically quiet day (left) and active day (right).

C/NOFS	5 January 2013		4 August 2010	
	(Quiet Day)		(Active Day)	
RMS Error	IGRF	T89	IGRF	T89
B_x (nT)	37.2	33.2	113.5	102.5
B_y (nT)	41.2	38.8	18.3	18.9
B_z (nT)	34.1	11.0	41.3	15.1
B_{tot} (nT)	80.6	74.8	153.3	141.1
Angle (deg)	0.1645	0.1545	0.1680	0.1406

Figure 5.8 illustrates the differences between the models and observations as well as between the models for SWARM A satellite during the magnetically quiet day (January 18, 2014) and active day (February 20, 2014) respectively. The panels from top to bottom are the same as in the previous figures. The magnetic field components from the satellite magnetometer and from the T89 and IGRF models are again orbit averaged using the running mean procedure. The top, right panel on the left ensures that the day is quiet with K_p varying between 0 and 1. The differences between the models and the observations are seen to be less than ± 10 nT in panels b and c. The close examination of the panels shows that the T89 model predicts B_y component as the best in this case; this is followed by the prediction of the B_z component. On average, both of them are close to zero which means that they are equal to observed B_y and B_z . T89 predicts the B_x component as the largest which means B_x deviates the most from the observed B_x component. IGRF model, on the other hand, predicts the B_z component the least by giving the largest deviation from the observed B_z component. It is about -25 nT which means that the observed B_z component is larger than the IGRF predicted B_z . The best-predicted component by IGRF is also B_y component being close to zero on the average. The difference for B_x is about 13 nT on average as well. These differences are small. Panel d in Figure 5.8 compares the model outputs for this case by taking the difference between IGRF and T89 models respectively. It is seen that the B_z component differs the most between the two models. Model differences between B_x and B_y components vary between ± 20 nT and close to zero on the average.

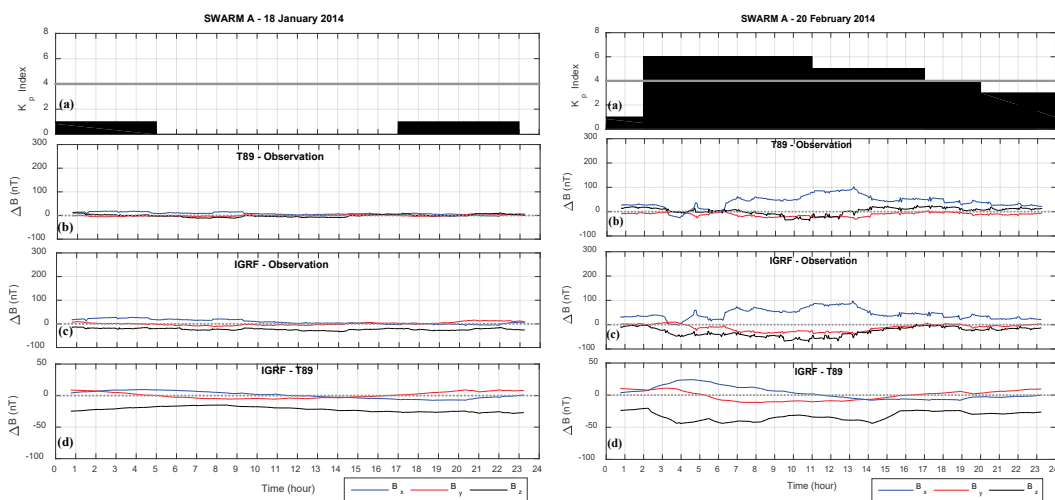


Figure 5.8 : Differences between the observations and the model result for magnetic field components from SWARM A satellite on January 18, 2014, when there is no geomagnetic activity (left); and on February 20, 2014, when there is a geomagnetic storm (right).

The second and third panels on the right of Figure 5.8 demonstrate the differences between the model and the SWARM data during the geomagnetically active day. Contrary to the panels on the left, magnetic field vectors from IGRF and T89 in these panels are seen to vary up to 100 nT during the geomagnetically active day. The first panel indicates the presence of moderate geomagnetic activity with a K_p maximum at 6 almost throughout the day. We can see that the differences with the observations in both models are large corresponding to the increased K_p . Examining the T89 panel shows that B_x has a maximum difference of about 100 nT while B_y and B_z differences are closer to zero. T89 model predicts B_y and B_z components the best. IGRF model, on the other hand, has larger differences compared to the T89 model in all components. B_x varies up to 100 nT at the maximum, and B_y and B_z vary up to 25 nT and 50 nT respectively. We can see this also in panel d where the differences between the two models are shown component to component. Both models differ the most in B_z , B_x , and then B_y starting at the time of the magnetic activity at about 02:00 UT.

Figure 5.9 gives the angle between the model and observed magnetic fields during the quiet (left) and magnetically active (right) day respectively. The first two panels on the left indicate the absence of a geomagnetic storm ($D_{st} > -40$ nT) and magnetospheric substorms ($AE > 100$) while the panels on the right indicate a very strong magnetospheric substorm ($AE > 100$ nT) and a strong geomagnetic storm with $D_{st} < -40$. Comparing the angles between the magnetic field vectors between the observations and the models shows that the differences are small. The differences are about 0.05° during the quiet day while it is maximum at 0.24° and 0.2° in the case of geomagnetically active day for IGRF and T89 models respectively. The magnetic field vector predicted by the T89 model is closer to the observed magnetic field vector while IGRF predicts slightly larger angles. The difference in angles is larger corresponding to the increased activity period from 02:00UT to 11:00 UT when K_p is equal to 6 for 9 hours.

In Table 5.6, RMS errors are presented for both quiet day and active day for SWARM events. As in the previous comparisons, when we examine the magnetic field components, it is seen that the smaller RMS errors are obtained during the quiet days as compared to the active days from both models. IGRF RMS errors increase almost twice during the active times. When the models are compared to each other during quiet and active days, the T89 model gives smaller errors during active times in general

for all components while during the quiet times, its RMS error is larger for B_x and B_{tot} but smaller for B_y and B_z compared to that of IGRF. When we look at the average angle, we see that the angles during the active times are much larger than those of quiet times for both model predictions. Between the models, the IGRF model gives larger angles for both quiet (35%) and active (3%) days than the T89 model. Also, both models predict larger angles during the active times by about 60-70% than those of quiet times.

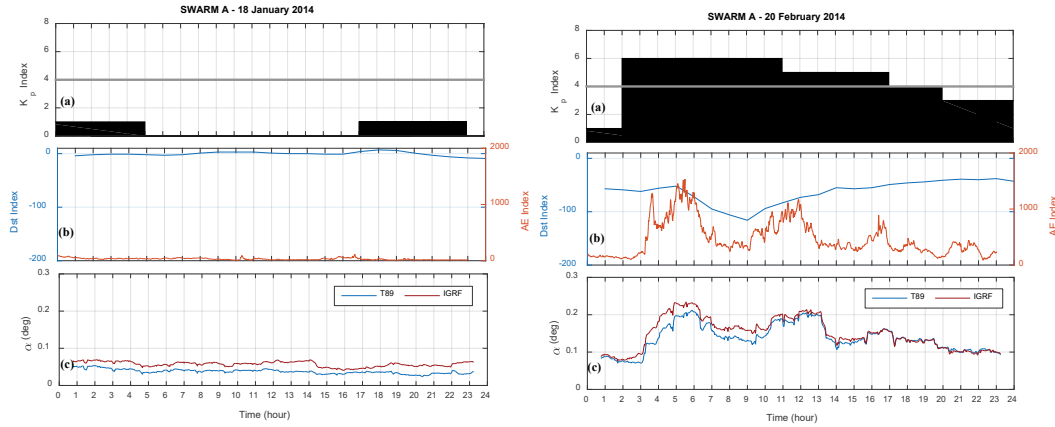


Figure 5.9 : Angles, between the vector magnetic fields from the models and the observations, for SWARM A satellite on January 18, 2014, when there is no geomagnetic activity (left); and on February 20, 2014, when there is a geomagnetic storm (right).

Table 5.6 : RMS errors for SWARM A (Case-3) comparisons for the geomagnetically quiet day (left) and active day (right).

SWARM A	18 January 2014		20 February 2014	
	(Quiet Day)		(Active Day)	
RMS Error	IGRF	T89	IGRF	T89
B_x (nT)	25.8	27.3	44.2	45.2
B_y (nT)	7.1	5.7	15.0	1.4
B_z (nT)	18.6	4.7	12.1	8.1
B_{tot} (nT)	9.1	11.4	22.5	15.0
Angle (deg)	0.058	0.038	0.1376	0.1342

Figure 5.10 is produced to present a statistical result on the angles predicted by the models based on these three geomagnetically active (blue) and quiet days (orange). The upper panel in the figure illustrates the bar plot of the angles between the magnetic field vector observed by both spacecraft and their corresponding IGRF magnetic field vectors while the lower panel gives the same for the T89 model. We notice from the figure, for both quiet and active days, the angles are less than 0.3° which seems to be the threshold for these spacecraft for the events studied. Comparing both panels shows that angles predicted by T89 are smaller than 0.175° during both quiet and active days and there are fewer cases for angles larger than 0.15° during the active times when compared to the IGRF model. The distribution of the active time average angles for the T89 model is skewed towards the lower angles than 0.15° while that for the IGRF model has a skew towards larger angles than 0.15° . On the lower end side, the angles from the IGRF model have more cases larger than 0.05° during the quiet days compared to T89 which presents more cases with angles less than 0.05° at these times. Overall the average angle for all cases for the IGRF model is 0.126° during the quiet days while it is 0.170° during active days. The average angles for the T89 model are seen to be 0.114° for the quiet days and 0.136° for the active days.

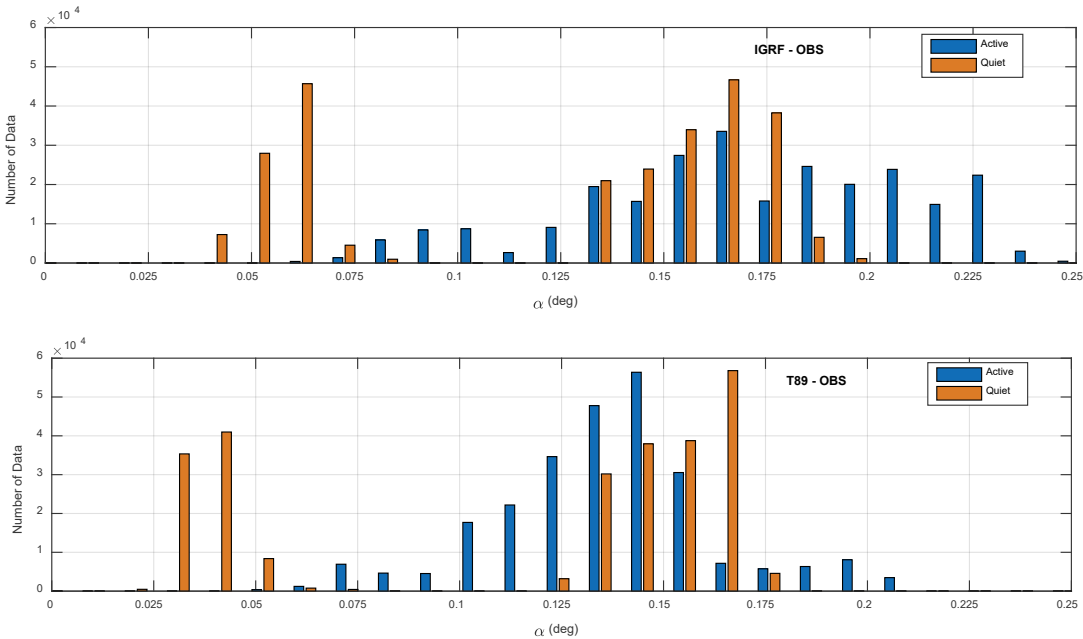


Figure 5.10 : Angle distributions for all cases for quiet (orange) and active (blue) cases. The upper panel is for the differences between the IGRF model and observations while the bottom panels are for the differences between the T89 model and observations.

Figure 5.11 compares the differences in angles from two models during the active (blue) and quiet (orange) times by subtracting T89 angles from IGRF angles. The vertical axis is normalized to the total number of data in each case. Several points that the figure shows are: First, the zero-degree angles indicate that the magnetic field vectors from both models are the same. Secondly, most of the differences are positive indicating that IGRF angles are larger than those of T89. Third, the negative angles, which are not the majority, show that T89 model angles are larger than those of IGRF. Considering these facts, this figure's highlights are below:

- During both the active and quiet days, most of the angles are positive indicating that IGRF gives larger angles than the T89 model does. In these cases, T89's magnetic field vectors are closer to the observed magnetic field.
- The differences between angles from the two models are larger during the active times than during the quiet times. Larger positive angles during active times show that IGRF differs the most from T89 during the active days than quiet days.
- Most of the time the angle between the magnetic field vectors of the models during both quiet and active times is smaller than 0.12° . The maximum is 0.033 for the quiet day and 0.011° for the active day. Most of the time, the angles can be different by about 0.01° and 0.018° for the quiet days and can often vary as 0.01° , 0.02° , 0.041° , 0.081° and 0.15° during the active days.
- The average angle difference for the cases when IGRF angles are larger than T89 angles is 0.0128° for the quiet days and it is 0.0370° for the active days.
- The average angle difference for the cases when T89 angles are larger than IGRF angles is 0.0026° for the quiet days and it is 0.023° for the active days.
- Table 5.7 gives a summary of the average angles from the models compared.

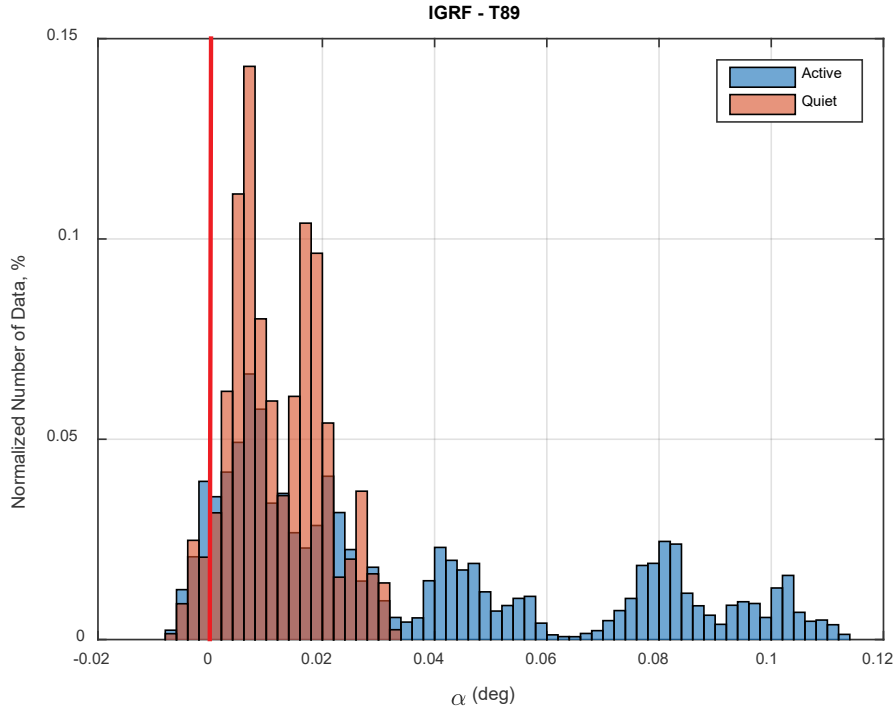


Figure 5.11 : Comparison of the difference in angles from the models: Blue is for active day and orange for quiet days.

Table 5.7 : Overall evaluation of average angles.

Case No	Satellite	Quiet Day average (degree)		Active Day average (degree)	
		IGRF	T89	IGRF	T89
Case-1	C/NOFS	0.156	0.150	0.197	0.134
Case-2	C/NOFS	0.165	0.155	0.168	0.141
Case-3	SWARM A	0.058	0.038	0.138	0.134

5.5 Discussion and Summary

One of the main motivations in our paper is to determine the effects of the geomagnetic disturbances on the satellite’s attitude at LEO orbits. This is related to the accuracy of the geomagnetic field predictions by the geomagnetic field models at the satellite’s position. The most commonly used geomagnetic model in determining the satellite’s attitude at LEO orbit is the IGRF model [50,146]. The accuracy of the IGRF-10 and

IGRF-11 models are tested against data from UARS, Oersted, and CHAMP spacecraft and found that the models are accurate within 1° for 92% times in the upper atmosphere [64]. However, the authors of this study cautioned that the variations in the magnetic field occur as a result of the geomagnetic storms and IGRF may not always be appropriate to model the magnetic field at LEO. Similarly, [51] used IGRF to calibrate the magnetometers on CINEMA CubeSat and found root mean squared deviations in field magnitudes from IGRF of 1.95% for the attitude mode. Such accuracy in the overall magnetic fields is found to be sufficient for attitude estimation [147]. Even though the IGRF model is found to be sufficient to represent the magnetic field required for the satellite attitude, concerns are raised in relation to the solar activity and geomagnetic activity [51,64].

In our study, we compare two geomagnetic field models, IGRF-12 and T89, to compare both with the magnetic field predictions at LEO orbit using two spacecraft magnetometer data. We found that both models differ from the observations during the geomagnetically active times as well as during the quiet times. The differences are larger in the case of the IGRF-12 model compared to the T89 models. Differences vary according to the magnetic field components. The comparisons with the data from two satellites, C/NOFS and SWARM, indicate that the largest differences are seen in B_x and B_y while the smallest differences are found in the B_z component. The differences between the observed magnetic field vector and that predicted by the model are obtained larger during the high geomagnetic periods. The angle between the vector magnetic field from the satellite measurements and models is shown to be smaller in the case of the T89 model, indicating that T89 model estimates are closer to the data. The differences in magnetic field components and the vector magnetic fields are found to be larger in the case of the IGRF model during both geomagnetically quiet and active times. T89 model is expected to agree better with the observations, especially during the geomagnetically active times, because it is constructed such that the model includes variations resulting from both internal sources from the Earth's dynamo and crust and also external sources such as solar wind, interplanetary magnetic field, consequently geomagnetic storms and substorms. The fact that IGRF shows larger discrepancies indicates that for better attitude predictions during especially geomagnetically active times, external sources are needed to be taken into account.

To summarize, in this study, we compared magnetic field measurements from magnetometers onboard two different satellites at LEO orbit with those from IGRF-12 and T89 models to address the noise referred to as the angle in our study that will eventually be used to determine the satellite attitude. A follow-up study is underway on how much these differences affect the attitude angles described as Euler angles. We highlight our results represented here as below:

- In general, both models show differences with the observed magnetic fields during the geomagnetically active times as well as quiet times.
- IGRF model gives larger differences compared to T89 during both quiet times as well as active times. Differences during active times are the largest.
- During the geomagnetically active time, the T89 model gives closer estimations to the observations.
- The largest differences are seen in B_x in general and the smallest in B_z .
- The differences in the strength of the magnetic field are much smaller than those of magnetic field components.
- Differences between the models are seen as the largest in B_z and smaller in B_x and B_y .
- Large differences in the angle and in the magnetic field components correspond to a large geomagnetic activity index, K_p .
- The angle between the vector magnetic field from the models and the data is obtained less than 1° for C/NOFS and SWARM data. The differences between the satellites stem from the properties of the instruments used onboard these satellites.

These differences imply that the model estimates the magnetic field orientations at the satellite location satisfactorily so that the angle between the vector magnetic fields is small. From the satellite attitude view, this agreement is very important. Also, the RMS errors for the field components are found to be small. Although both models are seen to be appropriate for calculating the magnetic fields at the satellite position at LEO, it is clear that the IGRF model gives larger differences compared to the T89 model during both quiet and active times. The difference in the angle between the model and the observed magnetic field directions which is calculated less than 1° is within the acceptable range and both models can be used for attitude predictions within

their error ranges. Both models have their advantages and disadvantages to be used in the attitude estimations. Since the differences are small, the attitude system controllers may continue to use IGRF instead of T89 to avoid its continuous need to acquire the magnetic index data such as Kp, AE, and Dst on board the satellite. This will depend on their preference. Here we demonstrated that an alternative model, physically improved, can be used during especially geomagnetically active times, for more accurate attitude estimations. Results of this study are especially important where high accuracy is needed for attitude control at LEO and where we need to decide which geomagnetic model to use to achieve a better attitude. To our knowledge, this is the first paper that studied the effects of the environment on the satellite attitude and it should be pursued with more statistical analysis with different types of satellite orbits at different altitudes, within different near-Earth space environment conditions, not just LEO but also where the magnetometers are used for detection of the satellite attitudes.

6. GEOMAGNETIC DISTURBANCE EFFECTS ON SATELLITE ATTITUDE ESTIMATION*

6.1 Abstract

This chapter investigates the effects of magnetic disturbances resulting from geospace storms on the satellite attitudes estimated by EKF. It is shown that the increasing levels of geomagnetic activity affect geomagnetic field vectors predicted by IGRF and T89 models. Various sensor combinations including magnetometer, gyroscope, and sun sensor are evaluated for magnetically quiet and active conditions. Errors are calculated for estimated attitude angles and differences are discussed. This study emphasizes the importance of environmental factors on the satellite attitude determination systems.

6.2 Introduction

The orientation of the geomagnetic field is one of the most critical data in the determination and control of the satellite's attitude especially at the low Earth orbits (LEOs) [36–39]. More accurate measurements of the geomagnetic field lead to more accurate predictions of the satellite attitude. The geomagnetic field may be obtained from: 1. In-situ measurements of an on-board spacecraft magnetometer, 2. empirical models of the geomagnetic field that utilize a large amount of spacecraft data, and 3. the simulated magnetometer. Simulated magnetometers are constructed on the ground before the satellite launch to reproduce the satellite magnetometer measurements of real space. In other words, a simulated magnetometer is an object simulated by software for obtaining the geomagnetic field used to estimate the satellite's attitude. In order to design a simulated magnetometer, a geomagnetic field model, the statistical characteristics of the magnetic field measurements in space and characteristics of on-

* This chapter is based on the paper “Cilden-Guler, D., Kaymaz, Z., and Hajiyev, C. (2021). Geomagnetic Disturbance Effects on Satellite Attitude Estimation, *Acta Astronautica*, **180**, 701712, doi: 10.1016/j.actaastro.2020.12.044”.

board satellite magnetometers are needed. The most commonly used geomagnetic field model to predict the Earth's magnetic field at the satellite location is the International Geomagnetic Reference Field (IGRF) model [6,40]. However, the angle between the magnetic field vector from the IGRF model and the magnetic field vector from the simulated magnetometer affects the accuracy of the attitude angles, namely roll, yaw, and pitch. When transformed the vectors into the same coordinates, the smaller this angle is the more precisely the attitude angles are determined. Therefore, the choice of geomagnetic field model used in the simulated magnetometer is very important in achieving high accuracy in attitude angles.

The main source of the geomagnetic field is the Earth's dynamo in its core that produces dipolar magnetic fields in the near-Earth space environment [41–43]. However, solar activities such as solar wind, coronal mass ejections (CMEs), high-speed streams (HSS), interplanetary shocks (IS), and their magnetospheric consequences geomagnetic storms and magnetospheric substorms produce disturbances superimposed on the dipole field of the Earth different strengths [44]. Charged particles from the geomagnetic tail flow into the upper atmosphere and drive electrical currents at the LEO altitudes which in turn modify the geomagnetic field at those altitudes [45–47]. We will refer to the variations caused by these or external sources as magnetic disturbances or magnetic anomalies. While on-board spacecraft magnetometer measurements inherently include these deviations from the dipole field, they need to be represented in the simulated magnetometer or within the geomagnetic field models for accurate predictions of the near-Earth magnetic fields.

In reality, neither the geomagnetic field models of the Earth nor the magnetometers are accurate. They both have various error sources resulting from several factors. The simulated magnetometers include bias and noise errors. While in many studies, magnetic disturbances in the space environment are treated as bias, in several others, they are accepted as noise [50,51]. However, in these studies, it should be remembered that the magnitude of the geomagnetic field deviations due to the magnetospheric storms can be obscured by the sensor-related noise used in the simulated magnetometers [52]. In order to estimate the magnetic moment of the satellite accurately, magnetometer bias resulting from other electrical devices on the satellite should be estimated and removed precisely. Therefore, online and offline magnetometer calibration methods for time-variable errors arising from both

magnetometer bias and the magnetic anomaly are introduced in [53] for two nanosatellites that need geomagnetic field data as accurate as possible for their mission requirements. In [53] and its extended version [54], the authors treated the magnetic anomaly as bias in the simulated magnetometer to improve the attitude estimation. In addition to the bias associated with the magnetic anomaly, they also added an additional magnetometer bias to build their simulated magnetometer. Both the magnetic anomaly bias and the magnetometer bias are used as the state vector elements within the simulated magnetometer. But, here we should also note that the magnetic anomalies in the space environment are not the errors resulting from the magnetometer itself, but they are the magnetic deviations overlapped on the geomagnetic field resulting from the magnetic storms and magnetospheric substorms. In other words, they have a physical cause and their properties vary depending on the properties of the source and they cannot be predicted using linear models. Therefore, treating them as bias or noise error does not correctly take into account their true nature and their contribution to the measurements of the simulated magnetometer. The studies in [53,54] treated the magnetic anomalies as a Gauss-Markov statistical process. Gauss-Markov model is a model frequently used to represent the sensor biases or disturbances [55–57]. However, it only depends on time and thus, it may be an inadequate representation of magnetic anomaly events which are linked to the geomagnetic storm and magnetospheric substorms, since these storms and substorms are not only time-dependent but also their effects vary depending on the magnetic latitude, the height in the atmosphere, and the strength of the magnetospheric activity, i.e. magnetotail dynamics, but eventually on the solar activity [58–61]. While auroral substorms occur more frequently and affect high latitudes, variations in the ring current strength, or the motion of the magnetopause boundary affect the magnetic structure of the Earth at the equatorial latitudes [26 and references therein]. In addition, the magnetic anomalies associated with the magnetic storms increase during the high solar activity periods and decrease as the solar activity ceases. These indicate that it would be incorrect to consider them as noise. In [63], the authors stated that the magnetic anomalies should be modeled separately to avoid tuning problems but they stated that the external disturbances hard to model because of their complex ambient nature.

Early models of the Earth's magnetic field represent only the dipole geomagnetic fields resulting from the Earth's internal dynamo. The effects of magnetic disturbances are

not included in these early models. As the satellite observations of the geospace environment increase, these models, consequently modeling the LEO environment, are improved such that the physics of the magnetic environment are incorporated in the models. The IGRF model is one of these early models of the geomagnetic field used for attitude determination at LEO altitudes. The accuracy of the IGRF models is investigated in several studies and is usually found satisfactory in predicting the satellite attitude [50,51,64].

First studies that take into account the effects of magnetic anomalies from the spacecraft attitude perspective are presented in [65–67]. These studies used IGRF and T89 models to evaluate the geomagnetic field at LEO altitudes during geomagnetically active days. T89 model developed by Tsyganenko in 1989 is an empirical geomagnetic field model [68,69] that is derived using a large amount of magnetic field data from 11 Earth-orbiting spacecraft measurements at various distances from LEO to 30 Earth Radii behind the Earth and thus covering vast magnetospheric regions including plasmasphere, the plasma sheet, radiation belts, neutral sheet, near-Earth magnetospheric tail, and the magnetospheric boundary [70]. In contrast to the IGRF model, the T89 model includes contributions from external magnetospheric sources such as ring current, magnetotail current system, magnetopause currents, and large-scale system of field-aligned currents. The model employs several physical conditions such as dipole tilt angle effects, neutral sheet curvature, and more or less realistic magnetopause boundary as well as the effects from the magnetospheric activity. In [65–67], the predicted and observed magnetic fields, and angles between magnetic field vectors from IGRF and T89 are analyzed for three selected geomagnetic storm events and compared the variations with those obtained during the quiet day. They showed that the T89 model gives closer magnetic field predictions to the observations, and the errors are smaller compared to those from the IGRF model. This further implies that the attitude angles will be estimated in a higher sensitivity if the T89 model is used. It is of primary interest here to investigate the effects of geomagnetic disturbances on the satellite attitude angles (roll, pitch, and yaw) using these models and quantify the effects. For this purpose, first, we demonstrate how the angle between the magnetic field vectors predicted by the models varies with the increasing levels of geomagnetic activity. Then, we show that how these geomagnetic activity effects are propagated onto the satellite attitude angles.

Our second purpose in this study is to explore the effect of the presence of one or more attitude sensors onboard the satellite in addition to the magnetometer. The sun sensors and gyroscopes are considered for this purpose. The mathematical models of these sensors can be implemented into the attitude estimation methods using e.g. Kalman-type filters. As the satellite's dynamical model and the simulated magnetometers are nonlinear, the extended Kalman filter (EKF) or its extensions can be used for obtaining the attitude angles [90]. Among the several types of Kalman filters are Linear Kalman Filter, EKF, Unscented Kalman Filter (UKF). In Kalman filters, generally, all three of the attitude sensors, namely sun sensor, magnetometer, and gyroscope, are employed together to increase the accuracy in the attitude estimation [21,25,90,146,148]. However, the magnetometers can be used alone to estimate a satellite's attitude in the absence of one or both of the other sensors. In this part, we utilize the various combinations of these sensors with EKF to compare the efficiency of the different sensor configurations under the low/high geomagnetic activity conditions. The configurations performed are magnetometer alone, magnetometer and gyroscope, magnetometer and sun sensor, and all sensor-configuration, i.e. magnetometer, sun sensor, and gyroscope. While model predictions of the geomagnetic field are needed for all configurations, it is clear that it will be more important for the success of the EKF procedure that uses magnetometer sensor configuration only.

The organization of the paper is as follows: Section 6.3 presents the satellite kinematic and dynamic equations while Section 6.4 describes the models, magnetic field, and the sun direction vectors used for satellite attitude estimation, respectively. This is followed by the attitude estimation method based on the traditional approach in Section 6.5. Section 6.6 shows how geomagnetic field models differ with the increasing level of geomagnetic activity. The analysis of the effects of the geomagnetic disturbances on the accuracy of the spacecraft attitude angles is presented in Section 6.7. Section 6.7 provides the results for four different sensor configurations. Finally, Section 6.8 concludes our chapter.

6.3 Satellite Equations of Motion

The orbit of the satellite is propagated in time using the SGP4 model [121]. The satellite position data are used in Earth-Centered, Earth-Fixed (ECEF) using

Geographic Coordinates (GEO). The angular motion of the satellite is defined in the Earth-Centered Inertial (ECI) system.

For the satellite rotational motion, the equation of kinematics is represented in terms of Euler angles of yaw, pitch roll as,

$$\begin{bmatrix} \dot{\psi} \\ \dot{\theta} \\ \dot{\phi} \end{bmatrix} = \begin{bmatrix} 0 & \sin(\phi)/\cos(\theta) & \cos(\phi)/\cos(\theta) \\ 0 & \cos(\phi) & -\sin(\phi) \\ 1 & \sin(\phi)\tan(\theta) & \cos(\phi)\tan(\theta) \end{bmatrix} \begin{bmatrix} p \\ q \\ r \end{bmatrix}, \quad (6.1)$$

where p , q , r are the components of the $\boldsymbol{\omega}_{BR}$ vector in the body frame with respect to the reference (orbit) frame. The angular velocities ($\boldsymbol{\omega}_{BI}$) in the body axis can be expressed with respect to the inertial coordinate system as

$$\boldsymbol{\omega}_{BI} = [\omega_x \quad \omega_y \quad \omega_z]^T, \quad (6.2)$$

and the angular velocities ($\boldsymbol{\omega}_{BI}, \boldsymbol{\omega}_{BR}$) have the relationship as,

$$\boldsymbol{\omega}_{BR} = \boldsymbol{\omega}_{BI} - \mathbf{A}[0 \quad -\omega_o \quad 0]^T, \quad (6.3)$$

where ω_o orbital angular velocity, computed as

$$\omega_o = (\mu / r_o^3)^{1/2}, \quad (6.4)$$

using μ -gravitational constant, r_o - the distance between the satellite and Earth's centers. ω_o is constant for circular/near-circular orbits. \mathbf{A} represents the transformation matrix from orbit to body frame in terms of (3-2-1) Euler angles sequence [1] as,

$$\mathbf{A} = \begin{bmatrix} \cos(\theta)\cos(\psi) & \cos(\theta)\sin(\psi) & -\sin(\theta) \\ -\cos(\phi)\sin(\psi) + \sin(\phi)\sin(\theta)\cos(\psi) & \cos(\phi)\cos(\psi) + \sin(\phi)\sin(\theta)\sin(\psi) & \sin(\phi)\cos(\theta) \\ \sin(\phi)\sin(\psi) + \cos(\phi)\sin(\theta)\cos(\psi) & -\sin(\phi)\cos(\psi) + \cos(\phi)\sin(\theta)\sin(\psi) & \cos(\phi)\cos(\theta) \end{bmatrix}. \quad (6.5)$$

Dynamic equations are also obtained by the principle of conservation of angular momentum.

$$J_x \frac{d\omega_x}{dt} = N_x + (J_y - J_z)\omega_y\omega_z, \quad (6.6a)$$

$$J_y \frac{d\omega_y}{dt} = N_y + (J_z - J_x) \omega_z \omega_x, \quad (6.6b)$$

$$J_z \frac{d\omega_z}{dt} = N_z + (J_x - J_y) \omega_x \omega_y, \quad (6.6c)$$

where J_x , J_y and J_z inertial moment elements, N_x , N_y and N_z are the external disturbances affecting the satellite.

6.4 Components of Satellite Attitude Determination System

6.4.1 Geomagnetic field models

Among the several geomagnetic field models currently available in the literature, T89 and IGRF models are used to evaluate the attitude angles in this study. A brief introduction to the properties of these models is given below.

6.4.1.1 International geomagnetic reference field model

The history of the IGRF model goes back to the 1900s. The model is revised every five years and released by the international association of geomagnetism and aeronomy (IAGA). The 13th version of IGRF was released in 2020. IGRF only considers the internal dynamo currents that produce the Earth's magnetic field [6]. It is based on the dipole approximation of the Earth's magnetic field with the coefficients determined from the spacecraft magnetic field data using spherical expansion analysis with the coefficients determined from the spacecraft magnetic field measurements. The model includes series of spherical harmonics at N=13th degree that are updated every 5 years. Equation (6.7) gives the expansion with the coefficients. The inputs (r, θ, ϕ, t) are the radial distance (km) from the center of the Earth, co-latitude (deg), longitude (deg) of the satellite position at the specific time (t). In the equation, the global variables (g and h) are Gauss coefficients while P denotes the Legendre function.

$$\mathbf{B}_{INT}(r, \theta, \phi, t) = -\nabla \left\{ a \sum_{n=1}^N \sum_{m=0}^n \left(\frac{a}{r} \right)^{n+1} [g_n^m(t) \cos(m\phi) + h_n^m(t) \sin(m\phi)] \times P_n^m(\cos \theta) \right\}. \quad (6.7)$$

Here, \mathbf{B}_{INT} is the magnetic field in the units of nanoTesla (nT). The major axis of the Earth is accepted as 6378.137 km in the model. In this study, the output magnetic field vector from the geomagnetic field model is shown as \mathbf{B}_{model} and it is given in magnetic

(MAG) coordinates. In MAG coordinate system, the z-axis aligns with the dipole axis and the y-axis is perpendicular to the plane containing the dipole axis and the rotation axis of the Earth. The x-axis completes the right-handed system. More information about the coordinate systems may be found in [133].

6.4.1.2 Tsyganenko's model

The variations in the space environment result from solar and magnetospheric activity. The magnetosphere is highly dynamic especially during strong solar disturbances. The currents from the geomagnetic tail during the geomagnetic storms and magnetospheric substorms produce variations in the geomagnetic fields at the LEO altitudes which are superimposed on the main geomagnetic field generated by the dynamo within the Earth's core. Consequently, it is expected that these external effects will affect the spacecrafts' attitude angles since they are determined by using the predictions of the geomagnetic field at the satellite altitudes. Therefore, it is anticipated that the inclusion of external effects in the predictions of geomagnetic fields will improve the accuracy of the attitude predictions. For this purpose, in this study, a second model, Tsyganenko 1989 model (T89) is used to predict the geomagnetic fields at the LEO orbit. Developed by Tsyganenko [68], the T89 model is an empirical model based on large satellite data ranging from LEO altitudes to a distance of approximately 30 Earth radii. An analysis in the Van Allen belts is also possible when considering the satellites' altitudes used in the data sets [70]. The number of spacecraft data decreases with distance in the magnetosphere, but the available spacecraft data cover the most significant dynamic part of the magnetospheric regions on the dayside and night side, i.e. magnetotail. In the model, the total magnetic field is obtained by the sum of both internal (\mathbf{B}_{INT}) and external (\mathbf{B}_{EXT}) magnetic fields. Equation (6.8) gives the total magnetic field disturbance (\mathbf{B}_{EXT}) produced by the external sources only. While the main (internal) field (\mathbf{B}_{INT}) is obtained from IGRF as given in Equation (6.7), the magnetic field disturbance (\mathbf{B}_{EXT}) is obtained from T89. In this equation, \mathbf{B}_{EXT} includes effects from magnetospheric ring current (\mathbf{B}_{ring}), tail current (\mathbf{B}_{tail}), magnetopause currents (\mathbf{B}_{mp}), and field-aligned currents (\mathbf{B}_{FC}) (please see [68,127,149–152] for more details).

$$\mathbf{B}_{EXT} = \mathbf{B}_{ring} + \mathbf{B}_{tail} + \mathbf{B}_{mp} + \mathbf{B}_{FC}. \quad (6.8)$$

Since the external magnetic field (\mathbf{B}_{EXT}) is superimposed on the main geomagnetic field, T89 returns the total geomagnetic field as $\mathbf{B}_{model} = \mathbf{B}_{INT} + \mathbf{B}_{EXT}$ at the specified location. Therefore, the T89 model is considered as an improved model over IGRF for predicting geomagnetic fields at LEO.

In the T89 model, satellite data sets are categorized according to the geomagnetic activity index called K_p . K_p (planetary K-index) is an indicator of disturbances in the Earth's magnetic field and is used to characterize geomagnetic storms' magnitudes [153,154]. Thus, from the modeling point of view, it gives a measure of the strength of the external source. It is calculated globally using mid-latitude magnetic stations at every 3-hours and has a scale from 0 to 9 expressed in thirds of a unit with 28 values, e.g. 4- is 3 2/3, 4o is 4 and 4+ is 4 1/3 [155,156]. K_p greater than 4 indicates strong geomagnetic activity in the magnetosphere. IOPT indicates the number used in the T89 algorithm related to activity level. Even though the level of activity can rise up to $K_p = 9$, the highest K_p accepted within the T89 code is 6- because of the smaller number of satellite data for higher K_p levels larger than 6-.

Table 6.1 : K_p index and model parameter IOPT range in T89 model.

IOPT	1	2	3	4	5	6	7
K_p	0o, 0+	1-, 1o, 1+	2-, 2o, 2+	3-, 3o, 3+	4-, 4o, 4+	5-, 5o, 5+	>=6-

6.4.2 Simulated magnetometer measurements

Because the magnetometers are cheap, reliable, and lightweight, they are the most widely used sensors for the determination of the attitude angles on LEO satellites. The satellite's angular motion is determined by defining the dynamics and kinematics of the satellite. Then, the Euler angles are found for each magnetic field model representation. The magnetometer measurements of the real space environment can be simulated as:

$$\mathbf{B}_m(k) = \mathbf{A}(k)\mathbf{B}_o(k) + \mathbf{v}_B(k), \quad (6.9)$$

where $\mathbf{B}_o(k)$ is the geomagnetic field vector components in the orbital frame that are found using a geomagnetic field model, $\mathbf{B}_m(k)$ represents the simulated magnetometer measurements in the body frame, $\mathbf{v}_B(k)$ is the zero-mean Gaussian magnetometer measurement noise, and $\mathbf{A}(k)$, is the transformation matrix from orbit to body frame. In this equation, $\mathbf{B}_o(k)$ is obtained using:

$$\mathbf{B}_o(k) = \mathbf{L}(k)\mathbf{B}_{\text{model}}(k), \quad (6.10)$$

where $\mathbf{B}_{\text{model}}$ is the geomagnetic field vector obtained from a geomagnetic model, such as IGRF or T89 in our case, and $\mathbf{L}(k)$ indicates the transformation matrix from MAG coordinates (see Section 6.4.1.1) to the orbital coordinate system. The success of the simulated magnetometer depends on how accurately these terms are predicted.

6.4.3 Simulated sun sensor measurements

Another attitude sensor used to predict the satellite's attitude is the sun sensor which determines the sun direction vector whenever the sun is visible. The sun direction model can be found in [103]. The sun direction vector measurements can be expressed in the following form:

$$\mathbf{S}_m(k) = \mathbf{A}(k)\mathbf{S}_o(k) + \mathbf{v}_s(k), \quad (6.11)$$

where $\mathbf{S}_m(k)$ is the measured sun direction vector as the direction cosines in body frame, $\mathbf{S}_o(k)$ represent the sun direction vector in the orbit frame as a function of time and orbit parameters, and $\mathbf{v}_s(k)$ is the zero-mean Gaussian sun sensor measurement noise.

6.4.4 Simulated rate gyro measurements

Rate gyros are used in order to measure the angular velocity of the satellite. The measurements can be modeled as,

$$\boldsymbol{\omega}_m(k) = \boldsymbol{\omega}_{BI}(k) + \mathbf{v}_g(k), \quad (6.12)$$

where $\boldsymbol{\omega}_m(k)$ is the measured angular rates of the satellite body frame with respect to the inertial frame, and $\mathbf{v}_g(k)$ is the zero-mean Gaussian gyroscope measurement noise.

6.5 Attitude Estimation Algorithm

For the satellite attitude and rate estimation, the 6-dimensional state vector $\mathbf{x}(k+1)$ is composed of attitude angles (ψ yaw; θ pitch; ϕ roll) and angular rates (ω_x angular velocity in x-axis, ω_y angular velocity in y-axis, ω_z angular velocity in z-axis). All three attitude angles describe the deviation between the orbit and the body reference frame.

$$\mathbf{x}(k+1) = [\psi(k+1) \quad \theta(k+1) \quad \phi(k+1) \quad \omega_x(k+1) \quad \omega_y(k+1) \quad \omega_z(k+1)]^T. \quad (6.13)$$

The satellite's rotational motion can be represented using a nonlinear mathematical model about its mass center driven by Gaussian white noise with white noise-corrupted measurements defined by,

$$\mathbf{x}(k+1) = \mathbf{f}[\mathbf{x}(k), k] + \mathbf{w}(k), \quad (6.14)$$

$$\mathbf{z}(k) = \mathbf{h}[\mathbf{x}(k), k] + \mathbf{v}(k), \quad (6.15)$$

where $\mathbf{z}(k)$ is the measurement vector at time k , $\mathbf{w}(k)$ is the system noise, $\mathbf{v}(k)$ is the measurement noise, $\mathbf{f}[\mathbf{x}(k), k]$ is the nonlinear state transition function mapping the previous state to the current state, $\mathbf{h}[\mathbf{x}(k), k]$ is a nonlinear measurement model mapping the current state to measurements. It is assumed that both noise vectors $\mathbf{v}(k)$ and $\mathbf{w}(k)$ are linearly additive Gaussian, temporally uncorrelated with zero mean with the corresponding covariance matrices \mathbf{Q} and \mathbf{R} respectively. It is assumed that process and measurement noises are uncorrelated.

We consider a real-time linear Taylor approximation of the system function at the previous state estimate and that of the observation function at the corresponding predicted position. The EKF algorithm is used for this purpose [14,35]. The EKF is applied using different sensor configurations on the LEO satellite in order to evaluate

the magnetic anomaly effects on the attitude estimation system. The scheme of the traditional EKF used in this study is presented in Figure 6.1. The magnetometer is the base sensor as it is used in all of the sensor configurations considered in this study. Four different sensor configuration scenarios are implemented within the algorithm: 1. magnetometer only, 2. magnetometer and gyroscope, 3. magnetometer and sun sensor, 4. all sensors (magnetometer, sun sensor, and gyroscope). In the traditional approach (see Figure 6.1), measurement models are based on nonlinear models of reference directions. Therefore, there is a nonlinear relation between the measurements and the states.

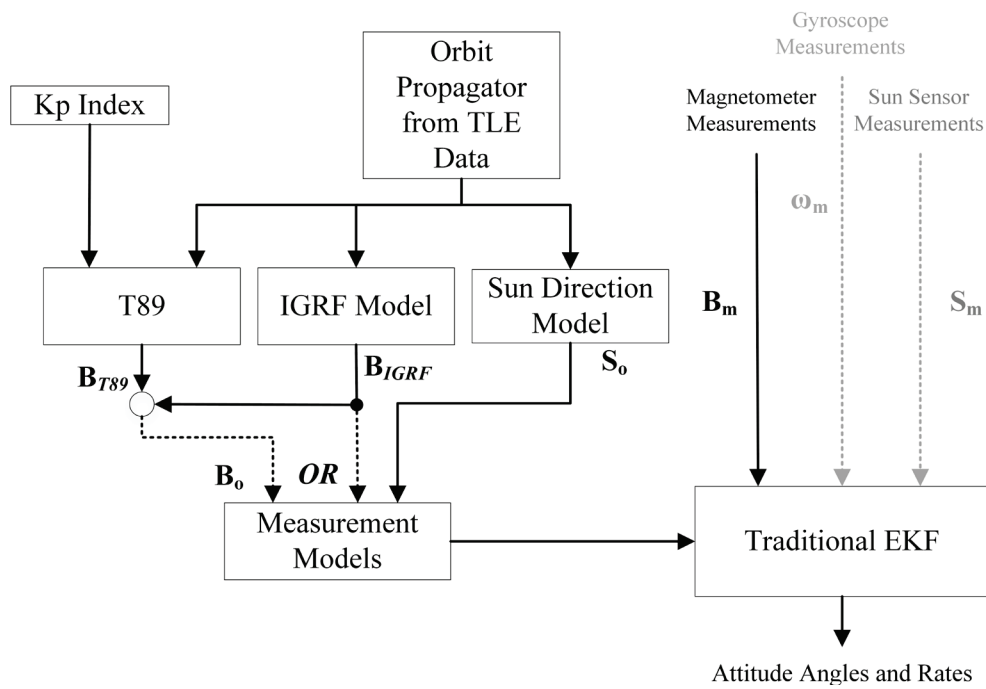


Figure 6.1 : Attitude estimation scheme using different magnetic field models and different sensors.

\mathbf{B}_{T89} and \mathbf{B}_{IGRF} represent magnetic field models, T89 and IGRF, respectively. \mathbf{B}_o and \mathbf{S}_o are the outputs from the geomagnetic field model and sun direction model, both in the orbital frame. Also \mathbf{B}_m , \mathbf{S}_m , and $\boldsymbol{\omega}_m$ are the magnetometer, sun sensor, and gyroscope measurements in the body frame. IGRF uses the position of the satellite, and orbital parameters to find the magnetic field vector in the orbital frame. Inputs for the T89 model are the K_p index, position of the satellite, and outputs from the IGRF model for the background geomagnetic field. In this algorithm, after the orbit propagation from TLE data, the position of the satellite for selected time interval and

sampling time are obtained in spherical coordinates and transformed into Cartesian (ECEF).

The four scenarios that use magnetic field predictions from both T89 and IGRF are adopted in the traditional EKF in the order given above. As magnetometers, the sun sensors are the other instruments used very commonly in satellite missions, therefore, it would be interesting to see how its presence affects the accuracy of satellite attitude.

6.6 Dependence on Geomagnetic Activity

Magnetic field measurements from magnetometers on board two different satellites at LEO orbit are analyzed and compared with those from IGRF and T89 models in [65] for three cases of selected geomagnetic activity events. The study in [65] demonstrated that both models indicate differences with the onboard magnetic fields regardless of the activity level, but more so when the activity level is high. Further, it is also shown that the IGRF model gives larger differences compared to the T89 model during both quiet and active times, with larger differences with increasing activity. During the geomagnetically active day, the T89 model gave closer estimations to the onboard observations. While the main purpose of the current paper is to investigate the effects of magnetospheric activity on the satellite attitude angles estimated by EKF, we first demonstrate the dependence of the angle between the predicted magnetic fields of the models on the increasing levels of geomagnetic activity. This is accomplished by using the increasing levels of activity K_p in the T89 model and calculating the angle between the predicted magnetic field from both T89 and IGRF models. IGRF is a function of time and position but independent of activity; however, it is used here as background geomagnetic levels to detect the deviations resulting from the geomagnetic activity. The calculated angle is, then, used as input in EKF analysis to calculate the attitude angles (yaw, pitch and roll) and for four different sensor configurations.

Before demonstrating the effects of the geomagnetic activity, we present Figure 6.2 in order to give an idea on the order of the disturbance fields, i.e. \mathbf{B}_{EXT} , seen in panel e. From top to bottom, Figure 6.2 shows K_p (panel a), noise (panel b), constant bias (panel c), accumulated bias (panel d), and disturbance field (panel e) along the satellite

trajectory. In order to create this figure, we run the T89 model for the selected K_p variation seen in panel a. Since the simulated magnetometer uses the components seen in panels b, c, d, and e to simulate the geomagnetic field anomaly, it is of purpose here to illustrate how independent these components from geomagnetic activity level and how the disturbance field vary for the selected geomagnetic activity level given in panel a. Figure 6.2 indicates that naturally, the noise, constant bias, and accumulated bias are seen to vary independent of the geomagnetic activity level by their description, while disturbance field in panel e indicates variations from 0 to -8 nT for $K_p = 5$ and from 0 to ± 15 nT for $K_p = 6$ in panel a and increasing with the increased levels of K_p .

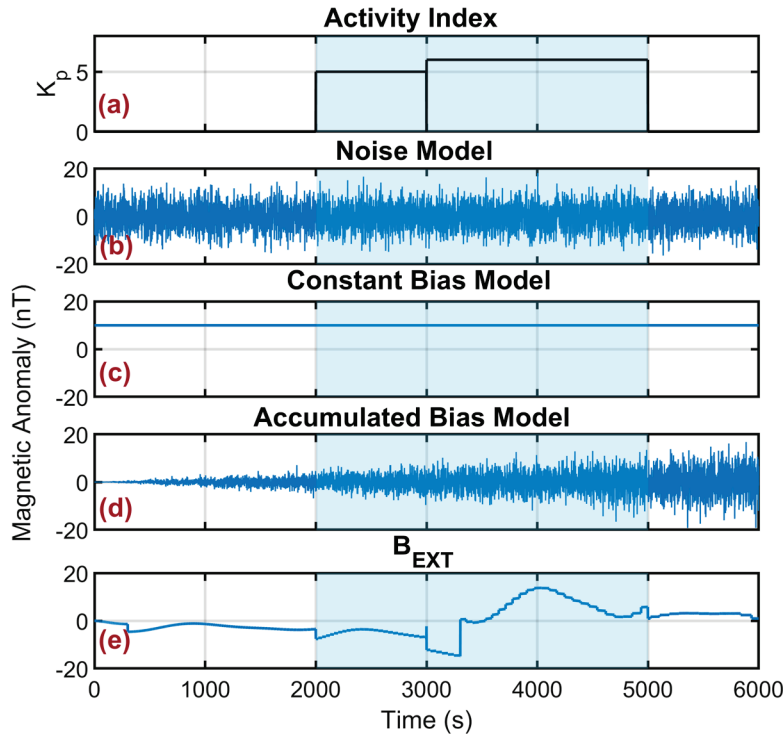


Figure 6.2 : Noise, constant bias, accumulated bias, and a sample of external magnetic field disturbance for different K_p levels.

Next, we demonstrate how the angle between the magnetic fields estimated from IGRF and T89 models. For this purpose, we consider a hypothetical nanosatellite with principal moments of inertia $\mathbf{J} = \text{diag}[2.1 \times 10^{-3} \quad 2.0 \times 10^{-3} \quad 1.9 \times 10^{-3}] \text{ kg m}^2$. The orbit is almost circular with inclination $i = 87.4^\circ$, eccentricity $e = 0.0009$, average altitude 600 km, and orbital period of approximately 6000 seconds. The satellite is tumbling with the initial state of

$\mathbf{x}_0 = [0.03 \text{ rad} \quad 0.02 \text{ rad} \quad 0.01 \text{ rad} \quad 0.001 \text{ rad/s} \quad 0.0015 \text{ rad/s} \quad 0.002 \text{ rad/s}]^T$ as described in Equation (13). For this designed orbit, the T89 model runs for each K_p level varying from 0 to 6. Since IGRF does not have a dependence on K_p , it is run only once. In Figure 6.3, the angle between the predicted magnetic fields of T89 and IGRF is plotted in a box-plot as a function of the activity level (IOPT) given in the horizontal axis. In the figure, the box gives the quartile range from 25% to 75% with a dent indicating the median. The dotted lines above and below each box identify the range of potential outliers where the maximum and minimum for each box lie. While the red solid line gives a line fit to the average in each box, the box colors only identify the different K_p levels. The figure clearly shows that with the increasing levels of geomagnetic activity, the angle between the model predictions increases. Moreover, the increased range of the outliers from the upper edge of the box indicates the increased scatter in the angle with the increased activity level. The differences in the angle can come from the activity level but also from the latitudinal variation of the moving spacecraft. Since both the IGRF model and T89 model include the same latitudinal variations in their background geomagnetic field predictions, we attribute the variations seen in this figure to the geomagnetic variations resulting from the storms and substorms in the magnetosphere at the satellite location, which otherwise expect the angle to be zero.

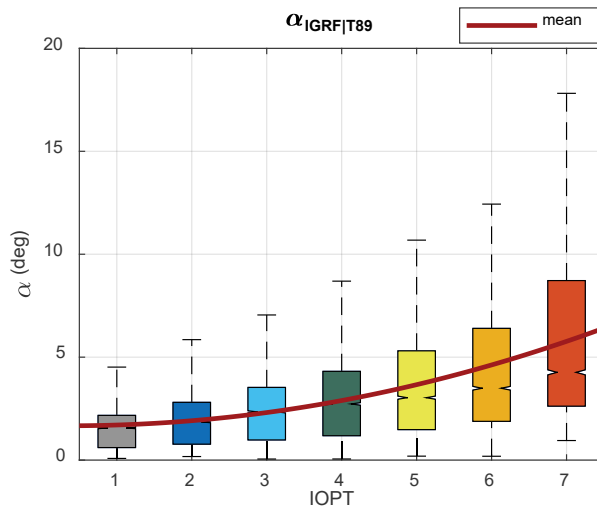


Figure 6.3 : The angle between IGRF and T89 magnetic field vectors for different K_p levels in the T89 model.

While both average and median angles show an increase with the increasing activity level, the maximum difference is found to be 18° corresponding to the highest level of activity in the T89 model. These results confirm the case studies presented in [65] in a statistical sense based on model simulations.

Next, to isolate the effects of the geomagnetic activity on the angle with respect to the satellite position, i.e. the latitude of the satellite, we split Figure 6.3 into three categories according to the latitude (λ) of the spacecraft as low latitudes ($0^\circ \leq \lambda < 30^\circ$), mid-latitudes ($30^\circ \leq \lambda < 50^\circ$), and high latitudes ($\lambda \geq 50^\circ$). The result is given in Figure 6.4 where panels a, b, c are for low, mid-, and high latitudes. As in Figure 6.3, the horizontal axis represents the activity level (K_p). Figure 6.4 illustrates that as the activity increases, the angle increases gently at all latitudes which means geomagnetic activity affects the angle at all latitudes at some degree being maximum for $K_p > 6$ at 6° for low latitudes, 5.5° for mid-latitudes, and 12° for high latitudes. It is interesting to note that when $K_p = \{0_0, 0+\}$, namely, when there is almost no geomagnetic activity, the results indicate a difference between the IGRF and T89 model field predictions at about 2° at all latitudes. This may be due to the fact that there are 30 coefficients defined for each IOPT level in the T89 model. IOPT = 1 in T89 model, corresponds to $K_p = \{0_0, 0+\}$ (see Table 6.1) and thus to non-zero coefficients which in turn give non-zero angles. The highest difference, on the other hand, is seen at high latitudes at 12° . Moreover, panel c shows that the highest scatter, indicated by the level of the outliers, is seen at high latitudes as the level of activity increases. It is the smallest at low latitudes. This suggests that the high latitudes are more prone to errors in the geomagnetic field orientations and thus in the angles.

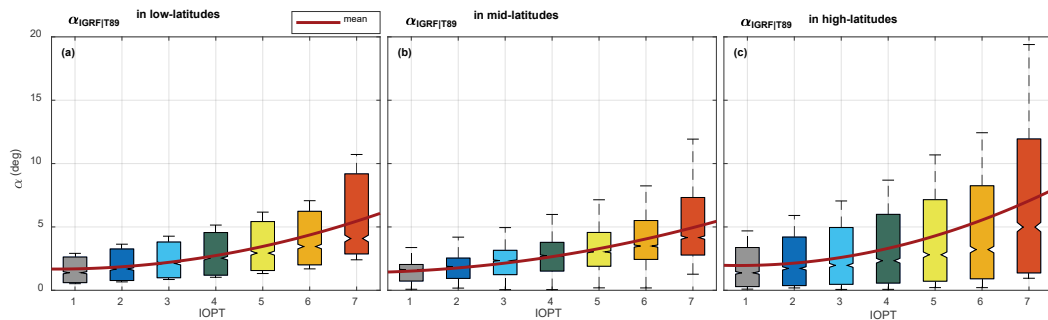


Figure 6.4 : Variations in angle with geomagnetic activity for low- (a), mid- (b) and high- (c) latitudes.

Another way of showing the differences between the two models involves the height variations of the geomagnetic field anomaly effects predicted by the models. This is demonstrated in Figure 6.5. Figure 6.5 illustrates the ratio between predicted external component (\mathbf{B}_{EXT}) to the total magnetic field ($\mathbf{B}_{model} = \mathbf{B}_{INT} + \mathbf{B}_{EXT}$) obtained from the T89 model for IOPT=1 and IOPT=7 that correspond to quiet and active times with respect to various altitudes starting from 500 km to 20000 km. For this purpose, the T89 model runs for each IOPT level at each altitude along the orbit. In the end, the orbital average at each altitude is plotted. The figure shows that the magnetic field anomalies affect the satellite more at higher altitudes as expected. In the beginning, for the altitude of 500 km, the mean rate is around 3% and 11% for IOPT={1, 7} respectively. For the altitude of 20,000 km, the mean rate is around 10% and 42% for IOPT={1, 7} respectively. The average effect of the external field over different altitudes presented in Figure 6.5 is found as 6% with $\bar{\mathbf{B}}_{EXT} = 24.6$ nT for IOPT = 1 and 23% $\bar{\mathbf{B}}_{EXT} = 109.3$ nT for IOPT = 7 .

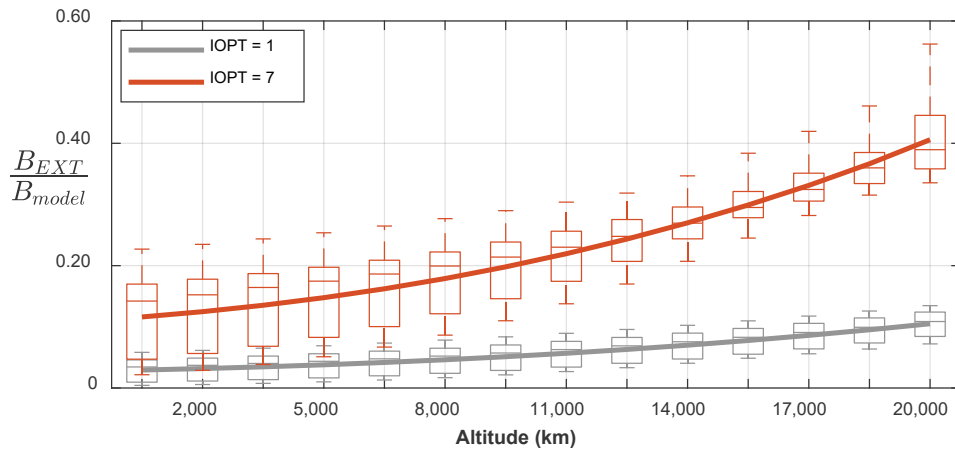


Figure 6.5 : Dependence of external field ($\mathbf{B}_{EXT}/\mathbf{B}_{model}$) on satellite's altitude obtained from T89 model for IOPT = 1 and IOPT = 7 in T89 model.

6.7 Influence of the Geomagnetic Activity on the Accuracy of Attitude

The previous section showed that geomagnetic activity increases the angles between the predicted magnetic fields by the models and the differences in angles at different K_p levels are largest at high latitudes. It is thus expected that these differences in the angles will propagate to the attitude angles which is the main subject in this section.

The actual attitude angles of roll, pitch, and yaw are calculated using the satellite’s orbital motion, and the estimated ones using EKF procedures are compared for the quiet (IOPT = 1 for T89) and active (IOPT = 7 for T89) geomagnetic days. The magnetic field vectors needed to estimate the attitude angles are obtained from the T89 and IGRF models and simulated satellite measurements. The satellite specifications used in this section are provided in the previous part. Additionally, the sun sensors and magnetometers have 3-axis measurements and both sensors have 1-Hz frequency; estimation time step is also 1 sec. The sensor noises are characterized using normalized standard deviations $\sigma_B = 0.008$ for magnetometers, $\sigma_S = 0.002$ for sun sensors, and the standard deviation of $\sigma_g = 0.005$ rad/s for rate gyros. We consider attitude estimation over a single orbit (6000 s). The satellite’s angular motion is determined by defining the dynamics and kinematics of the satellite which is described in Section 6.3. In the following sections, the extended Kalman filter is used in its traditional form, and the simulation results are presented for four different sensor configurations mentioned in Section 6.5 as scenarios. Figure 6.6 presents the attitude angles estimated by the EKF approach using the geomagnetic fields obtained from the T89 model for the selected LEO satellite for active geomagnetic conditions and for magnetometer-only scenario (i.e. scenario 1). In the figure, the solid line gives the estimated attitude angles while the dotted line presents the actual attitude angles obtained from Eq. (1). The panels from top to bottom are roll, pitch, and yaw. The horizontal axis on the panels is the time in seconds.

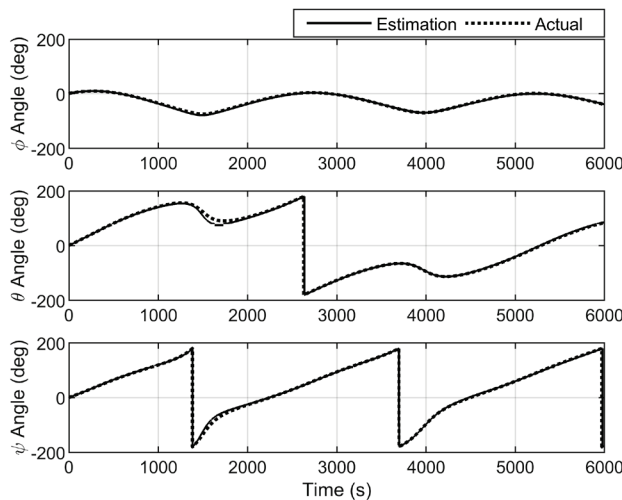


Figure 6.6 : Estimated and actual attitude angles using the T89 model in traditional EKF for the active geomagnetic conditions and for magnetometer configuration only (scenario 1).

Figure 6.6 shows that the differences between the estimated and actual attitude angles are noticeable but very small to be distinguished by eye. Actual attitude angles are computed using Eq. (1). We carried out the same analysis for all sensor configurations. The results are found to be very similar. We find that the differences between estimated and actual attitude angles are not large. Though small, it is of interest to quantify the difference. We carry out an error analysis for this purpose. For error analysis, we use two methods: One is the mean of the differences between the estimated and actual attitude angles, namely $\frac{1}{N} \sum_{k=1}^N \mathbf{e}_k$ in degrees, where $\mathbf{e}_k = \hat{\mathbf{x}}(k+1) - \mathbf{x}(k+1)$ and the other is the normalized root mean square error (NRMSE) calculated as $\left(\frac{100}{\bar{\mathbf{x}}} \sqrt{\frac{1}{N} \sum_{k=1}^N (\mathbf{e}_k)^2} \right)$ in percentages. Here $\hat{\mathbf{x}}(k+1)$ represents the estimated attitude angles using EKF, $\mathbf{x}(k+1)$ is the actual attitude angles, $\bar{\mathbf{x}}$ is the average of the actual attitude angles, and N is the number of data during the simulation we studied. The error (RMSE) is evaluated in Figures 6.7a and 6.7b, NRMSE results are discussed in Table 6.2.

We use IGRF results to represent the undisturbed conditions since the IGRF model is independent of the geomagnetic activity. Figure 6.7a shows how each attitude angle component estimated by EKF using IGRF varies corresponding to each scenario. Different colors in this panel correspond to different scenarios. The panel shows how the errors corresponding to different scenarios are distributed for each attitude angle. Figure 6.7b, on the other hand, presents how the errors corresponding to attitude angles are distributed for each scenario. Different colors in this panel correspond to different attitude angles such as black for roll, blue for pitch, and pink for yaw angles.

Representing quiet conditions, both figures give the following results:

1. The errors corresponding to all directional angles (roll, pitch, and yaw) are larger in the order of scenario 1, scenario 2, scenario 3, and scenario 4, respectively. The magnetometer-only scenario gives the largest error while the smallest error is obtained when all sensors (scenario 4) are used in attitude estimation. This result indicates that some of the errors caused by the IGRF estimation of geomagnetic fields are compensated by the addition of the other two sensors. In other words, adding sun sensor and gyroscope reduces attitude estimation error. However, comparing the errors for scenario 2 and scenario

- 3, it can be clearly noticed that the presence of sun sensor reduces the error more compared to the error reduction by the gyroscope.
- It is clearly seen that the errors corresponding to pitch and yaw angles are the largest for scenario 1 and scenario 2 compared to those for roll angle since the roll angle takes smaller values than the other two in the tumbling for our case (see Figure 6.6). Here, the error levels may differ if the initial conditions are changed. All sensor scenario or magnetometer and sun sensor scenarios give better estimates for pitch and yaw angles compared to those of magnetometer only or magnetometer and gyroscope scenarios.
 - The errors corresponding to roll angle are in the same order for all scenarios and differences between the scenarios are negligible. The roll angle seems to be insensitive to which sensor is used on the satellite. Even though scenario 4 is slightly better, only the magnetometer scenario gives an as good estimate as all sensor scenario. Adding sun sensor and gyroscope does not make an appreciable difference in reducing the errors in the yaw angle.

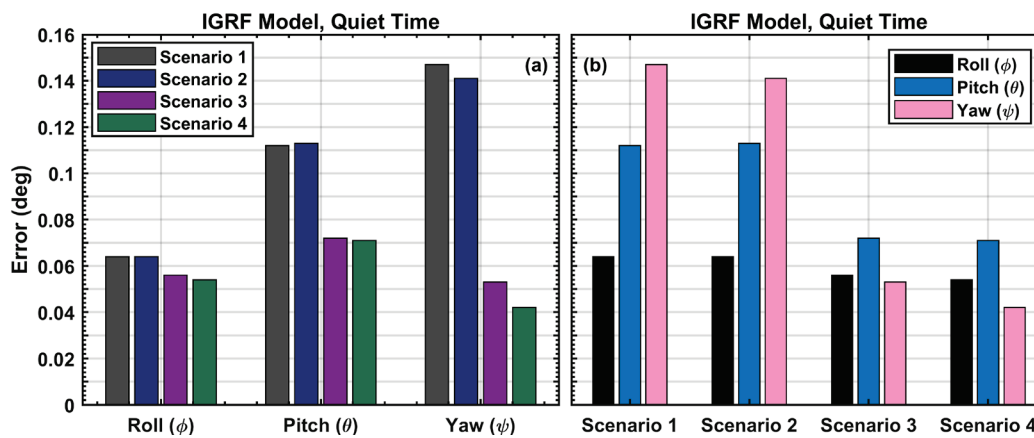


Figure 6.7 : Estimated errors using IGRF model during a quiet time for each attitude component (a) and for each scenario (b).

Similar evaluations for the IGRF model during active conditions can also be derived. Figure 6.8 is performed for this purpose and illustrates the errors obtained during quiet (solid lines) and active (dashed lines) times. The figure also compares the quiet and active day performance of the IGRF model between different scenarios. It is clear that the scenario 1 and 2 give higher errors for the active times for all attitude angles. The highest difference between active and quiet time errors is seen in scenario 1 while other

scenarios do not seem to be affected by the geomagnetic disturbance much and present a smaller difference.

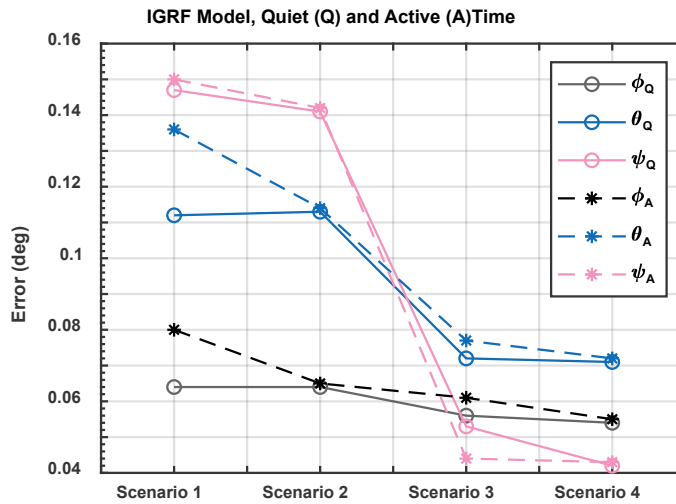


Figure 6.8 : Estimated errors for IGRF model predictions of the attitude angles during the quiet (solid) and active (dashed) geomagnetic conditions.

Figs. 6.9a and 6.9b are generated to demonstrate the differences calculated by subtracting T89 errors from those of IGRF for quiet (panel a) and active days (panel b) respectively. Positive differences indicate that IGRF errors are larger than those of T89. In both panels, it is clear that the errors associated with the IGRF model are larger than those of T89 for all attitude angles. Also, both panels show that the largest differences between the models for both activity levels occur in pitch and yaw angles in the case of scenario 1 and scenario 2. It can also be seen that the error differences are larger for active days especially for scenario 1 indicating the effect of the geomagnetic disturbances on the magnetometer measurements.

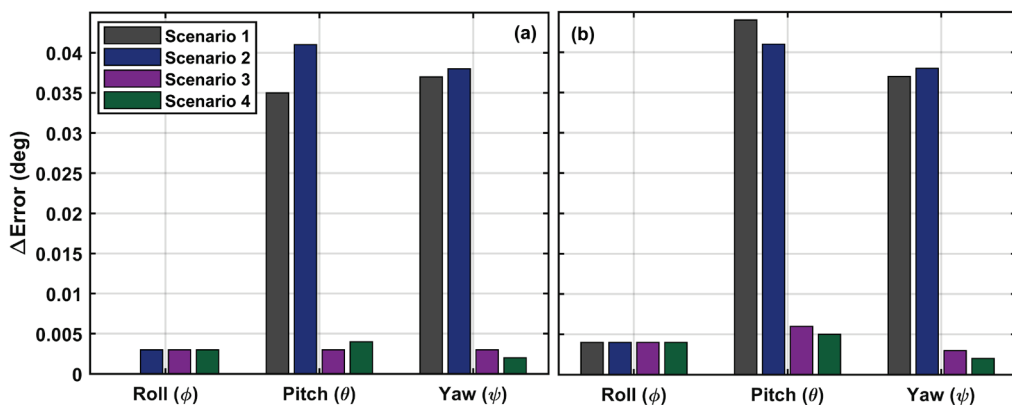


Figure 6.9 : Differences between the errors associated with both models for quiet (a) and active (b) days.

Lastly, we present Table 6.2 that displays the results of NRMSE to illustrate how the errors depend on the sensor configurations for both quiet (blue highlight) and active (yellow highlight) geomagnetic conditions. In the table, ϕ , θ , and ψ represent the roll, pitch, and yaw angles respectively. Since the geomagnetic disturbance effects are found to be larger in the case of scenario 1 for especially pitch angle, the results in Table 6.2 are evaluated by comparing IGRF and T89 model performances for scenario 1 only, and the addition of other sensors are evaluated qualitatively as same as given above. For scenario 1, we see that using the T89 model reduces the error and improves the attitude angles (roll, pitch, and yaw) by 0.03%, 0.06%, and 0.01% respectively during the quiet times and 0.02%, 0.02%, and 0.02% during the active geomagnetic conditions.

Table 6.2 : NRMSE between estimated and actual attitude angles.

Geo-magnetic State	NRMSE (%)	Scenario 1		Scenario 2		Scenario 3		Scenario 4	
		Mag. only		Mag. and Gyroscope		Mag. and Sun sensor		All sensors	
		IGRF	T89	IGRF	T89	IGRF	T89	IGRF	T89
Quiet	ϕ	0.72	0.69	0.67	0.66	0.03	0.03	0.02	0.02
	θ	0.50	0.44	0.36	0.34	0.03	0.02	0.01	0.01
	ψ	3.18	3.17	3.17	3.16	0.25	0.23	0.22	0.21
Active	ϕ	0.77	0.75	0.68	0.66	0.04	0.03	0.02	0.02
	θ	0.52	0.50	0.37	0.34	0.06	0.04	0.03	0.02
	ψ	3.20	3.18	3.17	3.17	0.27	0.25	0.24	0.23

As a summary, Table 6.2 indicate that the magnitude of errors in all angles is small for both quiet and active conditions which indicates that the attitude estimations are not severely affected by the geomagnetic disturbances. We can say that using T89 as the geomagnetic model improves the attitude predictions at least 0.01 % over using IGRF depending on the sensor configurations and reduces the errors in all attitude angles. Especially during the active days, this improvement is noticeably clear. As a result of these comparisons, whether the IGRF model or T89 model should be used when calculating the attitude angles at LEO altitudes depends on the intended accuracy of the attitude angles determined by the mission requirements. If the computational load on on-board computers of the satellite is considered, then one may use the conventional model IGRF as the geomagnetic field model of the satellite attitude since its model inputs are simpler. We showed that although small, the errors and the performance of

attitude estimation methods depend on which geomagnetic field model is used, i.e. whether it is IGRF or T89 in this case. We suggest that the most recent modeling techniques, such as T89, will be still an advantage when determining the attitude angles even during the undisturbed conditions, but more so under disturbed conditions.

Overall evaluation for IGRF indicates that the model produces larger errors in attitude angles during active days with respect to the quiet days for all four sensor configurations. On the second hand, adding other sensors seem to improve the errors resulting from the disturbances superimposed on the quiet time background geomagnetic field.

In this study, we also calculate the performance of the models with different sensor configurations as scenario 1, scenario 2, scenario 3, and scenario 4. Adding gyroscope to the magnetometer to improve the attitude angles does not make a considerable reduction in the errors during quiet times in all attitude angles. However, adding sun sensor improves the errors at these times. Table 6.2 indicates that the gyroscope reduces the errors by about 0.07% on average for all attitude angles with respect to scenario 1. Also, it reduces the errors by 0.02% in scenario 4 with respect to scenario 3. The sun sensor in scenario 3, on the other hand, reduces the errors by about 1.4% on average with respect to scenario 1; and by 1.3% in scenario 4 with respect to scenario 2. All sensors scenario has the smallest errors for the quiet days. However, the decrease in error is not due to the presence of gyroscope but the presence of sun sensor in this scenario. The use of gyroscope sensor in spacecraft attitude becomes more important in the absence or failure of the sun sensors. Earth's shadow or the eclipse period creates such unfavorable space conditions. To prevent the satellite from the effects of the eclipse, it is very common to use both magnetometers and gyroscope together for attitude purposes. Here, we showed that the gyroscopes do not provide a better estimate of attitude angles during the quiet times against using magnetometers only. However, using gyroscope during the active times together with magnetometers reduces the errors in the prediction of attitude angles. On the contrary to gyroscopes, the use of sun sensors makes a large improvement in reducing the errors in the estimated attitude angles during both quiet and active times. Between IGRF and T89 models, our comparisons show that using the T89 model in all scenarios, slightly but still, improves the estimated attitude angles. The only disadvantage that this will bring may be the increase in the computational load on the onboard computers.

6.8 Conclusions

In this study, the geomagnetic field models that are used to estimate the geomagnetic fields and satellite attitude angles are studied during the geomagnetically active and quiet days. It is the first time that the attitude angles (yaw, pitch, and roll) are studied using a global empirical model, the T89 model, of the magnetosphere which takes into account the magnetic disturbances resulting from the magnetospheric substorms and/or geomagnetic storms and compared with the results from the more conventional model, IGRF. Our analysis showed that the angles between the geomagnetic field vectors estimated by the models increases as the geomagnetic activity increase from quiet levels ($K_p = 0$) to strongly active days ($K_p \geq 6$) and it increases more over the high latitudes than over the equatorial regions especially during the strong activity days for $K_p \geq 6$. Similarly, it is shown that the magnetic field disturbances estimated from T89 at LEO are higher during the high geomagnetic activity as the satellite altitude becomes higher. Since this angle is one of the inputs in the estimation of the satellite attitude angle by EKF, the satellite attitude angles will be sensitive to its variations. Thus, it is expected that the attitude angles will increase as the geomagnetic activity enhances, especially at the high latitudes and at high altitudes.

Secondly, we show that although small, differences occur between the estimated attitude angles using T89 and IGRF models during the active days. When we analyze the magnetometer only case, we found that the errors in the predicted attitude angles using the IGRF model are larger than the errors obtained by using the T89 model. We also showed that the T89 model estimates smaller errors in the EKF estimated attitude angles during the active days. The largest errors are obtained for pitch and yaw angles during both quiet and active days.

Additionally, we used traditional EKF to estimate the attitude angles for different sensor configurations including magnetometer, sun sensor, and gyroscope for quiet and active times. We studied if the addition of other attitude sensors on board will change the accuracy of the estimated attitude angles during both quiet days and active days. We showed that the highest errors in the estimated attitude angles are obtained for magnetometer only and magnetometer plus gyroscope scenarios during the quiet days. Also, we found that during the quiet days, while the presence of sun sensor reduces the errors in the estimated attitude angles, the gyroscope has less effect in the

reduction of the errors. During the active days, while all scenarios give small errors, the magnetometer only and magnetometer and gyroscope scenarios show markedly the highest errors. The errors resulting from the geomagnetic disturbances are reduced drastically after we added the sun sensor measurements into the system. The most accurate results with the smallest errors are obtained for all sensor scenario. In this case, the predicted attitude angles are significantly improved and obtained close to the actual attitude angles. This study emphasizes the importance of the effects that the magnetic disturbances will have on the attitude angles and helps to choose the right sensor combination during both quiet and disturbed times for better attitude estimation.

7. ATTITUDE ESTIMATION WITH ALBEDO INTERFERENCE ON SUN SENSOR MEASUREMENTS*

7.1 Abstract

A three-axis attitude estimation scheme is presented using a set of Earth's albedo interfered coarse sun sensors (CSSs), which are inexpensive, small in size, and light in power consumption. For modeling the interference, a two-stage albedo estimation algorithm based on the autoregressive (AR) model is proposed. The algorithm does not require any data such as albedo coefficients, spacecraft position, sky condition, or ground coverage, other than albedo measurements. The results are compared with five albedo models on the basis of two reference conditions. The estimated albedo is fed to the CSS measurements for correction. The corrected CSS measurements are processed under three estimation techniques with two different sensor configurations. The relative performance of the attitude estimation schemes when using different albedo models is examined.

7.2 Introduction

Spacecraft instruments need to be oriented to achieve mission directives in space. Depending on the mission, there may be strict performance requirements in terms of attitude estimation or necessity to a safe-mode operation or sanity checks. For these purposes, additional attitude sensors such as magnetometers and sun sensors can be utilized with less accuracy but less power need, lower cost, and smaller size. Sun sensors are frequently used in both planet-orbiting satellites and interplanetary spacecraft missions in the solar system. They can be divided into two classes as fine or digital sun sensors (DSSs), and CSSs, which are commonly used in a form of photodiodes [7]. CSSs function almost proportional to the cosine angle between the

* This chapter is based on the paper “Cilden-Guler, D., Schaub, H., Hajiyev, C., and Kaymaz, Z. (2021). Attitude Estimation with Albedo Interference on Sun Sensor Measurements, *Journal of Spacecraft and Rockets*, **58**(1), 148-163, doi: 10.2514/1.A34814”.

sensor's boresight and the sun direction vector from the spacecraft. They are often used on platforms including multiple CSSs.

A spacecraft close enough to the sun and a planet receives electromagnetic radiation of direct solar flux, reflected radiation namely albedo, and emitted radiation of that planet. The solar flux is the largest source of radiation for the spacecraft while the albedo is the fraction of sunlight incident and reflected light from the planet. Spacecraft can be exposed to albedo when it sees the sunlit part of the planet (Figure 7.1).

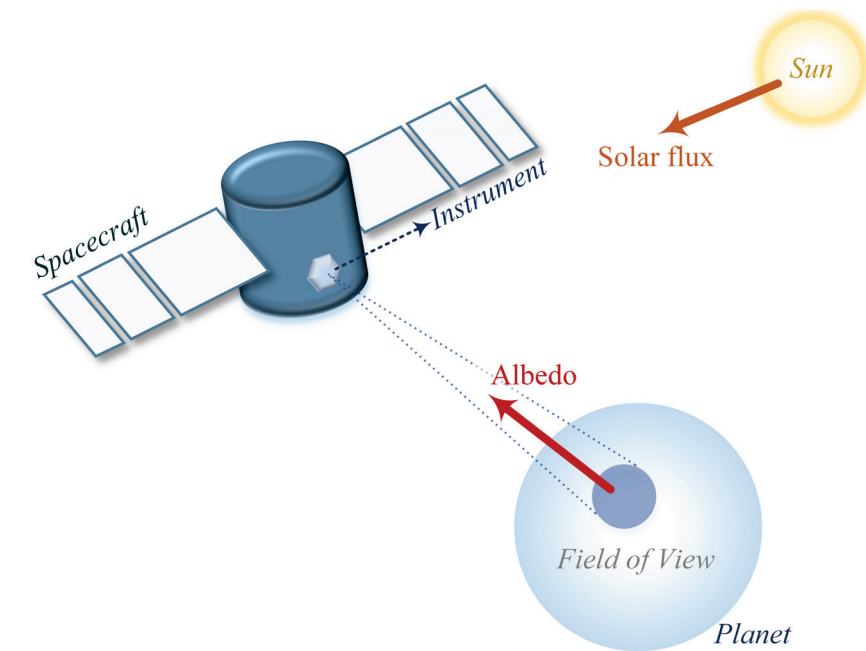


Figure 7.1 : Illustration of considered radiation sources on a spacecraft.

The albedo values vary depending on the seasonal, geographical, diurnal changes as well as the cloud coverage. The most reflectance is caused by thickest, highest clouds while the least by snowing clouds [71]. The CSS not only measures the light from the sun but also the albedo of the planet [8]. So, a planet's albedo interference can cause anomalous sun sensor readings. According to Reference [9], albedo might worsen the sun pointing accuracy by more than 20 degrees. On the other hand, albedo might be an important factor in selecting the characteristics of optical-sensor systems such as cameras or star trackers, and in spacecraft thermal and power design. For example, Reference [72] underlines that the thermal control system on the spacecraft must consider the light reflectance and emittance of the planets as it causes a highly dynamic variation in thermal load. Another study on a spacecraft thermal analysis is carried out in order to evaluate the thermal conditions for temperature stability of sensitive

instruments and radiators by using the albedo data from NASA's Clouds and Earth Radiant Energy System (CERES) instruments [73].

The mathematical model of the sun sensors can include diffusive and specular reflections from the planet which represents the perturbed sun sensor measurements. In Reference [74], perturbed sun sensor measurements are validated by the telemetry data of the Ørsted satellite. The currents of the modeled CSSs are improved about three times more than the case not including any albedo model on the measurements in Reference [74], and four times in Reference [75]. A sun heading estimation algorithm is also applied by Reference [76] using the extended Kalman filter (EKF). The sun direction is estimated with accuracy under 4-degrees based on albedo interfered CSS and rate gyro (RG) measurements, and 10 degrees without RGs despite the fact that an underdetermined sun sensor coverage is considered in the study [76].

References [77] and [78] present extended consider Kalman filter based on modified Rodrigues parameters (MRPs) for CSS calibration. The presented filters require inertial attitude measurements but it gives scale factor accuracy less than 1% and misalignment accuracy about 1-degree even under poor attitude knowledge. Another calibration filter is proposed for photodiodes through the estimation of attitude and calibration parameters simultaneously [79]. An arbitrary number of photodiodes along with an albedo model, are calibrated using both an EKF and an unscented filter. The filter estimates improve the sun vector measurements by 10-degrees and attitude by 1-degree, by combining a three-axis magnetometer (TAM) and RG in the study. In order to make the albedo model lighter in computations, two constant albedo coefficients are applied rather than various spatial data in Reference [80]. From the analyses, the errors are reduced by taking the average albedo coefficient as 0.105 instead of 0.30. Even though the presented model provides a significantly better CSS accuracy for most of the times than uncorrected outputs, its predictions based on the 0.30 value may occasionally overcorrect the CSS. This overcorrection causes an increase in the sensor error. It is stated that the detailed mathematical model including the albedo coefficient changes depending on the active surface elements can be used for the most accurate case but it is computationally expensive for online usage. Reference [80] concludes that because of the albedo model complexity, it is more reasonable to use a filter on the sun sensor that restricts the sensor not sensitive to the albedo. This suggestion might be more suitable for DSSs. In Reference [81], a less complex albedo model is

generated via polynomial functions with 13 parameters for each albedo component including functions based on latitude and longitude. The polynomial is fitted to the reflectivity dataset from Earth Probe's total ozone mapping spectrometer (TOMS) instead of using excessive data in look-up tables. The work also estimates the spacecraft attitude states with 1-degree accuracy in nominal mode and 2-degrees in worst mode by EKF with 0.5% noisy measurements from TAM and corrected CSS.

The main purpose of our study is to estimate the albedo by using a simple model with less parameter dependency than any albedo models and to estimate the attitude by comprising the corrected CSS measurements. The estimation process using only the CSS platform and using it along with TAM is presented to be considered during the sanity checks and/or in the safe-mode operations of spacecraft missions or in the validation algorithm of other sensors' outputs. This aids the mission by making the albedo estimates available for the other subsystems.

As a simple model, the AR albedo model is proposed. Here, the purpose is to estimate the albedo without using any data related to albedo coefficients that depend on position, time, ground, and cloud coverage parameters. AR model or enhanced versions of the AR model are widely used in forecasting geomagnetic storm indices and estimating gyro drifts as well as wind speed [157–160] but to the best of our knowledge, it is used in albedo estimation for the first time in this study. The CSS measurement equations contain disturbances, most notably due to Earth's albedo, which is dependent on too many parameters. Therefore, modeling albedo is complex and computationally heavy for online usage. In the meanwhile, the AR is a simple model based on only a couple of parameters in accordance with how many measurements are used. However, spacecraft's attitude information is necessary to estimate the albedo based on the AR model. So, an attitude estimation procedure is also presented using the estimated albedo. Reference [74] indicates that it is possible to perform a three-axis attitude estimation by using only CSSs with albedo interference but the output equations' non-differentiability makes the estimation harder. This is why the attitude estimation procedure proposed in this study is composed by estimating the albedo first and correcting the CSS after. In this way, any albedo model is not considered in the last output equations in the attitude estimation filter.

The remainder of the paper is organized as follows. Section 7.3 presents the albedo and CSS mathematical models. The attitude estimation filter and AR model-based two-

stage albedo estimation filter used in this study are given in Sections 7.4 and 7.5 respectively. In Section 7.6, the analysis and results of several scenarios for Earth's albedo data, albedo effects on CSSs, possible albedo models, and attitude estimation filters are presented and discussed. The last section summarizes and concludes the paper.

7.3 Albedo and Coarse Sun Sensor Modeling

7.3.1 Mathematical model for a planet's albedo

The mathematical model for the total albedo from a planet affecting an instrument (e.g. CSS) on a spacecraft is given in this section. The parameters affecting the albedo model can be itemized as the attitude and position of the spacecraft, instrument's field of view (FOV), placement of other instruments (that might block/shadow), and albedo coefficients related to the several parameters such as ground coverage, seasonal changes, and cloudiness.

The generic vectors can be described as a unit normal vector ($\hat{\mathbf{n}}$), sun heading vector ($\hat{\mathbf{s}}$), and direction vector from A to B ($\hat{\mathbf{r}}_{AB}$). In Figure 7.2, $\hat{\mathbf{n}}_A$ and $\hat{\mathbf{n}}_I$ are the unit normal vectors of the differential area (dA) on the planet and the instrument cell respectively, $\hat{\mathbf{s}}_p$ and $\hat{\mathbf{s}}_I$ are the sun heading vectors of the planet and of the instrument cell respectively. Here, the instrument's position vector from the incremental area is \mathbf{r}_{AI} and the unit direction vector is $\hat{\mathbf{r}}_{AI} = \frac{\mathbf{r}_{AI}}{\|\mathbf{r}_{AI}\|}$. The spacecraft's direction vector from dA can be expressed as $\hat{\mathbf{r}}_{sc}$.

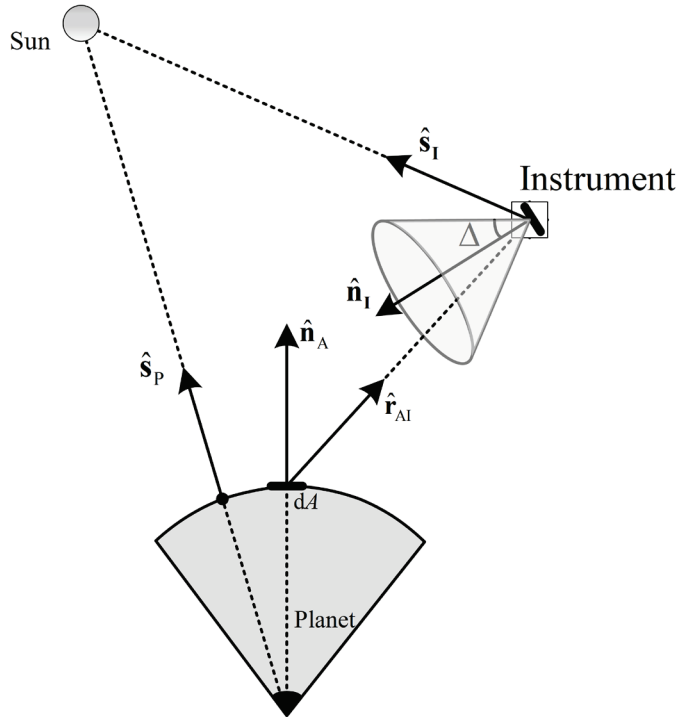


Figure 7.2 : Illustration of the unit normal, sun, and spacecraft heading vectors.

The differential areas,

- on the sunlit portion of the planet where $(\hat{\mathbf{s}}_p \cdot \hat{\mathbf{n}}_A > 0)$ forming A_s (sunlit region),
- in the instrument's field of view with a half angle of Δ where $(-\hat{\mathbf{r}}_{AI} \cdot \hat{\mathbf{n}}_I \geq \cos(\Delta))$ forming A_I (instrument FOV region),
- in the instrument cell's maximum field of view where $(\hat{\mathbf{r}}_{AI} \cdot \hat{\mathbf{n}}_A > 0)$ forming $A_{I_{\max}}$ (the maximum area that can be seen from the instrument cell),
- in the spacecraft's field of view where $(\hat{\mathbf{r}}_{sc} \cdot \hat{\mathbf{n}}_A > 0)$ forming A_{sc} (spacecraft FOV region),

can be used for the total albedo calculations contributing to the instrument or the spacecraft. The total area that is sunlit and visible to the instrument results in $A \equiv A_s \cap A_I$ (see Figure 7.3).

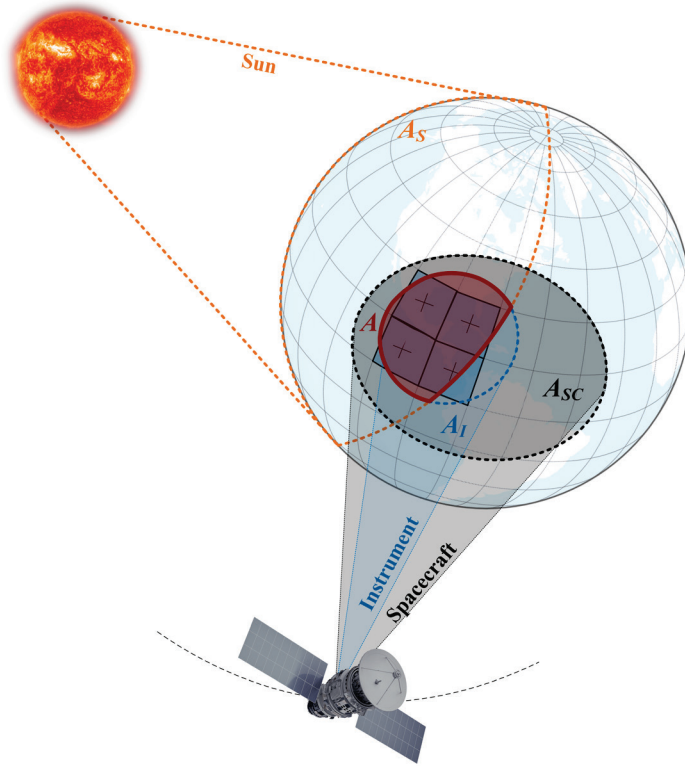


Figure 7.3 : Illustration of the observed illuminated area.

The solar flux reaching a point is found as $F_{\text{sun}} (\hat{\mathbf{s}} \cdot \hat{\mathbf{n}})$ in W/m^2 when using the generic vectors. So, the solar flux reaching the incremental area (F_{in}) is [8],

$$F_{\text{in}} = F_{\text{sun}} (\hat{\mathbf{s}}_p \cdot \hat{\mathbf{n}}_A), \quad (7.1)$$

where F_{sun} is the solar constant at the top of the atmosphere. The mean value of the solar flux at the mean distance of the sun-planet is called solar constant which slightly changes depending on the solar cycle and the planet's distance from the sun. The solar constant value for Earth is $1366.1 W/m^2$. The incoming solar flux is both absorbed and reflected partially. The reflected portion is proportional to the albedo coefficient (α) as,

$$\begin{aligned} F_{\text{out}} &= \alpha F_{\text{in}} \\ &= \alpha F_{\text{sun}} (\hat{\mathbf{s}}_p \cdot \hat{\mathbf{n}}_A). \end{aligned} \quad (7.2)$$

Using the conservation of energy [8], the irradiance due to the planet's albedo at the spacecraft's position is,

$$F_{\alpha} = \frac{F_{\text{sun}}}{\pi} \iint_A \frac{\alpha (\hat{\mathbf{s}}_p \cdot \hat{\mathbf{n}}_A) (\hat{\mathbf{r}}_{\text{AI}} \cdot \hat{\mathbf{n}}_A) (-\hat{\mathbf{r}}_{\text{AI}} \cdot \hat{\mathbf{n}}_I)}{\|\mathbf{r}_{\text{AI}}\|^2} dA, \quad (7.3)$$

where F_{sun} is the solar constant at the top of the atmosphere, $\hat{\mathbf{s}}_p$ is the sun heading vector of the planet, $\hat{\mathbf{n}}_A$ and $\hat{\mathbf{n}}_I$ are the unit normal vectors of dA and the instrument cell respectively, $\hat{\mathbf{r}}_{\text{AI}}$ is the unit direction vector to the instrument from dA . equation (7.3) is rewritten in a summation form in order to obtain a discrete version as [161],

$$F_{\alpha} = \frac{F_{\text{sun}}}{\pi} \sum_{i=1}^{N_A} \frac{\alpha (\hat{\mathbf{s}}_p \cdot \hat{\mathbf{n}}_{A_i}) (\hat{\mathbf{r}}_{\text{AI}_i} \cdot \hat{\mathbf{n}}_{A_i}) (-\hat{\mathbf{r}}_{\text{AI}_i} \cdot \hat{\mathbf{n}}_I)}{\|\mathbf{r}_{\text{AI}_i}\|^2} \Delta A, \quad (7.4)$$

where N_A is the number of differential areas (ΔA) inside the intersectional area, A .

7.3.2 Albedo coefficients

Albedo coefficient (α) is the ratio of the reflected and incoming solar radiation over a unit area that ranges from zero to one. As it is described in the previous section, the data is required to comprise albedo based on latitude and longitude of a planet and it might optionally include information of date/time, cloudiness, etc. The most reflective planet in the solar system is Venus by its global Bond albedo around 0.76 [162]. The Earth's average albedo evolved over time but converged to 0.29 in the mean in the last 40 years, and had only 0.2% interannual variability on global mean albedo [163]. In order not to model a complex albedo close to the real case which depends on many parameters as discussed, a constant global albedo coefficient can be used. However, the use of this kind of straightforward planet interference might be insufficiently accurate [80].

In order to determine the total albedo affecting the instrument, the planet should be divided into grids based on the albedo data size. Figure 7.4 shows an illustration of the albedo contributions from each grid element within the field of view to the instrument. The albedo data might include irregularities in the latitude and longitude (see Figure 7.5). The grid elements to be considered can be determined using their central points. The grid element with the central point within the field of view can be considered as

an active element. In Figure 7.5, regular and irregular grid examples are given. Even the area seen is the same (red elliptical area), the active grid elements to be used (blue rectangular areas) for the calculations differentiate. Another method to apply here is to utilize an interpolation technique [164] such as inverse distance weighting, kriging, bi-cubic, nearest-neighbor, etc. so as to use the exact area of interest in the calculations. It is also possible to convert the irregular grids into the regular version.

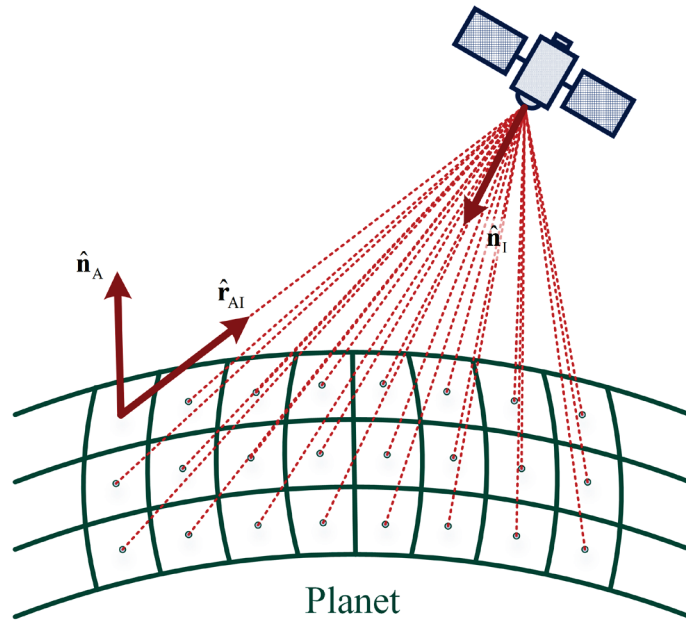


Figure 7.4 : Illustration of the albedo influence on an instrument from observed incremental areas of a planet.

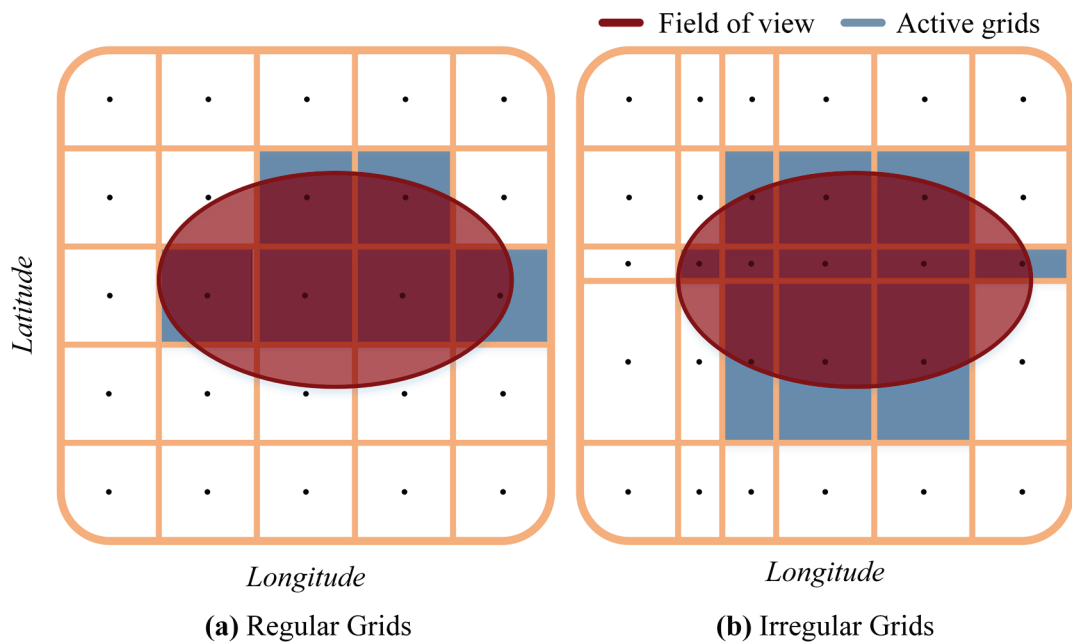


Figure 7.5 : Illuminated field of view area with regular (a) and irregular (b) grid examples.

The albedo data of Mars can be obtained from the instrument Thermal Emission Spectrometer (TES) on the Mars Global Surveyor (MGS) spacecraft launched in 1996. The data has irregularities in the sense of latitude and longitude intervals.

The Earth's albedo data can be obtained from the instruments such as TOMS and CERES. The TOMS measures the albedo of the Earth's atmosphere in the near-ultraviolet region. The data are mapped with a grid size of 180 x 288 and a latitude and longitude resolution of $1^\circ \times 1.25^\circ$. The most recent data are obtained from the Earth Probe mission between 1996 and 2006. The CERES shares the albedo data up to with $1^\circ \times 1^\circ$ resolution with surface albedo or top of the atmosphere (TOA) albedo options under clear-sky and all-sky conditions. The clear-sky monthly mean TOA fluxes from CERES are provided completely cloud-free according to moderate resolution imaging spectroradiometer (MODIS) data with 1-km resolution [165,166]. There are several satellites having CERES instrument on board such as the tropical rainfall measuring mission (TRMM), Terra, Aqua, Suomi NPP, and NOAA-20. Terra and Aqua satellites have two CERES instrument pair to provide an enhanced product quality. The hourly, daily, and monthly satellite pair (Terra-Aqua) data are available starting from 2002. A sample of Earth's albedo coefficient data from CERES averaged over 2018 is presented in Figure 7.6.

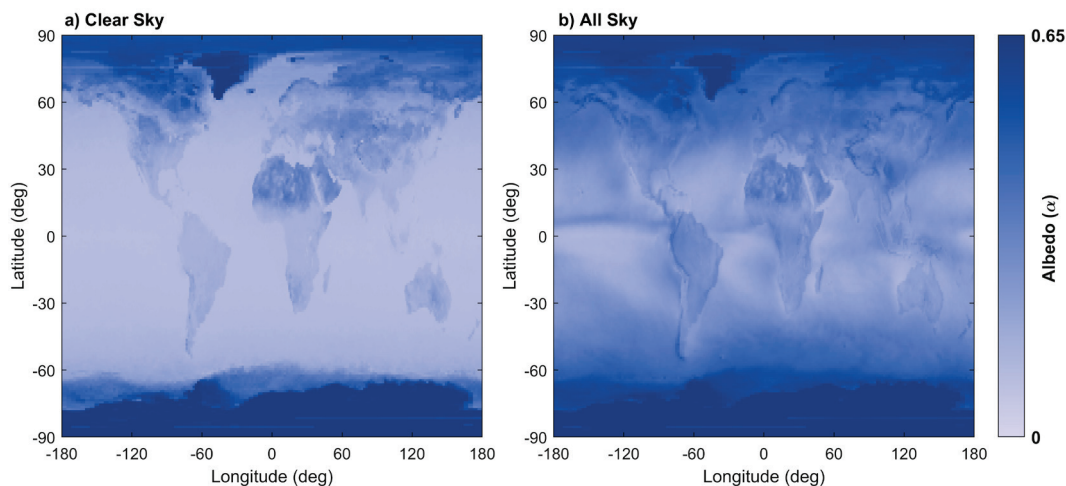


Figure 7.6 : Albedo coefficients averaged over CERES 2018 monthly data under clear-sky (a) and all-sky (b) conditions.

7.3.3 Modeling of coarse sun sensor measurements in the presence of albedo

As the CSS senses any light received, the light reflected from a celestial body will also affect the sensor. Here, one celestial body is considered close enough to a spacecraft for modeling the CSS measurements without having any blockage to the sensor's FOV from the structural components of the spacecraft. Adding more than one celestial body to the simulations is possible by adding another albedo summing term. The structural blockage can be avoided at the design stage or modeled in the FOV of the CSS. The process of simulating the CSS readings excited by the planet's albedo is given in Figure 7.7.

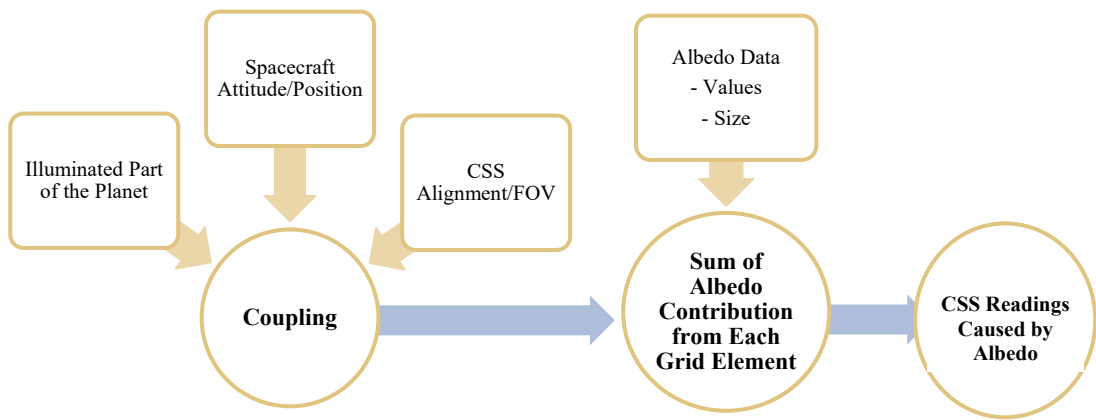


Figure 7.7 : The process for simulating the CSS albedo readings.

The output current of CSS is proportional to the angle between the sensor's boresight and the direction of the light source in general [8]. By using the solar irradiance formula on an instrument as $F_{\text{sun}}(\hat{\mathbf{s}}_1 \cdot \hat{\mathbf{n}}_1)$, the output current generated from CSS can be expressed as,

$$I_d = \begin{cases} I_{\text{max}} \frac{F_{\text{sun}}}{F_{\text{cal}}} (\hat{\mathbf{s}}_1 \cdot \hat{\mathbf{n}}_1) & \text{if } (\hat{\mathbf{s}}_p \cdot \hat{\mathbf{n}}_A > 0) \cap (\hat{\mathbf{s}}_1 \cdot \hat{\mathbf{n}}_1 \geq \cos(\Delta)) \\ 0 & \text{otherwise} \end{cases} \quad (7.5)$$

where F_{cal} is the calibration flux determined during ground testing, I_{max} is the possible maximum output current of CSS. The current of CSS contributed from albedo is written as [74],

$$I_\alpha = \begin{cases} I_{\max} \frac{F_{\text{sun}}}{F_{\text{cal}}} \sum_{i=1}^{N_A} \frac{\alpha (\hat{\mathbf{s}}_p \cdot \hat{\mathbf{n}}_{A_i}) (\hat{\mathbf{r}}_{AI_i} \cdot \hat{\mathbf{n}}_{A_i}) (-\hat{\mathbf{r}}_{AI_i} \cdot \hat{\mathbf{n}}_1)}{\pi \|\mathbf{r}_{AI_i}\|^2} \Delta A, & \text{if } \Delta A \in A \\ 0 & \text{if } \Delta A \notin A \end{cases} \quad (7.6)$$

The resulting CSS current gives,

$$I = I_d + I_\alpha + \varepsilon_{\text{CSS}}, \quad (7.7)$$

where ε_{CSS} is zero-mean Gaussian noise on the measurements. One might need to use voltage outputs depending on the given instrumental datasheet. The voltage output can be calculated in a similar manner by including the maximum voltage of CSS, V_{\max} instead of I_{\max} in calculating V_d and V_α . The resulting voltage of CSS is,

$$V = V_d + V_\alpha + \varepsilon_{\text{CSS}}. \quad (7.8)$$

The presented CSS readings in a current or a voltage format belong to only one photodiode and the calculations need to be repeated for as many photodiodes as are available.

7.4 Gaussian Estimation Filters

The general estimation state-space problem is expressed as,

$$\mathbf{x}_k = f(\mathbf{x}_{k-1}) + \mathbf{w}_k, \quad (7.9)$$

$$\mathbf{y}_k = h_k(\mathbf{x}_k) + \boldsymbol{\varepsilon}_k, \quad (7.10)$$

where $f(\cdot)$ is the system and $h(\cdot)$ is the measurement function, \mathbf{x}_k is the state vector at a time t_k , \mathbf{w}_k is the zero-mean Gaussian noise vector with the covariance of \mathbf{Q} , \mathbf{y}_k is the measurement vector, and $\boldsymbol{\varepsilon}_k$ is the zero-mean Gaussian noise vector with the covariance of \mathbf{R}_k . The initial state is \mathbf{x}_0 with mean $\boldsymbol{\mu}_0$ and covariance \mathbf{P}_0 ; its probability density function (PDF) can be denoted as $p(\mathbf{x}_0) = \mathcal{N}(\mathbf{x}_0 | \boldsymbol{\mu}_0, \mathbf{P}_0)$. Approximations based on Kalman filtering can be represented using the Gaussian filter

(GF) technique [109]. This technique uses the parameters $\boldsymbol{\mu}_k, \mathbf{P}_k$ in $p(\mathbf{x}_k | \mathbf{y}_{1:k}) = \mathcal{N}(\mathbf{x}_k | \boldsymbol{\mu}_k, \mathbf{P}_k)$ for the distribution of state estimation by two stages. The first stage is composed of predictions using the system function to determine the predicted mean,

$$\boldsymbol{\mu}_k^- = \int f(\mathbf{x}_{k-1}) \mathcal{N}(\mathbf{x}_{k-1} | \boldsymbol{\mu}_{k-1}, \mathbf{P}_{k-1}) d\mathbf{x}_{k-1}, \quad (7.11)$$

and the predicted covariance,

$$\mathbf{P}_k^- = \int (f(\mathbf{x}_{k-1}) - \boldsymbol{\mu}_{k-1})(f(\mathbf{x}_{k-1}) - \boldsymbol{\mu}_{k-1})^T \mathcal{N}(\mathbf{x}_{k-1} | \boldsymbol{\mu}_{k-1}, \mathbf{P}_{k-1}) d\mathbf{x}_{k-1} + \mathbf{Q}. \quad (7.12)$$

The second stage updates the predictions using the measurements as,

$$\hat{\mathbf{y}}_k = \int \mathbf{h}_k(\mathbf{x}_k) \mathcal{N}(\mathbf{x}_k | \boldsymbol{\mu}_k^-, \mathbf{P}_k^-) d\mathbf{x}_k, \quad (7.13)$$

$$\boldsymbol{\Psi}_k = \int (\mathbf{x}_k - \boldsymbol{\mu}_k^-)(\mathbf{h}_k(\mathbf{x}_k) - \hat{\mathbf{y}}_k)^T \mathcal{N}(\mathbf{x}_k | \boldsymbol{\mu}_k^-, \mathbf{P}_k^-) d\mathbf{x}_k, \quad (7.14)$$

$$\boldsymbol{\Phi}_k = \int (\mathbf{h}_k(\mathbf{x}_k) - \hat{\mathbf{y}}_k)(\mathbf{h}_k(\mathbf{x}_k) - \hat{\mathbf{y}}_k)^T \mathcal{N}(\mathbf{x}_k | \boldsymbol{\mu}_k^-, \mathbf{P}_k^-) d\mathbf{x}_k. \quad (7.15)$$

The innovation can be found as,

$$\mathbf{e}_k = \mathbf{y}_k - \hat{\mathbf{y}}_k, \quad (7.16)$$

with the innovation covariance,

$$\mathbf{S}_k = \boldsymbol{\Phi}_k + \mathbf{R}_k, \quad (7.17)$$

which is used in constituting the Kalman gain as,

$$\mathbf{K}_k = \boldsymbol{\Psi}_k \mathbf{S}_k^{-1}. \quad (7.18)$$

Finally, the posterior mean and the associated covariance can be found as:

$$\boldsymbol{\mu}_k = \boldsymbol{\mu}_k^- + \mathbf{K}_k \mathbf{e}_k, \quad (7.19)$$

$$\mathbf{P}_k = \mathbf{P}_k^- - \mathbf{K}_k \mathbf{S}_k \mathbf{K}_k^T, \quad (7.20)$$

The integrals given in equation (7.11) to (7.15) can be approximated using different Kalman-type filters [110,111]. The attitude of a spacecraft can be estimated using conventional approaches, namely, the EKF [10] or unscented Kalman filter (UKF), which is derivative-free [11], based on nonlinear system and measurement functions defined in equation (7.9) – (7.10). An EKF is used in this study and the attitude is represented using modified Rodrigues parameters (MRPs) indicated with $\sigma_{B/R}$ symbol, which is in body coordinates with respect to the reference (inertial) coordinates [2,167].

Another approach is using deterministic attitude determination techniques called single-frame methods (SFMs) as a sub-step in order to make the attitude part of the measurements linear with respect to the states [4,12,13,84,168]. The SFM based preprocessing step is also implemented before the update stage of the filter by minimizing Wahba's loss function [15],

$$L(\mathbf{A}_k) = \frac{1}{2} \sum_j \mathbf{a}_{j_k} \left| \mathbf{b}_{j_k} - [BR]_k \mathbf{r}_{j_k} \right|^2, \quad (7.21)$$

where $[BR]$ is the direction cosine matrix from reference coordinates to body coordinates, \mathbf{a}_j is the inverse variance of the sensor j , \mathbf{b}_j is the sensor observation vector in the body coordinates, and \mathbf{r}_j is the measurement model vector in the reference coordinates. The attitude can be determined by SFM and used in the Gaussian filters as linear attitude measurements. The loss function can be minimized using one of the SFM methods namely SVD, QUEST, q, FOAM, etc. [4,96].

The attitude measurements from SFM is,

$$\tilde{\mathbf{y}}_k = \mathbf{H}\mathbf{x}_k + \boldsymbol{\varepsilon}_k, \quad (7.22)$$

where the part of the measurement matrix corresponding to the attitude states is an identity matrix, $\tilde{\mathbf{y}}_k$ is the attitude measurements with covariance $\tilde{\mathbf{R}}_k$ which is updated inherently by SFM. The innovation in equation (7.16) is replaced by,

$$\mathbf{e}_k = \tilde{\mathbf{y}}_k - \hat{\mathbf{y}}_k \quad (7.23)$$

and equation (7.17) by,

$$\mathbf{S}_k = \mathbf{H}\mathbf{P}_k^{-1}\mathbf{H}^T + \tilde{\mathbf{R}}_k. \quad (7.24)$$

SFM-aided Kalman filters are expected to benefit from having the initial attitude determined by SFM, especially for the transient region of the estimations. According to Reference [4], the singular value decomposition (SVD) method is faster than the q method and more robust than the computationally fast methods e.g. FOAM and ESOQ [88]. In this regard, SVD, SVD-aided EKF, and conventional EKF estimation methods are implemented in the computer simulations in this work.

7.4.1 Measurement models of the attitude sensors

In this study, a spacecraft is considered to have two or three measurement sensors out of CSS, TAM, and RG, since these sensors are commonly used for spacecraft missions. Each CSS can be modeled using equation (7.7), which gives the current generated by one CSS in the body frame. For the platform, the sun direction measurement vector can be obtained as,

$$\mathbf{y}_{\text{css}} = \sum_{i=1}^{N_{\text{css}}} I_i \cdot \hat{\mathbf{n}}_{\text{css}_i}, \quad (7.25)$$

where $\hat{\mathbf{n}}_{\text{css}_i}$ is the unit normal vector of the i^{th} CSS cell and N_{css} is the number of CSSs.

TAM measurements can simply be modeled as,

$$\mathbf{B}_{\text{tam}} = [\mathbf{BN}] \mathbf{B}_{\text{model}} + \boldsymbol{\varepsilon}_{\text{tam}}, \quad (7.26)$$

where $[\mathbf{BN}]$ is the direction cosine matrix from inertial to the body frame, $\boldsymbol{\varepsilon}_{\text{tam}}$ is the zero-mean Gaussian magnetometer measurement noise vector, and $\mathbf{B}_{\text{model}}$ is the magnetic field model outputs, such as those of the international geomagnetic reference field (IGRF), world magnetic model (WMM), dipole model, etc. [6,169]. IGRF is used for this work.

Rate gyros are used in order to model the angular velocity of the spacecraft. The measurements can be modeled as,

$$\boldsymbol{\omega}_{\text{RG}} = \boldsymbol{\omega}_{\text{BN}} + \boldsymbol{\varepsilon}_{\text{RG}}, \quad (7.27)$$

where $\boldsymbol{\omega}_{RG}$ are the body measured angular rates based on the spacecraft dynamics model angular velocity $\boldsymbol{\omega}_{BN}$ of the body frame with respect to the inertial frame, and $\boldsymbol{\varepsilon}_{RG}$ is the zero-mean Gaussian gyroscope measurement noise vector.

7.5 Two-Stage Albedo Estimation Filter using Auto Regressive Model

This section presents a two-stage estimation using AR time-series approximation for the planet's albedo estimation. The AR model is based on a simple summing term, which uses a number of previous measurements, and a noise term as,

$$z_k = \sum_{i=1}^p (\varphi_i z_{k-i}) + \varepsilon_k, \quad (7.28)$$

where z_k represents one component of the albedo measurements (the difference between the sun sensor measurements in the body frame, and the sun direction model transformed into body frame using the spacecraft's attitude information), φ is the model parameters, p is the number of previous measurements to be used, and ε_k is the zero-mean Gaussian noise. Akaike criterion (AIC) can be used to determine the order of the AR model [170]. The first stage estimates the AR model parameters using the recursive least squares (RLS) method. By substituting the collected measurements of z_k , the matrix form of the measurement equation can be expressed as,

$$Y_k = \tilde{\mathbf{Z}}_k \boldsymbol{\Phi}_k + \varepsilon_k, \quad (7.29)$$

where $Y_k = z_k$, $\tilde{\mathbf{Z}}_k = [z_{k-1} \quad z_{k-2} \quad \cdots \quad z_1]$, $\boldsymbol{\Phi}_k = [\varphi_1 \quad \varphi_2 \quad \cdots \quad \varphi_{k-1}]^T$. The formula for the estimation of the model parameters can be written as [159],

$$\boldsymbol{\Phi}_{k+1} = \boldsymbol{\Phi}_k + \boldsymbol{\Xi}_k (Y_k - \tilde{\mathbf{Z}}_k \boldsymbol{\Phi}_k). \quad (7.30)$$

Here, the scaling ($\boldsymbol{\Xi}_k$) in the correction term is determined by,

$$\boldsymbol{\Xi}_k = \frac{1}{1 + \tilde{\mathbf{Z}}_k^T \boldsymbol{\Gamma}_k \tilde{\mathbf{Z}}_k} \boldsymbol{\Gamma}_k \tilde{\mathbf{Z}}_k^T, \quad (7.31)$$

where

$$\boldsymbol{\Gamma}_k = (\tilde{\mathbf{Z}}_k^T \tilde{\mathbf{Z}}_k)^{-1}. \quad (7.32)$$

The model parameters ($\boldsymbol{\Phi}_{k+1}$) estimated from equation (7.30) can be used in the second stage. The linear system is defined as [159],

$$\mathbf{X}_k = \mathbf{F}_k \mathbf{X}_{k-1} + \mathbf{B}_k \mathbf{U}_k, \quad (7.33)$$

and the measurement is,

$$\mathbf{Z}_k = \mathbf{H} \mathbf{X}_k + \mathbf{V}_k. \quad (7.34)$$

where $\mathbf{X}_k = [z_k \ z_{k-1} \ \dots \ z_{k-p+1}]^T$ is the state vector, $\mathbf{U}_k = [\varepsilon_k \ 0 \ \dots \ 0]^T$ is the zero-mean Gaussian noise vector with the process noise covariance matrix (\mathbf{Q}), \mathbf{V}_k is the zero-mean Gaussian noise vector with the measurement covariance matrix (\mathbf{R}), $\mathbf{H} = [1 \ 0 \ \dots \ 0]_{1 \times p}$ is the measurement matrix, and \mathbf{F}_k and \mathbf{B} are given as:

$$\mathbf{F}_k = \begin{bmatrix} \varphi_1 & \varphi_2 & \dots & \varphi_p \\ 1 & 0 & \dots & 0 \\ \vdots & \vdots & \ddots & \vdots \\ 0 & 0 & 0 & 0 \end{bmatrix}_{p \times p}, \quad (7.35)$$

$$\mathbf{B} = \begin{bmatrix} 1 & 0 & \dots & 0 \\ 0 & 0 & \dots & 0 \\ \vdots & \vdots & \ddots & \vdots \\ 0 & 0 & \dots & 0 \end{bmatrix}_{p \times p}. \quad (7.36)$$

The Kalman type filtering algorithm based on the defined system and the measurement functions estimate the albedo state vector using the same procedure described in the previous section defined the equation (7.16)–(7.20). The innovation in equation (7.16) is replaced by,

$$\mathbf{e}_k = \mathbf{Z}_k - \mathbf{H} \boldsymbol{\mu}_k^-. \quad (7.37)$$

The innovation covariance in equation (7.17) is replaced by,

$$\mathbf{S}_k = \mathbf{H} \mathbf{P}_k^- \mathbf{H}^T + \mathbf{R}. \quad (7.38)$$

Finally, the Kalman gain in equation (7.18) is replaced by,

$$\mathbf{K}_k = \mathbf{P}_k^- \mathbf{H}^T \mathbf{S}_k^{-1}, \quad (7.39)$$

for representing the Kalman filtering of the second stage estimation. By using the two-stage estimation form, the albedo of a planet can be estimated at each time step.

7.6 Analysis and Results

7.6.1 Earth's albedo data and sun sensor measurements

Eleven years of synoptic TOA and surface fluxes and clouds (SYN) 4.1 edition of Terra-Aqua satellite pair CERES data product is used with $1^\circ \times 1^\circ$ global grid of Earth. The global albedo for 11 years from 2008 to 2018 is presented using box plots for each month in Figure 7.8 under clear-sky and all-sky conditions. The small range of the box plots of each month demonstrates that the interannual albedo does not significantly change over the years for any month. While the averages slightly change or do not differ in years, values depending on the month grossly vary under both sky conditions with a similar trend. Especially the months between May and August, and the rest of the months are highly different than each other. The trend of the plots is similar for the clear-sky and all-sky cases. The lines on the figures are Fourier series model-based fitted curves to the mean values from the box plots of each month identified as the red color for the all-sky condition and blue for the clear-sky. All-sky condition is almost as twice as the clear-sky albedo averages. From the data, the global average of the albedo over the years and months is found to be about 0.23 under clear-sky and 0.37 under the all-sky condition.

The albedo coefficients given in Figure 7.9 are 11-year (2008-2018) averaged over 4 consecutive seasons as Season 1 (December-January-February), Season 2 (March-April-May), Season 3 (June-July-August), and Season 4 (September-October-November). The values are distributed based on the data under clear-sky and all-sky conditions globally. The albedo differentiates globally with the seasonal changes and with the sky conditions. The coefficients for each season and sky condition are presented by the maps prepared using the Hammer–Aitoff projection [171]. The null grids are shown with the white color, which is not excessive for the monthly mean data, and the continents with the black lines. In this way, the albedo dependency on the land coverage can be realized, which is more noticeable in the clear-sky condition than the all-sky. Because the cloud cover in the all-sky case causes the neighboring regions having similar albedo and reduces the ground cover effects. In addition to the cloud formations, the highest reflectivity are observed in the polar regions and Greenland [81].

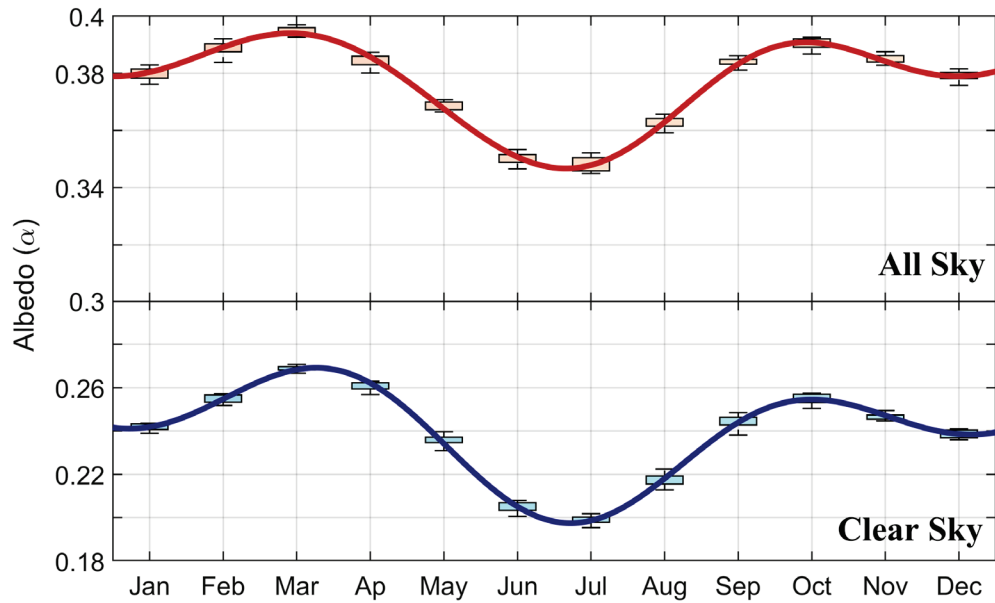


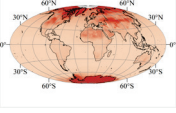
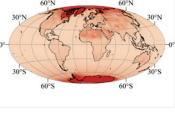
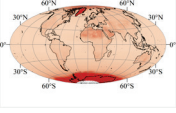
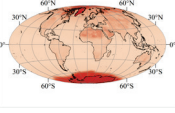
Figure 7.8 : Monthly albedo box plots for 11 years under clear-sky (bottom) and all-sky (top) conditions.

The albedo coefficients in Table 7.1 and Table 7.2 are also 11-year averaged values using spatial and seasonal scales. The spatial scales include global, tropics, polar, and midlatitude regions at the north (N) and south (S) hemispheres, while the seasonal scales have four-time intervals as described. The values are averaged based on clear-sky (Table 7.1) and all-sky (Table 7.2) conditions. The cells with no data are ignored in the averaging process. Several remarks can be itemized by looking at the albedo variations as,

- The maximum averaged albedo is at the polar regions under all cases.
- Albedo is the most effective in boreal winter (December-January-February) in the northern hemisphere and in austral winter (June-July-August) in the southern hemisphere under all cases.
- The peak values are found in the same spatial regions under the all-sky condition (minimum at the tropics and maximum at the polar south region).
- The peak values are found in slightly different spatial regions under clear-sky conditions.
- All values are greater in the all-sky case comparing to the clear-sky.

- The look-up table can be implemented for attitude estimation purposes by dividing the planet into spatial regions and seasonal periods for less computation instead of using every grid on the planet over several years.

Table 7.1 : 11-year averaged albedo coefficients over regions and seasons indicated (Clear-sky).

Averaging Scale	Season 1	Season 2	Season 3	Season 4
	Dec-Jan-Feb	Mar-Apr-May	Jun-Jul-Aug	Sep-Oct-Nov
				
Global	0.3017	0.2999	0.2704	0.2852
Polar North (60° – 90° N)	0.5310	0.5068	0.3093	0.4224
Midlatitude North (30° – 60° N)	0.2602	0.1798	0.1370	0.1792
Tropics (30° N – 30° S)	0.1210	0.1178	0.1195	0.1177
Midlatitude South (30° – 60° S)	0.1017	0.1476	0.1779	0.1165
Polar South (60° – 90° S)	0.4947	0.5475	0.6082	0.5905

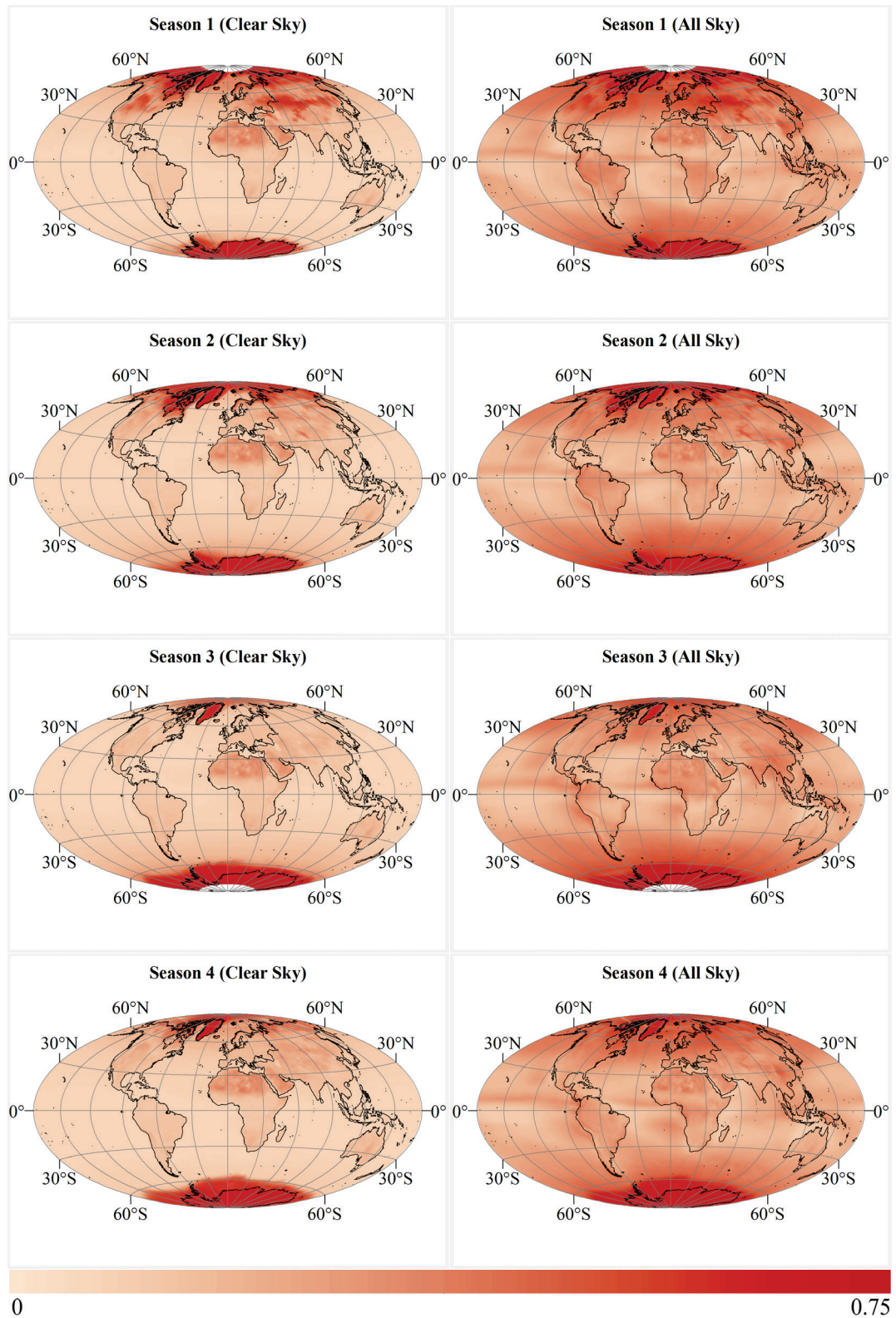
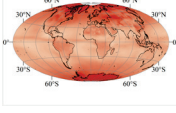
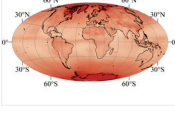
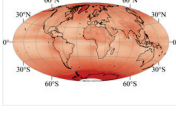
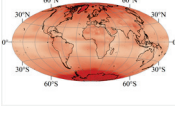


Figure 7.9 : 11-year averaged global albedo coefficients over 4-seasons under clear-sky (left) and all-sky (right) conditions.

Table 7.2 : 11-year averaged albedo coefficients over regions and seasons indicated (All-sky).

Averaging Scale	Season 1	Season 2	Season 3	Season 4
	Dec-Jan-Feb	Mar-Apr-May	Jun-Jul-Aug	Sep-Oct-Nov
				
Global	0.4346	0.4270	0.4110	0.4252
Polar North (60° – 90° N)	0.5910	0.5692	0.4636	0.5461
Midlatitude North (30° – 60° N)	0.4309	0.3465	0.3016	0.3536
Tropics (30° N – 30° S)	0.2350	0.2242	0.2361	0.2315
Midlatitude South (30° – 60° S)	0.3205	0.3687	0.3986	0.3414
Polar South (60° – 90° S)	0.5955	0.6261	0.6550	0.6535

For analyzing the effects of Earth’s albedo on CSS measurements, it is possible to use an arbitrary year rather than the exact year of spacecraft flight since the average values do not differ significantly in years by referring to Figure 7.8. The data sample averaged over an arbitrarily chosen year, 2018 is employed (Figure 7.6). A scenario is performed for observing the albedo effects on the CSS measurements particularly.

Here, CSS platforms are put on every face for convenience in Earth's albedo observation. Photo-diode placements on each CSS platform are illustrated in Figure 7.10 in platform coordinates $\{\hat{p}_1, \hat{p}_2, \hat{p}_3\}$. Each CSS has $\Delta = 60^\circ$ half field of view angle and is assumed to read a maximum of 1 A under direct sunlight.

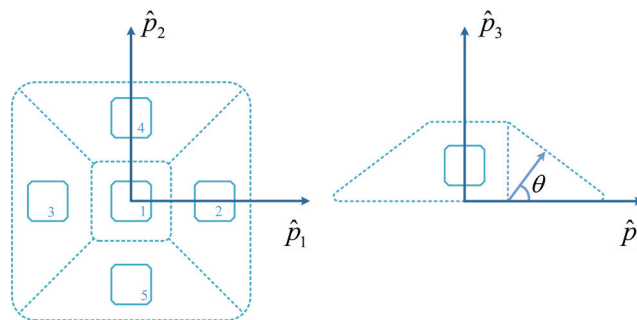


Figure 7.10 : Illustration of CSS placement on each platform.

For the first spacecraft setup, a fixed craft with no rotational dynamics is placed on the Sun-Earth line at 800 km altitude for simplicity in observing the CSS outputs. In Figure 7.11, the positions of the sun, spacecraft, and Earth are illustrated without scaling. In this scenario, a symmetrical behavior might be expected in CSS platform outputs on spacecraft-face-counterparts in terms of only sun exposure except for $+x$ and $-x$ directions. Here, $+x$ is pointing to the sun, and $-x$ to Earth. However, albedo also excites the CSS. The satellite faces are numbered respectively for $+x$, $+y$, $+z$, $-x$, $-y$, $-z$ directions in Figure 7.11.

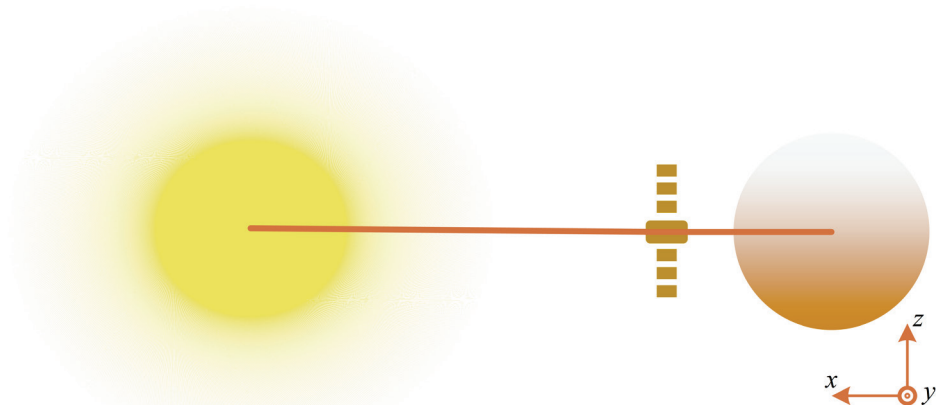


Figure 7.11 : Illustration of sun, spacecraft, and Earth positions for Scenario 1.

For the analysis, Face 4 ($-x$ direction) of the satellite, which is exposed only to Earth's albedo and not to the sun, is used. In order to inspect the parameter dependence of albedo, two parameters,

- Altitude
- Longitude

are tested by differentiating one parameter and fixing the others. The field of view of each CSS on Face-4, in which the outer frame is marked with a black line, can be seen in Figure 7.12. The base albedo map behind each region is the left panel (a) of Figure 7.6.

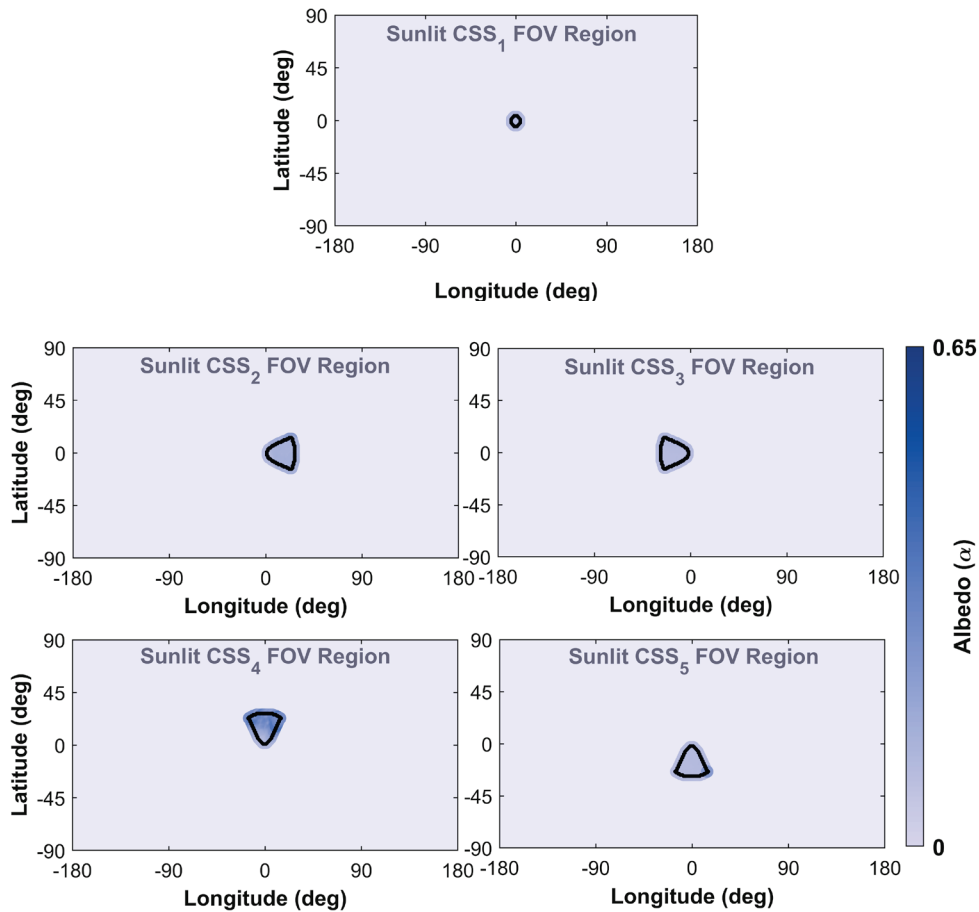


Figure 7.12 : CSS field of views on Face 4 of the satellite at 800 km altitude.

For better illustrative analysis, CSS-1 on Face-4 is presented. The CSS field of view region in the sunlit area of the planet in Figure 7.13 is marked with the colored base albedo map. The observed area is getting larger with rising altitude. However, even the observed area is getting larger, the current readings of each CSS caused by the albedo -without any noise on the sensor- decreases and converges to zero when going up from 500 km to 20,000 km altitude (see Figure 7.14) because of the inverse square law of the light intensity.

It is known that there is a large dependency on the latitude, but it is sometimes assumed that only a small dependency on longitude [9,81,172]. In order to inspect this assumption, the longitude dependency of the albedo on a CSS is examined for both cases (clear-sky and all-sky). CSS readings depending on the longitude changes are seen in Figure 7.15 for $\{60^\circ\text{N}, 30^\circ\text{N}, 0^\circ, 30^\circ\text{S}, 60^\circ\text{S}\}$ latitudinal lines. Even it is expected to have similar current readings caused by albedo when differentiating the longitude at high latitudes, outputs on the Panels 1 and 5 of the figures still highly depend on the longitude change of the spacecraft. In fact, 0° latitude differs the least

in the clear-sky case. The standard deviations are calculated respectively as $\sigma_{\text{clear}} = [0.018 \ 0.006 \ 0.004 \ 0.012 \ 0.018]$ for clear-sky condition, and $\sigma_{\text{all}} = [0.017 \ 0.005 \ 0.014 \ 0.011 \ 0.018]$ for all-sky. However, there is no regular trend seen for differentiating longitudes on the same latitude line; therefore, their effects need to be taken into account. The results from this examination are special to our case but point out that the albedo value at the instrument depends on the longitude. There might be some cases where the albedo is having almost a constant value on a latitude line or a region if several conditions meet simultaneously which is a rare case.

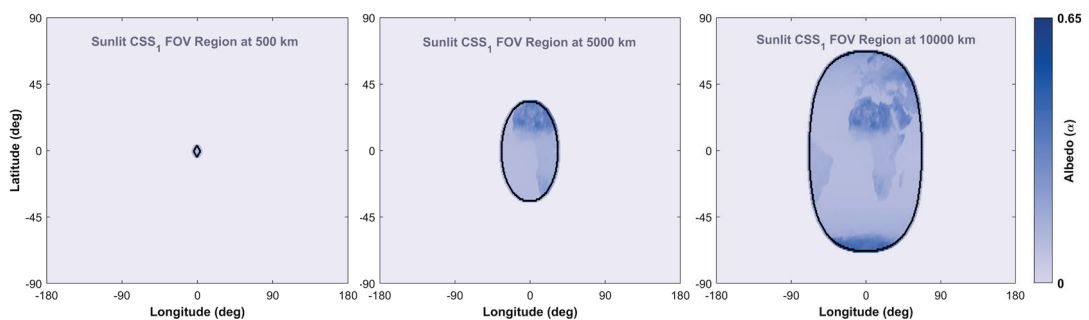


Figure 7.13 : CSS-1 field of view on Face 4 of the satellite at three different altitudes (left to right: 500 km, 5000 km, and 10000 km).

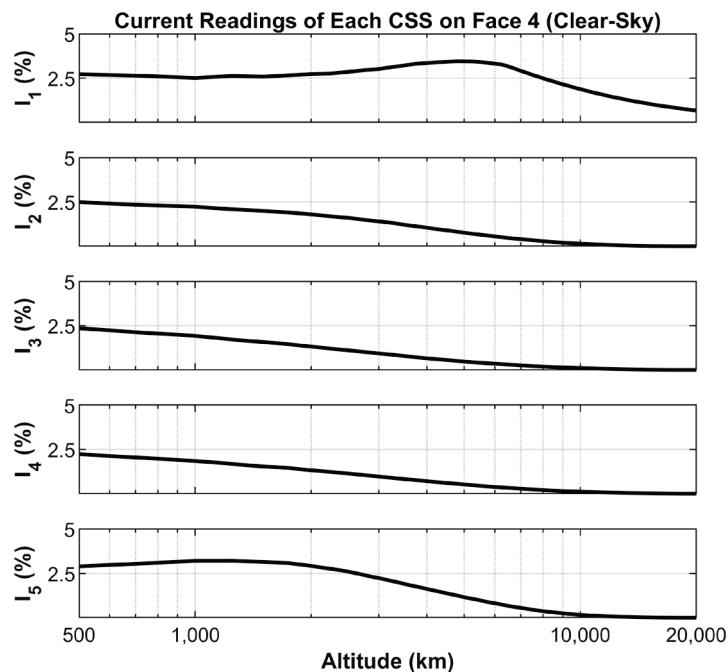


Figure 7.14 : Altitude dependent CSS current outputs on Face 4 of the satellite.

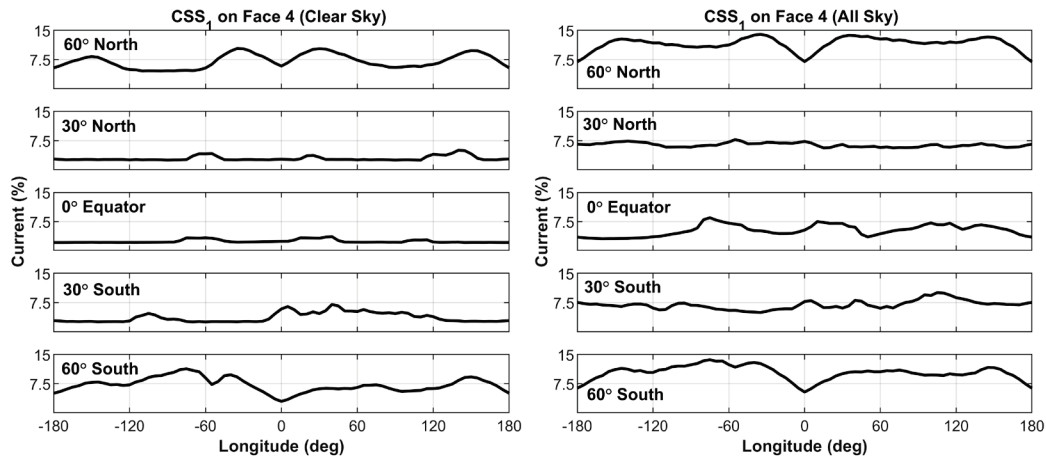


Figure 7.15 : Longitude dependent CSS-1 current outputs on Face 4 of the satellite at 800 km under clear-sky (left) and all-sky (right) conditions.

7.6.2 Spacecraft's attitude estimation using earth's albedo interfered sun sensors

In the second setup, the simulations are performed for a spacecraft with the principal moment of inertia $I = \text{diag}[0.055 \ 0.055 \ 0.017]$ kg m² on an almost circular near-Earth orbit with 730 km average altitude and with inclination $i = 96.5^\circ$ starting on 2018 March 1 or 2018 June 1 at 00:00 UTC. The spacecraft is tumbling during the simulations on an orbit propagated by employing the simplified general perturbation version 4 (SGP4) model introduced by Reference [121]. The sun direction is formulated using the model presented by Vallado [103]. The CSSs are processed at 1 Hz and corrupted by Gaussian zero-mean noise with a standard deviation of 2% (unitless).

The first part of this section is devoted to analyzing the albedo estimation using different albedo models. For this purpose, the models are divided into roughly two different categories of albedo data-based models (empirical albedo models), and the AR albedo model. The estimation procedures for each model category can be seen in Figure 7.16 (a) and (b) respectively. The attitude information for the sun direction vector transformation from inertial to body frame is assumed to be estimated by using star trackers with 1 arc second accuracy without considering any misalignments on the sensors. In Figure 7.16 (a), the albedo estimation procedure is based on the model requiring to find the sunlit area within the field of view of the sensor and to obtain the albedo coefficient data. Albedo estimation based on the AR model on the other hand does not require any of this information but a two-stage estimation. AR albedo model

is also tested for a one-stage estimation filter but the results were not promising so that only the two-stage estimation filter based on the AR model is proposed to be used for albedo estimation. The estimation procedures utilize the albedo measurements generated by the difference between the CSS's sun direction measurement vector and the modeled sun direction vector transformed into the body frame. However, as the albedo measurements are dependent on the CSS measurements directly, possible sensor-related continuous or time-varying biases will be treated as part of the albedo as well.

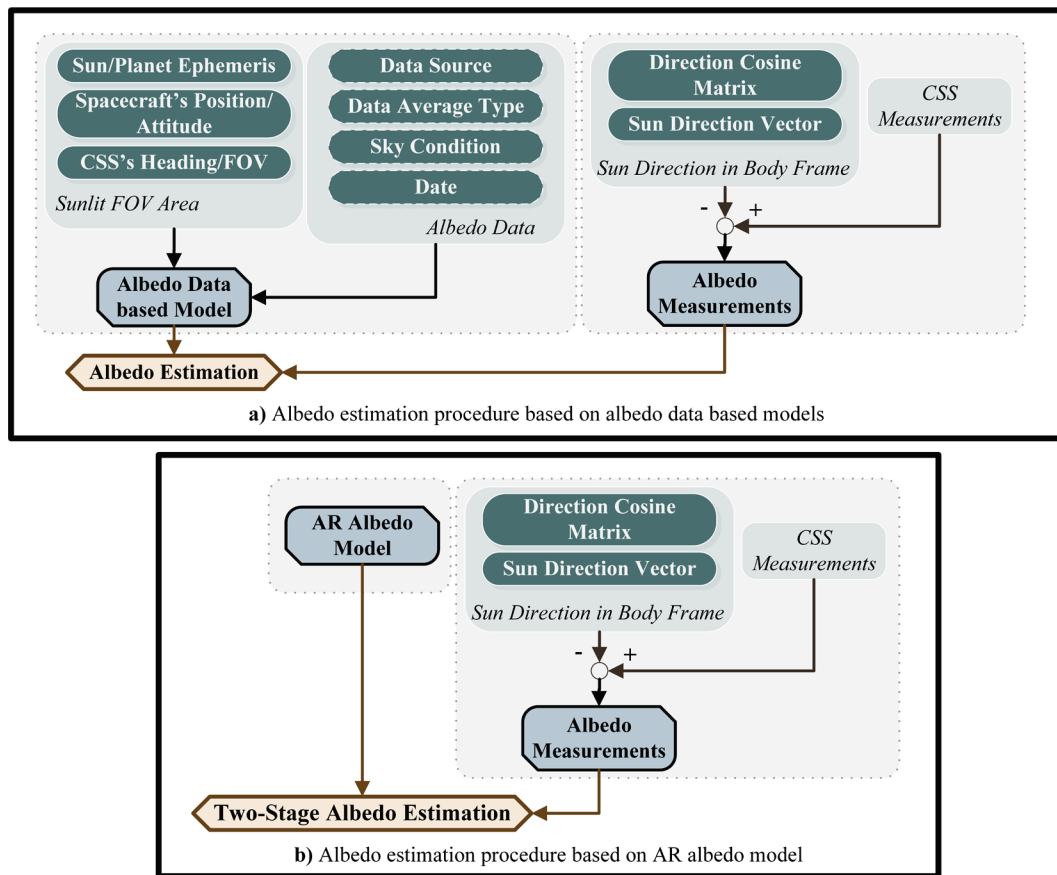


Figure 7.16 : Albedo estimation procedure based on albedo data based models (a) and AR albedo model (b).

The considered albedo models are presented in Table 7.3. The first two rows list the reference models used in creating the CSS measurements and the rest are selected to see the differences of the model outputs with respect to the references. More than 11 years of CERES albedo coefficient data of Earth is available for the public. So, the first reference model is based on one month-averaged data over March 2018 for the clear-sky condition while the second reference averaged over the 11 years of data from 2008 to 2018 for July under clear-sky. The first five albedo models are named by

sequential numbers and produced using CERES data or a constant value, and the last row shows the AR albedo model. Model 1 uses the albedo data averaged over March 2018 under all-sky. Model 2 uses the albedo data averaged over the whole year of 2018 under clear-sky. Model 3 uses the lookup table presented in Table 7.1. Model 4 and 5 are based upon the given constant values. Model 3 differs according to which spatial region of the instrument is looking at and in which season the spacecraft is flying. The references are based on two different months in our case, so Model 3 uses two seasons from the lookup table as Season 2 and 3 corresponding to Reference Models 1 and 2 respectively.

The albedo model outputs of Reference Model 1 and 2 are given for three orbits in Figure 7.17. There is no albedo contribution during the eclipse, as seen from the figure. Therefore, a portion of the simulation is analyzed. The first 1000 seconds are selected to be analyzed as the differences between the two reference models are more distinct. The albedo model outputs from several albedo models are presented in Figure 7.18 for comparing each one of them with Reference Model 1 on the left panel and Reference Model 2 on the right. As the same condition and configuration for the spacecraft and instrument are used, Models 1 to 5 do not differentiate from one case to another, except Model 3 with different seasonal values. From the results, it can be said that only the AR albedo model follows the reference models for both cases. Among the other albedo models, Model 4, which uses a constant albedo value $\alpha = 0.29$ over all spatial points on Earth, is superior under Reference Model 1 case, and Model 2 under Reference Model 2 case.

A complementary table is composed of albedo root mean square (RMS) error and the computational time for each model in Table 7.4. The RMS errors are calculated based on the albedo model outputs and the estimations with respect to the Reference Models. The RMS errors confirm the results of Figure 7.18. Albedo data-driven models are also processed under a conventional estimation filter in order to make a fair comparison with the AR albedo model, which is based on a two-stage estimation. The albedo estimations based on Models 1 to 5 give more than three times better accuracy than the AR model-based estimations. However, Models 1 to 5 depend on many parameters, unlike the AR model. In the meantime, the computational burden is lighter when it comes to the AR model as seen in Table 7.4. AR model does not require any data

processing at the beginning, and the total processing and estimation speed is around six times faster than the others.

Table 7.3 : Details of the models used for albedo estimation.

Model Name	Albedo Data	Average Type	Sky Condition	Additional Information
Reference Model 1 (Ref 1)	CERES	Monthly Average March 2018	Clear Sky	-
Reference Model 2 (Ref 2)	CERES	Monthly Average July 2008 - 2018	Clear Sky	-
Model 1	CERES	Monthly Average March 2018	All Sky	-
Model 2	CERES	Yearly Average 2018	Clear Sky	-
Model 3	CERES	Yearly Average 2008-2018	Clear Sky	Lookup table based on spatial and seasonal regions (see Table 7.1).
Model 4	Constant	-	-	$\alpha = 0.29$
Model 5	Constant	-	-	$\alpha = 0.15$
AR Model	-	-	-	No need to find the sunlit FOV area Model parameters to be estimated first

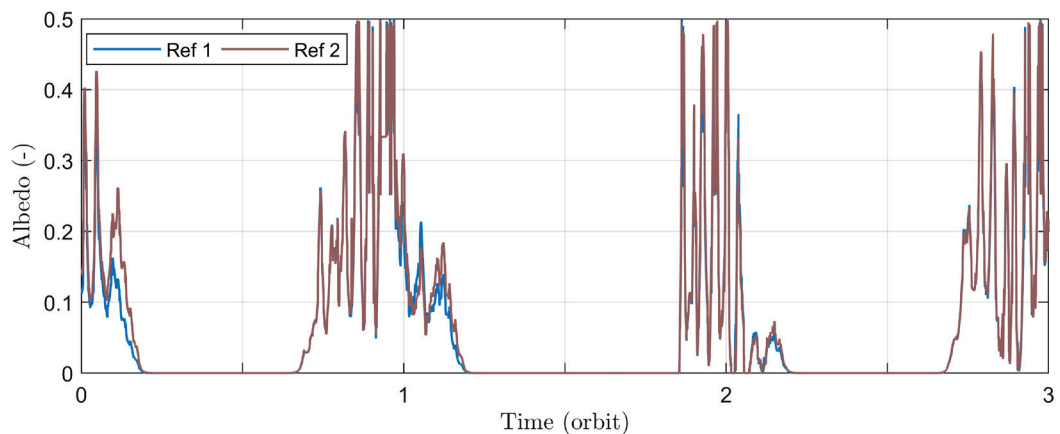


Figure 7.17 : Albedo model outputs of Reference Model 1 and 2 for three orbits.

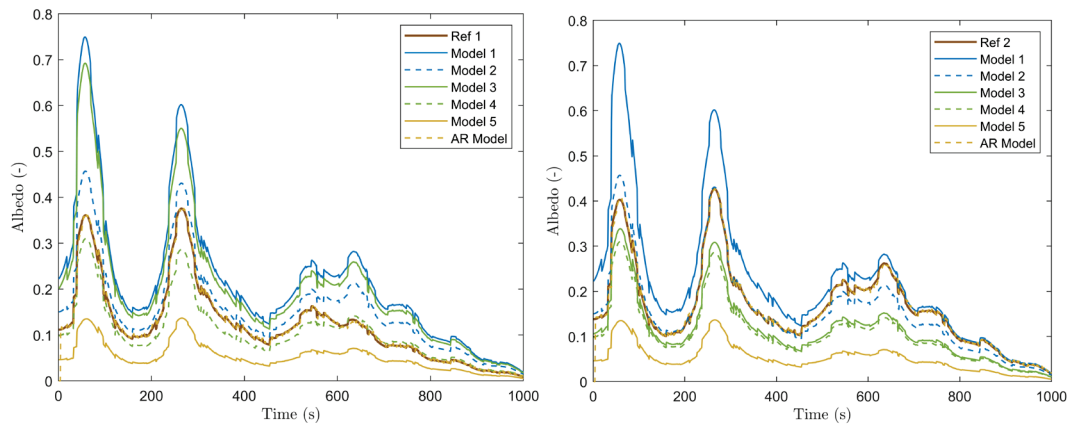


Figure 7.18 : Albedo model outputs of several models comparing to Reference Model 1 (left) and Reference Model 2 (right).

The limitation of the AR albedo model might be caused by inadequate or faulty albedo measurements as it highly depends on the measurements. For example, if there is a sensor-related bias on CSS in addition to the albedo, this will be compensated by the AR albedo model estimation procedure yet the albedo estimation will not represent the actual albedo this time. This might cause an issue for the other subsystems in need of estimated albedo information such as solar panels. On-ground calibration is suggested for preventing such a problem.

Attitude information is assumed to be known with high accuracy in the first part. As the AR albedo model is greatly dependent on the albedo measurements with a necessity of attitude information, albedo estimations are most likely to be disrupted in the case of no proper attitude information like a malfunction of the star trackers. If there are no star tracker outputs available, magnetometers and/or sun sensors could conceivably be used for attitude determination purposes. It is possible to use them separately as a single sensor in recursive estimation methods or together for an improved estimation. In the analysis, the estimations are first presented using TAM and CSS pair, then CSS without TAM. Using TAM measurements in the estimations is performed by closing the switches for TAM and Magnetic Field Model boxes seen in Figure 7.19 (a) and (b), and open switches are for not using them.

The albedo is assumed to be in the form of Reference Model 2 based on 11-year averaged July CERES albedo data under the clear-sky condition in all cases. A wrong albedo model in the form of Model 4 and AR model that does not require any information other than CSS measurements and attitude of the spacecraft is considered in the attitude and albedo estimation algorithms for comparison. The RG-driven

kinematic motion model is used for the attitude estimation filters in this study but the use of a dynamic model with no RGs is also an option [14,173].

The “Albedo Data based Model” box in Figure 7.19 (a) represents the wrong albedo model (Model 4) in the analysis. The CSS outputs are corrected by using the albedo models before using them in the attitude estimation methods. Attitude is represented by MRPs ($\sigma_{B/R}$) where B stands for the body and R for the reference (Earth-centered inertial) coordinates in the simulations but transformed into Euler 3-2-1 angles in degrees for presentation. The estimation error levels of the components vary between different simulations possibly due to the randomized values used in the models and the filters. Therefore, the attitude error norms are presented instead of giving the results in component-by-component.

The attitude error norms of the listed estimation methods are given in Figure 7.20 (a) using Model 4. The same procedure is applied by replacing Model 4 with the AR model as presented in Figure 7.19 (b). But this time the attitude error is a little more especially in the transient region until compensation at around 600th seconds seen in Figure 7.20 (b).

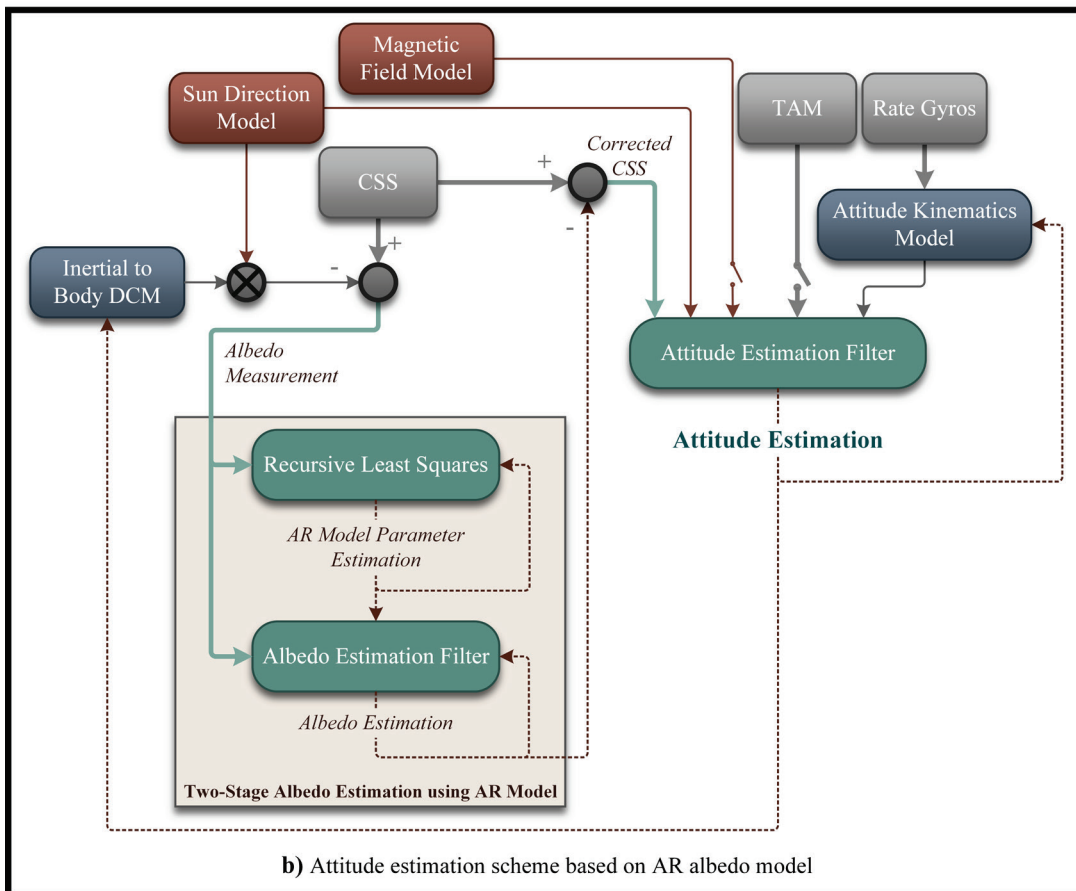
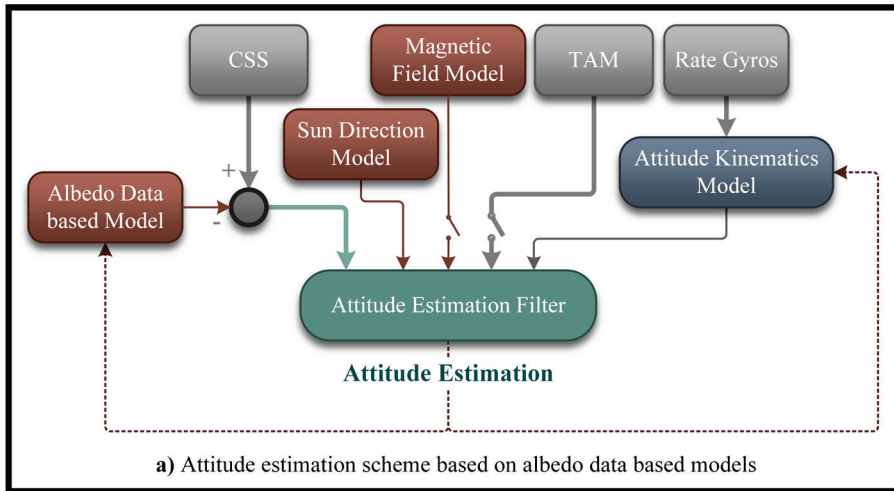


Figure 7.19 : Attitude estimation framework based on albedo data based models (a) and AR albedo model (b).

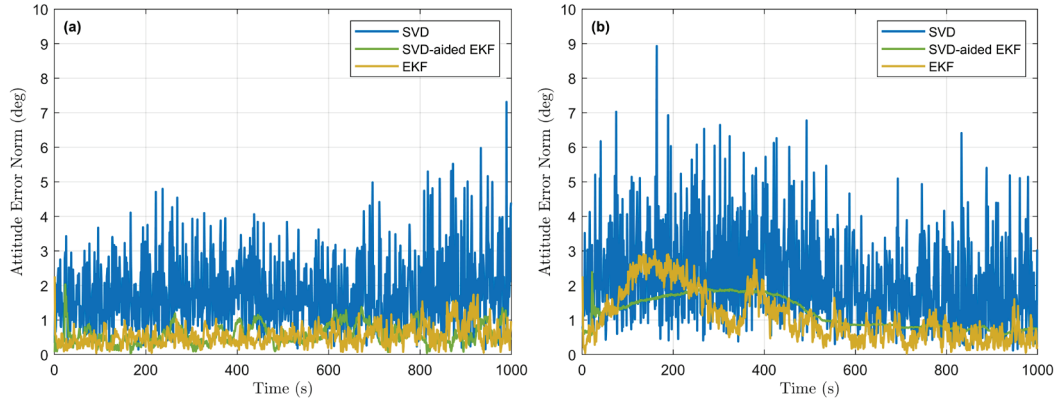


Figure 7.20 : Attitude error norms of the SVD, SVD-aided EKF and EKF methods using TAM and CSS with albedo interference based on Model 4 (a) and AR Model (b).

Table 7.4 : Performance comparison of the albedo models considered.

Model Name	RMS Error (-)				Computational Time (s)	
	Model Only		Estimation		Data Processing	Model Processing and Estimation
	Ref 1	Ref 2	Ref 1	Ref 2		
Model 1	0.1201	0.0902	0.0028	0.0027	1.3082	0.0188
Model 2	0.0395	0.0216	0.0028	0.0027	1.4038	0.0188
Model 3	0.0991	0.0612	0.0028	0.0027	0.0014	0.0188
Model 4	0.0277	0.0647	0.0028	0.0027	0.0004	0.0188
Model 5	0.0897	0.1274	0.0028	0.0027	0.0004	0.0188
AR Model	-	-	0.0094	0.0111	-	0.0030

It is possible to estimate the spacecraft's attitude using only one vector observation in the recursive estimation methods, CSS measurements are used in this case. The structures of Model 4 and AR Model-based estimation filters are shown in Figure 7.19 (a) and (b) respectively with open switches for magnetic field-related blocks. Having

the only CSS with albedo interference makes the results deteriorated more as seen in Figure 7.21 (a) and (b). The mean attitude estimation errors are given in Table 7.5.

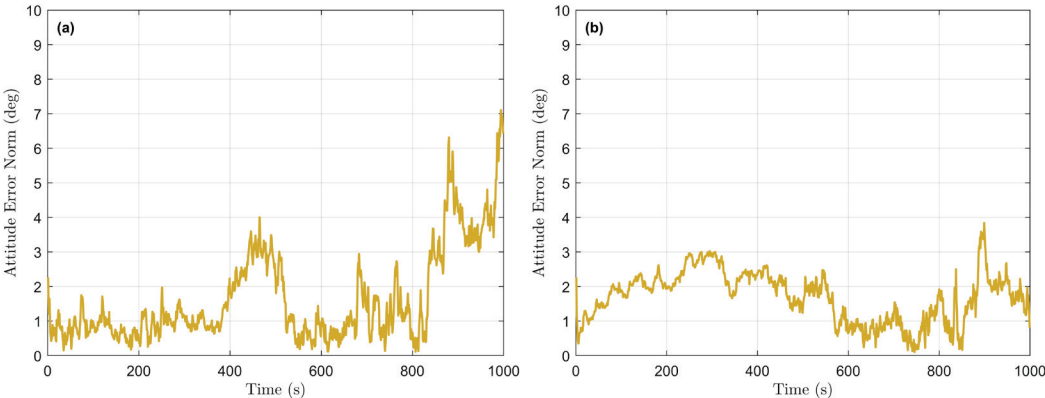


Figure 7.21 : Attitude error norms of EKF using CSS with albedo interference based on Model 4 (a) and AR Model (b).

Table 7.5 : Attitude angle estimation performance.

Sensor	Albedo Model	Mean Attitude Error (deg)		
		SVD	SVD-aided EKF	EKF
TAM and CSS	Model 4	1.87	0.58	0.54
	AR Model	2.35	1.45	1.09
CSS	Model 4	-	-	2.45
	AR Model	-	-	1.92

Table 7.6 is composed using normalized root mean square (NRMS) errors of attitude estimation averaged over 100 Monte Carlo simulations, which confirms the results except that EKF gives slightly improved results than presented in Figure 7.20 (b).

From the analyses, it is identified that albedo data-based models (Models 1-5) differ from the reference models case to case, but on the other hand, the AR albedo model follows the reference. So, it cannot be directly stated which model is the best among the five data-driven albedo models and they can only be evaluated case-by-case. For a fair comparison in the estimation sense, a conventional estimation filter is applied to the albedo models that also follow the reference trend like the AR albedo model. This comparison is made under the assumption of having highly accurate attitude

information from star trackers. In terms of computations, AR albedo model processing, and estimation speed are around six times faster than the others. Among the albedo data-based models, Model 4 ($\alpha = 0.29$) is found to be the best of confirming the first reference, and Model 2 (2018-yearly average) of confirming the second reference. Model 3 using the lookup table formed of seasonal and spatial regions underperformed from the expectations. Based on these, it is recommended to use the AR albedo model because of its consistency between cases. However, the AR albedo model is limited with the used albedo measurements which might include CSS-related bias. On-ground calibration is suggested for preventing such a problem.

Table 7.6 : Performance comparison of the attitude estimation algorithms considered (Averaged over 100 simulations).

Sensor	Method	Attitude NRMS Error (%)	
		Model 4	AR Model
	SVD	1.20	1.82
TAM and CSS	SVD-aided EKF	0.53	1.01
	EKF	0.38	0.38
CSS	EKF	2.34	1.70

Two sensor configurations and two albedo models (Model 4 and AR Model) are considered in the attitude estimation sense. Overall, EKF is an accurate attitude estimation method with less computational burden than the pre-processed filter (SVD-aided EKF) for TAM – CSS pair. It can be used in CSS-only case as well. The other attitude estimation methods can also be implemented using the proposed framework in Figure 7.19. TAM – CSS pair case provides the most accurate attitude estimation when using Model 4 corrections. CSS-only case, on the other hand, provides the most accurate attitude estimation when using AR Model corrections. Therefore, the albedo model to be used can be determined based on the configuration as well.

7.7 Conclusion

This study considers a spacecraft setup close enough to the sun and Earth receiving electromagnetic radiation of direct solar flux and reflected radiation namely albedo in which both are sensed by the sun sensors. Earth's albedo data are obtained from the CERES instrument. By evaluating the data, the maximum albedo of Earth is found in the polar regions and under all-sky conditions. Continental areas have higher albedo values, especially under clear-sky conditions. Albedo contributes to sun sensors from each incremental area of Earth in the sunlit area within the sensor field of view. The albedo intensity has a higher impact on sun sensors when getting closer to Earth.

The main purpose of this study is to find a simple model with less parameter dependency than the empirical albedo models. The second purpose is to estimate the attitude by comprising the corrected CSS measurements free from albedo so as to obtain better accuracy. AR albedo model is proposed, which does not use albedo coefficients depending on the position, time, ground, and cloud coverage parameters. To the best of our knowledge, the AR model is used in albedo estimation for the first time in this study. For comparison, five different models are evaluated under the albedo data-driven model in addition to the AR albedo model. The two-stage albedo estimation filter is applied based on the AR model so as to mitigate the albedo error source from the CSS measurements and to feed into the necessary subsystems. It is proposed to use the AR albedo model because of its simplicity and consistency between cases. However, spacecraft's attitude information is necessary to estimate the albedo based on the AR model. So, an attitude estimation procedure is also presented using the estimated albedo. The procedure is composed by estimating the albedo first and correcting the CSS after. In this way, it has the advantage that any albedo model is not considered in the last output equations of the attitude estimation filter. The attitude is estimated in accordance with two different sensor configurations by the Kalman-type estimation filters. Three-axis attitude is estimated with around 4° accuracy using only CSS measurements without any correction and around 2° accuracy when CSS is corrected by the AR model.

8. CONCLUSIONS AND RECOMMENDATIONS

The use of sun sensors and magnetometers in attitude estimation filters is examined for nanosatellites. In the presented SVD-aided EKF algorithm, the inputs are coming from SVD as the linear measurements of attitude angles and their error covariances. UD is factorizing the attitude angles error covariance with forming the measurements in order to obtain the appropriate inputs for the EKF. For malfunction scenarios in gyros, gyro and gyro-free cases are considered in the analysis. For the integration of SVD and EKF using the newly formed measurements and measurement noise covariance with UD factorization, the whole algorithm is run. SVD-aided EKF with assumption, which acts that the measurements are uncorrelated and removes the non-diagonal elements of the measurement noise covariance gives an overrated accuracy of the attitude angles. The attitude estimation method with UD factorization, on the other hand, provides a better attitude estimation accuracy. As the difference in the estimation results of the SVD-aided EKF with and without UD factorization is small enough, it can be said that the non-diagonal elements of SVD's angle error covariance matrix can be omitted from the input of the EKF, if high accuracy of error characteristics are not required or the computational load is limited. In case of an eclipse period, a switching based algorithm is suggested. The SVD-aided UKF is used when the sun sensor measurements are available; in the eclipse period the algorithm switches to the UKF.

Several other methods for estimating the spacecraft's orientation using magnetometer and coarse sun sensor measurements are reviewed and compared. The filters that cope well with different types of measurement faults have an adaptive rule for their measurement noise covariance. So, the filters cope with faulty measurement by adapting the scaling factors and having a lower gain. Single-frame method aided filter is found one of the computationally lightest filters and it deals with transient and long-term noise-increment faults reasonably well. It is identified that the outliers cause a difference in the estimation accuracy. If the measurement noises are non-Gaussian, the non-Gaussianity is a more significant source for estimation errors than nonlinearity

and it is more important to use the limited computational resources in nanosatellites to compensate for non-Gaussianity than using more complex nonlinear filters.

Two major environmental disturbances are examined under the spacecraft attitude estimation context, in this study. First, the effects of the geomagnetic disturbances on the satellite's attitude at LEO orbits are investigated. Two geomagnetic field models, IGRF and T89 are used. We found that both models differ from the observations during the geomagnetically active times as well as the quiet times. The differences are larger in the case of the IGRF model compared to the T89 model. The comparisons between the observed magnetic field vectors from two satellites, and that predicted by the models are obtained larger during the high geomagnetic periods. The angle between the magnetic field vector from the satellite measurements and models is shown to be smaller in the case of the T89 model, indicating that T89 model estimates are closer to the data. T89 model is expected to agree better with the observations, particularly during the geomagnetically active times. This is because it is constructed such that the model includes variations resulting from both internal sources from the Earth's dynamo and crust and also external sources such as solar wind, interplanetary magnetic field, consequently geomagnetic storms and substorms. The fact that IGRF shows larger discrepancies indicates that for better attitude predictions during especially geomagnetically active times, external sources are needed to be taken into account. The angle between the vector magnetic field from the models and the data is obtained less than 1° for C/NOFS and SWARM data. The differences between the satellites stem from the properties of the instruments used onboard these satellites. These differences imply that the model estimates the magnetic field orientations at the satellite location satisfactorily so that the angle between the vector magnetic fields is small. From the satellite attitude determination point of view, this agreement is very important. Although both models are seen to be appropriate for calculating the magnetic fields at the satellite position at LEO, it is clear that the IGRF model gives larger differences compared to the T89 model during both quiet and active times. The difference in the angle between the model and the observed magnetic field directions which is calculated less than 1° is within the acceptable range for small satellites, and both models can be used for attitude estimations within their error ranges. Both models have their advantages and disadvantages to be used in the attitude estimations. Since the differences are small, the ADCS developers may continue to use IGRF instead of

T89 to avoid its continuous need to acquire magnetic index data such as K_p , AE, and Dst on board the satellite. However, with the developing technology, the standard deviation of magnetometer measurement noise in small satellites is decreasing. This might expose the spacecraft to the external magnetic field more than the sensor noises. The selection of the model is especially important where high accuracy is needed for attitude estimation at LEO. The geomagnetic field models that are used to estimate the geomagnetic fields and satellite attitude angles are studied during the geomagnetically active and quiet days. The angles between the geomagnetic field vectors predicted by the models increase as the geomagnetic activity increase from quiet levels ($K_p = 0$) to strongly active days ($K_p \geq 6$) and it increases more over the high latitudes than over the equatorial regions especially during the strong activity days for $K_p \geq 6$. Similarly, it is shown that the magnetic field disturbances estimated from T89 at LEO are higher during the high geomagnetic activity as the satellite altitude becomes higher. Since this angle is one of the inputs in the attitude estimation filter, the satellite attitude angles will be sensitive to these variations. It is thus expected that the attitude angles will increase as the geomagnetic activity enhances, particularly at the high latitudes and at high altitudes. When only a magnetometer is used as an attitude sensor, the errors in the estimated attitude angles using the IGRF model are larger than the errors obtained by using the T89 model. EKF is used to estimate the attitude angles for different sensor configurations including magnetometer, sun sensor, and gyroscope for quiet and active times. The highest errors in the estimated attitude angles are obtained for magnetometer only and magnetometer plus gyroscope scenarios. During the quiet days, the presence of sun sensor reduces the errors in the estimated attitude angles, the gyroscope has less effect in the reduction of the errors. During the active days, while all scenarios give small errors, the magnetometer only and magnetometer and gyroscope scenarios show markedly the highest errors. The errors resulting from the geomagnetic disturbances are reduced drastically after we added the sun sensor measurements into the system. The most accurate results with the smallest errors are obtained for all sensor scenario. In this case, the estimated attitude angles are significantly improved and obtained close to the actual attitude angles. This study emphasizes the importance of the effects that the magnetic disturbances have on the attitude angles and helps to choose the right sensor combination during both quiet and disturbed times for better attitude estimation.

Another space environment disturbance is considered in the study for a spacecraft setup close enough to the sun and Earth receiving electromagnetic radiation of direct solar flux and reflected radiation, namely albedo, in which both are sensed by the sun sensors. Earth's albedo data are obtained from the CERES instrument. By evaluating the data, the maximum albedo of Earth is found in the polar regions and under all-sky conditions. Albedo contributes to sun sensors from each incremental area of Earth in the sunlit area within the sensor field of view. The albedo intensity has a higher impact on sun sensors when getting closer to Earth.

A simple model is designed with less parameter dependency than the empirical albedo models. And an attitude estimation procedure is designed by comprising the corrected CSS measurements free from albedo so as to obtain better accuracy. AR albedo model is proposed, which does not use albedo coefficients depending on the position, time, ground, and cloud coverage parameters. For comparison, different models are evaluated under the albedo data-driven model in addition to the AR albedo model. The two-stage albedo estimation filter is applied based on the AR model so as to mitigate the albedo error source from the CSS measurements and to feed into the necessary subsystems. It is proposed to use the AR albedo model because of its simplicity and consistency between cases. However, spacecraft's attitude information is necessary to estimate the albedo based on the AR model. So, an attitude estimation procedure is also presented using the estimated albedo. The procedure is composed by estimating the albedo first and correcting the CSS after. In this way, it has the advantage that any albedo model is not considered in the last output equations of the attitude estimation filter. Three-axis attitude is estimated in accordance with two different sensor configurations by the Kalman-type estimation filters.

Overall, attitude estimation filters are designed when two different environmental disturbances are applied to the spacecraft system. The consideration of the external magnetic field and planet's albedo models helps to get the simulated measurement model closer to the real case and to improve the reference models used in the filter. This, in the end, helps to improve the attitude estimation accuracy.

This research emphasizes improving the attitude estimation accuracy while not increasing the computational load much. To that end, Kalman filter extensions with less computational burden are examined. For further studies, different filters for measurements having non-Gaussian noises, could be implemented and compared with

the considered filters. Another interesting possibility would be to investigate whether the algorithms coping nonlinearities and non-Gaussianity could be fused into an algorithm that minimizes the nonlinearity and can cope with the heavy-tailed noises at the same time. For future work, algorithms can be tested for sensor faults of continuous bias type. This would require a calibration in which the state vector has more elements to be estimated.

For space environment disturbances, the analysis could be pursued with more detailed and enhanced analysis with different types of satellite orbits at different altitudes, within different near-Earth space environment conditions, not just LEO but also where the magnetometers are used for determination of the attitude angles of the satellite. For the external magnetic field model, there is a need for an activity index throughout the mission. This can be provided with telecommand by the ground stations but it would not be preferred in most of the spacecraft missions especially the nanosatellite missions. For this purpose, a lookup table can be composed for the onboard ADCS computer with date, position, known solar activity parameter inputs. Another option is to use machine learning techniques in estimating the activity index or directly the external magnetic field. This approach can also be used for estimating the planet's albedo for future studies.

REFERENCES

- [1] **Wertz, J. R.** (2002). *Spacecraft Attitude Determination and Control*, *Astrophysics and Space Science Library*, D.Reidel Publishing Company, Dordrecht, Holland.
- [2] **Schaub, H. and Junkins, J. L.** (2009). *Analytical Mechanics of Space Systems*, *Analytical Mechanics of Space Systems, Second Edition*, American Institute of Aeronautics and Astronautics, Reston, VA doi:10.2514/4.867231.
- [3] **Markley, F. L. and Crassidis, J. L.** (2014). *Fundamentals of Spacecraft Attitude Determination and Control*, Springer, New York doi:10.1007/978-1-4939-0802-8.
- [4] **Vinther, K., Jensen, K. F., Larsen, J. A. and Wisniewski, R.** (2011). Inexpensive Cubesat Attitude Estimation Using Quaternions And Unscented Kalman Filtering, *Autom. Control Aerosp.*, 4.
- [5] **Springmann, J. C. and Cutler, J. W.** (2014). Flight Results of a Low-cost Attitude Determination Systems, *Acta Astronaut.*, 99, 201–214.
- [6] **Thébault, E., Finlay, C. C., Beggan, C. D., Alken, P. and Al., E.** (2015). International Geomagnetic Reference Field: the 12th generation, *Earth, Planets Sp.*, 67, 79.
- [7] **Markley, F. L. and Crassidis, J. L.** (2014). Sensors and Actuators, in *Fundamentals of Spacecraft Attitude Determination and Control*, 123–181 doi:10.1007/978-1-4939-0802-8_4.
- [8] **Flatley, T. W. and Moore, W. A.** Report available at <<https://ntrs.nasa.gov/search.jsp?R=19940020024>>, date retrieved 7 January 2020. An Earth Albedo Model: A Mathematical Model for the Radiant Energy Input to an Orbiting Spacecraft Due to the Diffuse Reflectance of Solar Radiation From the Earth Below.
- [9] **Bhandari, D. and Bak, T.** (2005). Modeling Earth Albedo for Satellites in Earth Orbit, in *AIAA Guidance, Navigation, and Control Conference and Exhibit*, doi:10.2514/6.2005-6465.
- [10] **DaForno, R., Reali, F., Bristor, S. and Debei, S.** (2004). Autonomous Navigation of MegSat1: Attitude, Sensor Bias and Scale Factor Estimation by EKF and Magnetometer-Only Measurement, in *22nd AIAA International Communications Satellite Systems Conference and Exhibit*, doi:10.2514/6.2004-3183.
- [11] **Sekhavat, P., Gong, Q. and Ross, I. M.** (2007). NPSAT 1 Parameter Estimation using Unscented Kalman Filter, in *Proceedings of the 2007 American Control Conference*, 4445–4451 doi:10.1109/ACC.2007.4283031.

- [12] **Hajiyev, C. and Bahar, M.** (2003). Attitude Determination and Control System Design of the ITU-UUBF LEO1 Satellite, *Acta Astronaut.*, 52, 493–499.
- [13] **Ainscough, T., Zanetti, R., Christian, J. and Spanos, P. D.** (2015). Q Method Extended Kalman Filter, *J. Guid. Control. Dyn.*, 38, 752–760.
- [14] **Hajiyev, C., Cilden, D. and Somov, Y.** (2016). Gyro-free attitude and rate estimation for a small satellite using SVD and EKF, *Aerosp. Sci. Technol.*, 55, 324–331.
- [15] **Wahba, G.** (1965). Problem 65-1: A Least Squares Estimate of Satellite Attitude, *Soc. Ind. Appl. Math. Rev.*, 7, 409.
- [16] **Oshman, Y. and Markley, F. L.** (2000). Sequential gyroless attitude and attitude-rate estimation from vector observations, *Acta Astronaut.*, 46, 449–463.
- [17] **Markley, F. L.** (1999). Attitude determination using two vector measurements, *Flight Mechanics Symposium*, 39–52 doi:NASA/CP-19989-209235.
- [18] **Cordova-Alarcon, J. R., Mendoza-Barcenas, M. A. and Solis-Santome, A.** (2015). Attitude Determination System Based on Vector Observations for Satellites Experiencing Sun-Eclipse Phases, in *Multibody Mechatronic Systems*, (eds. Ceccarelli, M. & Martinez, E. E. H.) 75–85 doi:10.1007/978-3-319-09858-6_8.
- [19] **Psiaki, M. L., Martel, F. and Pal, P. K.** (1990). Three-axis attitude determination via Kalman filtering of magnetometer data, *J. Guid. Control Dyn.*, 13, 506–514.
- [20] **Soken, H. E. and Hajiyev, C.** (2014). Estimation of Pico Satellite Attitude Dynamics and External Torques via Unscented Kalman Filter, *J. Aerosp. Technol. Manag.*, 6, 149–157.
- [21] **Mimasu, B. Y., Van der Ha, J. C. and Narumi, T.** (2008). Attitude determination by magnetometer and gyros during eclipse, in *AIAA/AAS Astrodynamics Specialist Conference and Exhibit*, doi:10.2514/6.2008-6932.
- [22] **Mimasu, B. Y. and Van der Ha, J. C.** (2009). Attitude Determination Concept for QSAT, *Trans. Japan Soc. Aeronaut. Sp. Sci. Aerosp. Technol. Japan*, 7, 63–68.
- [23] **Quan, W., Xu, L., Zhang, H. and Fang, J.** (2013). Interlaced Optimal-REQUEST and unscented Kalman filtering for attitude determination, *Chinese J. Aeronaut.*, 26, 155–449.
- [24] **de Marina, H. G., Espinosa, F. and Santos, C.** (2012). Adaptive UAV Attitude Estimation Employing Unscented Kalman Filter, FOAM and Low-Cost MEMS Sensors, *Sensors*, 12, 9566–9585.
- [25] **Marins, J. L., Xiaoping Yun, Bachmann, E. R., McGhee, R. B. and Zyda, M. J.** An extended Kalman filter for quaternion-based orientation estimation using MARG sensors, in *Proceedings 2001 IEEE/RSJ International Conference on Intelligent Robots and Systems. Expanding the Societal Role of Robotics in the the Next Millennium (Cat. No.01CH37180)*, vol. 4 2003–2011.

- [26] **de Marina, H. G., Pereda, F. J., Giron-Sierra, J. M. and Espinosa, F.** (2012). UAV Attitude Estimation Using Unscented Kalman Filter and TRIAD, *IEEE Trans. Ind. Electron.*, 59, 4465–4474.
- [27] **Christian, J. A. and Lightsey, E. G.** (2010). Sequential optimal attitude recursion filter, *J. Guid. Control. Dyn.*, 33, 1787–1800.
- [28] **Raitoharju, M., García-Fernández, Á. and Piche, R.** (2016). Kullback-Leibler Divergence Approach to Partitioned Update Kalman Filter, *Signal Processing*, doi:10.1016/j.sigpro.2016.07.007.
- [29] **Ning, X., Ma, X., Peng, C., Quan, W. and Fang, J.** (2012). Analysis of filtering methods for satellite autonomous orbit determination using celestial and geomagnetic measurement, *Math. Probl. Eng.*, 2012, 1–16.
- [30] **Huang, Y., Zhang, Y., Li, N. and Chambers, J.** (2016). Robust student's t based nonlinear filter and smoother, *IEEE Trans. Aerosp. Electron. Syst.*, 52, 2586–2596.
- [31] **Piche, R., Sarkka, S. and Hartikainen, J.** (2012). Recursive outlier-robust filtering and smoothing for nonlinear systems using the multivariate student-t distribution, in *2012 IEEE International Workshop on Machine Learning for Signal Processing*, 1–6 doi:10.1109/MLSP.2012.6349794.
- [32] **Liu, X., Qu, H., Zhao, J., Yue, P. and Wang, M.** (2016). Maximum Correntropy Unscented Kalman Filter for Spacecraft Relative State Estimation., *Sensors*, 16.
- [33] **Xing, Y., Zhang, S., Zhang, J. and Cao, X.** (2012). Robust-extended Kalman filter for small satellite attitude estimation in the presence of measurement uncertainties and faults, *Proc. Inst. Mech. Eng. Part G J. Aerosp. Eng.*, 226, 30–41.
- [34] **Lee, D., Vukovich, G. and Lee, R.** (2017). Robust unscented Kalman filter for nanosat attitude estimation, *Int. J. Control. Autom. Syst.*, 15, 2161–2173.
- [35] **Soken, H. E., Hajiyev, C. and Sakai, S.** (2014). Robust Kalman Filtering for Small Satellite Attitude Estimation in the Presence of Measurement Faults, *Eur. J. Control*, 20, 64–72.
- [36] **Ovchinnikov, M. Y. and Ivanov, D. S.** (2014). Approach to study satellite attitude determination algorithms, *Acta Astronaut.*, 98, 133–137.
- [37] **Ma, H. and Xu, S.** (2014). Magnetometer-only attitude and angular velocity filtering estimation for attitude changing spacecraft, *Acta Astronaut.*, 102, 89–102.
- [38] **Mashtakov, Y., Ovchinnikov, M., Wöske, F., Rievers, B. and List, M.** (2020). Attitude determination & control system design for gravity recovery missions like GRACE, *Acta Astronaut.*, 173, 172–182.
- [39] **Ivanov, D., Ovchinnikov, M., Ivlev, N. and Karpenko, S.** (2015). Analytical study of microsatellite attitude determination algorithms, *Acta Astronaut.*, 116, 339–348.
- [40] **Alken, P.** <<https://www.ngdc.noaa.gov/IAGA/vmod/igrf.html>>, date retrieved

13/10/2020. International Geomagnetic Reference Field IGRF-13.

- [41] **Olsen, N., Hulot, G. and Sabaka, T. J.** (2010). Sources of the Geomagnetic Field and the Modern Data That Enable Their Investigation, in *Handbook of Geomathematics*, 105–124 doi:10.1007/978-3-642-01546-5_5.
- [42] **Constable, C.** (2016). Earth's Electromagnetic Environment, *Surveys in Geophysics*, vol. 37 27–45.
- [43] **Christensen, U. R.** (2019). Planetary Magnetic Fields and Dynamos, in *Oxford Research Encyclopedia of Planetary Science*, doi:10.1093/acrefore/9780190647926.013.31.
- [44] **Kilpua, E. K. J., Balogh, A., von Steiger, R. and Liu, Y. D.** (2017). Geoeffective Properties of Solar Transients and Stream Interaction Regions, *Space Science Reviews*, vol. 212 1271–1314.
- [45] **Mandea, M. and Chambodut, A.** (2020). Geomagnetic Field Processes and Their Implications for Space Weather, *Surveys in Geophysics*, vol. 41 1611–1627.
- [46] **Pirjola, R.** (2000). Geomagnetically induced currents during magnetic storms, *IEEE Trans. Plasma Sci.*, 28, 1867–1873.
- [47] **Zanetti, L. J. et al.** (1994). Ionospheric currents correlated with geomagnetic induced currents; Freja magnetic field measurements and the Sunburst Monitor System, *Geophys. Res. Lett.*, 21, 1867–1870.
- [48] **Alonso, R. and Shuster, M. D.** (2002). Attitude-Independent Magnetometer-Bias Determination: A Survey, *J. Astronaut. Sci.*, 50, 453–475.
- [49] **Alonso, R. and Shuster, M. D.** (2002). Two Step: A Fast Robust Algorithm for Attitude-Independent Magnetometer-Bias Determination, *he J. Astronaut. Sci.*, 50, 433–451.
- [50] **Inamori, T. and Nakasuka, S.** (2012). Application of Magnetic Sensors to Nano and Micro-Satellite Attitude Control Systems, in *Magnetic Sensors - Principles and Applications*, doi:10.5772/34307.
- [51] **Archer, M. O. et al.** (2015). The MAGIC of CINEMA: first in-flight science results from a miniaturised anisotropic magnetoresistive magnetometer, *Ann. Geophys.*, 33, 725–735.
- [52] **Cilden-Guler, D., Kaymaz, Z. and Hajiyev, C.** (2019). Assessment of Magnetic Storm Effects under Various Magnetometer Noise Levels for Satellite Attitude Estimation, in *9th International Conference on Recent Advances in Space Technologies (RAST)*, 769–773 doi:10.1109/RAST.2019.8767834.
- [53] **Inamori, T., Sako, N. and Nakasuka, S.** (2010). Strategy of Magnetometer Calibration for Nano-Satellite Missions and In-Orbit Performance, *AIAA Guidance, Navigation, and Control Conference*, vol. 7598.
- [54] **Inamori, T. et al.** (2016). Online Magnetometer Calibration in Consideration of Geomagnetic Anomalies Using Kalman Filters in Nanosatellites and Microsatellites, *J. Aerosp. Eng.*, 29, 04016046.
- [55] **Shorshi, G. and Bar-Itzhack, I. Y.** (1995). Satellite autonomous navigation based on magnetic field measurements, *J. Guid. Control. Dyn.*, 18, 843–

- [56] **Hough, M. E.** (2011). Orbit determination with improved covariance fidelity, including sensor measurement biases, *J. Guid. Control. Dyn.*, *34*, 903–911.
- [57] **Beaudoin, Y., Desbiens, A., Gagnon, E. and Landry, R.** (2018). Observability of satellite launcher navigation with INS, GPS, attitude sensors and reference trajectory, *Acta Astronaut.*, *142*, 277–288.
- [58] **Vorobev, A., Pilipenko, V., Sakharov, Y. and Selivanov, V.** (2019). Statistical relationships between variations of the geomagnetic field, auroral electrojet, and geomagnetically induced currents, *Solar-Terrestrial Phys.*, *5*, 35–42.
- [59] **Tozzi, R., Coco, I., De Michelis, P., Giannattasio, F. and Giannattasio, F.** (2018). Latitudinal dependence of geomagnetically induced currents during geomagnetic storms, *Ann. Geophys.*, *61*, GM448.
- [60] **Viljanen, A., Nevanlinna, H., Pajunpää, K. and Pulkkinen, A.** (2001). Time derivative of the horizontal geomagnetic field as an activity indicator, *Ann. Geophys.*, *19*, 1107–1118.
- [61] **Viljanen, A., Tanskanen, E. I. and Pulkkinen, A.** (2006). Relation between substorm characteristics and rapid temporal variations of the ground magnetic field, *Ann. Geophys.*, *24*, 725–733.
- [62] **Kalafatoğlu Eyigüler, E. C. and Kaymaz, Z.** (2017). Magnetic and electric field variations during geomagnetically active days over Turkey, *Adv. Sp. Res.*, *60*, 1921–1948.
- [63] **Fan, B., Li, Q. and Liu, T.** (2018). How Magnetic Disturbance Influences the Attitude and Heading in Magnetic and Inertial Sensor-Based Orientation Estimation, *Sensors*, *18*.
- [64] **Matteo, N. A. and Morton, Y. T.** (2011). Ionosphere Geomagnetic Field: Comparison of IGRF Model Prediction and Satellite Measurements 1991–2010, *Radio Sci.*, *46*.
- [65] **Cilden-Guler, D., Kaymaz, Z. and Hajiyev, C.** (2018). Evaluation of Geomagnetic Field Models using Magnetometer Measurements for Satellite Attitude Determination System at Low Earth Orbits: Case Studies, *Adv. Sp. Res.*, *61*, 513–529.
- [66] **Cilden, D., Kaymaz, Z. and Hajiyev, C.** (2015). Extraterrestrial magnetic field effects on attitude determination accuracy of small satellites, in *7th International Conference on Recent Advances in Space Technologies (RAST)*, 707–711 doi:10.1109/RAST.2015.7208433.
- [67] **Cilden-Guler, D. et al.** (2017). Geomagnetic Models at Low Earth Orbit and Their Use in Attitude Determination, in *8th International Conference on Recent Advances in Space Technologies (RAST)*, doi:10.1109/RAST.2017.8003011.
- [68] **Tsyganenko, N. A.** (1989). A Magnetospheric Magnetic Field Model with a Warped Tail Current Sheet, *Planet. Sp. Sci.*, *37*, 5.
- [69] **Tsyganenko, N. A.** <<http://geo.phys.spbu.ru/~tsyganenko/modeling.html>>

- [70] **Fairfield, D. H., Tsyganenko, N. A., Usmanov, A. V. and Malkov, M. V.** (1994). A large magnetosphere magnetic field database, *J. Geophys. Res.*, *99*, 11319.
- [71] **National Aeronautics and Space Administration.** Report available at <https://ntrs.nasa.gov/search.jsp?R=19710023628>, date retrieved 6 January 2020. Earth Albedo and Emitted Radiation.
- [72] **Kuvyrkin, G. N. and Menshaw, T. M.** (2016). Earth's Albedo Input to a Low-Earth-Orbit Satellite based on Local Albedo Coefficients, *J. Spacecr. Rockets*, *53*, 792–796.
- [73] **Peyrou-Lauga, R.** (2017). Using Real Earth Albedo and Earth IR Flux for Spacecraft Thermal Analysis, in *47th International Conference on Environmental Systems*.
- [74] **Bhandari, D.** (2006). Modeling Earth Albedo Currents On Sun Sensors for Improved Vector Observation, in *AIAA Guidance, Navigation, and Control Conference and Exhibit*, doi:10.2514/6.2006-6592.
- [75] **Lopes, R. V. F., Silva, A. R., Relloso, J., Absi, G. and Jun, Y.** (2011). Analysis of Albedo Effects on Coarse Sun Direction Determination Algorithms, in *22nd International Symposium on Space Flight Dynamics*.
- [76] **O'Keefe, S. A. and Schaub, H.** (2014). Sun-direction estimation using a partially underdetermined set of coarse sun sensors, *J. Astronaut. Sci.*, *61*, 85–106.
- [77] **O'Keefe, S. A. and Schaub, H.** (2017). Consider-Filter-Based On-Orbit Coarse Sun Sensor Calibration Sensitivity, *J. Guid. Control. Dyn.*, *40*, 1300–1303.
- [78] **O'Keefe, S. A. and Schaub, H.** (2015). On-Orbit Coarse Sun Sensor Calibration Sensitivity To Sensor And Model Error, in *AAS/AIAA Spaceflight Mechanics Meeting*, AAS 15-392.
- [79] **Springmann, J. C. and Cutler, J. W.** (2014). On-Orbit Calibration of Photodiodes for Attitude Determination, *J. Guid. Control. Dyn.*, *37*, 1808–1823.
- [80] **Brasoveanu, D. and Sedlak, J.** (1998). Analysis of Earth Albedo Effect on Sun Sensor Measurements based on Theoretical Model and Mission Experience, in *AAS/GSFC 13th International Symposium on Space Flight Dynamics*, vol. 1 435–447.
- [81] **Appel, P.** (2005). Attitude estimation from magnetometer and earth-albedo-corrected coarse sun sensor measurements, in *Acta Astronautica*, vol. 56 115–126.
- [82] **Cilden-Guler, D. and Hajiyev, C.** (2019). SVD-aided EKF attitude estimation with UD factorized measurement noise covariance, *Asian J. Control*, *21*, 1423–1432.
- [83] **Cilden, D., Soken, H. E. and Hajiyev, C.** (2017). Nanosatellite attitude estimation from vector measurements using SVD-AIDED UKF

- algorithm, *Metrol. Meas. Syst.*, 24, 113–125.
- [84] **Cilden-Guler, D., Raitoharju, M., Piche, R. and Hajiyev, C.** (2019). Nanosatellite attitude estimation using Kalman-type filters with non-Gaussian noise, *Aerosp. Sci. Technol.*, 92, 66–76.
- [85] **Cilden-Guler, D., Kaymaz, Z. and Hajiyev, C.** (2021). Geomagnetic disturbance effects on satellite attitude estimation, *Acta Astronaut.*, 180, 701–712.
- [86] **Cilden-Guler, D., Schaub, H., Hajiyev, C. and Kaymaz, Z.** (2021). Attitude Estimation with Albedo Interference on Sun Sensor Measurements, *J. Spacecr. Rockets*, 58, 148–163.
- [87] **Cilden, D., Conguroglu, E. S. and Hajiyev, C.** (2015). Covariance analysis of three-axis attitude determination using two vector measurements, in *7th International Conference on Recent Advances in Space Technologies (RAST)*, 701–706 doi:10.1109/RAST.2015.7208432.
- [88] **Markley, F. L. and Mortari, D.** (2000). Quaternion Attitude Estimation using Vector Observations, *J. Astronaut. Sci.*, 48, 359–380.
- [89] **Soken, H. E. and Hajiyev, C.** (2008). Unscented Kalman Filter Based Attitude Estimation of ITU-PSAT I Satellite Using Magnetometer Measurements, in *Proc. of the International Workshop on Small Satellites, New Missions and New Technologies*, 72–76.
- [90] **Hajiyev, C. and Cilden Guler, D.** (2017). Review on Gyroless Attitude Determination Methods for Small Satellites, *Prog. Aerosp. Sci.*, 90, 54–66.
- [91] **Hajiyev, C. and Bahar, M.** (2000). Multichannel Kalman Filter Based on Preliminary Data Compression for the Satellite Rotational Motion Parameters Identification, in *Proc. of the 3rd International Conference on Nonlinear Problems in Aviation and Aerospace*, vol. 1 277–284.
- [92] **Cilden-Guler, D. and Hajiyev, C.** (2017). Integrated SVD/EKF Attitude Estimation with UD Factorization of the Measurement Noise Covariance, in *8th International Conference on Recent Advances in Space Technologies (RAST)*, doi:10.1109/RAST.2017.8002963.
- [93] **Erisksson, K. R.** (2014). High Resolution Filter for Stable Spacecraft Attitude Estimation (Master's Thesis), KTH, School of Engineering Sciences (SCI), SWEDEN.
- [94] **Rhudy, M., Gu, Y., Gross, J., Gururajan, S. and Napolitano, M. R.** Sensitivity Analysis of Extended and Unscented Kalman Filters for Attitude Estimation, doi:10.2514/1.54899.
- [95] **Grewal, M. S. and Andrews, A. P.** (2001). *Kalman Filtering: Theory and Practice Using MATLAB*, John Wiley & Sons, Inc.,
- [96] **Cilden-Guler, D., Conguroglu, E. S. and Hajiyev, C.** (2017). Single-Frame Attitude Determination Methods for Nanosatellites, *Metrol. Meas. Syst.*, 24, 313–324.
- [97] **Saha, S. K.** (2003). Simulation of Industrial Manipulators Based on the UDU T Decomposition of Inertia Matrix, *Multibody Syst. Dyn.*, 9, 63–85.

- [98] **Soken, H. E. and Hajiyev, C.** (2012). UKF based in-flight calibration of magnetometers and rate gyros for pico satellite attitude determination, *Asian J. Control*, 14, 707–715.
- [99] **Hajiyev, C., Cilden, D. and Somov, Y.** (2015). Integrated SVD/EKF for small satellite attitude determination and rate gyro bias estimation, in *IFAC Proceedings Volumes (IFAC-PapersOnline)*, vol. 48 233–238.
- [100] **Cilden, D., Hajiyev, C. and Soken, H. E.** (2015). Attitude and Attitude Rate Estimation for a Nanosatellite Using SVD and UKF, in *7th International Conference on Recent Advances in Space Technologies (RAST)*, 695–700 doi:10.1109/RAST.2015.7208431.
- [101] **Alonso, R. and Shuster, M. D.** (2002). Complete Linear Attitude-Independent Magnetometer Calibration, *J. Astronaut. Sci.*, 50, 477–490.
- [102] **Soken, H. E. and Hajiyev, C.** (2012). UKF-Based Reconfigurable Attitude Parameters Estimation and Magnetometer Calibration, *IEEE Trans. Aerosp. Electron. Syst. Trans. Aerosp. Electron. Syst.*, 48, 2614–2627.
- [103] **Vallado, D. A.** (2007). *Fundamentals of Astrodynamics and Applications (3rd Ed.)*, *Space Technology Library*, vol. 21 Microcosm Press/Springer, USA.
- [104] **Julier, S. J., Uhlmann, J. K. and Durrant-Whyte, H. F.** (1995). A New Approach for Filtering Nonlinear Systems, in *American Control Conference*, vol. 3 1628–1632.
- [105] **Crassidis, J. L. and Markley, F. L.** (2003). Unscented Filtering for Spacecraft Attitude Estimation, *J. Guid. Control Dyn.*, 26, 536–542.
- [106] **Oshman, Y. and Dellus, F.** (2003). Spacecraft angular velocity estimation using sequential observations of a single directional vector, *J. Spacecr. Rockets*, 40, 234–247.
- [107] **Garcia-Fernandez, A. F., Svensson, L., Morelande, M. R. and Sarkka, S.** (2015). Posterior Linearization Filter: Principles and Implementation Using Sigma Points, *IEEE Trans. Signal Process.*, 63, 5561–5573.
- [108] **Raitoharju, M., Svensson, L., Garcia-Fernandez, A. F. and Piche, R.** (2018). Damped Posterior Linearization Filter, *IEEE Signal Process. Lett.*, 1–1 doi:10.1109/LSP.2018.2806304.
- [109] **Ito, K. and Xiong, K.** (2000). Gaussian filters for nonlinear filtering problems, *IEEE Trans. Automat. Contr.*, 45, 910–927.
- [110] **Wan, E. A. and Van Der Merwe, R.** (2000). The unscented Kalman filter for nonlinear estimation, in *Proceedings of the IEEE 2000 Adaptive Systems for Signal Processing, Communications, and Control Symposium (Cat. No.00EX373)*, 153–158 doi:10.1109/ASSPCC.2000.882463.
- [111] **Julier, S. J. and Uhlmann, J. K.** (1997). New extension of the Kalman filter to nonlinear systems, in *Proc. SPIE 3068, Signal Processing, Sensor Fusion, and Target Recognition VI*, (ed. Kadar, I.) vol. 3068.
- [112] **Mehra, R. K.** (1970). On the Identification of Variances and Adaptive Filtering, *IEEE Trans. Automat. Contr.*, 15, 175–184.

- [113] **Hajiyev, C.** (2012). Fault tolerant integrated radar/inertial altimeter based on Nonlinear Robust Adaptive Kalman filter, *Aerosp. Sci. Technol.*, *17*, 40–49.
- [114] **Kang, C. H., Kim, S. Y. and Park, C. G.** (2014). A GNSS Interference Identification and Tracking based on Adaptive Fading Kalman Filter, *IFAC Proc. Vol.*, *47*, 3250–3255.
- [115] **Scardua, L. A. and da Cruz, J. J.** (2017). Complete Offline Tuning of the Unscented Kalman Filter, *Automatica*, *80*, 54–61.
- [116] **Kullback, S. and Leibler, R. A.** (1951). On Information and Sufficiency, *Ann. Math. Stat.*, *22*, 79–86.
- [117] **Morelande, M. R. and Garcia-Fernandez, A. F.** (2013). Analysis of Kalman Filter Approximations for Nonlinear Measurements, *IEEE Trans. Signal Process.*, *61*, 5477–5484.
- [118] **Markley, F. L.** (1988). Attitude Determination Using Vector Observations and Singular Value Decomposition, *J. Astronaut. Sci.*, *36*, 245–258.
- [119] **Markley, F. L.** (1993). Attitude Determination Using Vector Observations: a Fast Optimal Matrix Algorithm, *J. Astronaut. Sci.*, *41*, 261–280.
- [120] **Hughes, P. C.** (2004). *Spacecraft Attitude Dynamics*, Dover Publications,.
- [121] **Vallado, D. A. and Crawford, P.** (2008). SGP4 orbit determination, in *AIAA/AAS Astrodynamics Specialist Conf.*, doi:10.2514/6.2008-6770.
- [122] **Fraser, M. D.** (2000). *Network models for control and processing*, Intellect,.
- [123] **Raitoharju, M., Piche, R. and Nurminen, H.** (2016). A Systematic Approach for Kalman-type Filtering with non-Gaussian Noises, in *Proceedings of the 19th International Conference on Information Fusion (Fusion 2016)*,.
- [124] **Url-1** <https://cdaweb.gsfc.nasa.gov/istp_public/>, date retrieved 29/07/2017. Coordinated Data Analysis Web (CDAWeb).
- [125] **Url-2** <<ftp://swarm-diss.eo.esa.int/>>, date retrieved 29/07/2017. Swarm Data Access - FTP.
- [126] **Farfield, D. H.** (1991). An Evaluation of the Tsyganenko Magnetic Field Model, *J. Geophys. Res.*, *96*, 1481–1494.
- [127] **Tsyganenko, N. A.** (1995). Modeling the Earth’s Magnetospheric Magnetic Field Confined within a Realistic Magnetopause, *J. Geophys. Res.*, *100*, 5599–5612.
- [128] **Peredo, M., Stern, D. P. and Tsyganenko, N. A.** (1993). Are existing magnetospheric models excessively stretched? , *J. Geophys. Res.*, *98*, 15,315-343,354.
- [129] **Olsen, N. et al.** (2006). CHAOS—a model of the Earth’s magnetic field derived from CHAMP, Ørsted, and SAC-C magnetic satellite data, *Geophys. J. Int.*, *166*, 67–75.
- [130] **Finlay, C. C., Olsen, N., Kotsiaros, S., Gillet, N. and Tøffner-Clausen, L.** <<http://www.spacecenter.dk/files/magnetic-models/CHAOS-6/>>, date retrieved 09/03/2017. The CHAOS-6 Geomagnetic Field Model.

- [131] **Maus, S., Manoj, C., Rauberg, J., Michaelis, I. and Lühr, H.** (2010). NOAA/NGDC candidate models for the 11th generation International Geomagnetic Reference Field and the concurrent release of the 6th generation Pomme magnetic model, *Earth Planets Space*, 62, 729–735.
- [132] **Lowes, F. J.** (2014). An estimate of the errors of the IGRF/DGRF fields 1945–2000, *Earth, Planets Sp.*, doi:10.1186/BF03352353.
- [133] **Russel, C. T.** (1971). Geophysical Coordinate Transformations, *Cosm. Electrodyn.*, 2, 184–196.
- [134] **Hapgood, M. A.** (1992). SPACE PHYSICS COORDINATE TRANSFORMATIONS : A USER GUIDE, *Plan. Sp. Sci*, 40, 71–717.
- [135] **Url-3** <<https://directory.eoportal.org/web/eoportal/satellite-missions/content/-/article/cnofs>>, date retrieved 11/08/2016. Communications/Navigation Outage Forecasting System (C/NOFS).
- [136] **European Space Agency.** <<https://directory.eoportal.org/web/eoportal/satellite-missions/s/swarm>>, date retrieved 11/08/2016. Swarm (Geomagnetic LEO Constellation).
- [137] **Krebs, G. D.** <http://space.skyrocket.de/doc_sdat/cnofs.htm>, date retrieved 11/08/2016. C/NOFS (Communications / Navigation Outage Forecasting System).
- [138] **Pfaff, R. et al.** (2010). Observations of DC electric fields in the low-latitude ionosphere and their variations with local time, longitude, and plasma density during extreme solar minimum, *J. Geophys. Res. Sp. Phys.*, 115, n/a-n/a.
- [139] **Pfaff, R.** <https://vefi.gsfc.nasa.gov/vefi/Resources/VEFI_DescriptionREV.pdf>, date retrieved 16/09/2017. Description of the Vector Electric Field Instrument (VEFI) on the C/NOFS Satellite.
- [140] **Lichten, S. M.** Report available at <<http://www.unoosa.org/documents/pdf/icg/activities/2008/icg3/22.pdf>>, date retrieved 16 September 2017. Cutting Edge GPS Science Applications.
- [141] **Data Analysis Center for Geomagnetism and Space Magnetism.** <<http://wdc.kugi.kyoto-u.ac.jp/wdc/Sec3.html>>, date retrieved 16/09/2017. Geomagnetic Data Service, Kyoto.
- [142] **Gonzalez, W. D. et al.** (1994). What is a geomagnetic storm?, *J. Geophys. Res.*, 99, 5771.
- [143] **Loewe, C. A. and Prölss, G. W.** (1997). Classification and mean behavior of magnetic storms, *J. Geophys. Res. Sp. Phys.*, 102, 14209–14213.
- [144] **NOAA.** <<http://www.swpc.noaa.gov/noaa-scales-explanation>>, date retrieved 29/07/2017. NOAA Space Weather Scales.
- [145] **Theil, S., Appel, P. and Schleicher, A.** (2003). Low Cost, Good Accuracy - Attitude Determination Using Magnetometer and Simple Sun Sensor, in *17th Annual AIAA/USU Conference on Small Satellites.*,
- [146] **Babcock, E. P. and Bretl, T.** (2011). CubeSat Attitude Determination via Kalman Filtering of Magnetometer and Solar Cell Data, in *25th Annual AIAA/USU Conference on Small Satellites.*,

- [147] **Natanson, G. A., Mclaughlin, S. F. and Nicklas, R. C.** (1990). A method of determining attitude from magnetometer data only, in *Flight Mechanics (Estimation Theory Symposium)*, 359–378.
- [148] **Kalman, R. E.** (1960). A New Approach to Linear Filtering and Prediction Problems, *Trans. ASME–Journal Basic Eng.*, 82, 35–45.
- [149] **Tsyganenko, N. A.** (1987). Global quantitative models of the geomagnetic field in the cislunar magnetosphere for different disturbance levels, *Planet. Space Sci.*, 35, 1347–1358.
- [150] **Tsyganenko, N. A.** (1990). Quantitative models of the magnetospheric magnetic field: Methods and results - A review, *Space Sci. Rev.*, 54, 75–186.
- [151] **Tsyganenko, N. A.** (1993). A global analytical representation of the magnetic field produced by the region 2 Birkeland currents and the partial ring current, *J. Geophys. Res. Sp. Phys.*, 98, 5677–5690.
- [152] **Tsyganenko, N. A.** (2002). A model of the near magnetosphere with a dawn-dusk asymmetry 1. Mathematical structure, *J. Geophys. Res. Sp. Phys.*, 107, SMP 12-1-SMP 12-15.
- [153] **Url-4** <<https://www.swpc.noaa.gov/products/planetary-k-index>>, date retrieved 13/10/2020. Planetary K-index | NOAA / NWS Space Weather Prediction Center.
- [154] **Url-5** <<https://www.gfz-potsdam.de/en/kp-index/>>, date retrieved 03/11/2020. Kp Index.
- [155] **Siebert, M. and Meyer, J.** (1996). Geomagnetic Activity Indices, in *The Upper Atmosphere*, (eds. Dieminger, W., Hartmann, G. K. & Leitinger, R.) 887–911 doi:10.1007/978-3-642-78717-1_26.
- [156] **Url-6** <https://www.ngdc.noaa.gov/stp/GEOMAG/kp_ap.html>, date retrieved 13/10/2020. Geomagnetic Kp and Ap Indices | NCEI.
- [157] **Ailliot, P. and Monbet, V.** (2012). Markov-switching autoregressive models for wind time series, *Environ. Model. Softw.*, 30, 92–101.
- [158] **Chandorkar, M., Camporeale, E. and Wing, S.** (2017). Probabilistic forecasting of the disturbance storm time index: An autoregressive Gaussian process approach, *Sp. Weather*, 15, 1004–1019.
- [159] **Wang, D., Xu, X., Yao, Y., Zhu, Y. and Tong, J.** (2019). A Hybrid Approach Based on Improved AR Model and MAA for INS/DVL Integrated Navigation Systems, *IEEE Access*, 7, 82794–82808.
- [160] **Narasimhappa, M.** (2019). Modeling of Inertial Rate Sensor Errors Using Autoregressive and Moving Average (ARMA) Models, in *Gyroscopes - Principles and Applications [Working Title]*, doi:10.5772/intechopen.86735.
- [161] **O’Keefe, S. A.** (2015). Autonomous Sun-Direction Estimation Using Partially Underdetermined Coarse Sun Sensor Configurations, *Aerospace Engineering Sciences Graduate Theses & Dissertations*.
- [162] **Titov, D. V. et al.** (2007). Radiation in the atmosphere of Venus, in 121–138 doi:10.1029/176GM08.

- [163] **Stephens, G. L. et al.** (2015). The albedo of Earth, *Rev. Geophys.*, 53, 141–163.
- [164] **Smith, M. J., Goodchild, M. F. and Longley, P. A.** (2018). Surface and Field Analysis, in *Geospatial Analysis: A Comprehensive Guide to Principle Techniques and Software Tools*, 339–425.
- [165] **Loeb, N. G. et al.** (2009). Toward Optimal Closure of the Earth’s Top of Atmosphere Radiation Budget, *J. Clim.*, 22, 748–766.
- [166] **Kato, S., Loeb, N. G., Rutan, D. A. and Rose, F. G.** (2015). Clouds and the Earth’s Radiant Energy System (CERES) Data Products for Climate Research, *J. Meteorol. Soc. Japan*, 93, 597–612.
- [167] **Karlgaard, C. D. and Schaub, H.** (2009). Nonsingular attitude filtering using modified rodrigues parameters, *J. Astronaut. Sci.*, 57, 777–791.
- [168] **Soken, H. E., Cilden, D. and Hajiyev, C.** (2016). Integration of single-frame and filtering methods for nanosatellite attitude estimation, in *Multisensor Attitude Estimation: Fundamental Concepts and Applications*, (eds. Fourati, H. & Belkhiat, D. E. C.) 463–484 doi:10.1201/9781315368795.
- [169] **Markley, F. and Crassidis, J.** (2014). Environment Models, in *Fundamentals of Spacecraft Attitude Determination and Control*, 403–425 doi:10.1007/978-1-4939-0802-8_11.
- [170] **Chen, L. et al.** (2014). Earth polar motion parameters high accuracy differential prediction, in *Lecture Notes in Electrical Engineering*, vol. 323 71–79.
- [171] **Snyder, J. P. and Voxland, P. M.** Report available at <<http://pubs.er.usgs.gov/publication/pp1453>> An album of map projections *Professional Paper*, doi:10.3133/pp1453.
- [172] **Khalifa, N. S. and Sharaf-Eldin, T. E.** (2013). Earth albedo perturbations on low earth orbit cubesats, *Int. J. Aeronaut. Sp. Sci.*, 14, 193–199.
- [173] **Burton, R., Rock, S., Springmann, J. and Cutler, J.** (2017). Online attitude determination of a passively magnetically stabilized spacecraft, *Acta Astronaut.*, 133, 269–281.

CURRICULUM VITAE

Name Surname : Demet ÇILDEN GÜLER

EDUCATION :

B.Sc.: 2014, Istanbul Technical University, Faculty of Aeronautics and Astronautics, Astronautical Engineering Department

M.Sc.: 2016, Istanbul Technical University, Graduate School, Aeronautics and Astronautics Engineering Department

PROFESSIONAL EXPERIENCE AND REWARDS:

2014 – Present: Teaching Assistant, Istanbul Medeniyet University.

2019 – 2020: Visiting Scholar, University of Colorado Boulder.

2017 – 2017: Visiting Scholar, Tampere University.

2015 – 2018: Research and Teaching Assistant, Istanbul Technical University.

2020: Gold Medal for “An Air Data Computer” Invention, 5th Istanbul International Inventions Fair (ISIF’20) by Turkish Patent and Trademark Office.

2020: Bronze Medal for “A Navigation System” Invention, 5th Istanbul International Inventions Fair (ISIF’20) by Turkish Patent and Trademark Office.

2018: Amelia Earhart Fellowship Award, Zonta International Foundation (The first student to receive this award by pursuing a Ph.D. at Istanbul Technical University).

2018: Best Oral Presentation Award, 9th International Conference on Mechanical and Aerospace Engineering.

2015: Best Student Paper Award, 7th International Conference on Recent Advances in Space Technologies.

PUBLICATIONS, PRESENTATIONS AND PATENTS ON THE THESIS:

International Publications in Journals (Science Citation Index (SCI) or SCI-Expanded)

- C. Hajiyev, **D. Cilden-Guler**, *Satellite Attitude Estimation using SVD-Aided EKF with Simultaneous Process and Measurement Covariance Adaptation*. Advances in Space Research, 2021. DOI: 10.1016/j.asr.2021.07.006 (accepted).

- **D. Cilden-Guler**, Z. Kaymaz, C. Hajiyev, *Geomagnetic Disturbance Effects on Satellite Attitude Estimation*. Acta Astronautica, 180, pp. 701-712, 2021. DOI: 10.1016/j.actaastro.2020.12.044.
- **D. Cilden-Guler**, H. Schaub, C. Hajiyev, Z. Kaymaz, *Attitude Estimation with Albedo Interference on Sun Sensor Measurements*. Journal of Spacecraft and Rockets, 58 (1), pp. 148-163, 2021. DOI: 10.2514/1.A34814.
- **D. Cilden-Guler**, C. Hajiyev. *SVD-aided EKF attitude estimation with UD factorized measurement noise covariance*. Asian Journal of Control, 21, pp. 1423-1432, 2019. DOI: 10.1002/asjc.1979.
- **D. Cilden-Guler**, M. Raitoharju, R. Piche, C. Hajiyev, *Nanosatellite attitude estimation using Kalman-type filters with non-Gaussian noise*. in Aerospace Science and Technology, 92, pp. 66-76, 2019 DOI: 10.1016/j.ast.2019.05.055.
- C. Hajiyev, H. E. Soken, and **D. Cilden-Guler**, *Nontraditional Attitude Filtering with Simultaneous Process and Measurement Covariance Adaptation*. in Journal of Aerospace Engineering, Vol.32 (5), pp. 04019054-1-13, 2019 DOI: 10.1061/(ASCE)AS.1943-5525.0001038.
- **D. Cilden-Guler**, Z. Kaymaz, C. Hajiyev. *Evaluation of geomagnetic field models using magnetometer measurements for satellite attitude determination system at low earth orbits: Case studies*, Advances in Space Research, 61 (1), pp. 513-529, 2018. DOI: <https://doi.org/10.1016/j.asr.2017.10.041>.
- **D. Cilden-Guler**, E.S. Conguroglu, C. Hajiyev. *Single-Frame Attitude Determination Methods for Nanosatellites*, Metrology and Measurement Systems, 24 (2), pp. 313–324, 2017. DOI: 10.1515/mms-2017-0023.
- C. Hajiyev and **D. Cilden Guler**, *Review on gyroless attitude determination methods for small satellites*. Progress in Aerospace Sciences, 90, pp. 54-66, 2017. DOI: 10.1016/j.paerosci.2017.03.003.
- **D. Cilden**, H.E. Soken, and C. Hajiyev. *Nanosatellite Attitude Estimation from Vector Measurements using SVD-aided UKF Algorithm*, Metrology and Measurement Systems, 24, pp. 113-128, 2017, DOI: 10.1515/mms-2017-0011.

The doctoral dissertation consists of six of the above scientific publications in accordance with the rules specified by the Graduate School of Istanbul Technical University. The publications are listed below in the same order as in the thesis:

1. **D. Cilden-Guler**, C. Hajiyev. *SVD-aided EKF attitude estimation with UD factorized measurement noise covariance*. Asian Journal of Control, 21, pp. 1423-1432, 2019. DOI: 10.1002/asjc.1979.
2. **D. Cilden**, H.E. Soken, and C. Hajiyev. *Nanosatellite Attitude Estimation from Vector Measurements using SVD-aided UKF Algorithm*, Metrology and Measurement Systems, 24, pp. 113-128, 2017, DOI: 10.1515/mms-2017-0011.
3. **D. Cilden-Guler**, M. Raitoharju, R. Piche, C. Hajiyev, *Nanosatellite attitude estimation using Kalman-type filters with non-Gaussian noise*. in Aerospace Science and Technology, 92, pp. 66-76, 2019 DOI: 10.1016/j.ast.2019.05.055.
4. **D. Cilden-Guler**, Z. Kaymaz, C. Hajiyev. *Evaluation of geomagnetic field models using magnetometer measurements for satellite attitude determination system at low earth orbits: Case studies*, Advances in Space Research, 61 (1), pp. 513-529, 2018. DOI: 10.1016/j.asr.2017.10.041.

5. **D. Cilden-Guler**, Z. Kaymaz, C. Hajiyev, *Geomagnetic Disturbance Effects on Satellite Attitude Estimation*. Acta Astronautica, 180, pp. 701-712, 2021. DOI: 10.1016/j.actaastro.2020.12.044.
6. **D. Cilden-Guler**, H. Schaub, C. Hajiyev, Z. Kaymaz, *Attitude Estimation with Albedo Interference on Sun Sensor Measurements*. Journal of Spacecraft and Rockets, 58 (1), pp. 148-163, 2021. DOI: 10.2514/1.A34814.

International Publications in Journals (Other Indexes)

- **D. Cilden Guler**, C. Hajiyev. *Singular Value Decomposition Based Satellite Attitude Determination Using Different Sensor Configurations*, International Journal of Metrology and Quality Engineering, EDP Sciences, 8 (15), DOI: 10.1051/ijmqe/2017010 (Scopus Index).
- C. Hajiyev, and **D. Cilden**, *Nontraditional Approach to Satellite Attitude Estimation*, International Journal of Control Systems and Robotics, 1, pp.19-28, ISSN:2367-8917, 2016 (Engineering Index).

International Book Chapters

- Soken, H. E., **Cilden, D.**, Hajiyev, C. Chapter 26: *Integration of Single-Frame and Filtering Methods for Nanosatellite Attitude Estimation* in Multisensor Attitude Estimation: Fundamental Concepts and Applications, CRC Press, ISBN 9781498745710, 2016. <https://www.crcpress.com/Multisensor-Attitude-Estimation-Fundamental-Concepts-and-Applications/Fourati-Belkhiat/p/book/9781498745710>

International Publications in Conference Proceedings

- C. Hajiyev, **D. Cilden-Guler**, *SVD-Aided EKF with Process Noise Covariance Adaptation Applied to Satellite Attitude Dynamics* in Proceedings of The Fourth International Workshop on Computer Modeling and Intelligent Systems (CMIS-2021). 27 April 2021: Zaporizhzhia, Ukraine.
- **D. Cilden Guler**, Z. Kaymaz, and C. Hajiyev, *Are External Magnetic Disturbances Suppressed by Magnetometer Noise when Estimating a Nanosatellite's Rotational Motion?* in 21st IFAC World Congress - 1st Virtual IFAC World Congress. 11-17 July 2020: Berlin, Germany.
- **D. Cilden Guler**, Z. Kaymaz and C. Hajiyev, *Assessment of Magnetic Storm Effects under Various Magnetometer Noise Levels for Satellite Attitude Estimation* in 9th International Conference on Recent Advances in Space Technologies. 11-14 June 2019: Istanbul, Turkey.
- **D. Cilden Guler**, and C. Hajiyev. *UD Factorization Based Non-Traditional Attitude Estimation of Nanosatellite with Rate Gyros FDI*, 18th IFAC International Conference on International Stability, Technology and Culture (TECIS), 13-15 September 2018, Baku, Azerbaijan. (Published in: IFAC-PapersOnLine, vol. 51, no. 30, pp. 95–100, Jan. 2018)
- C. Hajiyev, and **D. Cilden Guler**. *Gyroless Nanosatellite Attitude Estimation in Loss of Sun Sensor Measurements*, 18th IFAC International Conference on

International Stability, Technology and Culture (TECIS), 13-15 September 2018, Baku, Azerbaijan (One of the Finalists of the Young Author Award). (Published in: IFAC-PapersOnLine, vol. 51, no. 30, pp. 89–94, Jan. 2018.)

- **D. Cilden Guler**, Z. Kaymaz, and C. Hajiyev. *Attitude Estimation of Small Satellites in Consideration of Geomagnetic Field Anomalies*, 42nd COSPAR Scientific Assembly, 14-22 July 2018, Pasadena, California, USA. (Poster)
- **D. Cilden Guler**, and C. Hajiyev. *Attitude Estimation by SVD/EKF using Reformed Measurements and Decomposed Noise Covariance*, 9th International Conference on Mechanical and Aerospace Engineering (ICMAE). 10-13 July, 2018, Budapest, Hungary.
- C. Hajiyev, H.E. Soken, **D. Cilden Guler**. *Q-Adaptation of SVD-Aided UKF Algorithm for Nanosatellite Attitude Estimation*, The 20th World Congress of the International Federation of Automatic Control (IFAC), 9-14 July 2017, Toulouse, France.
- **D. Cilden Guler**, and C. Hajiyev. *Integrated SVD/EKF for Nano-satellite Attitude Determination In The Case Of Magnetometer Faults*, 7th European Conference for Aeronautics and Space Sciences (EUCASS). 3-6 July, 2017, Milan, Italy.
- **D. Cilden Guler** and C. Hajiyev. *Integrated SVD/EKF Attitude Estimation with UD Factorization of the Measurement Noise Covariance*. 8th International Conference on Recent Advances in Space Technologies 2017. Istanbul.
- **D. Cilden Guler**, Z. Kaymaz, and C. Hajiyev. *Geomagnetic Models at Low Earth Orbit and Their Use in Attitude Determination*. 8th International Conference on Recent Advances in Space Technologies 2017. Istanbul.
- H.E. Soken, C. Hajiyev, and **D. Cilden Guler**. *Nontraditional UKF Based Nanosatellite Attitude Estimation with the Process and Measurement Noise Covariances Adaptation*. 8th International Conference on Recent Advances in Space Technologies 2017. Istanbul.
- **D. Cilden Guler**, H.E. Soken, and C. Hajiyev. *Non-Traditional Robust UKF Against Attitude Sensors Faults*, 31th International Symposium on Space Technology and Science (ISTS). 3-9 June, 2017, Himegin Hall, Matsuyama-Ehime, Japan.

OTHER PUBLICATIONS, PRESENTATIONS AND PATENTS:

International Publications in Journals (SCI or SCI-Expanded)

- C. Hajiyev, U. Hacizade, **D. Cilden-Guler**, *Integration of barometric and GPS altimeters via adaptive data fusion algorithm*. International Journal of Adaptive Control and Signal Processing, 35 (1), pp. 2-14, 2021. DOI: 10.1002/acs.3184.

- C. Hajiyev, **D. Cilden-Guler**, U. Hacizade. *Two-Stage Kalman Filter for Fault Tolerant Estimation of Wind Speed and UAV Flight Parameters*. Measurement Science Review, 20 (1), pp. 35-42, 2020. DOI: 10.2478/msr-2020-0005.
- C. Hajiyev, **D. Cilden**, and Y. Somov. *Gyro-free attitude and rate estimation for a small satellite using SVD and EKF*, Aerospace Science and Technology, 55, pp.324-331, ISSN:1270-9638, 2016.

International Publications in Journals (Other Indexes)

- **D. Cilden-Guler**, C. Hajiyev, J. Dasdemiir *Fault Tolerant Control of Attitude Dynamics of Nanosatellites*, International Journal of Sustainable Aviation (IJSA), 4 (2), pp. 99-113, 2018. DOI: 10.1504/IJSA.2018.10015446. (ESCI Index)
- **D. Cilden-Guler**, H.E. Soken, C. Hajiyev, *Attitude and Rate Estimation for Nanosatellite from Vector Measurements Using SVD-Aided UKF Algorithm*, International Journal of Mathematical and Computational Methods, 2, 346-353, 2017.

International Books

- **D. Cilden Guler**, C. Hajiyev. *Gyroless Attitude Determination of Nanosatellites* (24 Feb 2017), LAP LAMBERT Academic Publishing, ISBN:978-3-330-04781-5.

International Publications in Conference Proceedings

- C. Hajiyev, **D. Cilden Guler**, and U. Hacizade, *EKF for Wind Speed Estimation and Sensor Fault Detection Using Pitot Tube Measurements* in 9th International Conference on Recent Advances in Space Technologies. 11-14 June 2019: Istanbul, Turkey.
- C. Hajiyev, **D. Cilden Guler**, and U. Hacizade, *Two-Stage Kalman Filter for Estimation of Wind Speed and UAV Flight Parameters Based on GPS/INS and Pitot Tube Measurements* in 9th International Conference on Recent Advances in Space Technologies. 11-14 June 2019: Istanbul, Turkey.
- C. Hajiyev, U. Hacizade, and **D. Cilden Guler**, *Data Fusion for Integrated Baro/GPS Altimeter* in 9th International Conference on Recent Advances in Space Technologies. 11-14 June 2019: Istanbul, Turkey.
- A. Kutlu, **D. Cilden Guler**, and C. Hajiyev. *Test Platform for Small Satellite Attitude Determination and Control System*, 9th International Conference on Mechanical and Aerospace Engineering (ICMAE). 10-13 July, 2018, Budapest, Hungary. (Best Oral Presentation Award)
- **D. Cilden Guler**, J. Dasdemiir, and C. Hajiyev. *Fault Tolerant Control of Attitude Dynamics of Nano Satellites*. 8th International Conference on Recent Advances in Space Technologies 2017. Istanbul.
- C. Hajiyev, **D. Cilden Guler**, and Y. Somov. *Attitude Determination of Nanosatellites in the Sun-Eclipse Phases*. 8th International Conference on Recent Advances in Space Technologies 2017. Istanbul.

- **D. Cilden**, and C. Hajiyev, *Attitude Determination and Uncertainty Analysis in Eclipse of Small LEO Satellites*, SIAM Conference on Uncertainty Quantification. 4-8 April 2016: Lausanne, Switzerland (Chair of the Session).
- C. Hajiyev, **D. Cilden**, and Y. Somov, *Integrated SVD/EKF for Small Satellite Attitude Determination and Rate Gyro Bias Estimation*, Workshop on Advanced Control and Navigation for Autonomous Aerospace Vehicles (ACNAAV). Seville, Spain.
- C. Hajiyev, **D. Cilden**, and Y. Somov, *Gyroless Attitude and Rate Estimation of Small Satellites Using Singular Value Decomposition and Extended Kalman Filter*, 16th International Carpathian Control Conference (ICCC). 2015: Szilvásvárad, Hungary.
- **D. Cilden**, Z. Kaymaz, and C. Hajiyev, *Comparison of Geomagnetic Field from Models and Satellite Observations for Attitude Determination Purposes*, 7th International Conference on Recent Advances in Space Technologies-RAST. 2015: Istanbul, Turkey.
- **D. Cilden**, E.S. Conguroglu, and C. Hajiyev, *Covariance Analysis of Three-Axis Attitude Determination Using Two Vector Measurements*, 7th International Conference on Recent Advances in Space Technologies-RAST. 2015: Istanbul, Turkey.
- **D. Cilden**, Z. Kaymaz, and C. Hajiyev, *Extraterrestrial Magnetic Field Effects on Attitude Determination Accuracy of Small Satellites*, 7th International Conference on Recent Advances in Space Technologies-RAST. 2015: Istanbul, Turkey.
- **D. Cilden**, H.E. Soken, and C. Hajiyev, *Attitude and Attitude Rate Estimation for a Nanosatellite Using SVD and UKF*, 7th International Conference on Recent Advances in Space Technologies-RAST. 2015: Istanbul, Turkey (Best Student Paper Award).
- C. Hajiyev and **D. Cilden**. *Integrated SVD/EKF for Small Satellite Attitude and Rate Estimation*, 6TH European Conference for Aeronautics and Space Sciences (EUCASS). 2015. Krakow, Poland.
- **D. Cilden** and C. Hajiyev. *Error Analysis of the Vector Measurements Based Attitude Determination Methods for Small Satellites*, International Symposium on Space Technology and Science (ISTS). 2015. Kobe, Hyogo, Japan.
- H.E. Soken, **D. Cilden**, and C. Hajiyev. *Attitude Estimation for Nanosatellites Using Singular Value Decomposition and Unscented Kalman Filter*, International Symposium on Space Technology and Science (ISTS). 2015. Kobe, Hyogo, Japan.
- E. Yakut, **D. Cilden**, C. Oran and E. Erdogan. *Meteorological Observations and Establishing a Base for Future Mars Missions (Poster)*, International Planetary Probe Workshop 11. 2014: Pasadena, California, USA.

- **D. Cilden**, E. Yakut, C. Oran *CubeSat Technology on Titan Exploration* (Poster), International Planetary Probe Workshop 10. 2013: San Jose, California, USA.

National Publications in Conference Proceedings

- Y. Cay, **D. Cilden**, A. Mirzai, N. Genckal, E. Aydin, I. Kirci, *Uzay Ortamında Gaz Giderme Laboratuvarı, Mikrouydu Görevi ISOLDE (In-Space Outgassing Laboratory Microsatellite Mission ISOLDE)*, 6. Ulusal Havacılık ve Uzay Konferansı (UHUK). 28-30 Sept 2016: Kocaeli, Turkey.
- **D. Cilden**, J. Daşdemir, and C. Hacıoğlu, *Uydunun Dönme Hareketinin Arıza Toleranslı Kontrolü (Fault Tolerant Control of the Satellite's Rotational Motion)*, Otomatik Kontrol Ulusal Toplantısı (TOK). 29 Sept - 1 Oct 2016: Eskişehir, Turkey.
- **D. Cilden**, C. Hacıoğlu. *Attitude Determination with Two and Three Vector Configurations on Small Satellites*, V. UHUK. 8-10 September 2014: Kayseri, Turkey, (in Turkish).

National Publications in Journals

- **D. Cilden**, C. Hacıoğlu. *Attitude Determination Methods using Vector Observations in Small Satellite*, Journal of Aeronautics and Space Technologies 07/2014; 7(2):35-43, DOI: 10.13140/2.1.3638.3365 (in Turkish).